EFFECTS OF INTENTIONALLY INTRODUCED MISMATCH STRAIN ON THE OPERATING CHARACTERISTICS AND TEMPERATURE PERFORMANCE OF InGaAsP/InP LONG WAVELENGTH SEMICONDUCTOR LASERS

By

JOHN DOUGLAS EVANS, B.Eng.

A Thesis
Submitted to the School of Graduate Studies
in Partial Fulfillment of the Requirements
for the Degree
Doctor of Philosophy

McMaster University

STRAINED InGaAsP/InP LONG WAVELENGTH SEMICONDUCTOR LASERS

DOCTOR OF PHILOSOPHY (1993) McMASTER UNIVERSITY
(Engineering Physics) Hamilton, Ontario

TITLE: Effects of Intentionally Introduced Mismatch Strain on the Operating Characteristics and Temperature Performance of InGaAsP/InP Long Wavelength Semiconductor Lasers

AUTHOR: John Douglas Evans, B.Eng. (McMaster University)

SUPERVISOR: Professor J. G. Simmons, and Professor D. A. Thompson

NUMBER OF PAGES: xxiii, 268

ABSTRACT

An investigation into the effects of material strain on the temperature sensitivity and operating characteristics of InGaAsP/InP strained-layer multiple-quantum-well (MQW) ridge-waveguide lasers is reported. This thesis contains the first comparison between the performance of strained and unstrained all quaternary MQW lasers having, not only similar emission wavelength, but also identical quantum well thicknesses. Results show that significant improvements in device performance can be obtained through the application of strain. These improvements include; a substantial reduction in the temperature sensitivity of laser threshold current, I_{th}; a reduction in I_{th}; an increase in maximum output power; an increase in the maximum operating temperature; and, and increase in the internal device efficiency, η. From investigations into the effects of strain, and QW width on the temperature performance of InGaAsP/InP lasers, the root of the temperature sensitivity of I_{th} is found to be much more complicated than can be explained by a single dominant physical process, as proposed by other authors. In addition the exponential relationship proposed by Pankove in 1968, which is commonly used to describe the I_{th}-T sensitivity in terms of the parameter, T_o, is found to be inappropriate. A new, relationship to describe the variation of I_{th} with temperature for InGaAsP/InP based lasers is proposed, and the parameter T_o is replaced by the parameter T_{max} which represents the lasers' maximum operating temperature. In addition an expression relating T_{max} to adjustable device parameters, such as: cavity length; facet reflectivity; optical confinement factor; internal efficiency; and transparency current density, is derived mathematically from an empirically determined relationship between the temperature rate of change of the threshold current density, $\nabla_T J_{th}$, and the threshold current density, J_{th}. Achieved are the highest reported maximum operating temperature (140°C) and largest characteristic temperature (T_o=88 K) for InGaAsP based lasers.

ACKNOWLEDGMENTS

I would very much like to express my appreciation to my supervisors Dr. Thompson and Dr. Simmons for their support, encouragement, and guidance, and also for their faith in me, and in allowing me considerable freedom in my choice of experimental investigations. I would also like to thank them for providing me with considerable financial support with regards to purchasing the experimental apparatus required to conduct the empirical investigations of this thesis. I would particularly like to thank Dr. Simmons for his: enthusiasm; his leadership; his beneficial, insightful and stimulating discussions; and, for introducing me to the world of Macintosh computers: without them writing this thesis would have been much more difficult, and important empirical findings would have been left undiscovered. I would also like to thank Dr. Simmons for all the challenging squash games, and for letting me win one once in a while.

I would also like to thank all the members of scientific staff at Bell Northern Research's Advanced Technology Lab in Ottawa for their kindness and support. In particular I would like to than Dr. J. Glinski, Dr. G. Chik and Dr. T. Makino for inviting me to work at the Advanced Technology Lab as a visiting scientist, and for getting me started on a very interesting and challenging research topic. I would additionally like to thank: Dr. N. Puetz for growing the laser structures for me; C. Tan and Dr. C. Miner for aiding me in obtaining TEM and scanning PL results; Dr. F. Shepherd, C. Maritan, and R. Bruce for processing the laser structures; and, L. Raine and Z. Husain for cleaving and bonding the laser devices. Thanks also go to L. Tarof for persuading me to participate in my first triathlon - it was fun.

In addition, financial support from the Natural Sciences and Engineering Research Council of Canada, the Ontario Center for Material Research and The Ontario Ministry of Colleges and Universities is also gratefully acknowledged.

Special thanks go to my family and friends for their moral support, especially during the emotionally trying times of the past few years. In particular I'd like to thank Anthony Vetter for his assistance and enthusiasm in the lab, for introducing me to the world of rock climbing, and especially for his support over the past few weeks. Finally I'd like to acknowledge the stress endured by those closest to my heart as a consequence of my preoccupation with finishing this thesis. In particular I would like to acknowledge Kelli-Anne Webb. I'm sorry it was so difficult.

TABLE OF CONTENTS

LIST OF FIGURES

LIST OF TABLES

CHAPTER 1: INTRODUCTION

1.0 QUANTUM WELL AND STRAINED QUANTUM WELL LASERS

Since the late 1970's the ability to epitaxially grow a semiconductor layer having one composition on another with a different composition has improved dramatically. With the development of growth techniques such as MBE and MOCVD it is now possible to grow such epitaxial layers with atomic scale precision in thickness. When a layer of semiconductor material having a small band-gap energy is epitaxially grown such that it becomes sandwiched between two semiconductor layers possessing larger band-gap energies, and when the thickness of the small band-gap epilayer is less than that of the effective Bohr radius of an electron (≈ 200Å), a quantum well is formed.

In the past decade quantum wells have gained increasing importance in a number of electronic, optical and optoelectronic devices including, resonant tunneling and high electron mobility transistors [Yokyoma, 1985,1986],[Capasso, 1985,1986],[Brennan, 1987], optical modulators [Chen, 1992],[Wood, 1988],[Guy, 1988] polarization insensitive amplifiers and wavelength tunable detectors and lasers [Okamoto, 1991],[Levine, 1988],[Choi, 1987]. Today, for performance considerations quantum well laser structures are preferred over double heterostructure type structures for most semiconductor laser applications [Zory, 1993].

The growing popularity of quantum well (QW) laser structures stems from the many performance advantages that can be obtained through their use in optoelectronic applications [Thijs, 1991], [Kasukawa, 1989]. For example, quantum confinement leads

to the creation of discrete energy levels for both electrons and holes within the well. Since the position of these discrete energy levels is dependent upon the geometry of the quantum well, quantum wells offer the ability to tune a laser's emission and detector's absorption wavelength, simply by adjusting the well dimensions. Quantum confinement also results in a modification to the density of states for carriers within the well. This modification to the density of states, along with the small thickness and energy level quantization in the well region, leads to lower laser threshold currents, higher output powers, higher differential gain (and therefore narrower linewidths which are important for long wavelength, long haul communications at λ=1.55μm) and better TE/TM mode selectivity for QW over bulk lasers [Okamoto, 1991], [Thijs, 1991],[Kano, 1993],[Namegaya, 1993], [Fukushima, 1993]. It has been found that even further improvements in both laser operating characteristics and wavelength tuneability can be obtained if material strain is introduced into the quantum well [Evans, 1992],[Thijs, 1991],[Zah, 1993],[Lipsanen, 1992],[Loehr, 1991]. Strain is created by epitaxially growing the quantum well such that it has a lattice constant that is different from that of the substrate, but is pseudomorphic in the growth state.

This thesis is primarily concerned with the effects of quantum well material strain on the performance of InGaAsP/InP multiple quantum well lasers and, in particular, the effects of strain on the temperature sensitivity of the threshold current and maximum operating temperature of these devices.

1.1 TEMPERATURE DEPENDENCE OF InGaAsP-InP BASED LASERS FOR USE IN OPTICAL COMMUNICATIONS

The usefulness of InGaAsP-InP based lasers for optical communications systems is now well established [Horikoshi, 1982] and stems from the ability of lasers with $In_{1-x}Ga_xAs_yP_{1-y}$ active regions to emit light at 1.55 μm and 1.3 μm which are the low loss

and the low dispersion wavelengths of optical fibers, respectively. When put to practical use, however, difficulties arise because the lasing characteristics of InGaAsP-based lasers, especially the threshold current, are very sensitive to temperature variations. Due to a marked increase in the operating current of these devices with increasing temperatures, as the laser diode experiences an increase in the ambient temperature, it may also experience increased heating due to ohmic losses. This increased heating causes a further increase in the threshold current of the laser; thus, thermal runaway eventually limits the temperature range for stable continuous wave (CW) operation of these devices.

The heat sink temperature of an InGaAsP/InP laser diode in a repeater of an optical communications line can exceed 50°C [Horikoshi, 1982]. Thus, because of the temperature sensitivity of the threshold current and, therefore, the laser output power, thermoelectric coolers are required in order to maintain and control the ambient temperature of the laser. However, thermoelectric coolers are an added cost in packaging, and can also require over one hundred times the power of the lasers they are keeping cool. Therefore, it is desirable to be able to design "coolerless" lasers which may operate at high temperatures without the assistance of thermoelectric coolers. Two approaches to designing lasers to operate at high temperatures can be taken. One approach is to attempt to decrease the threshold current of the laser and to minimize junction heating, for example, by thinning the substrates and bonding the lasers with the active region (p-side) down on a heat sink in order to minimize the temperature increases due to ohmic losses. A second approach is to clarify the origins of the temperature sensitivity of laser diodes and then, if possible, to remove them by appropriate design choices.

In the past twenty years or so, there has been considerable effort spent in attempting to explain the temperature dependence of the threshold current, I_{th}, of semiconductor lasers. A widely accepted relationship, first proposed by Pankove in 1968, is the empirically derived exponential relationship:

$$I_{th} = I_o \exp(T/T_o), \tag{1.1.1}$$

where T_o and I_o are the characteristic temperature and current, respectively, and are obtained experimentally. It is important to note that, in his original article, Pankove mentions that, although numerical data existed from sophisticated theoretical treatments of recombination and absorption in lasers, "there [was] no explicit demonstration that an exponential dependence [of the threshold current] on temperature should be obtained." Nevertheless, since first proposing this relationship, the temperature dependence of semiconductor lasers has been described in the literature in terms of the parameter T_o. From (1.1.1) it will be apparent that a high characteristic temperature, T_o, indicates that the laser threshold current is less sensitive to temperature variations.

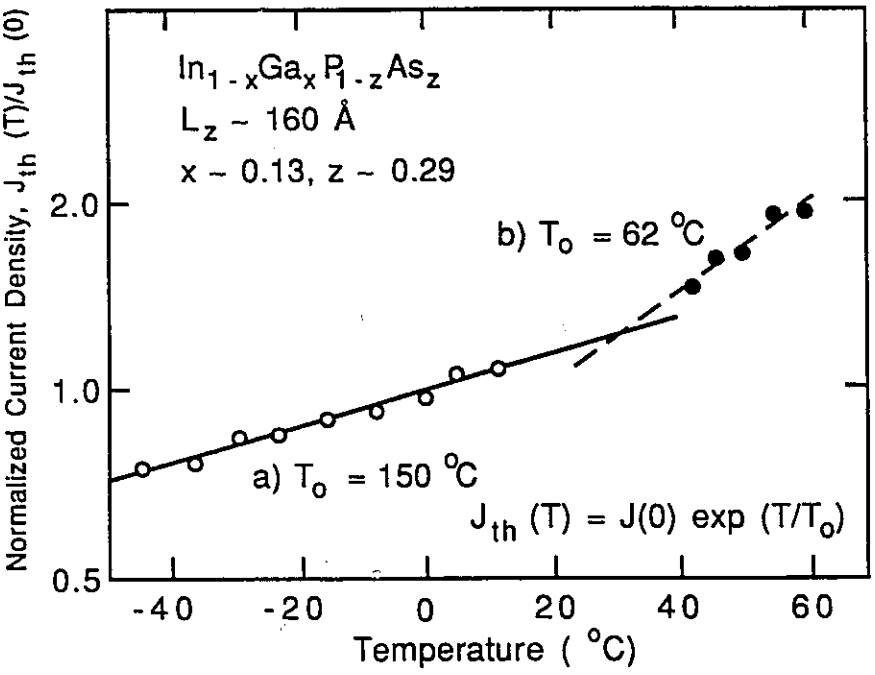

Figure 1.1: The temperature dependence of the normalized threshold current density for a multiple quantum-well quaternary heterostructure laser. The straight lines represent the least-squares fit of the data to (1.1.1). Below the break-point temperature of ≈ 300 K the diode is characterized by a T_o of ≈ 150°C [curve (a), solid line]. Above the break-point temperature the same diode exhibits a T_o of ≈ 62°C at higher temperatures [curve (b), broken line]. [From Rezek, 1980].

Although defined as characteristic parameters, *T_o and I_o actually vary with temperature!* T_0 for GaAs/AlGaAs bulk lasers is typically reported to be in the range of 120-180 K for 100 K<T<350K [Rezek, 1980], [Dutta, 1982]. For InGaAsP/InP devices, T_0 values are typically ≈ 110 K for temperatures below a "break point temperature" of about 285 K [Rezek, 1980], [Dutta, 1981] with a transition to a smaller value in the range of 40-70 K at room temperature [Agrawal, 1986], [Su, 1984], as shown in Fig. 1.1.

It has been found for GaAs/AlGaAs lasers that the use of quantum wells (QWs) in the active region results in an increase in T_0 over the values found for bulk double heterostructure (DH) lasers. For QW GaAs/AlGaAs lasers, T_0 is in the range 200-400 K [Dutta, 1982], [Hess, 1980], [Tsang, 1992]. This increase in T_0 for the QW over the DH lasers has been attributed to a weaker temperature dependence of the Fermi energies in a quasi-two-dimensional system, as well as a steeper optical gain *vs.* carrier density profile [Zhu, 1989] than that found in bulk semiconductors. However, no significant improvements in T_0 have been observed thus far for multiple quantum well (MQW) lasers over DH lasers in the InGaAsP/InP system [Tsang, 1992], [O'Gorman, 1992]. This observation and the smaller T_0 for InGaAsP/InP lasers in comparison to GaAs/AlGaAs lasers, suggests that the reduced T_0 for the quaternary-based lasers is due to a fundamental physical property of the quaternary materials.

The importance of InGaAsP/InP lasers for optical communications systems, and the variation of the operating characteristics of these devices with temperature, has lead many researchers to investigate the causes for the low T_0 in InGaAsP/InP-based lasers. The mechanisms proposed to explain the temperature dependence of these lasers and the existence of a "break point" temperature have been physical mechanisms which depend, or are proposed to depend, exponentially on temperature. It is likely that much of this work has been influenced by the existence of the exponential relationship proposed by Pankove in 1968. However, some of the literature that exists on the temperature dependence of the

threshold current notes that the I_{th} dependence on temperature shows more of a superlinear rather than an exponential relationship [Ettenberg, 1979]. Recently, Leopold, [1987] has suggested that (1.1.1) needs to be re-examined or is inappropriate. O'Gorman *et. al.* [1992] have recently pointed out that (1.1.1) is inappropriate and that an analogy exists between the statistical properties of laser light and thermodynamic phase transitions. According to O'Gorman *et. al.* the lasing component of the laser emission in long wavelength lasers has a temperature dependence that is well characterized by a power law (and not an exponential relationship) in direct analogy with the Landau-Ginzburg theory of second-order phase transitions.

1.2 MATERIAL COVERED IN THIS THESIS

In this thesis an extensive study of MQW and strained MQW lasers fabricated in the InGaAsP/InP material system is reported.

Chapter 2 of this thesis examines the effects and implications of quantization on laser performance, As well, the theoretical background relevant to the design of the InGaAsP multiple quantum-well (MQW) and strained MQW lasers, which are studied in this thesis, is developed.

Chapter 3 presents an overview of the physical mechanisms responsible for the temperature sensitivity of the laser threshold current in InGaAsP-InP based lasers. These physical mechanisms are discussed within the context of the phenomenological relationship proposed by Pankove in 1968 (equation (1.1.1)). The influence of the existence of this exponential relationship is illustrated and discussed.

Chapter 4 presents a description of the laser device structures grown and processed for the purposes of this thesis. The investigations of this thesis into the effects of strain and quantum-well structure on device performance is unique in comparison to the

investigations made by other authors in that, for the first time, strained and unstrained structures with the *same* quantum well thickness, and also similar emission wavelengths are compared. Previous studies into the effects of strain on device performance [Zou, 1993], have considered strained and unstrained MQW devices with different quantum-well (QW) thicknesses. Problems arise from a comparison between devices with different QW thicknesses because changes in the density of states for carriers due to strain cannot be separated from those changes due to quantum well thickness.

Chapter 4 also presents the method used to design the MQW laser structures studied for this thesis along with some example calculations. In addition, this chapter reviews and discusses the methodology for determining the magnitude of the $In_{1-x}Ga_xAs_yP_{1-y}$ material parameters which are required in order to perform the design calculations. These parameters include: the conduction- and valence-band effective masses; the material lattice constants and energy gaps; the magnitude of the conduction- and valence-band discontinuities at the heterojunction boundaries; the elastic stiffness and compliance constants, and the deformation potentials.

In Chapter 5 the results from the experimental investigations into the material quality and consistency of the laser structures studied in this thesis are presented. A knowledge and assurance of good crystal quality for the device structures is essential if one wishes to examine the effects of changing material parameters, such as QW width and strain on device performance. Otherwise, performance changes between devices could be attributed to, for example, a greater dislocation density in one structure over another. The crystal quality and uniformity of the laser structures studied in this thesis, as investigated by: cross-sectional and plan view transmission electron microscopy; polarization resolved photoluminescence (PL); scanning PL; and power and temperature dependent PL measurements, is found to be excellent for all device structures. Differences in the

temperature dependence of the peak PL wavelength are related to device performance in Chapter 6.

Chapter 6 presents the results of the empirical investigations into the effects of strain and quantum well thickness on the laser operating characteristics. Emphasis is placed on the temperature sensitivity of: the laser threshold current; internal efficiency; carrier leakage into the InP confinement regions; optical gain *vs.* injected current relations; and internal optical absorption losses. From an examination of the experimental results of this chapter, it is revealed that strain has a significant effect on such laser operating characteristics as: the maximum output power; the maximum operating temperature; the internal efficiency; the magnitude of the laser threshold current; and the laser linewidth. It is found from these investigation that, as discussed in Chapter 7, a combination of strain and quantization effects can be used to decrease the temperature sensitivity of the laser threshold current of InGaAsP lasers. In addition, it is found from these results that the temperature dependence of the laser threshold current is much more complicated than can be explained by a single dominant physical process, as proposed by many authors and reviewed in Chapter 3. It is concluded that Pankove's exponential relationship (1.1.1) is inappropriate to describe the temperature dependence of the laser threshold current. An examination of the results of Chapter 6 also show that the laser devices designed for this thesis have the highest ever obtained continuous wave (CW) characteristic temperature, T_o (88 K) and the highest ever observed CW maximum operating temperature (140°C) for quaternary-based semiconductor lasers emitting at a wavelength between 1.3 μm and 1.55 μm. These high values for T_o and the maximum operating temperature were obtained for a 1.5 per cent, compressively strained, MQW laser structure having five-38 Å thick QWs in the active region, and a single step-graded index separate-confinement heterostructure guiding region.

In Chapter 7, the concept of the characteristic temperature, T_o, is discarded and the temperature sensitivity of the laser threshold current is described in terms of the differential change in the laser threshold current density, J_{th}, with temperature, $\nabla_T J_{th}$. The parameter $\nabla_T J_{th}$ has been investigated in relation to the magnitude of the threshold current density, J_{th}. A strong power law correlation is found between $\nabla_T J_{th}$ and J_{th}, given by the expression

$$\frac{J_{th}^{\ m}}{\nabla_T J_{th}} = C, \qquad (1.3.1)$$

where, m appears to be universally constant with a value of $3/2 \pm 3\%$ for all devices, and C is determined to be related to the active region density of states. From the relation of (1.3.1), a mathematical relationship is derived to describe the temperature dependence of J_{th}. This new mathematical description of the temperature dependence of J_{th} is found to fit to the J_{th} *vs.* temperature data (correlation factor R=0.9999) much better than the exponential relationship proposed by Pankove, and over the entire temperature range of operation considered (-50°C to 100°C) in performing the measurements of Chapter 6.

The new mathematical J_{th}-T relation found in Chapter 7 is expected to have some physical significance as it relates J_{th} to the temperature through constants that, unlike I_o and T_o of (1.1.1), are truly constant independent of temperature. In addition, a constant representing the maximum operating temperature, T_{max}, of the laser is found from this mathematical expression. This new constant T_{max}, has much more physical significance than T_o since it gives information to the device designer on the maximum operating temperature of the laser. And, in the search for a "coolerless" laser, it is the maximum operating temperature, not T_o, that is important. The constant T_{max} is found to depend on device length: it increases with increasing device length. By relating the new expression for the temperature dependence of J_{th} to the theoretically derived (and experimentally

confirmed in this thesis) relation between J_{th} and device length, an expression for T_{max} in relation to other device parameters, apart from the laser cavity length is obtained. It is found from this additionally new expression that T_{max}, in addition to being related to the device cavity length, is also related to parameters such as: the facet reflectivity, R; the internal efficiency, η; the gain coefficient, β; the transparency current density, J_o; the internal absorption coefficient, α; and, the optical confinement factor, Γ. All of these parameters are adjustable by changing QW thickness, number of QWs and QW strain. Therefore, it is possible to optimize the maximum operating temperature of an InGaAsP semiconductor laser, by appropriate design choices, against such other factors as: laser linewidth; operating speed; threshold current density; and, external quantum efficiency.

Chapter 8 presents the conclusions of this thesis.

CHAPTER 2: QUANTUM WELL LASER THEORY

2.0 INTRODUCTION

This chapter introduces the concepts of energy level quantization for both electrons and holes in a quantum well. The dependence of the energy of the quantized levels on the dimensions of the quantum well is presented and the effect of energy level quantization on the density of states for carriers within the well is discussed. Following this discussion, the effects of energy level quantization and changes to the density of states on laser performance are revealed through an examination of the expression for the material gain of a quantum well structure as a function of the injected carrier density. Finally, the effects of strain on the quantum well band structure and the resulting implications on laser performance are developed and discussed.

2.1 SINGLE AND MULTIPLE QUANTUM WELL ENERGY SOLUTIONS

Figure 2.1 shows schematically the energy band structure (at $\mathbf{k}$ =0, where $\mathbf{k}$ is the electron momentum vector) *vs.* growth direction for a single quantum well structure. An electron or hole traveling perpendicular to the small band-gap quantum well layer (z-direction) may become trapped in the quantum well by giving up some of its energy to optical phonons through successive electron-phonon interactions. Once an electron or hole is trapped by the well the momentum vector, $\mathbf{k_z}$, for that carrier becomes quantized. The quantization of the perpendicular momentum vector gives rise to discrete band edge ($\mathbf{k_{x,y}}$ = **0**) energy levels within the well. A description of how these energy levels are

determined for carriers in both the non-degenerate conduction band and in the degenerate valence bands is presented separately below.

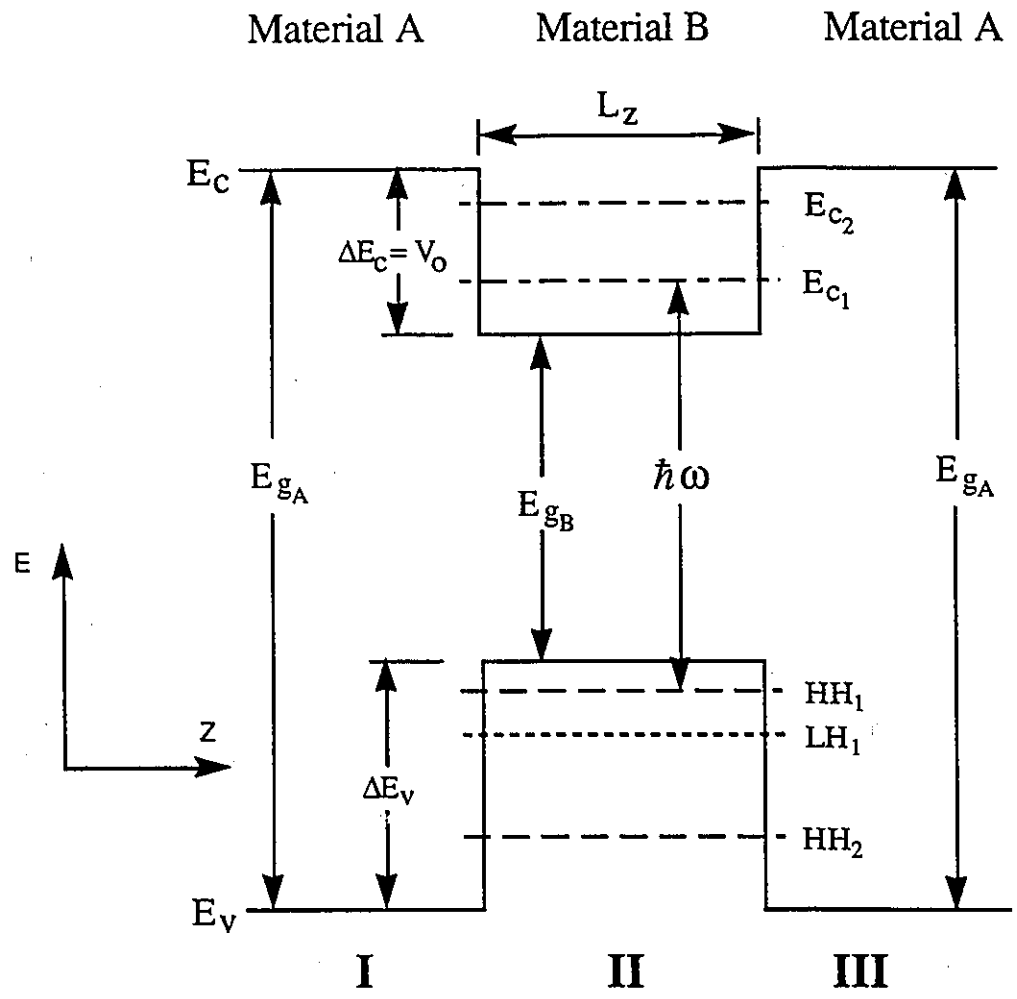

Figure 2.1: Energy band structure (at **k**=0) vs growth direction (z) for a single quantum well. E_C and E_V are the conduction and valence band edge energies respectively, ΔE_C and ΔE_V are the well depth for the conduction and valence band QWs and E_g is the energy gap.

2.1.1 Single Quantum Well Conduction Band Energy Solutions

The eigenenergies for an electron trapped within the quantum well formed by the non-degenerate conduction band may be found by making use of the envelope function

approximation (EFA) and solving an "effective mass" or Schrödinger-like equation for the envelope function [Corzine, 1993].

In the EFA the localized wavefunction of an electron in the QW is expressed as a linear combination of the Bloch wave solutions of the Schrödinger equation for the bulk crystal. The Bloch waves have the form:

$$\psi = e^{i\mathbf{k}\cdot\mathbf{r}}u(\mathbf{k},\mathbf{r}) \tag{2.1.1}$$

where **k** is the wave vector of the electron, and u is the Bloch function having the same periodicity as the crystal lattice. The spatially localized wavefunction is therefore given by:

$$\psi = \int A(k)e^{i\mathbf{k}\cdot\mathbf{r}}u(\mathbf{k},\mathbf{r})d^3\mathbf{k} \approx u(0,\mathbf{r})\int A(k)e^{i\mathbf{k}\cdot\mathbf{r}}d^3\mathbf{k} \equiv F(\mathbf{r})u(\mathbf{r}) \tag{2.1.2}$$

were A(k) represents an arbitrary set of expansion coefficients, and F(**r**) is the envelope function whose Fourier spectrum is made up of the plane wave components of the solutions in (2.1.1). In (2.1.2) it has been assumed that the Bloch function, u, is not a strong function of **k** and can be approximately represented by the band edge (k=0) Bloch functions. Thus the Bloch function u(**k**,**r**) has been set to u(0,**r**)=u(**r**) and the localized electron wavefunction consists of two components: the band edge Bloch functions of the bulk crystal, u(**r**), multiplied by a slowly varying envelope function F(**r**).

The "effective mass equation" for the conduction band envelope function F_e, is given by:

$$(H_c + V)F_e = E_cF_e \tag{2.1.3}$$

where the Hamiltonian, H_c, for the conduction band is given by:

$$H_c = -\frac{\hbar^2}{2m_c}\nabla^2 \tag{2.1.4}$$

Equation (2.1.3) is similar to the Schrödinger equation; however, in (2.1.3) the Bloch functions have been removed and the effect of the periodic potential of the crystal lattice has been replaced by a conduction band effective mass, m_c.

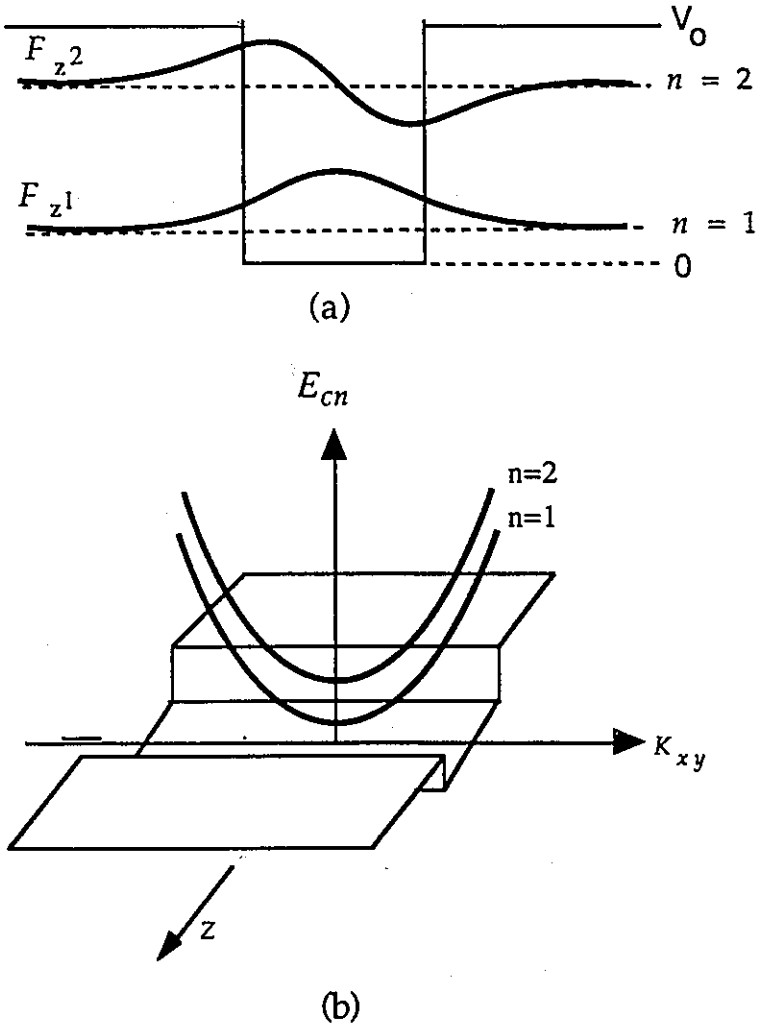

Figure 2.2: Conduction band quantum well solutions. Part (a) illustrates the form of lowest even and odd wavefunction solutions of (2.1.6). Part (b) shows schematically the subband structure for the quantized energy levels corresponding to these two solutions.

For a one-dimensional variation along the z-direction, such as that shown in Fig. 2.1 where V = V(z), one can assume the envelope function solutions of (2.1.3) to be of the form [Corzine, 1993]:

$$F_e = F_z(z)\exp\left[i(k_x x + k_y y)\right]. \tag{2.1.5}$$

From (2.1.3), (2.1.4) and (2.1.5), one then obtains:

$$\frac{\hbar^2}{2m_i}\frac{d^2F_z}{dz^2} + \left(V_i + V_{k,i}\right)F_z = E_c F_z, \qquad \text{where } V_{k,i} = \frac{\hbar^2 k_{xy}^2}{2m_i}. \tag{2.1.6}$$

In (2.1.6) the subscript i indicates the well or barrier region of Fig. 2.1 and $k_{xy}^2 \equiv k_x^2 + k_y^2$ is the in-plane **k** vector of the electron. For the lowest (band-edge) energy solutions of (2.1.6) the electron will have negligible in-plane momentum; consequently, $k_{xy}^2 = 0$ and therefore $V_{k,i} = 0$. In addition, from Fig. 2.1, in the well region $V_{II} = 0$ and in the barrier region $V_I = V_{III} = V_o$. Given this information and that

$$F_z(z) \quad \text{and} \quad \frac{1}{m_{z,i}}\frac{dF_z(z)}{dz}, \tag{2.1.7}$$

are continuous across the well/barrier interface, [Bastard, (1981)], (2.1.6) can be solved to give the energy eigenvalue equations

$$\tan\left\{L_z\sqrt{\frac{m_w E_n}{2\hbar^2}}\right\} = \sqrt{\frac{m_w}{m_b}\left(\frac{V_o}{E_n} - 1\right)}, \quad \text{for even solutions, } n \in \{1,3,5,\ldots\}$$

and (2.1.8)

$$\cot\left\{L_z\sqrt{\frac{m_w E_n}{2\hbar^2}}\right\} = -\sqrt{\frac{m_w}{m_b}\left(\frac{V_o}{E_n} - 1\right)}, \quad \text{for odd solutions, } n \in \{2,4,6,\ldots\}$$

where L_z is the width of the quantum well, m_w^* and m_b^* are the effective masses in the well and barrier regions respectively, and E_n is the discrete energy of the n^{th} level with respect to the bottom of the quantum well. From an inspection of (2.1.8) it can be seen that the eigenenergy for a carrier within the well can be adjusted by altering the width, L_z, or the depth, V_o, of the well.

For each quantized eigenvalue solution of (2.1.8) - (each value of E_n) - there exists a two-dimensional subband of energies in the plane of the well. These subbands arise due to the freedom of motion that exists for electrons in the plane of the quantum well. When the in-plane momentum of the electrons is included as a perturbation in (2.1.6) by setting the term $V_{k,i} \neq 0$, one can obtain an approximate expression for the energy of the electron confined to the well. This expression is [Corzine, 1993]:

$$E_n\left(k_{xy}\right) = E_n(0) + \frac{\hbar^2 {k_{xy}}^2}{2m_{eff}} \tag{2.1.9}$$

where

$$E_n(0) = \frac{\hbar^2}{2m_z^*}\left(\frac{n\pi}{L_z}\right)^2,$$

$$\frac{1}{m_{eff}} = \frac{\Gamma}{m_w} + \frac{1-\Gamma}{m_b},$$

and

$$\Gamma = \int_{-L_z/2}^{L_z/2} |F_{zno}|^2 \, dz \Big/ \int_{-\infty}^{\infty} |F_{zno}|^2 \, dz .$$

From (2.1.9) the energy as a function of the in-plane **k** vector is parabolic with an in-plane effective mass that is the weighted average of the bulk well and barrier effective masses. The lowest even and odd wavefunction solutions for a confined electron, as obtained from (2.1.6) and (2.1.8), are shown in Fig. 2.2(a). The subband structure for these quantized levels is shown in Fig. 2.2(b).

In the above analysis it has been assumed (see equation (2.1.4)) that the effective mass is constant and independent of energy (i.e., the conduction band is parabolic). In reality, however, non-parabolicity does exist in the conduction band, and the effective mass depends on energy with an approximate dependence [Nag, 1991,1980, Kinch, 1985]:

$$m^*_{c,i} = m^*_{c,i}(0)\left[1 + 2\frac{E_{n,i}}{E_{g,i}}\right], \qquad (2.1.10)$$

where E_g, is the energy gap of the material, i is a subscript to indicate the well or barrier material, and $m_{c,i}^*$ is the effective mass at the band edge. From (2.1.10) the constant effective mass eigenvalue calculation will only be valid when the band-gap of the well material is much greater than the well depth, V_o. Calculations of the energy levels within QW structures were required in the design of the laser structures grown for this thesis. For these calculations the constant effective mass, or parabolic band assumption was made. From (2.1.10), this assumption would result in an effective mass at the first quantized energy level that is approximately 20-50% too small.

2.1.2 Single Quantum Well Valence Band Energy Solutions

Figure 2.3 shows a schematic of a typical bulk III-V compound semiconductor energy band structure. From this diagram it is seen that the conduction band edge is well separated in energy from the other conduction and valence bands and so interacts only weakly with them. By constrast the valence bands are degenerate; consequently, the interaction between them is relatively strong.

Since the interaction of the conduction band with the other energy bands is weak, it is possible to write an effective mass equation (equation (2.1.3)) for an electron in this band such that the interaction with the other bands is replaced by a simple conduction band effective mass, m^*. For the degenerate valence bands, however, the effective mass equation must be modified to account for the strong interaction between the light and heavy hole valence bands explicitly. Briodo and Sham (1985), building upon the work of

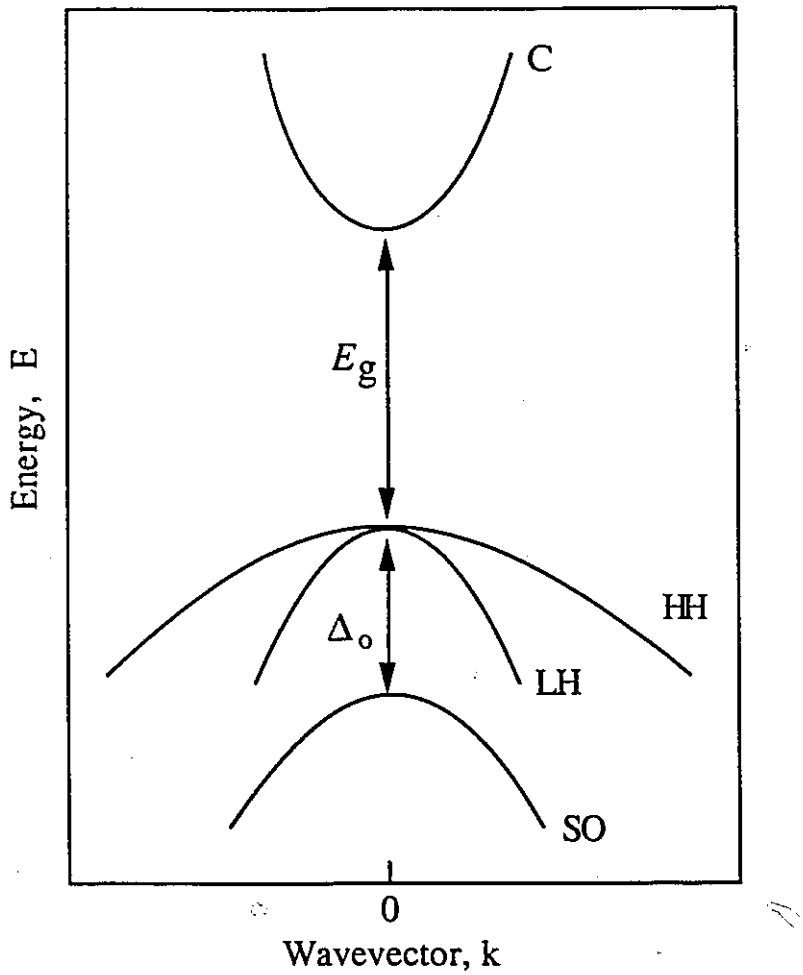

Figure 2.3: Schematic of a typical bulk III-V compound semiconductor energy band structure illustrating the conduction (C), heavy hole (HH), light hole (LH) and spin split-off (SO) energy bands and their relative separation.

Luttinger and Kohn (1955), derived effective mass equations for the light and heavy hole valence bands such that the interaction between the bands is included through a coupling term. The coupled light and heavy hole effective mass equations are [Ahn, 1990],[Chuang, 1991],[Corzine, 1993]:

$$(H_h + V)F_h + WF_l = E_v F_h \tag{2.1.11}$$

$$(H_l + V)F_l + W^+ F_h = E_v F_l \tag{2.1.12}$$

where W is the coupling term given by [Chuang, 1991]

$$W = \sqrt{3}\left[\hbar^2/(2m_o)\right]k_t\left(\gamma_2 k_t - i2\gamma_3 k_z\right) \text{ for } \{100\} \text{ planes,} \qquad (2.1.13a)$$

$$W = \sqrt{3}\left[\hbar^2/(2m_o)\right]k_t\left(\gamma_3 k_t - i2\gamma_3 k_z\right) \text{ for } \{110\} \text{ planes,} \qquad (2.1.13b)$$

and $W^=$ is the Hermetian conjugate of W. F_h and F_l are the heavy and light hole envelope functions, and the Hamiltonians H_h and H_l are given by

$$H_h = \left[\hbar^2(\gamma_1 - 2\gamma_2)/(2m_o)\right]k_z^2 + \left[\hbar^2(\gamma_1 + \gamma_2)/(2m_o)\right]k_t^2, \qquad (2.1.14a)$$

$$H_l = \left[\hbar^2(\gamma_1 + 2\gamma_2)/(2m_o)\right]k_z^2 + \left[\hbar^2(\gamma_1 - \gamma_2)/(2m_o)\right]k_t^2. \qquad (2.1.14b)$$

The material parameters γ_1 ,γ_2, and γ_3, are the Luttinger parameters and are related to the bulk heavy and light hole masses, m_{hh} and m_{lh}, respectively, by the relations [Luttinger, 1956],[Weisbuch, 1991]:

$$\gamma_1 - 2\gamma_2 \equiv \frac{m_o}{m_{hh}}, \qquad \gamma_1 + 2\gamma_2 \equiv \frac{m_o}{m_{lh}}. \qquad (2.1.15)$$

In deriving the coupled equations (2.1.11) and (2.1.12), the coupling of the heavy and light hole valence bands with the split-off (SO) band and the conduction band has been neglected. The coupling was neglected because the interaction with the SO band need only be considered when one is concerned with energy levels that are deep enough into the valence band to be comparable in energy to the quantity Δ, indicated in Fig. 2.3. In addition, (2.1.11) and (2.1.12) remain completely general only for the {100} and {110} crystal planes. This restriction is due to the mathematics of reducing four coupled valence band equations (there is normally one effective mass equation for each of two spin directions for each band) to two equations. In (2.1.14a) and (2.1.14b), two perpendicular k-vector components k_z and k_t have been defined such that k_z is directed along the <100> direction and k_t is along either <100> or <110>.

In determining the band-edge (lowest energy) solutions in the quantum well, one is interested in the case where $k_t \approx 0$. From (2.1.13a) and (2.1.13b) it is seen that under this condition the coupling term disappears so that (2.1.11) and (2.1.12) reduce to the form of (2.1.3). These equations can then be solved independently using the same boundary conditions as those for the case of the conduction band quantum well. Thus, (2.1.8) may be used to obtain the quantized energy levels, $E_{vn}(0)$, for the quantum wells formed by the HH and LH valence bands. It should be noted that the use of (2.1.8) assumes that the valence band dispersion relation perpendicular to the quantum well growth direction is parabolic. This is a commonly used assumption and is used in the calculations of this thesis.

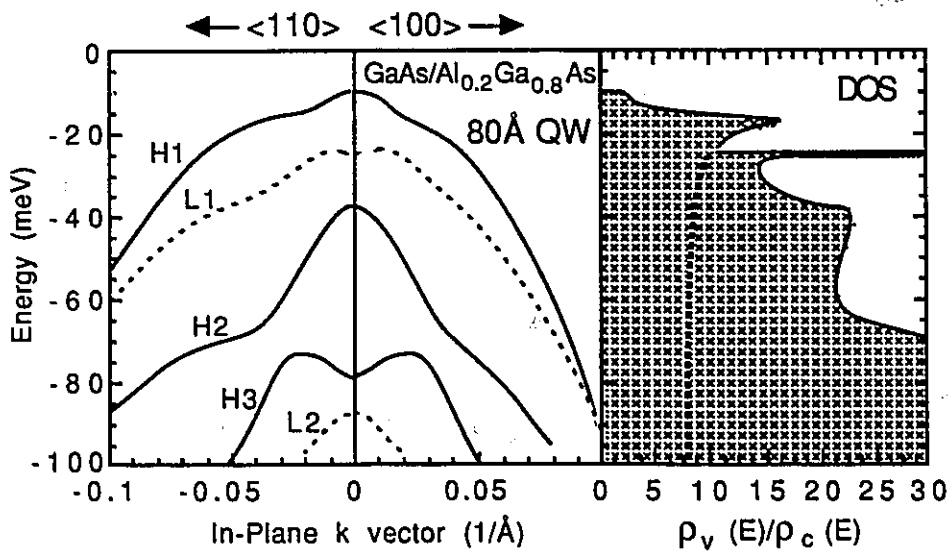

Figure 2.4: The valence subband structure of an 80Å $GaAs/Al_{0.2}Ga_{0.8}As$ quantum well ($V_0 \approx$ 95meV) with the inclusion of coupling between the HH and LH bands plotted at the left. At the right are the total (solid curve) and the H1 subband (dashed curve) density of states plotted relative to the density of states in the first conduction (C1) subband.

Determining the in-plane subband dispersion relation, $E_v(k)$, for carriers in the valence band quantum wells is much more involved than the case for the conduction band.

The added complexity arises due to the interaction of the LH and HH bands away from k_t =0. An excellent description of the procedure for obtaining the $E_V(k)$ relationship in the plane of the well is given by Corzine [1993]. A typical in-plane valence subband structure for an 80Å unstrained GaAs quantum well with barriers of composition $Al_{0.2}Ga_{0.8}As$ is shown in Fig. 2.4 [Corzine, 1993].

The effects of quantum confinement on the valence band structure are as follows. Because the band-edge energy solutions in the quantum well, as determined from (2.1.6) and (2.1.7), depend on the effective mass of the carriers, the degeneracy of the heavy and light hole bands at $k_t = 0$ is removed. Defining the hole energy to be increasing downward from the bottom (bulk band-edge) of the quantum well, the heavier carriers of the HH band have lower energies than those carriers associated with the LH band. The heavy hole therefore has the lowest energy subband. In addition, the separation of the light and heavy hole bands reduces the interaction of these bands at k_t =0. This reduced interaction results in a lighter in-plane effective mass for heavy holes near the band edge while that along the confinement (z) direction remains unchanged [Bastard, 1982] [Chuang, 1991]. As seen in Fig. 2.4, as the carrier energy increases away from the band-edge (i.e., $k_t \neq 0$), the interaction between bands increases and band-mixing between the LH and HH wavefunctions produces non-parabolicities in the subband structure [Chuang, 1991], [Marzin, 1990]. These non-parabolicities, and the valence band mixing associated with them, have important implications regarding the performance of quantum well lasers. These implications will be revealed in §2.2 where it will also become apparent that non-parabolicities in the valence subband structure also greatly complicate accurate calculations of the density of states and, therefore, the gain in these structures.

2.1.3 Multiple Quantum Well Energy Solutions

Figure 2.5 shows a schematic of the **k**=0 energy band structure *vs.* growth direction for a multiple quantum well (MQW) structure. If the width of the barriers, L_b, for such a structure is less than a certain thickness then there is a finite probability that the wavefunction solutions of adjacent wells may overlap and resonant tunneling of carriers between wells may occur. The thickness at which wavefunction overlap between adjacent wells occurs depends on the effective mass of the carriers and the depth of the QW.

In the case of wavefunction overlap, the long-range behavior of the envelope functions, $F_{c,v}$, is governed by the Bloch theorem [Bastard,(1981)]:

$$F_{c,v}(z+md) = \exp(iqmd)F_{c,v}(z), \tag{2.1.16}$$

where, m, is an integer, q is the wave vector along the growth direction, and d reflects the periodicity of the structure, such that $d = l_a + l_b$ where l_a is the width of the well. The potential, V, in (2.1.3) now also depends on z, such that, V(z+md)=V(z). The periodicity of the MQW structure thus adds two more boundary conditions which must be satisfied in solving (2.1.6). Referring to Fig. 2.5, these conditions are:

$$F_{a_{c,v}}(a) = e^{iq(a+b)}F_{b_{c,v}}(-b), \tag{2.1.17a}$$

and

$$\left.\frac{1}{m_{z,a}}\frac{dF_{a_{c,v}}}{dz}\right|_a = e^{iq(a+b)}\left.\frac{1}{m_{z,b}}\frac{dF_{b_{c,v}}}{dz}\right|_{-b}. \tag{2.1.17b}$$

With these added boundary conditions, the solution to (2.1.6) gives the dispersion relation [Bastard, (1981)]:

$$\cos(qd) = \cos(k_a l_a)\cos(k_b l_b) - \tfrac{1}{2}\left[x + \tfrac{1}{x}\right]\sin(k_a l_a)\sin(k_b l_b) \tag{2.1.18}$$

$$\text{for } E < V_o$$

where:

$$k_a^2 = \left[\frac{2m_a^*}{\hbar^2}\right] E_n, \tag{2.1.19}$$

$$k_b^2 = \left[\frac{2m_b^*}{\hbar^2}\right] \left(E_n - V_{o_{c,v}}\right), \tag{2.1.20}$$

and

$$x = \frac{m_a k_b}{m_b k_a}. \tag{2.1.21}$$

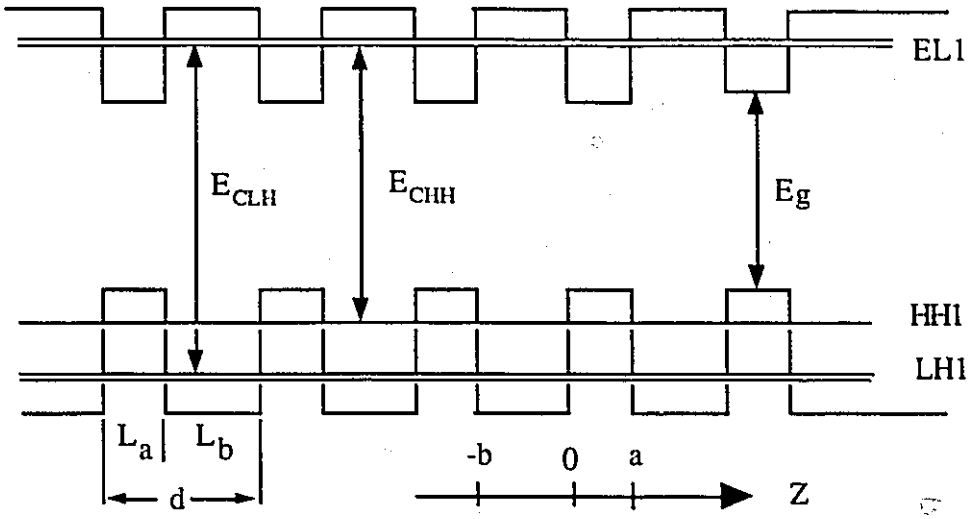

Figure 2.5: Schematic of the k=0 energy band structure *vs.* growth direction (z) for a multiple quantum well (MQW) structure. Shown are the E_{C1}-E_{LH1} and the E_{C1}-E_{HH1} transition, as well as the finite width of the k_{xy}=0 energy levels due to wavefunction overlap between adjacent wells.

From (2.1.18) and (2.1.21), it is seen that for $m_a = m_b$, then (2.1.18) is identical to the solution obtained from the Kronig-Penney analysis for an electron of mass, m , and fixed energy E, in a periodic potential [Pierret, (1989)]. The difference between (2.1.18) and (2.1.8) is that the existence of the free variable, q, leads to energy solutions, E_n , that are no longer discrete, but which form a miniband of allowed energies. For the quantum well and barrier materials used in this thesis, if the thickness of the QW barriers is greater

than ≈ 150Å the widths of all minibands are negligible and (2.1.8) may be used to find the eigenenergies for electrons and holes without much error.

The effects of quantization on the shape of the valence subband structure for a MQW structure will be similar to that for a single quantum well. In §2.1.2 it was indicated that the shape of the valence subband structure has important implications regarding the performance of quantum well lasers. The importance of the subband structure arises because the carrier effective mass within an energy band is related to the curvature of the band through the tensor relation [Nag, 1980]:

$$\left[m^{-1}(k)\right]_{ij} = \frac{1}{\hbar^2}\frac{\partial^2 E(k)}{\partial k_i \partial k_j}. \tag{2.1.22}$$

The effective mass, as revealed in §2.2, is in turn related to the density of states (in units of number per unit energy per unit volume) for carriers within the band, which in turn, is a very important parameter affecting the operating characteristics of semiconductor lasers.

2.2 THE DENSITY OF STATES AND MATERIAL GAIN IN QUANTUM WELL LASERS

The density of states affects the operating characteristics of a laser through its impact on both the magnitude of the material gain and the rate of change of the material gain with injected carrier density. This section illustrates, not only how the density of states can affect the operating characteristics of a laser through its relation to material gain, but also how, through its influence on the density of states, quantization can lead to improved laser performance. However, before illustrating these points, it is necessary to develop an expression for the material gain in a semiconductor laser and to compare the differences between the density of states for a bulk material and that for a quantum well. A comparison between the density of states for bulk and QW materials is presented in §2.2.1. An

expression for the material gain in bulk and quantum well materials is developed in §2.2.2. The expression for the gain is developed through a detailed examination of the optical transition rates in materials where it is found that the effects of quantization, not only increase the magnitude of the material gain over that found in bulk material, but also give it a strong polarization dependence.

2.2.1 The Density of States Function

A comparison between the energy dependence of the density of states for carriers in a quantum well and the energy dependence of the density of states for carriers in bulk material is shown in Fig. 2.6. The density of states function, $\rho(E)$, is determined by finding the number of allowed states per unit volume (including spin degeneracy) that have a k-vector with a magnitude between k and k +dk. The relationship between the magnitude of the carrier wavevector, k, and its energy, E, is then used to convert this quantity to the number of allowed states for carriers that have an energy, E, between E and E+dE. In relating the energy of a carrier to its wavevector, the parabolic band assumption is commonly used. In the parabolic assumption, the relationship between the magnitude of the carrier wavevector and its energy is given by $E=(\hbar k_{xyz})^2/(2m^*)$ for bulk materials, and by (2.1.9) for quantum wells.

In bulk material, when $k_{xyz}=0$, the electron's kinetic energy, E, = 0, so the electron (hole) rests at the edge of the conduction (valence) band. For energies away from the band edge, the density of states function increases with the square root of the energy according to the relation [Verdeyen, 1989]:

$$\rho_{c,v}(E)=\frac{1}{2\pi^2}\left[\frac{2m^*_{c,v}}{\hbar^2}\right]^{3/2}(E)^{1/2}. \qquad (2.2.1)$$

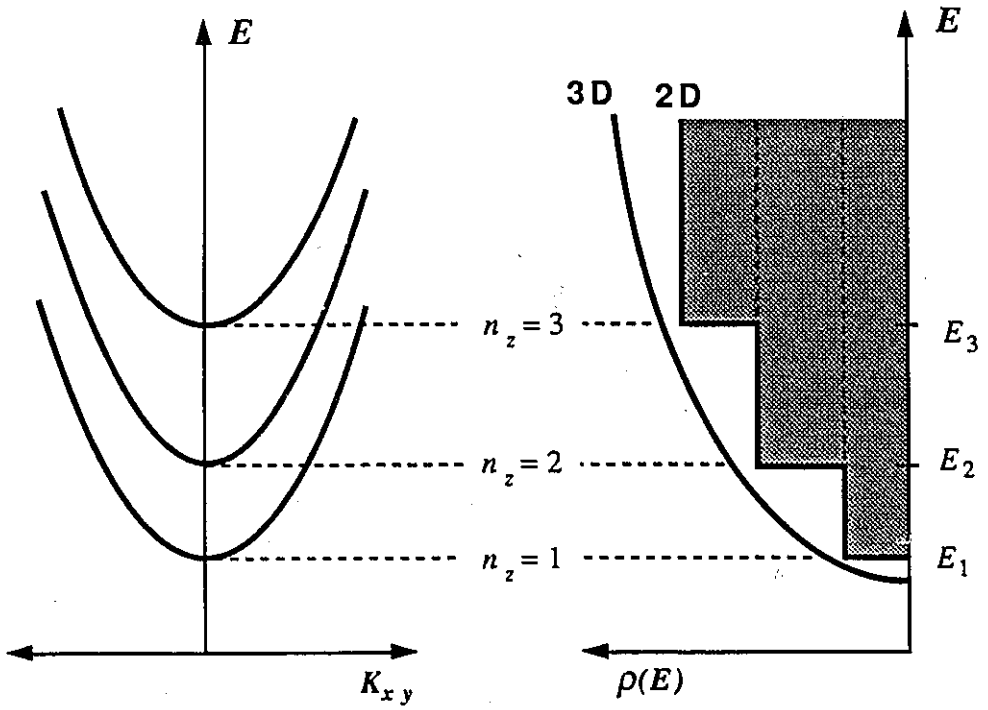

Figure 2.6: The right hand side shows schematically a comparison between the 2-dimensional electron density of states in a quantum well (shaded area) and the 3-D electron density of states in bulk material (parabolic envelope). Since each QW subband (left hand side) contributes to the density of states, the 2-D density of states displays step like behavior. In the case of an infinite potential well, each step touches the parabolic envelope.

In a quantum well, the noticeable quantization of the electron momentum, k_z, in the direction perpendicular to the plane of the quantum well (the z-direction) means that the minimum electron energy, as given by (2.1.9) when $k_{xy}=0$, is greater than that for an electron at the bulk band edge. In addition, when $k_{xy}=0$, each discrete jump in the value of k_z is responsible for creating a new set of energy levels (as was shown in Sect 2.1.1 and Fig. 2.2). This new set of energy levels arises because, for each discrete value of k_z, the in-plane k-vector, k_{xy}, can increase quasi-continuously ($k_{x,y}=n(\pi/L_{x,y})$ and $L_{x,y} >> L_z$). Since k_{xy} can increase quasi-continuously there is a large density of states for carriers within the plane of the quantum well. This density of states is constant and independent of energy as long as the parabolic band approximation holds and E is larger than the first

allowed energy state, E_1, and less than the next allowed energy state E_2. As indicated in Fig. 2.6, when the energy E, reaches the next allowed energy state, there is a discrete increase in the density of states. This discrete increase arises due to the addition of the density of states associated with the new subband and the discrete increase in k_z, to the density of states associated with all subbands belonging to lesser values of k_z. Thus the density of states function for a QW is a steplike function which increases each time k_z increases by a discrete value.

The density of states function for a quantum well is given by the relation [Tsang, 1987]:

$$\rho_{c,v}(E) = \sum_n \frac{1}{2\pi^2}\left(\frac{2m^*_{//c,v}}{\hbar^2}\right)\left(\frac{\pi}{L_z}\right)H\left(E - E_{nc,v}\right) \qquad (2.2.2)$$

where $m^*_{//c,v}$ is the carrier effective mass in the plane of the quantum well, $H\left(E - E_{nc,v}\right)$ is the unitary Heaviside function, and v represents either light or heavy holes. How a change in the density of states function from one that depends on energy in bulk material to one that is independent of energy in a quantum well can affect the material gain characteristics, and therefore the operating characteristics of a laser, is discussed in §2.2.3. First, however, an expression for the material gain in both a bulk semiconductor medium and a quantum well is arrived at in §2.2.2, and the concepts of forbidden and allowed transitions are introduced.

2.2.2 Material Gain in Semiconductors

Optical gain is possible in a semiconductor medium when the rate of photon-induced transitions of electrons from the conduction band to the valence band (stimulated emission) exceeds the rate of photon-induced transition of electrons from the valence band to the conduction band (stimulated absorption). The magnitude of the optical gain thus

depends upon the probability that an electron will undergo an optical transition between energy states in the conduction band and energy states in the valence band. It also depends upon: the density of the initial and final states; the probability that any of the initial and final states are already occupied; and energy state broadening due to the finite lifetime of the initial and final states. In arriving at the expression for the optical gain in a semiconductor material, the photon-induced interband transition probability for an electron is discussed in detail, and it is found that the transition probability depends upon the polarization of the photon inducing the transition, as well as the quantum number of the subbands involved in the transition.

The probability that an electron will undergo a transition between an energy state in the conduction band and an energy state in the valence band, at any given time, in response to the electromagnetic field of a photon can be determined using the techniques of time-dependent perturbation theory. The transition rate for an electron between a single pair of conduction and valence band states, when evaluated using time-dependent perturbation theory, can be expressed using Fermi's Golden Rule by [Datta, 1989],[Agrawal, 1986]:

$$W_{e\to h} = \frac{2\pi}{\hbar}\left|\left\langle \psi_h^* \middle| H_p^e \middle| \psi_e \right\rangle\right|^2 \delta(E_c - E_v - \hbar\omega), \qquad (2.2.3)$$

where H_p^c characterizes the electron-photon interactions in a crystal and is called the interaction Hamiltonian, and $\psi_{c,h}$ (for a quantum well) is given by (2.1.2) and (2.1.5) such that:

$$\psi_{e,h} = u_{e,h}(r)F_{e,h}(z)e^{ik_t\cdot r_t}. \qquad (2.2.4)$$

The delta function in (2.2.3) indicates that the difference between the energy of the initial and final states must be equal to the energy, $\hbar\omega$, of the photon that induced the transition. The quantity, $\left\langle \psi_h^* \middle| H_p^e \middle| \psi_e \right\rangle$ is called the matrix element of the interaction Hamiltonian between the final and initial electron states ψ_h^* and ψ_e.

The interaction Hamiltonian H_p is given by [Datta, 1989],[Casey, 1978]:

$$H_p = -\frac{iq\hbar}{m_o}\mathbf{A}\cdot\nabla + q^2\frac{\mathbf{A}\cdot\mathbf{A}}{2m_o}, \tag{2.2.5}$$

where **A** is the vector potential created by the electromagnetic field of the photon. The vector potential is given by [Datta, 1989]:

$$\mathbf{A}(r,t) = \hat{\mathbf{e}}_v\sqrt{\frac{\hbar}{2\omega\varepsilon\Omega}}\left(e^{i(\bar{\beta}\cdot\mathbf{r}-\omega t)} + e^{-i(\bar{\beta}\cdot\mathbf{r}-\omega t)}\right) \tag{2.2.6}$$

where Ω is the normalization volume, $\bar{\beta}$ is the wavevector of the photon with a unit polarization vector $\hat{\mathbf{e}}$ in the direction v, and ε is the dielectric constant. It is the frequency (ω) components of **A** that are responsible for the delta function term in (2.2.3).

The second order term in (2.2.5) is often neglected since this term does not perturb the system if the fields are weak or if ψ_c and ψ_h are orthogonal, and one can neglect the spatial variation of **A** within a unit cell. In addition, it can be shown that the left hand exponential term of **A** produces an annihilation operator while the right hand term produces a creation operator. The annihilation operator results in the absorption of a photon, while the creation operator results in the emission of a photon. Since a downward transition of an electron from the conduction band to the valence band results in the emission of a photon, the interaction Hamiltonian for use in (2.2.3) becomes:

$$H_p^e = \frac{q}{m_o}\sqrt{\frac{\hbar}{2\omega\varepsilon\Omega}}\hat{\mathbf{e}}_v e^{-i\beta\cdot r}\cdot\mathbf{p}, \tag{2.2.7}$$

where **p** is the momentum operator.

From (2.2.3),(2.2.4) and (2.2.7), the downward transition rate is given by:

$$W_{e\to h} = \frac{\pi q^2}{m_o\omega\varepsilon}\delta(k_h - \beta - k_e)\left|M_T\right|^2\delta(E_c - E_v - \hbar\omega), \tag{2.2.8}$$

where $|M_T|$ is the transition momentum (or dipole) matrix element, $|\langle u_v|\hat{e}\cdot\mathbf{p}|u_c\rangle|$, multiplied by the overlap integral between the electron and hole envelope functions, $|\langle F_h|F_e\rangle|$. Thus $|M_T|^2$ is given by [Casey, 1978], [Corzine, 1993]:

$$|M_T|^2 = |\langle u_v|\hat{e}\cdot\mathbf{p}|u_c\rangle|^2 |\langle F_h|F_e\rangle|^2. \tag{2.2.9}$$

The appearance of the delta function, $\delta(k_h-\beta-k_e)$, in (2.2.8) indicates that in order for a transition to occur, k_h must equal $k_e+\beta$. This requirement reflects the momentum conservation, or k-selection rule for transitions. Since β is typically much smaller than the wavevector for an electron, this k-selection rule can be approximated by $k_h=k_e$. It should be noted from (2.2.3), however, that the k-selection rule only applies to transitions between two plane wave states (i.e. band to band transition in undoped material). As the materials used in the active region of the lasers studied in this thesis are undoped, the k-selection rule is applicable.

Evaluation of the envelope function overlap integral, $|\langle F_h|F_e\rangle|$, in (2.2.9) leads to the concept of allowed and forbidden transitions as follows [Corzine, 1993]. From (2.1.6),(2.1.11) and (2.1.12) one can find the eigenfunctions of the band edge conduction and valence band states. These eigenfunctions are denoted by the quantum numbers n_c and n_v respectively. For an infinite potential well (i.e. $V_b=\infty$ in (2.1.6)) there is no penetration of the wavefunctions into the barrier region and the eigenfunctions are found to be independent of the electron or hole effective masses. The eigenfunctions also form an orthonormal set. When $n_c=n_v$ the envelope functions in the conduction band and the valence band are identical and $|\langle F_h|F_e\rangle|^2=1$. When $n_c\neq n_v$, however, $|\langle F_h|F_e\rangle|^2=0$ due to the orthogonality relations. Therefore, band-edge transitions in a quantum well with infinite barriers are only allowed to occur when $n_c=n_v$.

For finite-barrier QWs, because electrons and holes have different effective masses, and since the penetration of the wavefunctions into the barrier region depends on the effective mass, the conduction and valence band eigenfunctions with the same quantum number, n, are not completely identical. Consequently, when $n_c=n_v$, the envelope function overlap integral is slightly less than unity and $\left|\langle F_h | F_e \rangle\right|^2 \approx 0.95 \sim 1$. Likewise, when $n_c \neq n_v$, the conduction and valence band wavefunctions are no longer strictly orthogonal and $\left|\langle F_h | F_e \rangle\right|^2 \approx 0 \sim 0.1$. In addition, from (2.1.11) and (2.1.12), for energies away from the band edge, the coupling term W is finite and band-mixing effects cause transitions which are normally forbidden to be allowed to some small extent (e.g., C_1-HH_3 or C_2-HH_3 transitions).

Evaluation of the transition probability, $|M_T|^2$, when $\left|\langle F_h | F_e \rangle\right|^2 = 1$ in (2.2.9), leads to the concept of polarization dependent optical transitions, which allows one to quantify the transition rate, $W_{e\text{-}h}$. To arrive at the polarization dependence of the optical transitions, one must first examine the Bloch functions that are operated on by the momentum operator, **p**, when evaluating the transition dipole matrix element, $\left|\langle u_v | \hat{\mathbf{e}} \cdot \mathbf{p} | u_c \rangle\right|$. These Bloch functions are described as follows. The conduction band Bloch function, $u_c=u_s$, is similar to that of an s atomic orbital and has even symmetry in all three directions. The valence-band Bloch functions, on the other hand, are made up of a linear combination of "basis" Bloch functions, u_i, which correspond to the Bloch function of the three p atomic orbitals, p_i (i=x,y,z). Since the Bloch functions, u_i , have odd symmetry along the i^{th} direction, the valence band Bloch functions also possess some odd symmetry [Datta, 1989]. Defining the electron's k-vector to be directed along the z-direction, the valence band Bloch functions are written in terms of the u_i basis functions as [Corzine, 1993], [Datta, 1989]:

$$
\begin{aligned}
u_{hh} &= -\frac{1}{\sqrt{2}}\left(u_x + iu_y\right), & \overline{u}_{hh} &= \frac{1}{\sqrt{2}}\left(\overline{u}_x - i\overline{u}_y\right), \\
u_{lh} &= -\frac{1}{\sqrt{6}}\left(\overline{u}_x + i\overline{u}_y - 2u_z\right), & \overline{u}_{lh} &= \frac{1}{\sqrt{6}}\left(u_x - iu_y + 2\overline{u}_z\right), \\
u_{so} &= -\frac{1}{\sqrt{3}}\left(\overline{u}_x + i\overline{u}_y + u_z\right), & u_{so} &= \frac{1}{\sqrt{3}}\left(u_x - iu_y - u_z\right).
\end{aligned}
\tag{2.2.10}
$$

where u_i and $\overline{u}_i$ indicate spin up and spin down functions respectively.

With the valence band Bloch functions now described in terms of their basis states, the transition dipole matrix element, $\left|\langle u_v|\hat{\mathbf{e}}\cdot\mathbf{p}|u_c\rangle\right|$, and therefore $|M_T|^2$, can be evaluated theoretically using the **k·p** method and some symmetry arguments. From the **k·p** method, the curvature of the conduction band is related to the quantity, $\left|\langle u_n|p_i|u_s\rangle\right|^2$, where u_n are the valence and higher lying band basis Bloch functions. The relationship is [Kane, 1979]:

$$
\frac{1}{m_{c,i}} = \frac{1}{m_o} + \frac{2}{m_o^2}\sum_{n\neq s}\frac{\left|\langle u_s|p_i|u_n\rangle\right|^2}{E_{c,k_o} - E_{n,k_o}}, \tag{2.2.11}
$$

where the subscript *i* indicates the direction (i=x,y,z) and k_o indicates the band extremum.

From symmetry arguments, it can be shown that [Datta, 1989]:

$$
\left|\langle u_j|p_i|u_s\rangle\right| \equiv P_o \quad \text{when i=j} \tag{2.2.12a}
$$

and

$$
\left|\langle u_j|p_i|u_s\rangle\right| = 0 \quad \text{when i}\neq\text{j}. \tag{2.2.12b}
$$

Neglecting all contributions to $\left|\langle u_n|p_i|u_s\rangle\right|^2$ save those of the three valence bands (i.e., neglecting the effects on $m_{c,i}$ due to higher lying bands) one obtains from (2.2.11) and (2.2.12) [Datta, 1989]:

$$
|P_o|^2 = \left(\frac{m_o}{m_c^*} - 1\right)\frac{\left(E_g + \Delta\right)}{2\left(E_g + \frac{2}{3}\Delta\right)}m_o E_g. \tag{2.2.13}
$$

From (2.2.12), and by putting (2.2.10) into (2.2.9) and summing over all possible u_c-u_v transitions of either spin, the transition probability, $|M_T|^2$, between the conduction and valence band Bloch functions, assuming $\left|\langle F_h | F_e \rangle\right|^2 = 1$, is given by [Corzine, 1993]:

$$|M_T|_{hh}^2 = |P_o|^2\left(1 - \left|\hat{\mathbf{k}}\cdot\hat{\mathbf{e}}\right|^2\right) \quad \text{for the HH band,} \qquad (2.2.14a)$$

$$|M_T|_{lh}^2 = |P_o|^2\left(\frac{1}{3} + \left|\hat{\mathbf{k}}\cdot\hat{\mathbf{e}}\right|^2\right) \quad \text{for the LH band,} \qquad (2.2.14b)$$

and

$$|M_T|_{so}^2 = \frac{2}{3}|P_o|^2 \quad \text{for the SO band,} \qquad (2.2.14c)$$

where use has been made of the relation that $\hat{e}_z^2 = \left|\hat{k}\cdot\hat{e}\right|^2 = 1 - \hat{e}_x^2 - \hat{e}_y^2$.

The polarization dependence of the optical transitions can now be obtained from (2.2.14), since the dot product in (2.2.14) gives the component of $\hat{\mathbf{e}}$ that is parallel to the electron k-vector, which in defining (2.2.10) was assumed to be along the z-direction. For example, in bulk material, photons of a given polarization interact with a large number of electrons having k-vectors pointing in all directions. The average of the dot product, $\left|\hat{k}\cdot\hat{e}\right|^2$, for $\hat{\mathbf{k}}$ sweeping over all three dimensions in this case is equal to 1/3. Therefore, from (2.2.14), the transition probability for all three valence bands in bulk material is $2/3\cdot|P_o|^2$ for any field polarization. (Bulk lasers; however, emit TE polarized radiation due to the larger optical confinement factor for TE over TM modes in the laser cavity).

In quantum well structures, unlike in bulk material, the electron wavevector is quantized, and at the band-edge, $\hat{\mathbf{k}} = \hat{\mathbf{k}}_z$. Defining TE polarization to be that for which $\hat{\mathbf{e}}$ is parallel to the QW plane, the dot product in (2.2.14) indicates that all band-edge optical transitions to the HH band are TE polarized with a probability that is 3/2 times larger than that in bulk material. Optical transitions to the LH band, on the other hand, are four times more likely to emit TM polarized radiation than TE polarized radiation [Chong, 1989]. As

the electron energy increases away from the band-edge k_{xy} becomes finite and so $\hat{k}$ is no longer parallel to $\hat{k}_z$. Therefore, the transition probability from (2.2.14) changes with energy. A comparison between the band edge transition probabilities due to TE and TM polarized radiation in bulk and QW structures is given in Fig. 2.7.

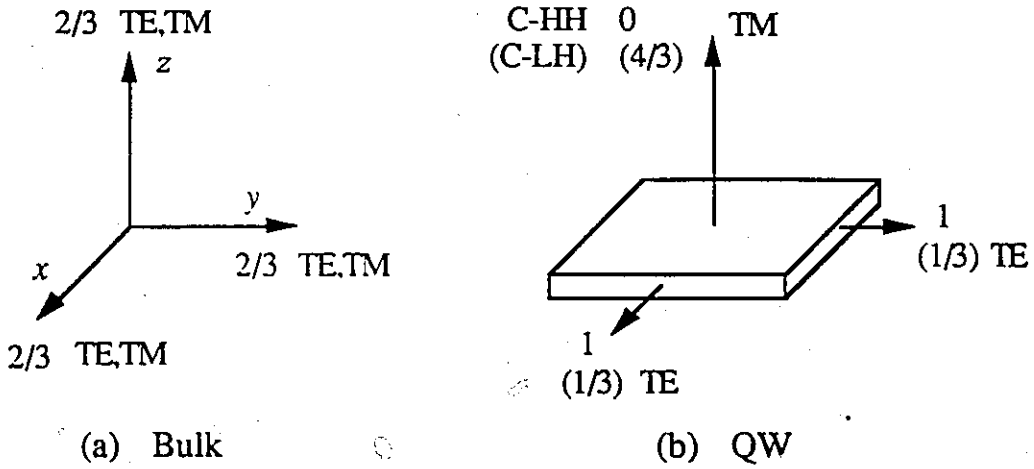

Figure 2.7: Comparison between the band edge transition probabilities (in units of $|P_0|^2$) at different polarizations for bulk and quantum well structures.

From the above analysis, the transition rate $W_{e\text{-}h}$ for optical transitions between any single pair of conduction and valence band states in response to a flux of photons of any polarization is now known. To find the total transition rate, a sum over all allowed transition pairs corresponding to the many possible k-state combinations must be performed. In performing this sum, however, it must be noted that from the k-selection rule in (2.2.8), transitions cannot take place between just any energy levels in the conduction and valence bands. This restriction due to momentum conservation reduces the number of allowed energy state pairs that can be involved in a transition and leads to the concept of the reduced density of states. Assuming parabolic bands, the reduced density of states for bulk and QW materials is obtained by dividing (2.2.1) and (2.2.2) respectively by two and by replacing the effective mass terms by the reduced mass, m_r^*. The division

by two reflects the fact that spin must be conserved in the transitions and the reduced mass, m_r^*, is given by [Verdeyen, 1989]:

$$m_r^* = \frac{m_c^* m_v^*}{m_c^* + m_v^*} \tag{2.2.15}$$

In summing the transition rate for a single pair of energy states over all the energy states that are allowed to participate in a transition, one must also account for the probability that a state in the conduction band is full and that a state in the valence band is empty. Whether or not a state is full is given by the electron occupation probability, which in turn is determined from the Fermi-Dirac distribution and is given by:

$$f_{c,v} = \frac{1}{1 + \exp\left[\dfrac{\left(E_{e,h} - E_{fc,fv}\right)}{k_B T}\right]}, \tag{2.2.16}$$

where, $E_{fc,fv}$, are the quasi-Fermi levels for the conduction and valence band respectively. Due to k-conservation, $E_{e,h}$ in (2.2.16) are given by:

$$E_e = E_{c_n} + \frac{m_r^*}{m_c^*}\left(E_{eh} - E_g\right),$$

and (2.2.17)

$$E_h = E_{v_n} + \frac{m_r^*}{m_v^*}\left(E_{eh} - E_g\right),$$

where E_{eh} is the transition energy and $E_g = E_{cn} - E_{vn}$ is the bandgap between two subbands.

When the reduced density of states, ρ_{red}, and the occupation probabilities are included in (2.2.8), and when (2.2.8) is integrated over all possible energy state combinations that can participate in a downward transition (stimulated emission of a photon), the downward transition rate in response to a flux of incident photons of a given energy, is:

$$W_{c\to v} = \frac{\pi q^2}{m_o^2 \omega \varepsilon} |M_T|^2 \rho_{red}\left(E_{eh} - E_g\right) f_c\left(1 - f_v\right). \qquad (2.2.18)$$

The total upward transition rate (stimulated absorption) in response to a flux of incident photons is obtained by inserting into (2.2.3) the annihilation operator part of the interaction Hamiltonian and interchanging the subscripts c and v. Following this procedure one obtains for the transition rate for the absorption of photons:

$$W_{v\to c} = \frac{\pi q^2}{m_o^2 \omega \varepsilon} |M_T|^2 \rho_{red}\left(E_{eh} - E_g\right) f_v\left(1 - f_c\right). \qquad (2.2.19)$$

Using (2.2.18) and (2.2.19), it is now possible to continue towards arriving at an expression for the optical gain in a semiconductor. From (2.2.18) and (2.2.19), the difference between the rate of stimulated emission and the rate of stimulated absorption of photons is:

$$W_{net} = W_{c\to v} - W_{v\to c} = \frac{\pi q^2 \hbar}{m_o^2 \varepsilon E_{eh}} |M_T|^2 \rho_{red}\left(E_{eh} - E_g\right)\left(f_c - f_v\right). \qquad (2.2.20)$$

When (2.2.20) is inserted into a photon continuity equation which is analogous to the current continuity equation, it becomes evident that the quantity $(n_r/c)\cdot W_{net}$, where n_r is the refractive index of the medium, gives the net number of photons emitted or absorbed per unit distance in the medium. If this quantity is positive, the photon flux in the medium increases with distance and it represents the gain coefficient, $g(\omega)$. If this quantity is negative, the photon flux decreases with distance and it represents the absorption coefficient, $\alpha(\omega)$.

To more accurately describe the gain/absorption coefficient, consideration must be made of the fact that each allowed transition has an energy spread due to energy level broadening caused by intraband relaxation processes, such as, electron-electron, and electron-phonon scattering. To account for this energy level broadening the function that

describes the spectral broadening of the transitions, L(E), must be convolved with the gain expression of (2.2.20) over all possible transition energies, E_{eh}. The function that is commonly used to describe the spectral broadening of the transitions is a Lorentzian function. It is given by [Asada, 1984,1993]:

$$L(E_{eh}) = \frac{1}{\pi} \frac{\hbar/\tau_{in}}{\left(E_{eh} - \hbar\omega\right)^2 - \left(\hbar/\tau_{in}\right)^2}, \tag{2.2.21}$$

where, τ_{in}, is the intraband relaxation time (≈0.1ps). When this function is convolved with (2.2.20) one obtains the following general expression for the gain in bulk material:

$$g(\omega) = \frac{\pi q^2 \hbar}{m_0^2 n_r c \varepsilon_o \hbar\omega} \int_{E_g}^{\infty} |M_T|^2 \rho_{red}(E_{eh} - E_g) \cdot L(E_{eh}) \cdot (f_c - f_v) dE_{eh} . \tag{2.2.22}$$

It should be noted from (2.2.20) that the photon energy term, E_{eh}, in the denominator of (2.2.20) has not been included in the convolution. This is because it is related, not to the energy of the state, but to the actual photon energy, as seen by the ω term in the denominator of (2.2.6).

For quantum wells the gain expression of (2.2.22) must be modified to account for the fact that transitions may occur between different quantized levels. Denoting the subbands in the conduction and the valence bands by the quantum numbers, n_c and n_v, and the heavy or the light hole bands by the subscript, J (=lh or hh), the total gain for a quantum well structure at a particular photon energy, and for a particular polarization, is found by summing over all allowed subband transition pairs. The gain for a quantum well structure is therefore given by [Rosenzwig, 1991],[Asada, 1984]:

$$g(\omega) = \frac{\pi q^2}{m_0^2 n_r c \varepsilon_o \omega} \sum_J \sum_n^M \int_{E_g'}^{\infty} |M_T^J(E_{eh})|^2 \rho_{red}^J(E_{eh} - E_g') \cdot L(E_{eh}) \cdot (f_{cn}^J - f_{vn}^J) dE_{eh}, \tag{2.2.23}$$

where:
$$E_g' = E_{cn} - E_{vn}^J,$$

and $$\rho_{red}^{J}\left(E_{eh}-E_g'\right)=\frac{\pi}{2\hbar^2 L_z}\left(\frac{m_v^J m_c}{m_v^J+m_c}\right)H\left(E-E_g'\right),$$

for $$E_g' < E < E_g + \Delta E_C + \Delta E_V .$$

With expressions for the material gain in both bulk and quantum well material now developed, it is possible to examine how the material gain, and hence laser performance, is affected by modifications to the density of states. To examine how changes to the density of states, and therefore quantization, can affect laser performance, it is first necessary to determine explicitly how changes to the density of states can affect the material gain, and then to relate these changes in the material gain to changes in laser performance. From (2.2.22) and (2.2.23) the material gain depends on the density of states, not only explicitly through the term, ρ_{red}, but also, and more importantly, implicitly through the terms f_c and f_v. Exactly how the gain and, therefore, laser performance depends on the density of states through the terms f_c and f_v will be described in the following section.

2.2.3 Impact of the Density of States on Material Gain and Laser Performance

From (2.2.22) and (2.2.23) it is clear that when $f_c > f_v$, the gain is positive and light of frequency ω will be amplified in the material. From (2.2.16), this inequality is equivalent to stating that the requirement for positive gain is:

$$E_{fc}-E_{fv} > E_e-E_h > E_{cn}-E_{vn} . \qquad (2.2.24)$$

Equation (2.2.24) is the well known Bernard-Duraffourg condition for optical gain in a semiconductor and indicates that when the quasi-Fermi level separation (E_{fc}-E_{fv}) is greater than the band gap energy E_g, the rate of stimulated emission of photons will exceed the rate of stimulated absorption of photons, for photons which have an energy, $\hbar\omega$, that is greater

than E_g but less than E_{fc}-E_{fv}. Of fundamental importance then are the parameters E_{fc} and E_{fv}. Their importance is illustrated in Fig. 2.8.

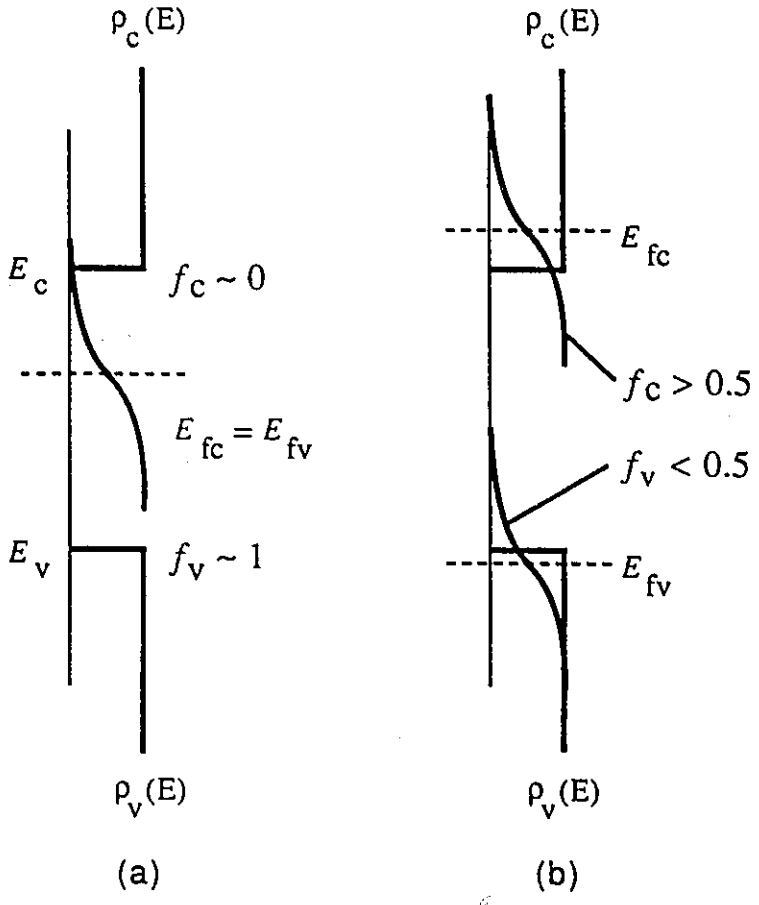

Figure 2.8: Illustration of the quasi-Fermi functions superimposed on the two dimensional density of states functions of the conduction and valence subbands in a quantum well for the case (a) of a lightly doped n-type material under equilibrium conditions and (b) for an undoped material under strong nonequilibrium conditions such that a large concentration of both electrons and holes exists (From [Corzine, 1993]).

As shown in Fig. 2.8(a), under equilibrium conditions, by definition, E_{fc}=E_{fv}. For lightly doped n-type material E_{fc}=E_{fv} leads to the condition that, f_c-f_v is ≈-1. From (2.2.23) when f_c-f_v is negative, the gain is negative, so the material is absorbing. In order to create gain then, it is necessary to create a non-equilibrium situation such that the quasi-Fermi levels are separated by the amount dictated by (2.2.24). The required quasi-Fermi level separation can be achieved by injecting a concentration of electrons, N, and holes, P,

into the active region of the device by forward-biasing the laser. The corresponding non-equilibrium condition is shown in Fig. 2.8(b).

The positions of the quasi-Fermi levels depend, not only upon the magnitude of the injected electron and hole carrier concentrations N and P in the conduction and valence bands, respectively, but also on the density of states. The quasi-Fermi levels are implicitly related to the density of states and the carrier concentrations N and P through (2.2.16) and the general relations:

$$N = \int_{E_c}^{\infty} \rho_c (E - E_c) f_c dE, \tag{2.2.25a}$$

and

$$P = \int_{-\infty}^{E_v} \rho_v (E_v - E)[1 - f_v] dE. \tag{2.2.25b}$$

For bulk material, the density of states function, $\rho(E)$, as given by (2.2.1) prevents one from obtaining a closed form expression for N or P, and therefore an explicit relation for E_{fc} and E_{fv}, when the quasi-Fermi levels $E_{fc,fv}$, are within $\approx 3 \cdot kT$ from the band edge (as will be the case for laser operation). As a result equations (2.2.25) must be solved numerically. For quantum well materials, however, since $\rho(E)$, as given by (2.2.2), is independent of energy for each quantized subband, equations (2.2.25) may be evaluated analytically. It should be noted, however, that the total density of electrons (or holes) in a QW, $N(P)_{TOT}$, consists of two components: the density of electrons(holes) bound in the quantum well, $N(P)_{QW}$, and the density of free (unbound) electrons(holes), $N(P)_{UB}$, in the quantum well which have an energy higher that the barrier height. Thus, the electron (or hole) carrier concentration in a QW is given by:

$$N(P)_{TOT} = N(P)_{QW} + N(P)_{UB}, \tag{2.2.26}$$

It should also be noted when considering the component consisting of the density of electrons (or holes) $N(P)_{QW}$ bound in the QW, that a sum over all the quantized subbands must be performed. From (2.2.25) and (2.2.2), N_{QW} and P_{QW}, with the parabolic band assumption, are given by[1] [Rosenzweig, 1991], [Asada, 1984]:

$$N_{QW} = \rho_c \sum_n \int_{E_{cn}}^{\Delta E_c} f_c dE_e = \left(\frac{m_c^* k_B T}{\pi \hbar^2 L_z}\right) \sum_n \ln\left[\frac{1+\exp\left\{\left(E_{fc} - E_{cn}\right)/k_B T\right\}}{1+\exp\left\{\left(E_{fc} - \Delta E_c\right)/k_B T\right\}}\right], \quad (2.2.27a)$$

and

$$P_{QW} = \sum_J \rho_v^J \sum_n \int_{-\Delta E_v}^{E_{vn}} \left(1 - f_v^J\right) dE_h = \sum_J \left(\frac{m_v^{J*} k_B T}{\pi \hbar^2 L_z}\right) \sum_n \ln\left[\frac{1+\exp\left\{-\left(E_{fv} - E_{vn}^J\right)/k_B T\right\}}{1+\exp\left\{-\left(E_{fv} + \Delta E_v\right)/k_B T\right\}}\right] \quad (2.2.27b)$$

Also, N_{UB}, P_{UB} are given by (2.2.25) with the appropriate changes to the integration limits. For example:

$$N_{UB} = \frac{1}{2\pi^2}\left[\frac{2m_c^*}{\hbar^2}\right]^{3/2} \int_{\Delta E_c}^{\infty} f_c \sqrt{E_e}\, dE_e. \quad (2.2.28)$$

Due to the phenomenological nature of this thesis, no attempt has been made to accurately take into account conduction- and valence-band non-parabolicities in performing gain and threshold current calculations; rather, use of the parabolic band assumption (equation (2.1.9)) has been made. The parabolic band assumption is commonly employed in making gain calculations in quantum well lasers and should not lead to great errors in this thesis (no more so than other assumptions and approximations that are made in the determination of both the relevant parameters and the theoretical expressions presented). However, the existence of valence band non-parabolicities, particularly in unstrained QW lasers, must be kept in mind when interpreting and analyzing device data. When one wishes to be absolutely rigorous in evaluating (2.2.25), for example, when considering the

[1] For clarity E_{vn} is not measured positively into the valence band quantum well, but is measured relative to some arbitrary reference point from which all energies are defined and ΔE_v is taken to be a positive quantity.

case of the valence subbands of an unstrained quantum well, the parabolic band assumption cannot be used and it is more appropriate to find the carrier density by numerically integrating over k space. It is more appropriate to integrate over k space because k states are uniformly distributed in k space regardless of the shape of the energy band. When considering non-parabolicities, then, (2.2.25b) may be replaced by the relation:

$$P = \sum_{J}\sum_{n}\int_{0}^{k_{max}} \rho_v^J\left(k_{xy}\right)\left[1 - f_v^J\left\{E_{vn}\left(k_{xy}\right)\right\}\right]dk_{xy}. \qquad (2.2.29)$$

In order to obtain E_{fc} and E_{fv}, and hence, f_c-f_v in (2.2.23), one assumes an injected carrier density, say N, and then uses (2.2.26) and (2.2.27a) to obtain E_{fc}. The charge neutrality condition, which requires that: $N + N_A^- = P + N_D^+$, where N_D^+ and N_A^- are the ionized donor and acceptor concentrations in the material (and are negligible in the case of this thesis), is then applied to obtain P (=N), and E_{fv} is calculated from (2.2.7b).

The injected carrier density required to produce enough gain to achieve the lasing condition in the laser is called the threshold carrier density, N_{th}. The threshold carrier density and, therefore, the threshold current for the laser may be assumed to consist of two parts: the transparency carrier density, N_{tr}, needed to maintain the electron density at the optical transparency level (which occurs when E_{fc}-E_{fv}=E_g); and N_{inc} (= N_{th} - N_{tr}), which is required to increase E_{fc}-E_{fv}, and therefore f_c-f_v, to the point where the gain is sufficient to overcome all the photonic losses in the laser cavity. The quantity N_{tr} represents the fundamental limit to achieving the lowest lasing threshold current in a semiconductor laser for the situation when all photonic losses are negligible. The losses that must be overcome to achieve lasing include: internal cavity losses, α_{int}, such as, intervalence-band and free-carrier absorption; external cavity losses, α_{ext}, such as, scattering and absorption losses due to the waveguide material and the metal contact layer; and, finally, the distributed mirror losses which are commonly given by [Agrawal, 1986]:

$$\alpha_m = \frac{1}{2L}\ln\left(\frac{1}{R_1 R_2}\right), \tag{2.2.30}$$

where L is the cavity length and R_1 and R_2 are the end facet reflectivities.

The gain required to reach the lasing condition is called the threshold gain, g_{th}, and is given by the relation [Agrawal, 1986]:

$$g_{th} = \alpha_{\text{int}} + \frac{(1-\Gamma)}{\Gamma}\alpha_{ext} + \frac{1}{2\Gamma L}\ln\left(\frac{1}{R_1 R_2}\right), \tag{2.2.31}$$

where Γ is the optical confinement factor, which, as in (2.1.9), represents that fraction of the optical mode intensity that overlaps the active, or gain, region of the laser. The current density, J_{th}, required to achieve the threshold gain, g_{th}, is called the threshold current density, and is given by the relation:

$$J_{th} = \frac{n_w q L_z N_{th}}{\tau_{th}}, \tag{2.2.32}$$

where, n_w, represents the number of quantum wells in the active region, L_z, is the well thickness, τ_{th}, is the carrier lifetime at the carrier density N_{th}.

The threshold current density is an important parameter, and much work in the semiconductor field has been done to minimize it. The minimization of the threshold current is sought in order to reduce both power dissipation (for optical communications systems) and total power requirements (for optical arrays). Clearly from (2.2.32), in order to minimize J_{th}, one must minimize N_{th}, which also can result in a beneficial increase in τ_{th}, as will become clear in Chapter 3. Since N_{tr} represents the fundamental limit on N_{th} as the sum of the cavity losses are reduced, it appears that in order to minimize N_{th}, one must minimize both the total cavity losses and the quantity N_{tr}. In principle the cavity losses may be reduced in a number of ways; in practice, however, it is only possible to minimize

cavity losses to a certain value. In addition, the steps that can be taken to minimize cavity losses can actually have undesirable effects on overall laser performance. For example, from (2.2.31) it is seen that the cavity losses may be minimized by: (i) applying high reflectivity coatings (but this results in a reduced external efficiency, η_{ext}), by; (ii) increasing L (but this increases device capacitance and possibly the threshold current, I_{th}), or by (iii) increasing Γ (which requires increasing n_w and/or L_z, which may in turn increase J_{th} and therefore I_{th}). A means of optimizing the value of n_w, L_z, and L in order to minimize I_{th} will be discussed in Chapter 4. Thus, it appears that the most desirable means of reducing N_{th} is to reduce N_{tr}.

The quantity N_{tr} can be reduced, as discussed below, by modifying both the valence-band and the conduction-band density of states. However, even when the cavity losses have been minimized, a structure with a smaller N_{tr} may not necessarily have a smaller threshold carrier density N_{th}. It may not have a smaller N_{th} since the additional carrier concentration above N_{tr} (i.e., N_{th}-N_{tr}) required to produce enough gain, g_{th}, to overcome cavity losses may be smaller in a structure with the larger N_{tr} than in a structure with the smaller N_{tr}. This is because the rate of change of gain with carrier concentration, called the differential gain (dg/dN), may be greater in the structure with the larger N_{tr}, and this fact could result in a lower value for N_{th} for that structure. Figure 2.9. illustrates this point.

Fig. 2.9 shows the peak gain *vs.* carrier concentration curves, as determined from (2.2.23) when $E_{ch} = E_{cn}$-E_{vn}, for two structures which are similar in all respects except for the dimensions of the quantum wells. The structure with 180Å thick quantum wells, and the smaller density of states ($\rho_{c,v} \propto L_z^{-1}$), has a much smaller N_{tr} than the structure with 60Å thick quantum wells; however, if the threshold gain requirement as given by (2.2.31) is greater than $\approx 475 cm^{-1}$, the laser with the 60Å thick quantum wells will have the lower N_{th} and therefore a lower threshold current density. The lower threshold density in the

structure with 60Å wells is due to a greater rate of change of gain with injected carrier density, dg/dN, in this structure over that with the 180Å thick quantum wells and the smaller N_{tr}. Since a large dg/dN is also associated with superior high speed characteristics and narrower linewidths, the structure with the larger dg/dN may have superior performance in other respects [Agrawal, 1986].

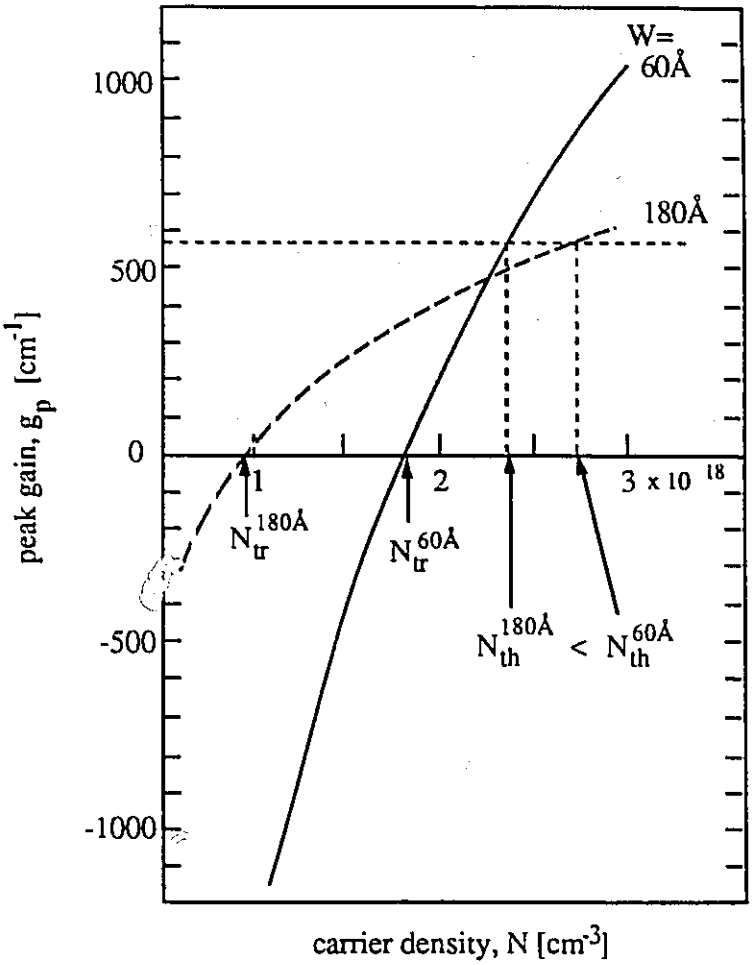

Figure 2.9: Illustration of the peak gain, g_p, vs carrier concentration relation for two $Ga_{0.28}In_{0.72}As_{0.6}P_{0.4}$/InP QW structures with different quantum well thicknesses. The peak gain is obtained from the maximum of the $g(\omega)$ vs ω relation found in (2.2.23). The solid curve is for a structure with 60Å thick quantum wells, the dashed curve is for a structure with 180Å thick quantum wells.

With the above information, the connection and importance of the density of states to laser performance will become apparent. From (2.2.25), f_c and f_v and, therefore, the magnitude of f_c-f_v and N_{tr} are fundamentally related to the density of states ρ_c and ρ_v of a material. By examining this relation, it can be shown that the absolute lowest transparency electron density results when the electron and hole density of states are small and identical (i.e., ρ_c=ρ_v). That a smaller density of states results in a smaller N_{tr} should be evident from an inspection of (2.2.25). To recap, however, the transparency condition is reached when E_{fc}-E_{fv}=E_g. For the case when the density of states, say ρ_c, is small, E_{fc} will move further up in energy for a given increment in the injected carrier density than it will for the case when the density of states is large. As a result of the greater sensitivity of E_{fc} to the injected carrier concentration when ρ_c is small, the transparency condition is reached at smaller current levels for structures with a smaller density of states ρ_c or ρ_v.

That the minimum N_{tr} is obtained when ρ_v=ρ_c may be shown mathematically from the following relation obtained using the charge neutrality condition, N=P, and (2.2.25), using the conditions that the electron and hole density of states functions are identical in functional form, and that ρ_v=Dρ_c, (where D is an arbitrary constant):

$$\int_0^\infty \rho_c dE \left(\frac{1}{\exp\left\{\left(E - E_{fc}\right)/k_B T\right\}} - \frac{D}{\exp\left\{\left(E - \bar{E}_{fv}\right)/k_B T\right\}} \right) = 0 \quad (2.2.33)$$

In this expression the Fermi-Dirac distribution for the valence band has been altered to give the hole occupation probability:

$$\bar{f}_v = \frac{1}{1 + \exp\left[\left(E - \bar{E}_{fv}\right)/k_B T\right]}, \quad (2.2.34)$$

where, rather than defined for (2.2.16), E is measured positive into both the conduction and valence bands from the respective band edges. With this change in the reference energy level for E_{fc} and E_{fv}, the transparency condition, from (2.2.33) for D=1 (i.e., when

$\rho_v=\rho_c$), is $E_{fc}-\overline{E}_{fv}=0$. For D>1, then the integral contribution of the "hole" term in (2.2.33) must be reduced to satisfy the charge neutrality condition which requires that $\overline{E}_{fv}$ must decrease. If $\overline{E}_{fv}$ decreases then in order to satisfy the transparency condition, E_{fc} in (2.2.33) must increase. An increase in E_{fc} in turn, from (2.2.25), results in a higher transparency electron density than the case when D=1.

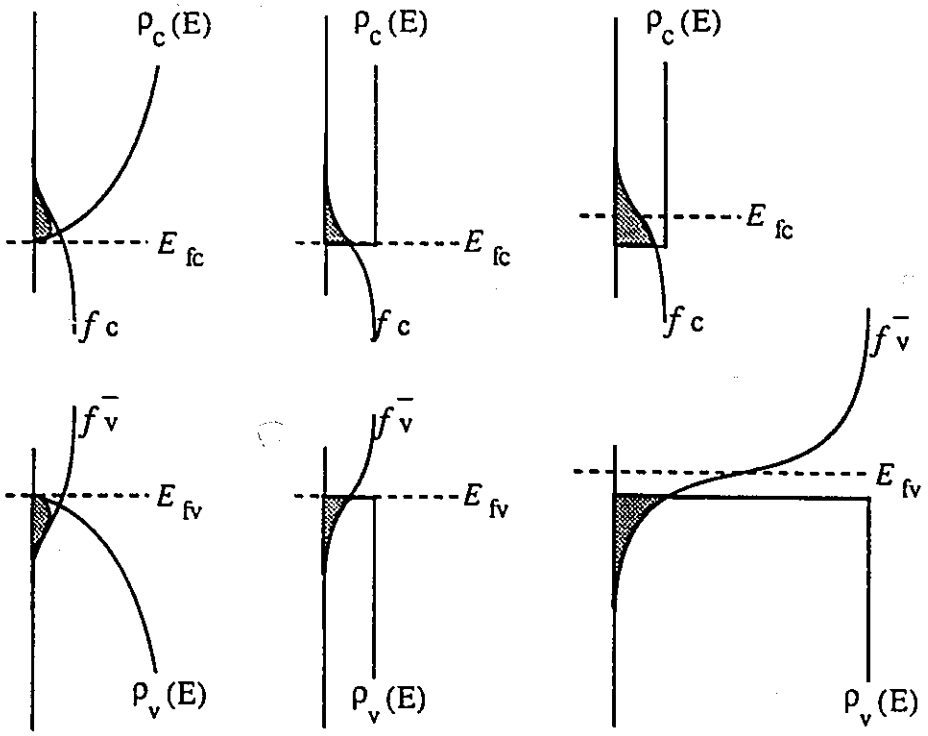

(a) Bulk, $m_v=m_c$ (b) QW, $m_v=m_c$ (c) QW, $m_v=5m_c$

Figure 2.10: Illustration of the band edge transparency condition (E_{fc}-E_{fv}=E_g) for three different idealized cases: (a) bulk material with $\rho_c=\rho_v$, (b) quantum well structure with $\rho_c=\rho_v$, and (c) quantum well structure with $\rho_v=5\rho_c$. In each case, the carrier filling of each band is indicated by the shaded overlap region between the Fermi function and the density of states. The "hole" Fermi function $\bar{f}_v \equiv 1-f_v$ is used in the figure for clarity.

That the smallest values of N_{tr} are reached when the density of states ρ_c and ρ_v are small and identical is also shown in Fig. 2.10. Fig. 2.10 shows the transparency condition

for three cases: that for bulk material in which $\rho_v=\rho_c$, that for a quantum well in which $\rho_v=\rho_c$, and that for a QW in which $\rho_v=5\rho_c$. From (2.2.25), the shaded region in the figure represents the carrier density in the band. From this figure it should be apparent that a smaller density of states $\rho(E)$ will result in a smaller shaded area, and therefore a smaller N_{tr}. It may also be noted in comparing Fig. 2.10(a) with 2.10(b), that the parabolic band edge of the bulk material yields $N_{tr}(bulk)<N_{tr}(QW)$. (Nevertheless, the QW structure should still have a much smaller threshold carrier density since, from (2.2.32), the thickness of the active region of the QW laser ($n_w \cdot L_z$) is typically an order of magnitude, or more, smaller than the active region of a bulk material.) From Fig 2.10(c) it is seen that when the density of states of the valence band is much larger than that of the conduction band, both Fermi functions are shifted toward the band with the smaller density of states in order to maintain charge neutrality. As already shown, the result is that N_{tr} increases over the case when $\rho_v=\rho_c$.

The greatest differential gain, dg/dN is also achieved when $\rho_c=\rho_v$ and is greatly enhanced in a quantum well structure over a bulk structure due to the sharp band edge and the step like density of states in a quantum well. Qualitatively how the differential gain depends on the symmetry and form of the density of states is as follows. From (2.2.23), the differential gain depends on the rate of change of the quantity $[\rho_{red}f_c+\rho_{red}(1-f_v)] - \rho_{red}$ with injected carrier concentration. The quantities $\rho_{red}f_c$ and $\rho_{red}(1-f_v)$ are in turn directly associated with the band edge carrier densities of the material since $\rho_{red}=\rho_{c,v}/2$ when the bands are symmetric. As seen in Fig. 2.10, the rate of change of the band edge carrier concentration in response to a change in $E_{fc}-E_{fv}$, (which is altered due to the injection of carriers) depends upon the slope of the Fermi function $f_{c,v}$ at the band edge. The maximum rate of change of the band edge carrier densities with a change in $E_{fc}-E_{fv}$ occurs when E_{fc} and E_{fv} are at the band edge, (i.e., at the transparency condition when $\rho_c=\rho_v$). Also, as

seen in Fig. 2.10, and from (2.2.33), when $\rho_v > \rho_c$, the Fermi level E_{fc} is well into the conduction band. Now, due to the smaller ρ_c, E_{fc} changes more than E_{fv} in response to an increment in E_{fc}-E_{fv}, (i.e., a change in N), and since the slope of the Fermi function at the conduction band edge is shallow in this case, the band edge carrier density, and therefore the gain, changes less in response to a change in E_{fc}-E_{fv} than for the case where $\rho_v < \rho_c$. Therefore, the maximum rate of change of the gain with an increment in N, which causes the change in E_{fc}-E_{fv}, occurs when $\rho_c = \rho_v$. A more exact treatment on the effects of asymmetries between and ρ_c and ρ_v on the differential gain is given by Lau, [1993].

The increased differential gain in a quantum well over bulk material can be inferred by comparing Fig. 2.10(b) with Fig. 2.10(a). Clearly the band edge carrier concentration, and therefore the gain is less in the bulk material than in the quantum well due to the stepwise nature of the density of states in the QW. In addition, since the density of states in the QW for energies above the QW band edge is very much less than that in the bulk material, a discrete increase in N may cause a much larger change in E_{fc}-E_{fv}, and therefore, in f_c-f_v and the gain in a quantum well, than in bulk material. It is for this reason that quantum wells are predicted and observed to have superior high speed characteristics and linewidths over bulk lasers.

In summary it has been revealed that the gain and the differential gain and, therefore, the performance of semiconductor lasers is highly dependent, not only on the functional form and magnitude of the density of states function, but also upon the degree of asymmetry between the conduction band and the valence band density of states $\rho_c(E)$ and $\rho_v(E)$ respectively. It was found that the smallest transparency current density, and therefore the lower limit on the threshold current density occurs when the density of states is small (i.e., when the conduction band and valence bands are symmetric, such that $\rho_c = \rho_v$ (i.e., $m_c^* = m_v^*$)), and when the band edge is parabolic as in the bulk case. A smaller

transparency current density for bulk over quantum well materials is of little consequence since the active region in quantum well lasers is much smaller than in bulk lasers [Lau, 1993]. The smaller active region thickness for QW lasers more that compensates for the increased N_{tr} for quantum well over bulk lasers and, as a result, quantum well lasers have been reported to have significantly smaller threshold current densities than bulk lasers. In addition, quantum well lasers maintain a significant advantage over bulk lasers in that their steep and step-like density of states results in a higher differential gain in QW over bulk lasers. A high differential gain, dg/dN, is linked to better linewidth characteristics and higher speed devices and, like the transparency current density, N_{tr}, is optimized when the conduction and valence band density of states are symmetric such that $\rho_c=\rho_v$.

It is clear from the above arguments that if one had the ability to alter the valence band density of states such that it could be made smaller and have greater symmetry with the conduction band density of states, then the performance of quantum well lasers could be be improved significantly. Such altered lasers would have smaller threshold current densities and narrower linewidths. It will be shown in the next section that the use of material strain in quantum well materials may provide the laser designer with some of these advantages.

2.3 STRAIN IN QUANTUM WELL LASERS

It has been shown above that improvements in laser performance are expected for quantum well over bulk lasers. These improvements are expected due to the effects of quantum confinement, such as: the creation of a constant density of states function in the quantum well; and a reduced effective mass and, therefore, reduced density of states, for heavy holes near the top of the valence band. Further improvements in laser performance have been predicted and observed for laser structures in which the quantum well material is

under strain [Yablonovitch, 1988], [Thijs, 1991], [Evans, 1992]. These predictions come about, as will be discussed below, because strain allows for the possibility of reducing the magnitude of the valence band effective mass and thus the valence band density of states so that they are more symmetrical with the conduction band density of states. Such changes in the valence band structure may, according to §2.2.3, result in decreased values of N_{tr} and increased values for dg/dN, and consequently, reduced threshold currents and laser linewidths for strained over unstrained quantum well lasers. This section discusses the implication and means of introducing strain into the quantum well. The theory and illustrations of the effects of strain on the quantum well band structure are presented along with commonly employed approximations and assumptions.

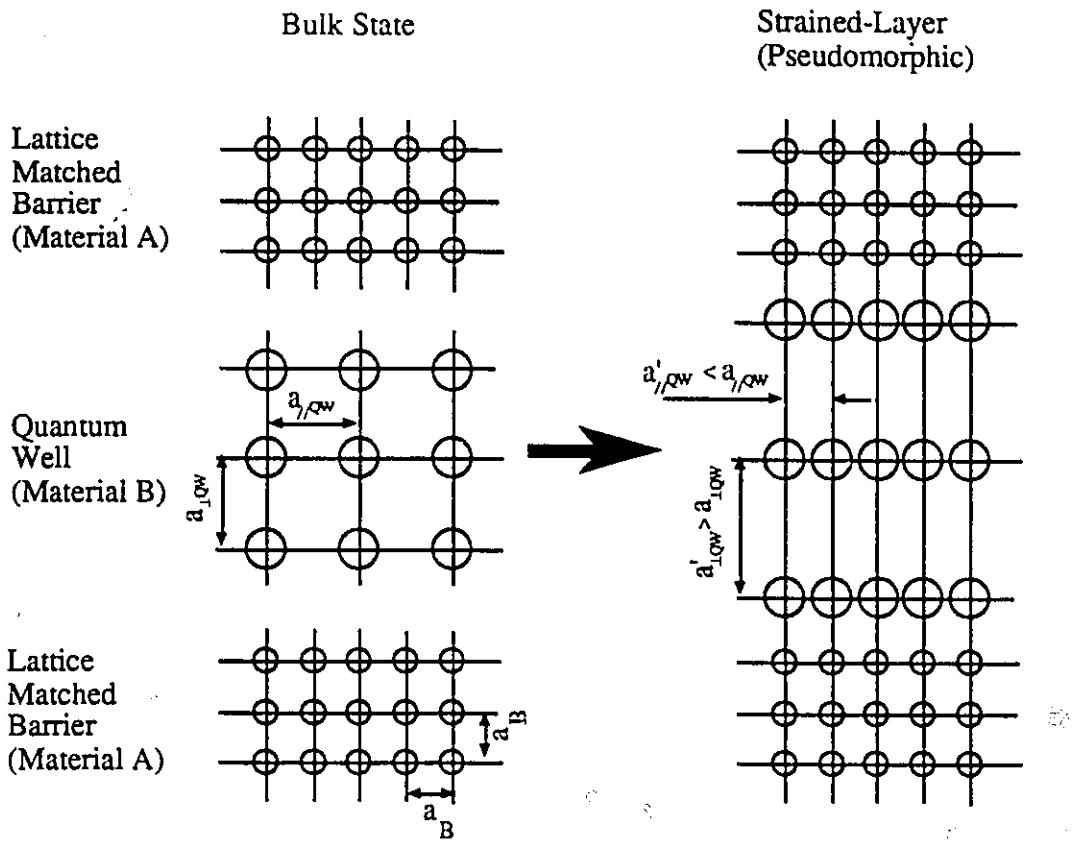

Figure 2.11: Schematic representation of the introduction of compressive strain into a thin (QW) layer of material by epitaxially depositing it onto a substrate layer consisting of material with a larger lattice constant.

Strain is introduced into the quantum well region of the laser by growing the quantum well from material which has a natural bulk lattice constant that is slightly mismatched from that of the underlying substrate. As shown schematically in Fig. 2.11, when the quantum well material is deposited onto a substrate with a different lattice constant, in order for the interface between the well material and the substrate to be defect free, the in-plane lattice constant of the QW epilayer must conform to that of the substrate. As a result, the lattice structure of the epilayer undergoes a tetragonal deformation. If the lattice constant of the epilayer is larger(smaller) than that of the substrate, then a biaxial compression(tension) is created in the plane parallel to the interface, and a corresponding expansion(compression) occurs in the direction perpendicular to the interface.

For a strained layer superlattice, the lattice constant of the strained layers A and B in the plane parallel to the interface ($a_{||}$) is given by [Osbourn, 1982]:

$$a_{||} = a_A\left[1 + \frac{fG_B h_B}{G_A h_A + G_B h_B}\right],$$

or (2.3.1)

$$a_{||} = a_B\left[1 - \frac{fG_A h_A}{G_A h_A + G_B h_B}\right],$$

where,
- $a_{A,B}$ = the unstrained lattice constant of material A or B
- $h_{A,B}$ = the thickness of material A or B
- $G_{A,B}$ = the shear modulus of the respective material
- f = the fractional lattice mismatch between the unstrained materials, A and B.

The net biaxial strain in the layer plane, $\varepsilon_{||}^{A,B}$, for layers A and B is given by:

$$\varepsilon_{||}^{A,B} = \varepsilon_{xx} = \varepsilon_{yy} = \left(a_{||} - a_{A,B}\right)\Big/a_{A,B}. \qquad (2.3.2)$$

For cubic structures grown in the (001) direction, the strain along the growth direction, as determined from (2.3.11) in Section 2.3.2, is given by [People,1990]:

$$\varepsilon_{zz} = -(2C_{12}/C_{11})\varepsilon_{\parallel}^{A,B}. \tag{2.3.3}$$

From (2.3.1) and (2.3.2), the ratio of the strain parallel to the interfaces for a strained epilayer is inversely proportional to the thicknesses of the layer; consequently, the thinnest of two strained epilayers will have the greatest layer strain. The situation depicted in Fig, 2.11 is that for which the substrate is infinitely thick ($h_A = \infty$). Thus, the entire mismatch is taken up by the quantum well epilayer.

2.3.1 The Strained Layer Critical Thickness

The strain, ε, produced in a quantum well epilayer can be accommodated without the formation of misfit dislocations provided the thickness of the quantum well layer is less than a certain critical thickness, h_C. A knowledge of this critical thickness limit is important because the defects that are produced through strain relaxation when the critical thickness is exceeded are extremely detrimental to device performance. In lasers, defects in the quantum well active region, which are due to misfit dislocations, act as non-radiative recombination pathways for electrons. This non-radiative recombination will in turn adversely affect the threshold current and the internal efficiency of the laser [Agrawal, 1986].

The critical thickness for a single strained quantum well layer grown on a (001) oriented surfaces is given by the expression [Matthews and Blakeslee (1974)]:

$$h_c = \frac{a}{\sqrt{2}\varepsilon}\frac{(1-\nu/4)}{2\pi(1+\nu)}\left[\ln\left(\frac{\sqrt{2}h_c}{a}\right)+1\right], \tag{2.3.4}$$

where **a** is the lattice constant of the strained layer, and ν is Poisson's ratio. This expression for the critical thickness of a single strained quantum well layer has been verified experimentally by several authors [Andersson, 1987], [Fritz, 1985].

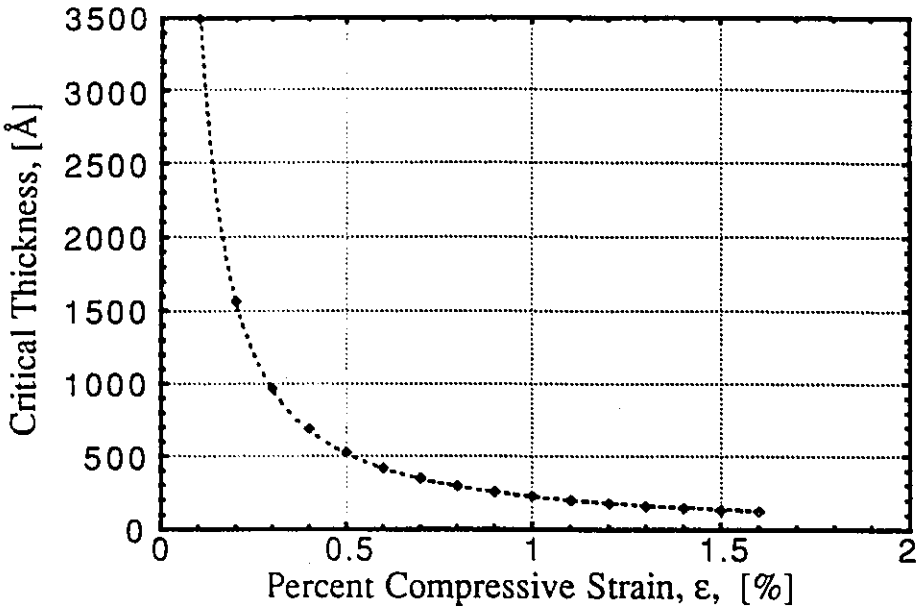

Figure 2.12: The single layer critical thickness as a function of compressive strain for an $In_{1-x}Ga_xAs_yP_{1-y}$ epilayer with a bulk band gap of 0.83eV grown on InP.

Figure 2.12 shows the critical thickness *vs.* strain for a single quantum well comprised of an $In_{1-x}Ga_xAs_yP_{1-y}$ epilayer with a bulk band gap of 0.8eV grown on InP. From this figure, the critical thickness is about 200Å for a strain on the order of 1%. Figure 2.13 shows a transmission electron micrograph (TEM) of a single quantum well structure in which the critical thickness of the strained quantum well was exceeded. The large number of defects generated due to the formation of misfit and threading dislocations completely quenched the quantum well photoluminescence from this structure and made lasing in devices fabricated from this material impossible.

For multiple quantum well structures, a moderate increase in the structural stability of the strained layers arises due to the presence of the lattice matched (to the substrate) barrier regions. The critical thickness, h_c^m, of a multi-layer structure consisting of N

layers of strained material B sandwiched between N+1 layers of lattice-matched material A (see Fig. 2.5) is given by [Houghton, 1990]:

$$h_c^m = Nl_B = \frac{a}{4\sqrt{2}} \frac{(1-\nu/4)}{\varepsilon\pi(1+\nu)} \left[\ln\left(4\sqrt{2}N\left(\frac{l_A + l_B}{a} \right) \right) \right]. \qquad (2.3.5)$$

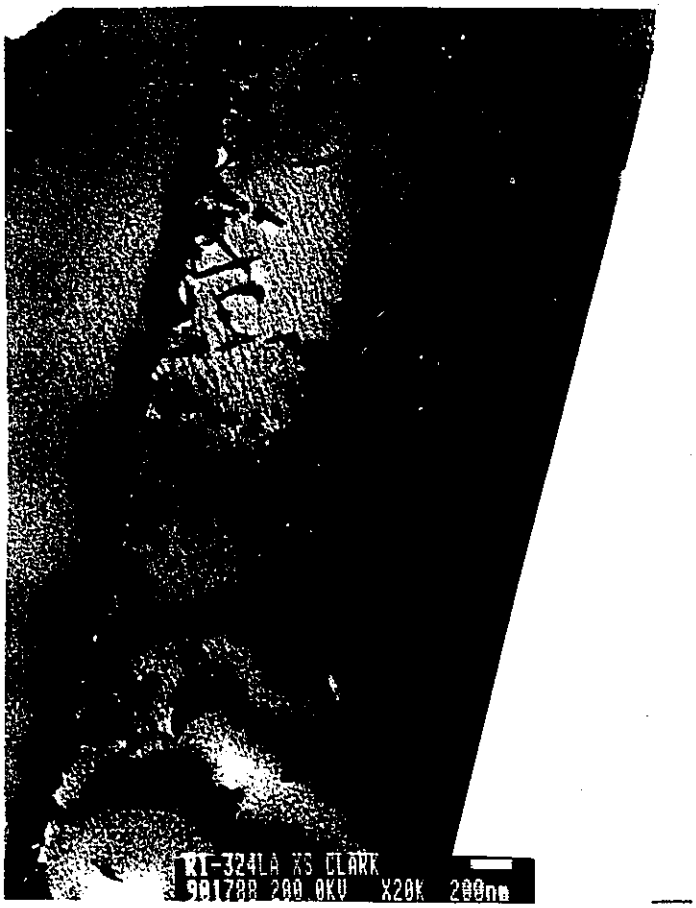

Figure 2.13: TEM photomicrograph of a single quantum well structure in which the critical layer thickness was exeeded. The strain relaxed by the formation of dislocations which act as nonradiative recombination centers and prevented luminescence from the quantum well. The dislocations are clearly seen in the image as dark jagged lines.

2.3.2 Stress Strain Relations in Cubic Crystals

If the stress in a crystal is below the elastic limit, the resulting strain is related to the applied stress through Hooke's Law:

$$\varepsilon_{ij} = S_{ijkl}\sigma_{kl}, \tag{2.3.6}$$

where S_{ijkl}, are the elements of the elastic compliance tensor for the crystal. Alternatively, the stress may be expressed in terms of the induced strain through the relation:

$$\sigma_{ij} = C_{ijkl}\varepsilon_{kl}, \tag{2.3.7}$$

where C_{ijkl}, are the elements of the elastic stiffness tensor.

In the absence of body torques, such as those induced in anisotropic crystals by magnetic fields, the following relations hold:

$$\begin{aligned} S_{ijkl} &= S_{ijlk} : S_{ijkl} = S_{jikl}, \\ C_{ijkl} &= C_{ijlk} : C_{ijkl} = C_{jikl}. \end{aligned} \tag{2.3.8}$$

This symmetry of S_{ijkl} and C_{ijkl} makes it possible to represent the fourth rank elastic stiffness and compliance tensors using matrix notation [Nye, 1957]:

$$\varepsilon_i = S_{ij}\sigma_j \quad \text{or} \quad \sigma_i = C_{ij}\varepsilon_j . \tag{2.3.9}$$

In addition, crystal symmetry effects reduce the number of independent S_{ij} and C_{ij} tensor components. For cubic crystals, such as those formed by III-V compounds, and in the absence of true shear stresses, equations (2.3.9) become:

$$\begin{bmatrix} \varepsilon_{xx} \\ \varepsilon_{yy} \\ \varepsilon_{zz} \end{bmatrix} = \begin{bmatrix} s_{11} & s_{12} & s_{12} \\ s_{12} & s_{11} & s_{12} \\ s_{12} & s_{12} & s_{11} \end{bmatrix} \begin{bmatrix} \sigma_{xx} \\ \sigma_{yy} \\ \sigma_{zz} \end{bmatrix} \tag{2.3.10}$$

$$\begin{bmatrix} \sigma_{xx} \\ \sigma_{yy} \\ \sigma_{zz} \end{bmatrix} = \begin{bmatrix} c_{11} & c_{12} & c_{12} \\ c_{12} & c_{11} & c_{12} \\ c_{12} & c_{12} & c_{11} \end{bmatrix} \begin{bmatrix} \varepsilon_{xx} \\ \varepsilon_{yy} \\ \varepsilon_{zz} \end{bmatrix} \tag{2.3.11}$$

The elastic stiffness and compliance constants appearing in (2.3.10) and (2.3.11) are related through an inverse matrix relation which gives:

$$c_{11} = \frac{s_{11} + s_{12}}{(s_{11} - s_{12})(s_{11} + 2s_{12})},$$

and (2.3.12)

$$c_{12} = \frac{-s_{12}}{(s_{11} - s_{12})(s_{11} + 2s_{12})},$$

and Poisson's ratio, v, which appears in (2.3.4) and (2.3.5) is given by:

$$v = -\frac{s_{12}}{s_{11}}. \tag{2.3.13}$$

2.3.3 Effects of Strain on the Semiconductor Band Structure

From (2.3.3) a biaxial strain in the plane of a quantum well epilayer is accompanied by a strain in the growth direction. This deformation of the crystal along the growth direction is similar to that produced by a uniaxial stress. A biaxial stress, in the matrix notation of (2.3.10) may therefore be considered to be the sum of an isotropic or hydrostatic stress and a uniaxial stress:

$$\left[\bar{X}\right]_{biaxial} = \begin{bmatrix} \sigma \\ \sigma \\ 0 \end{bmatrix} = \begin{bmatrix} \sigma \\ \sigma \\ \sigma \end{bmatrix} + \begin{bmatrix} 0 \\ 0 \\ -\sigma \end{bmatrix}. \tag{2.3.14}$$

The hydrostatic component of the stress gives rise to a volume change without disturbing the crystal symmetry while the uniaxial component, due to the expansion or compression of the strained crystal along the growth direction, reduces the crystal symmetry. Since the energy gap of a semiconductor is related to its lattice spacing, it is expected that the strain

induced distortions to the crystal lattice will lead to alterations in the energy band structure of strained material.

The hydrostatic component of a biaxial stress shifts the position of the conduction band and the valence bands, and results in a change in the overall band-gap energy by an amount, δE_H, (which is positive for compressive strain and negative for tensile strain). The uniaxial component of the stress splits the degeneracy of the light hole ($J = 3/2$, $M_J = \pm 1/2$ in spherical notation) and heavy hole ($J = 3/2$, $M_J = \pm 3/2$) bands and separates them, to first order, by an amount δE_S (which is negative for biaxial compression and positive for biaxial tension).

The magnitudes of the band gap shifts due to strain are determined by finding the eigenenergies at the band edge (where k=0) of the total Hamiltonian, H_t, for electrons in the crystal which is given by:

$$H_t = H_k + H_{so} + H_\varepsilon^{(c)} + H_\varepsilon^{(1)} + H_\varepsilon^{(2)}, \tag{2.3.15}$$

where, H_k, is the Hamiltonian given by Kane [1966] including the $\mathbf{k}\cdot\mathbf{p}$ perturbation:

$$H_k = \left(-\frac{\hbar^2}{2m}\right)\nabla^2 + V(r) + \left(\frac{\hbar^2 k}{2m}\right) + \left(\frac{\hbar}{m}\right)\mathbf{k}\cdot\mathbf{p}, \tag{2.3.16}$$

$H_\varepsilon^{(c)}$, is the Hamiltonian describing the hydrostatic shift in the conduction band due to strain [Pollak, 1993], [Laude, 1971]:

$$H_\varepsilon^{(c)} = a_c\left(\varepsilon_{xx} + \varepsilon_{yy} + \varepsilon_{zz}\right), \tag{2.3.17}$$

where a_c, is the hydrostatic deformation potential of the conduction band and ε_{ij} denotes the components of the strain tensor.

$H_\varepsilon^{(1)}$, is the orbital-strain Hamiltonian for the $P_{3/2}$ and $P_{1/2}$-like multiplet valence bands [Asai,1983],[Pikus and Bir, 1974], [Pollak, 1990]:

$$H_\varepsilon^{(1)} = -a_1(\varepsilon_{xx}+\varepsilon_{yy}+\varepsilon_{zz}) - 3b_1\left[\left(L_x^2 - \frac{1}{3}L^2\right)\varepsilon_{xx} + cp\right] - \sqrt{3}d_1\left[\left(L_xL_y + L_yL_x\right)\varepsilon_{xy} + cp\right], \tag{2.3.18}$$

where **L** is the angular momentum operator, a_1 is the hydrostatic deformation potential for the valence band, b_1 and d_1 are the shear deformation potentials for strain of tetragonal and rhombohedral symmetries, respectively, and cp denotes cyclic permutation with respect to the indices x,y,z.

$H_\varepsilon^{(2)}$ is the stress-dependent spin-orbit Hamiltonian describing the effects of strain on the spin-orbit interaction [Pollak, 1990], [Laude,1971]:

$$H_\varepsilon^{(2)} = -a_2(\mathrm{L}\cdot\sigma)\left(\varepsilon_{xx}+\varepsilon_{yy}+\varepsilon_{zz}\right) - 3b_2\left[\left(L_x\sigma_x - \frac{1}{3}\mathrm{L}\cdot\sigma\right)\varepsilon_{xx} + cp\right] - \sqrt{3}d_2\left[\left(L_x\sigma_y + L_y\sigma_x\right)\varepsilon_{xy} + cp\right], \tag{2.3.19}$$

where, a_2, b_2, and d_2 are the deformation potentials and σ is the Pauli matrix vector.

And, H_{SO} describes the effect of the spin-orbit interaction [Datta, 1989]:

$$H_{so} = \frac{\hbar}{4m_o^2c^2}[\nabla V \times \mathbf{p}]. \tag{2.3.20}$$

The total Hamiltonian has been solved for the eigenenergies using perturbation theory by Pollak, (1990), Chandrasekhar, (1977) and Laude, (1971). The set of unperturbed wavefunction which were used as the basis functions to solve the total Hamiltonian were those for which the spin-orbit Hamiltonian is diagonal. These wavefunctions are given by (2.2.10) and separately by Datta, (1989), Laude (1971) and

Pollak (1990). In the $|J,M_J\rangle$ representation the s-like, conduction band states are denoted by $|1/2,\pm 1/2\rangle_C = |S\uparrow\downarrow\rangle$, and the p-like heavy-hole, light-hole and spin orbit split off valence band states are denoted by $|3/2,\pm 3/2\rangle$, $|3/2,\pm 1/2\rangle$ and $|1/2,\pm 1/2\rangle$, respectively. In this basis, the Hamiltonian matrix of equation (2.3.15) at **k**=0, for a uniaxial strain along [001] or [111], or for a biaxial strain in the (001), or (111) plane, reduces to two 4 x 4 blocks for +mj or -mj [Lu, 1988], [Pollak, 1990], [Chandrasekhar, 1977]. The Hamiltonian for both manifolds is similar and is given by:

$$\begin{array}{cccc} |S\uparrow\rangle & |3/2,3/2\rangle & |3/2,1/2\rangle & |1/2,1/2\rangle \\ \begin{bmatrix} E_o+\delta E_{H,c} & 0 & 0 & 0 \\ 0 & -\delta E_{H,v}-\frac{1}{2}\delta E_s & 0 & 0 \\ 0 & 0 & -\delta E_{H,v}+\frac{1}{2}\delta E_s & (1/\sqrt{2})\delta E_s' \\ 0 & 0 & (1/\sqrt{2})\delta E_s' & -\Delta_o-\delta E_H' \end{bmatrix} \end{array} \quad (2.3.21)$$

where for a biaxial strain in the (001) plane:

$$\delta E_{H,c} = 2a_c(S_{11}+2S_{12})X, \quad (2.3.22a)$$

$$\delta E_{H,v} = 2(a_1+a_2)(S_{11}+2S_{12})X = 2a_v(S_{11}+2S_{12})X, \quad (2.3.22b)$$

$$\delta E'_{H,v} = 2(a_1-2a_2)(S_{11}+2S_{12})X = 2a'_v(S_{11}+2S_{12})X, \quad (2.3.22c)$$

$$\delta E_s = -2(b_1+2b_2)(S_{11}-S_{12})X = -2b(S_{11}-S_{12})X, \quad (2.3.22d)$$

$$\delta E'_s = -2(b_1-b_2)(S_{11}-S_{12})X = -2b'(S_{11}-S_{12})X, \quad (2.3.22e)$$

in terms of the applied stress, X, (which is negative in the case of compression and positive in tension), or:

$$\delta E_{H,c} = 2a_c[(C_{11}-C_{12})/C_{11}]\varepsilon, \quad (2.3.23a)$$

$$\delta E_{H,v} = 2a_v\left[(C_{11} - C_{12})/C_{11}\right]\varepsilon, \tag{2.3.23b}$$

$$\delta E'_{H,v} = 2a'_v\left[(C_{11} - C_{12})/C_{11}\right]\varepsilon, \tag{2.3.23c}$$

$$\delta E_s = -2b\left[(C_{11} + 2C_{12})/C_{11}\right]\varepsilon, \tag{2.3.23d}$$

$$\delta E'_s = -2b'\left[(C_{11} + 2C_{12})/C_{11}\right]\varepsilon, \tag{2.3.23e}$$

in terms of the strain, ε, (which is also negative in the case of compression).

The eigenvalues of (2.3.21) can be expanded in powers of the stress, X, if one ignores the strain-dependence of the spin-orbit splitting (i.e., a_2=0, b_2=0 so that $\delta E_{H,v} = \delta E'_{H,v}$ and $\delta E_S = \delta E'_S$.) [Pollak, 1990], and assumes that the stress-induced splitting and shifts of the valence bands are much smaller than the spin-orbit splitting, Δ_O [Lu, 1988]. When expanded in terms of the stress X, the eigenenergies of (2.3.21) are:

$$\delta E_{v_2} = -\delta E_H - \frac{1}{2}\delta E_s, \tag{2.3.24a}$$

$$\delta E_{v_1} = -\delta E_H + \frac{1}{2}\delta E_s + \frac{(\delta E'_s)^2}{2\Delta_o} + \ldots, \tag{2.3.24b}$$

and

$$\delta E_{v_3} = -\Delta_o - \delta E'_H - \frac{(\delta E'_s)^2}{2\Delta_o} + \ldots. \tag{2.3.24c}$$

If the stress-induced splittings and shifts of the valence bands are not much smaller than the spin-orbit splitting, Δ_O, then exact expressions for the eigenvalues of (2.3.21), neglecting the strain dependence of the spin-orbit splitting, should be used to determine the conduction and valence band shifts due to strain. These expressions can be found in Pollak (1990), People (1990), or Ji (1987). It should be noted, however, that most authors express the eigenvalues of (2.3.24) to first order only and neglect even the second order stress/strain terms. The omission of the quadratic and higher order stress/strain terms is

valid for strained epilayers of composition relevant to this thesis as long as the layer strains are less than about 1.5% [Kato, (1985)], [Asai, (1983)],[Kuo, (1985)], [Chuang,(1991)].

From the eigenvalues of (2.3.24), the stress dependence of the conduction to valence band energy gaps are given (to second order) by:

$$E_c - E_{v_2} = E_{g_o} + \delta E_H + \frac{1}{2}\delta E_s, \tag{2.3.25a}$$

$$E_c - E_{v_1} = E_{g_o} + \delta E_H - \frac{1}{2}\delta E_s - \frac{(\delta E_s')^2}{2\Delta_o}, \tag{2.3.25b}$$

$$E_c - E_{v_3} = E_{g_o} + \Delta_o + \delta E_H' + \frac{(\delta E_s')^2}{2\Delta_o}, \tag{2.3.25c}$$

where δE_H, is the net shift in the band gap due to the hydrostatic component of the strain and is given by the expression:

$$\delta E_H = 2(a_c + a_v)(S_{11} + 2S_{12})X = 2a(S_{11} + 2S_{12})X, \tag{2.3.26}$$

where a is the total hydrostatic deformation potential and can be obtained from the pressure dependence of the band gap, dE_g^o/dP :

$$a = a_v + a_c = \frac{(C_{11} + 2C_{12})}{3}\frac{dE_g^o}{dP}. \tag{2.3.27}$$

In (2.3.26) the quantity δE_H is expressed in terms of the single hydrostatic deformation potential, a, since only the sum $\delta E_{H,c} + \delta E_{H,v}$ can be observed experimentally. This limitation raises some questions on how to partition the hydrostatic shift in the band gap between the valence band and the conduction band. In this regard, some authors attribute two thirds of the total hydrostatic shift in the band gap to the conduction band, ($a_C = (2a/3)$), and one third to the valence band, ($a_V = (a/3)$) [Chuang, 1991], while some authors attribute the entire hydrostatic shift in the band gap to the conduction band ($a_C = a$, $a_V = 0$) [Ji, 1987], [Kato, 1986]. For calculations performed in

this thesis, the hydrostatic shift in the Γ_8 valence band is taken to be equivalent to the negative of the shift in the ionization potential due to strain [Camphausen, 1971]. The shift in the valence band edge due to the hydrostatic component of a biaxial strain, when determined in this manner, is given by

$$\delta\Gamma_8 = \frac{2}{3}\left(\frac{\partial I}{\partial P}\right)X, \tag{2.3.28}$$

where I is the ionization potential, and P is the pressure. Values of the quantity (∂I/∂P) for several binary compounds may be found in the literature [Camphausen, 1971].

In (2.3.24) and (2.3.25) the stress dependent "heavy hole", "light hole" and "spin-orbit split" valence band states are denoted by $|v_2\rangle$, $|v_1\rangle$ and $|v_3\rangle$ respectively. The reason for this notation is because the off-diagonal terms in (2.3.21) couple the light hole and spin-orbit split states altering them slightly. The stress-dependent wave functions for the k=0 valence bands therefore become:

$$|v_2\rangle = |3/2, \pm 3/2\rangle \tag{2.3.29a}$$

$$|v_1\rangle = \alpha|3/2, \pm 1/2\rangle + \beta|1/2, \pm 1/2\rangle \tag{2.3.29b}$$

$$|v_3\rangle = -\beta|3/2, \pm 1/2\rangle + \alpha|1/2, \pm 1/2\rangle \tag{2.3.29c}$$

From (2.3.25), the effects of a biaxial stress on the semiconductor band structure are as follows. In the case of a biaxial compressive (negative) stress, X, the net band-gap energy increases and the "heavy-hole" (v_2) band moves up in energy while the "light-hole" (v_1) band moves down. In the case of a biaxial tensile (positive) stress the net band-gap energy decreases and the "light-hole" band moves up in energy while the "heavy-hole" band moves down.

The splitting of the light and heavy hole bands due to strain is similar to the removal of the degeneracy of these bands at $k_{||}=0$ in a quantum well due to the effects of

quantization. Therefore, it follows that in strained materials, as in the case of a quantum well, the decoupling of the light and heavy hole bands near k=0 affects the valence band E-k dispersion relations. It is found that strain alters the effective mass and, therefore, the density of states of the carriers in the plane of the biaxial stress, while leaving it essentially unchanged in the direction normal to this plane (i.e., in the direction parallel to the uniaxial component of the stress).

The effects of strain on the energy-band structure of bulk material under a biaxial compressive stress, no stress, and a biaxial tensile stress are shown in Fig. 2.14. The detailed effects of strain on the dispersion relations of the light and heavy hole valence bands have been determined numerically for variously strained materials by a number of authors: [Sanders, 1985], [Chong, 1989],[Pikus,1960], [Marzin, 1990] and [Chuang, 1991]. Chuang (1991), including the mixing of only the $|3/2,\pm 3/2\rangle$ and $|3/2,\pm 1/2\rangle$ basis states, has solved the general strain Hamiltonian and found analytical expressions for the valence band dispersion relations in the k_x-k_z plane, (where k_z is the direction normal to the plane of the biaxial stress). On the k_x-k_z plane, the energy dispersion relations arrived at by Chuang are given by:

$$E = \left\{ \frac{\hbar^2 \gamma_1}{2m}\left(k_x^2 + k_z^2\right) \pm \left[\left(\frac{\hbar^2 \gamma_2}{2m}\left(k_x^2 - 2k_z^2\right) + \zeta \right)^2 + 3\left(\frac{\hbar^2 \gamma_2}{2m} k_x^2 \right)^2 + 12\left(\frac{\hbar^2 \gamma_3}{2m} \right)^2 k_x^2 k_z^2 \right]^{1/2} \right\} \quad (2.3.30)$$

where $\zeta = \delta E_S/2$, and the energy E for holes is positive downward. From (2.3.23), ζ is negative in the case of compressive strain and positive in the case of tensile strain. In (2.3.30) the "+" sign applies to the heavy-hole (v_2) band while the "-" sign applies to the light-hole (v_1) band. Therefore, from (2.3.30), the dispersion relation along the k_x direction (when $k_y = k_z = 0$) for the heavy-hole band is:

$$E = \left\{ \frac{\hbar^2 \gamma_1}{2m} k_x^2 + \left[\left(\zeta + \frac{\hbar^2 \gamma_2}{2m} k_x^2 \right)^2 + 3 \left(\frac{\hbar^2 \gamma_2}{2m} \right)^2 k_x^4 \right]^{1/2} \right\}, \textbf{(HH)} \quad (2.3.31)$$

and the dispersion relation along the k_X direction (when $k_Y = k_Z = 0$) for the light-hole band, is:

$$E = \left\{ \frac{\hbar^2 \gamma_1}{2m} k_x^2 - \left[\left(\zeta + \frac{\hbar^2 \gamma_2}{2m} k_x^2 \right)^2 + 3 \left(\frac{\hbar^2 \gamma_2}{2m} \right)^2 k_x^4 \right]^{1/2} \right\}, \textbf{(LH)} \quad (2.3.32)$$

Along the k_Z-direction, the dispersion relations in the case of both compressive and tensile strain, are:

$$E = \frac{\hbar^2}{2m} (\gamma_1 \mp 2\gamma_2) k_z^2 \pm \zeta \quad (2.3.33)$$

where the upper sign applies to the heavy hole band and the lower sign applies to the light hole band.

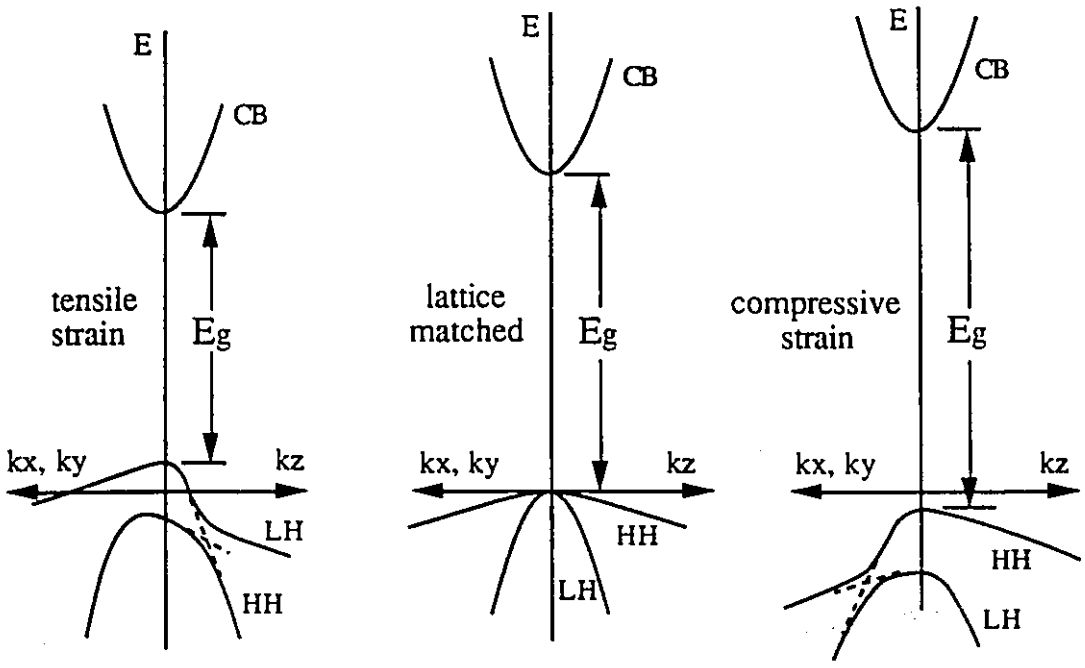

Figure 2.14: Effects of strain on the energy-band structure of bulk material under biaxial compressinve stress, no stress, and biaxial tensile stress. The non-parabolicities at finite k_{xy} results from a strong **k·p** interaction between the bands where they would tend to cross due to the effective mass reversal. The result is the appearance of "anti-crossing" effects which are manifested as band non-parabolicities.

From the above dispersion relations, the effect of a biaxial stress are to cause the effective mass of the "heavy-hole" (v_2) to become lighter, and the effective mass of the "light-hole" (v_1) to become heavier (near k=0) in the plane normal to the growth direction. From (2.3.31) and (2.3.32), for small k_x, the in-plane effective masses for the light and heavy holes become:

$$m_{hh} = \frac{m_o}{\gamma_1 + \gamma_2}$$
$$m_{lh} = \frac{m_o}{\gamma_1 - \gamma_2} \qquad (2.3.34)$$

From (2.3.33) it is seen that the light and heavy hole masses in the growth direction remain unaffected by the strain and are as given in (2.1.15).

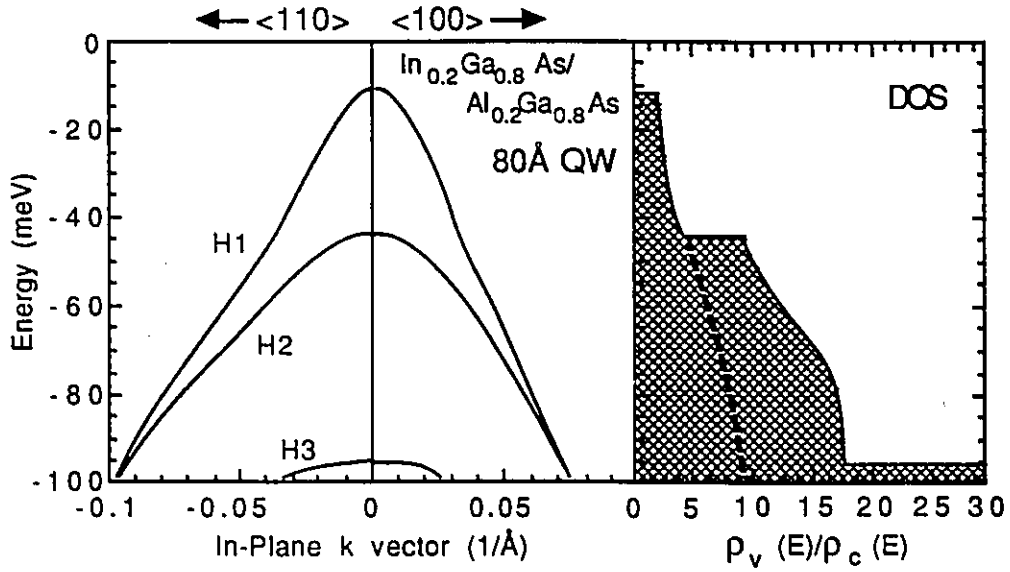

Figure 2.15: The valence subband dispersion relation for an ≈1.4% compressively strained $In_{0.2}Ga_{0.8}As/Al_{0.2}Ga_{0.8}As$ quantum well (V_o≈175meV) with the same width as that of Fig. 2.4. The LH bands have been pushed further out of the well as a result of the strain. The effective removal of the LH subbands has drastically reduced the band-mixing effects that are responsible for the obvious non-parabolicities in the band structure shown in Fig. 2.4. The result is an overal "lighter" effective mass, and a reduced and more energy independent density of states for holes. The dashed curve represents the density of states associated with the H1 subband plotted relative to the conduction (C1) band density of states. [Corzine, 1993].

The range of in-plane **k**-vectors ($k_{||}$) over which the effective masses of the valence bands are reversed (and thus are given by (2.3.34)) depends upon the magnitude of the energy separation between the **LH** and **HH** bands at **k**=0. As seen from Fig. 2.14, the reversal of the effective masses due to either strain or quantum size effects would cause the two J=3/2 bands to eventually cross at some finite $k_{||}$ vector. However, the strong **k·p** interaction between the bands with increasing k-vector prevents this from happening and "anti-crossing" effects occur. The non-parabolicities which appear in Fig. 2.14 with increasing $k_{||}$ ($=k_x,k_y$) are due to these "anti-crossing" effects. The larger the energy separation between the bands at **k**=0, the larger the in plane k-vector (i.e., hole energy) must be in order for the anti-crossing effects to become important.

Figure 2.15 shows the in plane valence subband dispersion relations for an ≈1.4% compressively strained $In_{0.2}Ga_{0.8}As/Al_{0.2}Ga_{0.8}As$ quantum well of the same dimensions as that of Fig. 2.4 (i.e., well width = 80Å). In comparing Fig. 2.15 with Fig. 2.4, it is seen that the effective mass of the heavy hole band in the strained QW structure is lighter over a much larger energy range than that in the unstrained QW structure. Since the effective mass is related to the density of states through (2.2.2), the density of states is also smaller over a larger energy range in the strained structure than in the unstrained structure. In addition, since nonparabolicities do not appear in the lowest valence subband structure of the compressively strained quantum well until much larger **k** values than in the unstrained QW, the density of states is constant over a much larger energy range in the strained over the unstrained material. Hence, from the discussions of §2.2.3, a laser having compressively strained QWs is expected to have much-improved performance (i.e., reduced threshold current and higher dg/dN) over lasers containing unstrained QWs.

In Fig. 2.15 the reason why nonparabolicities begin to occur at larger $k_{||}$ values in the strained QW structure than in the unstrained QW structure is because the quantum size

effects and the effects of strain are additive in the case of compressive strain: both effects tend to separate the $|3/2,\pm 3/2\rangle$ and $|3/2,\pm 1/2\rangle$ bands in the same direction. The resulting increased separation of the LH and HH bands in the compressively strained QW increases the energy range over which the interaction between the bands is negligible and therefore the energy range over which the heavy hole band displays light-hole-like behavior in the plane of the well.

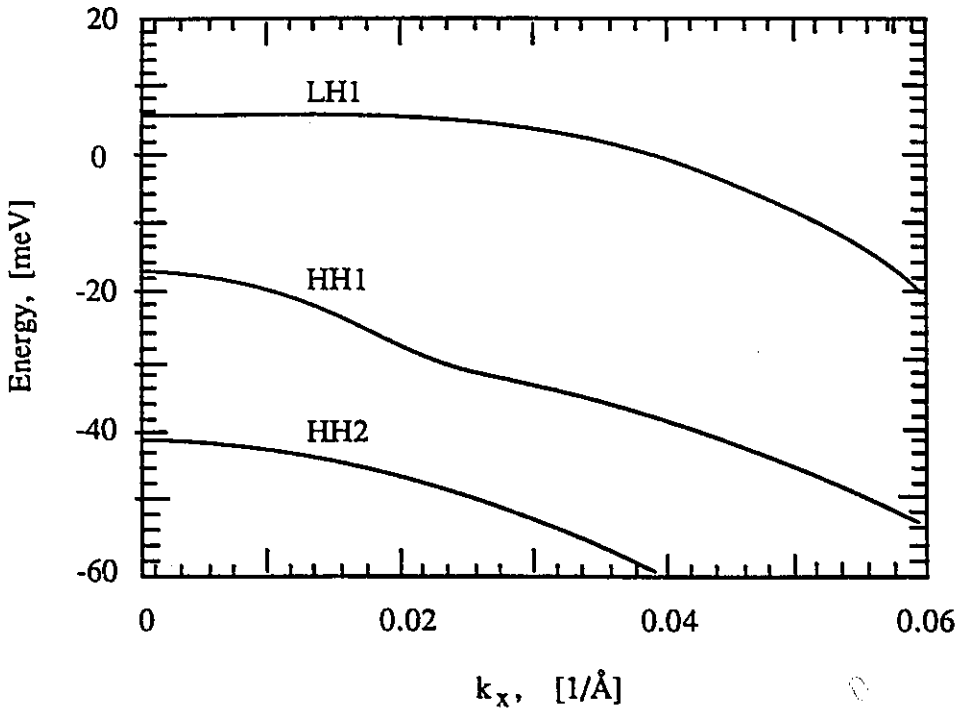

Figure 2.16: The calculated valence subband structure for a 60Å wide, ≈0.9% tensile strained, $Ga_xIn_{1-x}As$ quantum well with lattice matched $In_{1-x}Ga_xAs_yP_{1-y}$ (band-gap wavelength of 1.3μm) barriers. The light hole (LH1) subband has been pushed above the first heavy hole (HH1) subband. The effective mass of the LH1 band has become heavy and the density of states for carriers in this band will be large. From (2.2.14b) transitions to this band will be predominantly TM polarized.

In the case of a tensile strained QW, the effects of strain tend to raise the LH (v_1) band above the HH (v_2) band; however, the lighter effective mass of the LH band in the growth direction, combined with quantum size effects, tends to raise the HH band above the LH band. These opposite trends mean that in order for the LH band to have a higher energy than the HH band in a tensile strained QW laser (i.e., smallest band gap is

E_{C1}-E_{LH1}), the tensile stress must be sufficiently large to compensate for the effects of quantization. Figure 2.16 shows the calculated valence subband structure for a 60Å wide, ≈0.9% tensile strained, $Ga_xIn_{1-x}As$ quantum well with lattice matched $In_{1-x}Ga_xAs_yP_{1-y}$ (band-gap wavelength of 1.3μm) barriers.

2.4 SUMMARY

In this chapter, the concepts of energy level quantization for electrons and holes in a quantum well were presented. The dependence of the energy of the quantized levels for electrons and holes on the physical dimensions of the quantum well was revealed. Since the quantized energy levels for electrons and holes were found to depend on QW geometry, it was determined to be possible to tune a lasers emission, and a detectors absorption, wavelength by making appropriate design changes to the width and the depth of the quantum well.

The effects of energy level quantization on the density of states for carriers in a quantum well were also presented. The density of states was found to be different for a QW structure than that for bulk material. In a QW structure the density of states for a given quantized subband, in the parabolic band approximation, was shown to be independent of energy. By contrast, the density of states for bulk material was found to increase as the square root of the carrier energy. Therefore, the density of states for a QW, for energies above the first quantized energy level, was found to be smaller for a QW material than a bulk material. In addition, due to quantum size effects, the light and heavy hole valence bands were found to be decoupled near the energy band edge and the degeneracy between them was removed. This decoupling of the light and heavy hole valence bands at the band edge was found to result in a smaller heavy hole valence-band effective mass, and therefore density of states, ρ_v, for a quantum well over bulk material.

The effects of the changes to the density of states for carriers in a quantum well on the magnitude of the material gain, and the rate of change of material gain with injected carrier density in a laser, and therefore laser performance, were revealed in §2.2.3. It was found that by changing the QW dimensions, the rate of change of the material gain with injected carrier density, and therefore a lasers maximum operating speed and linewidth, could be improved due to an associated change in the QW density of states. It was also determined in §2.2.3 that the threshold current density of a QW laser could be reduced in comparison to that of a bulk laser due to the effects of quantization and a reduced active region volume for QW lasers over bulk lasers. It was found that the smallest transparency current density for a laser structure occurs when the density of states for carriers is small and when the conduction band and upper valence bands are symmetric, such that $\rho_c=\rho_v$.

In §2.3, the effects of strain on the energy band structure for quantum wells was discussed. It was found in §2.3.3, that compressive strain could be used to increase the decoupling of the light and heavy hole bands, and therefore to reduce the in-plane effective mass of the heavy hole valence band over a larger range of energies than could be achieved due to the decoupling of the valence bands due to quantum size effects in an unstrained QW structure. A reduction in the heavy-hole effective mass over a larger energy range for strained QW laser structures was found to increase the symmetry between the conduction and valence band density of states. Therefore, it was predicted that the application of compressive strain would result in a reduced threshold current density for strained QW laser structures over unstrained QW, and bulk, laser structures. In addition, due to an ability to tailor semiconductor band structures using strain, the use of strained QW structures results in a greater degree of flexibility in the use of materials for designing laser structures. This additional flexibility arises due to an increased degree of freedom through the use of strain.

CHAPTER 3: TEMPERATURE DEPENDENCE OF LASER THRESHOLD CURRENT

3.0 INTRODUCTION

In this chapter the mechanisms that have been proposed as being predominantly responsible for the high temperature sensitivity (low T_o) of InGaAsP/InP based lasers, especially above the "break point" temperature, are reviewed. These proposed mechanisms are:

(i) the temperature dependence of the optical gain, [Zhu, 1989], [Ishikawa, 1991],[O'Gorman, 1992], [Tsang, 1992],[Zou, 1993];

(ii) the temperature dependence of optical absorption loss, [Asada, 1983, 1981], [Adams, 1980];

(iii) the temperature-dependent loss of injected carriers by non-radiative Auger recombination processes, [Sermage, 1985], [Dutta, 1981, 1991], [Su, 1984], [Thompson, 1981], [Liu, 1984],[Huag, 1988],[Lui, 1993];

(iv) the leakage of the injected carriers into the confinement layers due to thermionic emission, [Ettenburg, 1979], [Yano, 1980, 1981]; and,

(v) the leakage of the injected carriers into the confinement layers due to Auger recombination induced energetic carriers [Chik, 1988, 1990], [Zhuang, 1985], [Chen, 1984], [Casey, 1984], [Chiu, 1983], [Yamakoshi, 1982].

Before presenting a description of the processes that may contribute to the temperature sensitivity of the threshold current (I_{th}-T relation) of long wavelength lasers, it should be noted that many authors attempt to label one of the five mechanisms listed above

as being dominant in determining this sensitivity. The tendency to label one physical mechanism as being more important than any others stems to some extent from an attempt to fit the I_{th}-T relation to the exponential relationship proposed by Pankove [1968] and given by (1.1.1) in Chapter 1 and repeated below:

$$I_{th} = I_o \exp(T/T_o), \tag{1.1.1}$$

In actuality, however, it is likely that all the above-mentioned factors play some role, either minor (as in the case of intervalence band absorption which will be shown in Chapter 6) or significant, in determining the temperature dependence of semiconductor lasers.

3.1 TEMPERATURE DEPENDENCE OF THE OPTICAL GAIN

One of the mechanisms believed to be responsible for the temperature dependence of I_{th} of both bulk and quantum well lasers is the temperature dependence of the peak optical gain. The temperature dependence of I_{th} arises because the slope of the optical gain *vs.* injected carrier density relation decreases, and the transparency and threshold carrier concentrations increase, with temperature as shown schematically in Fig. 3.1, [Tsang, 1992], [Zhu, 1989]. From (2.2.31) a minimum optical gain, g_{th}, must be attained before lasing can occur. Assuming that the required threshold gain, g_{th}, is independent of temperature, from (2.2.23), (2.2.32) and Fig. 3.1, the threshold current, I_{th}, increases with temperature. I_{th} increases with temperature since, as the temperature increases, a larger injected carrier concentration, N_{th}, is required in order to obtain a level of gain equivalent to g_{th}. (Note, as discussed in §3.2, g_{th} may also increase with temperature through an increase in the α_{int} term of (2.2.31) with temperature). From Fig. 3.1, if the slope of the gain *vs.* injected carrier density (g-N) relation were to decrease at a slower rate with an increase in temperature, or if the threshold gain, g_{th}, could be made smaller by

limiting optical losses (for example, by applying high reflectivity coatings) it follows from Fig. 3.1 that the temperature sensitivity of I_{th} could be decreased.

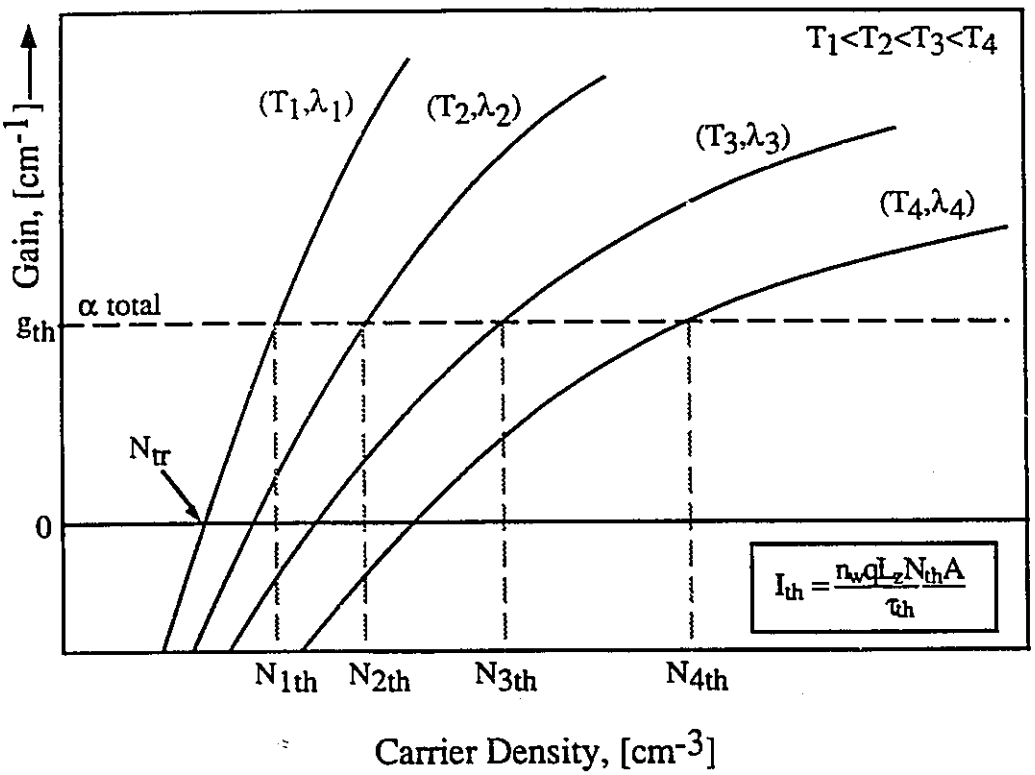

Figure 3.1: Schematic diagram of the change in the material gain *vs.* carrier density relation for a quantum well laser as a function of temperature. Since the slope of the gain *vs.* carrier concentration profile decreases with increasing temperature, as the temperature increases, more injected carriers are required in order to reach the threshold gain condition, g_{th}. As a result, as the temperature increases, more current is required to produce lasing and the threshold current increases with temperature. If the rate of change of the slope of the gain *vs.* concentration profile with temperature were to decrease, so may the temperature sensitivity of the laser threshold current.

For AlGaAs-GaAs double heterostructure (DH) lasers the I_{th}-T relation is considered to be almost completely explained by the temperature dependence of the calculated peak optical gain versus current relations [Horikoshi, 1982]. Dutta, *et. al.* [1991,1982] have calculated the temperature dependence of the optical gain and the I_{th}-T relation for both QW and DH InGaAsP/InP based lasers. They theoretically determined the

characteristic temperature, T_o, for DH lasers to be ≈100 K for 100 K < T < 250 K, in agreement with experimental results. However, in the temperature range 250 K < T < 350 K the temperature dependence of the optical gain gives a T_o of ≈200 K while the empirically arrived at characteristic temperature is only ≈ 65 K. A similar agreement at low temperatures, and disagreement at higher temperatures, between experimental values of T_o and those derived from the temperature dependence of the optical gain was also observed by Ishikawa *et. al* [1991] for InGaAlP laser diodes. These results show that the temperature dependence of the optical gain is no doubt an important factor in determining the temperature dependence of the threshold current of semiconductor lasers. However, the temperature dependence of the optical gain does not appear to be capable of explaining the low T_o at higher temperatures; *indeed, it predicts that T_o should increase at higher temperatures, not decrease!*

The failure of the calculated temperature dependence of the optical gain to explain the greater temperature sensitivity of InGaAsP and InGaAlP lasers above the break-point temperature has led many authors to propose additional mechanisms which may contribute to the temperature sensitivity of these lasers at larger temperatures. However, before discussing these additional mechanisms, it should be noted that even the limited agreement between the experimental I_{th}-T relations and theory at low temperatures may be fortuitous. Agreement between theory and experiment may be fortuitous because it depends on many factors, including: the magnitude of internal losses; radiative carrier lifetimes; assumptions about the internal quantum efficiency; the band structure and effective masses away from **k**=0; the gain model used (i.e. parabolic or non-parabolic bands, **k**-selection rules or no **k**-selection rule, the inclusion of band tail states or not, and how they are modeled) and how all of these parameters vary with temperature.

3.2 TEMPERATURE DEPENDENCE OF OPTICAL ABSORPTION LOSS

Asada *et. al.* [1981,1983] and Adams [1980] have examined the rapid increase in I_{th} with temperature above the "break point" temperature (see Fig. 1.1) for both 1.5-1.6 μm and 1.3 μm InGaAsP/InP DH lasers. They determined that the low T_o above room temperature in these lasers is primarily due to the effects of temperature dependent optical losses caused by intervalence band absorption. In particular, photon-induced transitions between the split-off and the heavy-hole valence bands were determined to be the dominant optical loss mechanism.

How temperature dependent optical losses due to intervalence band and free-carrier absorption can affect the temperature dependence of I_{th} can be seen from (2.2.31) where the effective absorption losses are represented by the relation† :

$$\alpha_{loss} = \Gamma\alpha_{int} + (1-\Gamma)\alpha_{ext} \tag{3.2.1}$$

where Γ is the optical confinement factor and α_{int} and α_{ext}, as described in §2.2.3, are the loss coefficients in the active region and the cladding regions of the laser, respectively. From (2.2.31), if the optical losses increase with temperature, then so does the threshold gain, g_{th}. From Fig. 3.1, if the threshold gain increases, the value of N_{th} and, therefore, the threshold current density, as given by (2.2.32) for quantum well lasers, will also increase. For convenience (2.2.32) is repeated here in a general form for bulk lasers as:

$$J_{th} = \frac{qN_{th}d}{\tau_{th}} \tag{3.2.2}$$

where τ_{th} is the carrier lifetime at threshold, and d is the active region thickness.

---

† Note: In (3.2.1) α_{loss} is divided by the optical confinement factor, Γ, in arriving at the threshold gain condition of (2.2.31) since only that part of the optical field (i.e., Γ) that overlaps the active region of the laser experiences gain.

The loss term, α_{int} in (3.2.1) is mainly due to intervalence band absorption. For doped active regions it is written as [Asada, 1983]:

$$\alpha_{int} = \alpha_1 + \alpha_2.$$

The loss term α_1, as shown in Fig. 3.2, represents optical losses due to transitions between the split-off and the heavy-hole valence bands. It is given by the relation:

$$\alpha_1 = B_1 \Big/ \left\{1 + \exp\left(E_1 - E_F\right) / k_B T\right\}, \tag{3.2.3}$$

where B_1 is a parameter [Adams, 1980] adjusted to give a best fit to experimental data, and the parameters E_1 and E_F are the final state energy level in the heavy-hole valence band of the carrier and the quasi-Fermi energy, respectively. The loss term α_2 is due to transitions between the split-off band and the acceptor level, and has been deemed to be negligible in comparison to α_1 above 250 K [Asada, 1983].

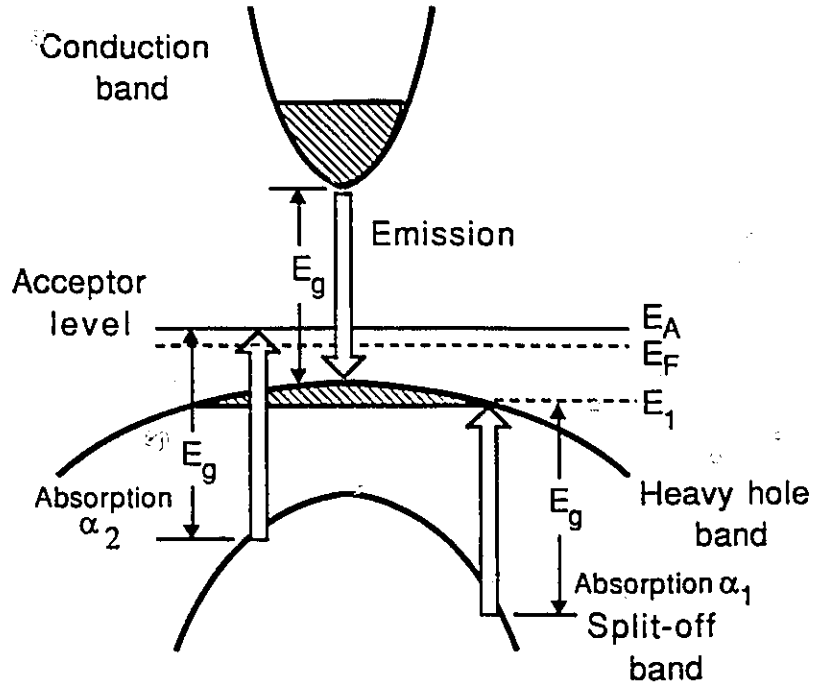

Figure 3.2: Schematic diagram of the band structure of the quaternary indicating photon emission across the band gap and its re absorption by transitions from the split-off band into the heavy hole band at energy E_1 and into the acceptor level at energy E_A. These are designated α_1 and α_2 respectively. From [Asada, 1981].

The conclusion of Asada *et. al.* [1981,1983] and Adams [1980] that the temperature dependence of optical loss is the dominant mechanism responsible for the low T_o of quaternary lasers above room temperature was based on the fact that the differential quantum efficiency of a laser at threshold decreases with temperature. The differential quantum efficiency at threshold is given by the relation [Asada, 1983], [Agrawal, 1986]:

$$\eta_d = \eta_i \frac{L^{-1}\ln(1/R)}{\Gamma\alpha_{int} + (1-\Gamma)\alpha_{ext} + L^{-1}\ln(1/R)} \tag{3.2.4}$$

where, η_i is the internal quantum efficiency, L is the laser cavity length, and R is the reflectivity of the end mirrors. Asada and Adams assume that the internal quantum efficiency, is given by the relation :

$$\eta_i = \frac{1}{1+\tau_R/\tau_{NR}} \approx 1, \tag{3.2.5}$$

(where τ_R is the radiative carrier lifetime and τ_{NR} is the non-radiative carrier lifetime) and is unity at threshold. They assume η_i is unity at threshold since the radiative lifetime at threshold, $\tau_R = \tau_R^{st}$, has been shown to be on the order of 10^{-13} s, and the nonradiative lifetime, τ_{NR}, has been determined to be on the order of 10^{-9}s. Given that η_i is unity at threshold, Asada and Adams reason that the only explanation for the decrease in η_d with temperature must come from the loss terms α_{int} and α_{ext}. Asada and Adams calculated the I_{th}-T relation including and excluding the temperature dependence of the optical loss. They found that without absorption losses the calculated T_o was 145 K; however, when absorption losses were included the calculated T_o was 60 K in agreement with empirical results. A comparison of the experimental and theoretical results of Asada is shown in Fig. 3.3.

The theoretical calculations shown in Fig. 3.3 were based on measurements of the temperature dependence of the gain *vs.* current relations, (which were obtained using the method of Hakki and Paoli, [1975]) and measurement of the carrier lifetime just below

threshold using the turn-on delay technique [Agrawal, 1986]. The calculations, therefore, take into consideration that the carrier lifetime, τ_{th}, in (3.2.2) changes with carrier concentration and temperature. However, in the determination of the carrier lifetime by the turn-on delay technique, and also in the determination of the carrier density from the injected current, contributions due to non-radiative recombination processes, such as, Auger recombination were neglected. In addition, Asada and Adams have assumed that carrier leakage into the cladding regions with temperature was negligible. However, it has been determined that carrier leakage in InGaAsP/InP DH lasers can be up to 35 per cent or more [Casey, 1984], [Chik, 1990]. The effect of carrier leakage, as is discussed in §3.5 and §3.6, is to reduce the internal efficiency, η_i, appearing in (3.2.4), making the primary assumption of Asada's and Adams' incorrect.

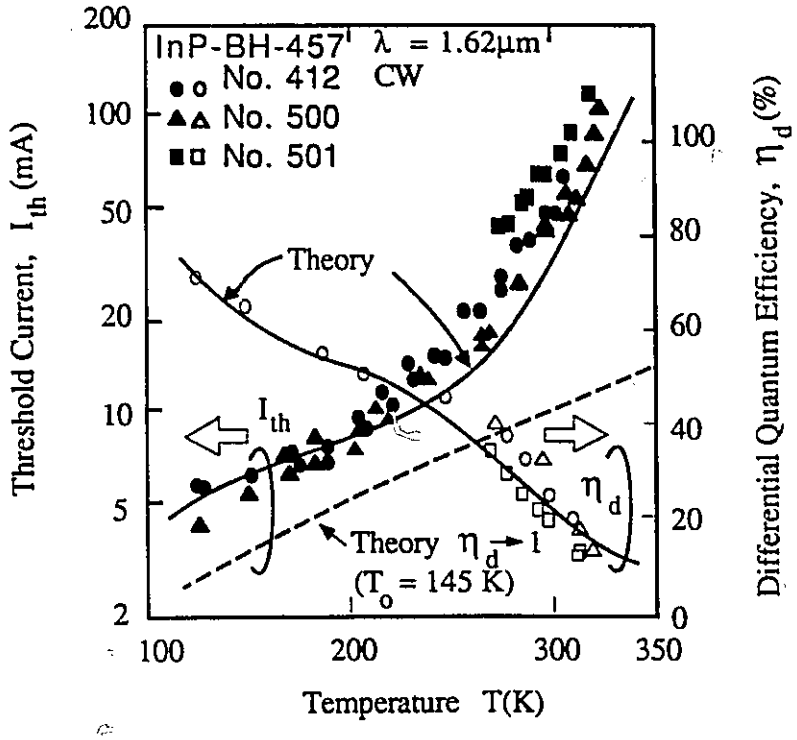

Figure 3.3: Temperature dependence of the threshold current, I_{th}, and the differential quantum efficiency, η_d, showing the experimental and theoretical data of Asada, [1981]. The dashed curve indicates the theoretically predicted variation of I_{th} in the absence of intervalence band absorption.

3.3 EFFECTS OF SPONTANEOUS AND NON-RADIATIVE RECOMBINATION ON LASER THRESHOLD CURRENT AND ITS TEMPERATURE DEPENDENCE

The temperature dependent loss of injected carriers by spontaneous and non-radiative recombination affects the temperature dependence of the threshold current through the effects of non-radiative recombination on the carrier lifetime term, τ_{th}, appearing in (3.2.2). The carrier lifetime is often expressed as [Agrawal, 1986]:

$$\tau(n) = \left(A_{nr} + Bn + Cn^2\right)^{-1}, \tag{3.3.1}$$

where: A_{nr} is the nonradiative recombination coefficient which characterizes the recombination of carriers due to traps, etc.; B is the radiative recombination coefficient; C is the Auger recombination coefficient; and n is the injected carrier density. The effect of A_{nr} on the lifetime, τ, has been determined to be negligible in comparison to the contributions due to the other two terms in (3.3.1) [Su, 1984], [Sermage, 1985], [Olshansky, 1984]. Therefore, the carrier lifetime can be approximated as:

$$1/\tau = 1/\tau_r + 1/\tau_a, \tag{3.3.2}$$

where τ_a is the Auger lifetime, and τ_r is the spontaneous radiative lifetime and is related to the radiative recombination rate, R_r, and the bimolecular recombination coefficient, B, by:

$$\tau_r = n/R_r = 1/(Bn). \tag{3.3.3}$$

Several experimental results have led to the suggestion that the Auger lifetime, τ_a, has a significant influence on the recombination lifetime, τ, in InGaAsP DH lasers. These results include the observation that the lifetime varies as n^{-2}, [Sermage, 1985], [Thompson, 1981], [Dutta, 1982] and that the spontaneous emission as a function of current shows a sublinear dependence, as expected for Auger recombination, [Dutta,

1981], [Sugimura, 1981]. The Auger lifetime is related to the nonradiative Auger recombination rate, R_a, as given by the relation:

$$\tau_a = n / R_a = 1 / Cn^2. \tag{3.3.4}$$

The radiative recombination coefficient, B, has been determined experimentally to depend on both the carrier concentration and the temperature. In bulk InGaAsP material B depends on the carrier concentration as $B(n) = B_0 - B_1 x n$, where B_1/B_0 is on the order of $2x10^{-19}$ cm^3 [Olshansky, 1984], and on temperature* as $T^{-0.8}$ [Yano, 1980]. The carrier dependence of the Auger lifetime, and the temperature dependence of the Auger recombination coefficient, C, are discussed below, and can be evaluated by examining the theoretically determined Auger recombination rate.

3.4 AUGER RECOMBINATION

There are several nonradiative Auger recombination processes that contribute to the Auger recombination rate in InGaAsP materials. These processes include direct (phononless) band-to-band Auger processes and indirect (phonon-assisted) Auger processes. For temperatures greater than about 200K, the phonon-assisted Auger rate is negligible in comparison to the direct Auger recombination rate due to its much weaker temperature dependence in comparison to the direct Auger recombination rate [Agrawal, 1986]. Therefore, the direct Auger recombination processes dominate the Auger recombination rate, and the phonon-assisted Auger recombination rate is ignored in comparison to the direct Auger recombination processes. The possible direct Auger recombination processes, are shown in Fig. 3.4, where C denotes the conduction band, H

* Note: There are several authors who reference this result. However, the initial reference for the temperature dependence of the bimolecular recombination coefficient is from a private communication; therefore, this result must be considered to be somewhat suspect. Some authors [Casey, Jr. 1984] take B to be constant with temperature.

denotes the valence (hole) band, and S denotes the split-off band. The total Auger rate is given by: $R_a = R_{CCHC} + R_{CHHS} + R_{CHHL}$ [Agrawal, 1986]. The theoretically derived Auger recombination rates for the R_{CCHC}, the R_{CHHS}, and the R_{CHHL} Auger processes in a quantum well are discussed below.

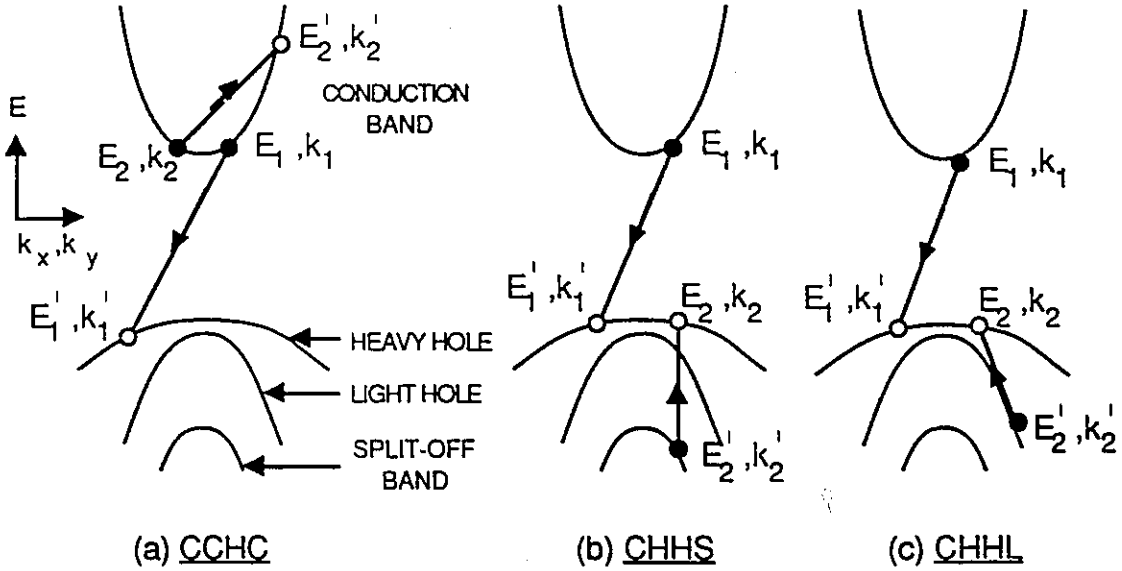

Figure 3.4: Schematic diagram of the different band-to-band Auger recombination process for a quantum well laser. (a) the CCHC Auger process as described in §3.3.1, (b) the CHHS Auger process as described in §3.3.2, (c) the CHHL Auger process as described in §3.3.3.

3.4.1 The CCHC Auger Process

In the CCHC process two conduction band (C) electrons interact as shown in Fig. 3.4(a). One electron drops to an empty hole (H) state in the valence band while the second electron assumes the recombination energy (equivalent to the energy difference between the initial electron energy in the conduction band and the hole energy in the valence band ($\approx E_g$)), and moves to a higher energy state in the conduction band. In the process both energy ($E_1 + E_2 = E_2' - E_g - E_1'$) and momentum ($k_2 + k_1 = k_1' + k_2'$) are conserved. Once excited to a higher energy state, the second electron then relaxes to the thermal distribution by processes such as carrier-lattice interactions by phonon scattering.

The Auger recombination rate for the CCHC process, R_{CCHC}, is related to the temperature, T, and the carrier concentrations, n and p, by:

$$R_{CCHC} \propto \frac{n^2 p}{N_c^2 N_v} \exp\left(-\frac{\Delta E_c}{k_B T}\right), \tag{3.4.1}$$

where:

$$\Delta E_c = E_T - E_q = \frac{m_{ct} E_q}{m_v + 2m_c - m_{ct}}. \tag{3.4.2}$$

E_q is the separation between the n=1 quantized levels in the conduction and the valence bands, and E_T is a threshold energy that defines the minimum energy the excited second electron (2' in Fig. 3.4) must have for the process to occur. The threshold energy, E_T, for the CCHC process is given by:

$$E_T = \frac{2m_c + m_v}{2m_c + m_v - m_{ct}} E_q \tag{3.4.3}$$

where m_c and m_v are the electron and hole effective masses at the band edge, and m_{ct} is the electron effective mass at the energy E_2' (See Fig. 3.4). N_c and N_v are the effective density of states in the conduction and valence band respectively. For an undoped semiconductor under high injection the electron carrier concentration, n, is equal to the hole concentration, p, due to charge neutrality.

3.4.2 The CHHS Auger Process

In the CHHS process, as shown in Fig. 3.4(b), two holes interact. One hole recombines with an electron in the conduction band while the other is excited to the split-off valence band, by the energy E_g. As in the CCHC Auger process, the excited carrier relaxes to the thermal distribution through carrier-lattice interactions.

The Auger recombination rate for the CHHS process, R_{CHHS}, is related to the temperature, T, and the carrier concentrations, n and p, by:

$$R_{CHHS} \propto \frac{np^2}{N_c N_v^2} \exp\left(-\frac{\Delta E_s}{k_B T}\right), \tag{3.4.4}$$

where:

$$\Delta E_s = E_{Ts} - E_q = \frac{m_s\left(E_q - \Delta_1\right)}{m_v + 2m_c - m_s}, \tag{3.4.5}$$

E_{TS} is the threshold energy for the process to occur, and Δ_1 is the energy separation of the split-off band from the top of the heavy-hole band. The threshold energy for the CHHS process is given by:

$$E_{Ts} = \frac{2m_v + m_c}{2m_v + m_c - m_s}\left(E_q - \Delta_1\right) \tag{3.4.6}$$

where m_S is the mass of the split-off hole at the energy E_{TS}.

3.4.3 The CHHL Auger Process

The CHHL process, as shown in Fig. 3.4(c) is similar to the CHHS process, save two holes interact with one conduction band electron leaving a high-energy hole in the light hole band. The expression for the Auger rate for the CHHL process is similar to that for the CHHS process except that the split-off-band mass m_S is replaced by the light-hole mass m_l, and the quantity $(E_q - \Delta_1)$ is replaced by E_q. The threshold energy for the CHHL process is given by:

$$E_{Th} = \frac{2m_v + m_c}{2m_v + m_c - m_l} E_q \tag{3.4.7}$$

3.5 COMPARISON OF SPONTANEOUS RADIATIVE AND NON-RADIATIVE RECOMBINATION

From the above expressions for the Auger recombination rate the following observations can be made. Firstly, the recombination rate for the CCHC process increases

strongly with a decrease in the band gap energy, E_q, and thus becomes important for narrow gap semiconductors such as InGaAsP materials. Secondly, for the CHHS Auger process, for the case where $E_q < \Delta_1$ there is no threshold energy. In addition the Auger rate increases as the term $E_q - \Delta_1$ decreases. Finally, all the Auger rates increase strongly with temperature and with n^3. Therefore, from (3.3.4) and (3.3.2) the carrier lifetime that appears in the expression for the threshold current (3.2.2) will be a strong function of the carrier concentration, and temperature, when the Auger lifetime, τ_a, is of the same order of magnitude, or smaller, than the spontaneous radiative lifetime, τ_r.

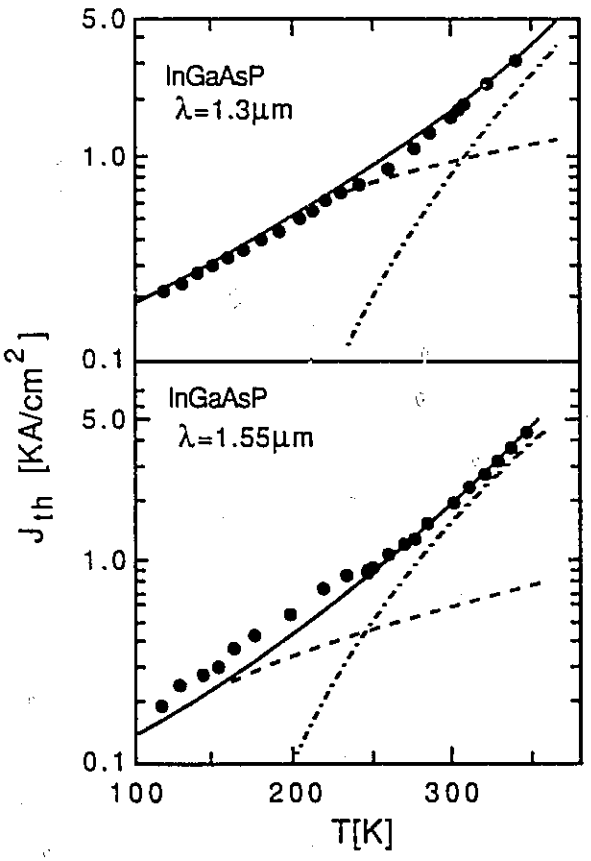

Figure 3.5: Comparison of the theoretical and experimental I_{th}-T relations for 1.3 μm and 1.55 μm InGaAsP/InP DH lasers. The solid lines are the calculated threshold currents. The dashed lines and the dot-dashed lines are the radiative and nonradiative (Auger) component of J_{th}, respectively. From Dutta [1981].

Dutta *et. al.* calculated the spontaneous radiative and Auger recombination rates for both InGaAsP/InP DH lasers [1981] and strained InGaAs/GaAs QW lasers [1991] as a function of temperature. From these calculations they determined the I_{th}-T relation for the given laser structures and compared this relation to that obtained from empirical results. Their comparisons of the calculated and empirical I_{th}-T relations for 1.3 μm and 1.55 μm DH lasers are shown in Fig. 3.5.

From Fig. 3.5 it appears that there is close agreement between the calculated curves and the empirical points, and that the rapid increase in the Auger recombination rate above 250 K is responsible for the low T_0 of these lasers above this temperature. However, Dutta *et. al.* have neglected carrier leakage over the heterobarrier and had to divide their empirical results by a factor of 2.1 to account for current spreading in order to obtain the fit. Even still, the apparent agreement between theory and experiment may be fortuitous as Dutta *et. al.* made a number of assumptions in their calculations. For example, they have assumed parabolic bands which is difficult to accept since the combined restrictions of energy and momentum conservation that are imposed when deriving the Auger recombination rates make the Auger rate very sensitive to band non-parabolicities. In addition, the effective masses at the larger band energies, for instance m_{ct}, are not known. Assumptions about the effective mass can have a large influence on the calculated Auger rate. For example, if the ratio m_{ct}/m_c in (3.4.2) were to increase from 1 to 2, the Auger rate for a given band gap could decrease by more than an order of magnitude [Agrawal, 1986].

Because the theoretical Auger rate is sensitive to band structure, it has been predicted that the use of strained and unstrained quantum wells in semiconductor lasers may significantly reduce the Auger recombination rate [Agrawal, 1986], [Dutta, 1991],[O'Gorman, 1992], [Poguntke, 1992],[Zou,Y], [Lui, 1993], and thereby allow long-wavelength quantum well lasers to have a relatively low temperature sensitivity.

Strained and unstrained lasers are predicted to produce a reduction in the Auger recombination rate because, as discussed in Chapter 2, the material band structure is affected by quantization and strain. However, to date, apart from the work of Thijs, [1991] and Evans [1992], there have been no obvious improvements in the temperature sensitivity of InGaAsP based lasers due to the implementation of quantum wells or strain [Zou, 1993]. However, it has been shown that strain can be used to reduce the Auger recombination rate in InGaAsP/InP QW laser structures [Poguntke, 1992], [Lui, 1993], [Zou, 1993]. Therefore, the link between an increasing Auger recombination rate with temperature and an increased temperature sensitivity of I_{th} for long wavelength lasers above 250 K is questionable.

Recently the influence of Auger recombination on the temperature dependence of InGaAsP laser diodes has been questioned by O'Gorman *et. al.* [1992] who compared the temperature dependent characteristics of MQW semiconductor laser diodes and light emitting diodes (LEDs) operating at a wavelength, λ=1.3 μm. The temperature dependence of LED emission is often characterized by the phenomenological exponential relationship: $P_{LED} = P_o exp(-T/T_o^{LED})$. O'Gorman *et. al.* determined the temperature dependence of the LED emission and the I_{th}-T relationship for laser diodes using a model in which temperature dependent Auger recombination was the dominant nonradiative recombination process. In this model, the temperature dependence of the Auger coefficient, C, was adjusted to fit to the empirical I_{th}-T relation. They then compared the ratio of the calculated T_o^{LED}/T_o^{LD} ratio with the empirical ratio, and found large discrepancies. O'Gorman *et. al.* concluded that Auger recombination could not simultaneously explain the high-temperature behavior of the laser threshold current and the LED emission, and that no model in which Auger recombination was the dominant temperature sensitive parameter could explain their experimental observations. They

suggested that the influence of optical gain on the I_{th}-T relationship has been underestimated.

Sermage *et. al.* [1985] measured the carrier lifetime in 1.3 μm InGaAsP and determined that, at high carrier concentrations, the carrier decay rate increases more rapidly than the radiative rate at around room temperature. This result was accounted for by a recombination mechanism that had a variation with excitation that was typical of an Auger process. From their measurements, they determined the Auger coefficient, C and found it to be independent of temperature, as did Lui [1993]. They conclude that, while Auger recombination is in large part responsible for the low T_0 of InGaAsP lasers, the temperature dependence of the Auger coefficient does not contribute to it.

Finally, Casey determined the I_{th}-T relationship for InGaAsP/InP DH lasers emitting at 1.3 μm and found that the temperature dependence of gain gave $T_0 \approx 200$ K between 250 and 350 K. When the temperature dependence of the Auger recombination was included in the calculations, $T_0 \approx 100$ K was obtained in this same temperature range. Casey found that in order to obtain the empirically determined $T_0 \approx 65$ K, it was necessary to include a leakage current of one-third the total current at 300 K. He, therefore, concluded that the temperature dependence of the leakage currents over the heterobarrier had to be considered in order to explain the observed low T_0 of InGaAsP lasers above 300K. However, Casey also assumed that the bimolecular recombination coefficient was independent of temperature in his calculations.

3.6 TEMPERATURE DEPENDENT CARRIER LEAKAGE DUE TO THERMIONIC EMISSION

In semiconductor DH lasers, it has been proposed that carriers injected into the active region partially escape beyond the heterobarriers without contributing to the optical gain [Yano, 1981], [Casey, 1984], [Chik, 1990]. The leakage of electrons and holes from

the active region into the cladding region of the laser is caused by the drift and diffusion of carriers which possess kinetic energies exceeding the heterojunction potential barriers as shown schematically in Fig. 3.6 [Agrawal, 1986]. There are two main processes by which carriers can acquire sufficient kinetic energy to surmount the heterojunction barrier. These are via lattice interactions, which are responsible for the thermal distribution of carriers and which drive thermionic emission, and via hot carrier production due to Auger recombination. In the following the effects of leakage due to thermionic emission on the I_{th}-T relation is considered.

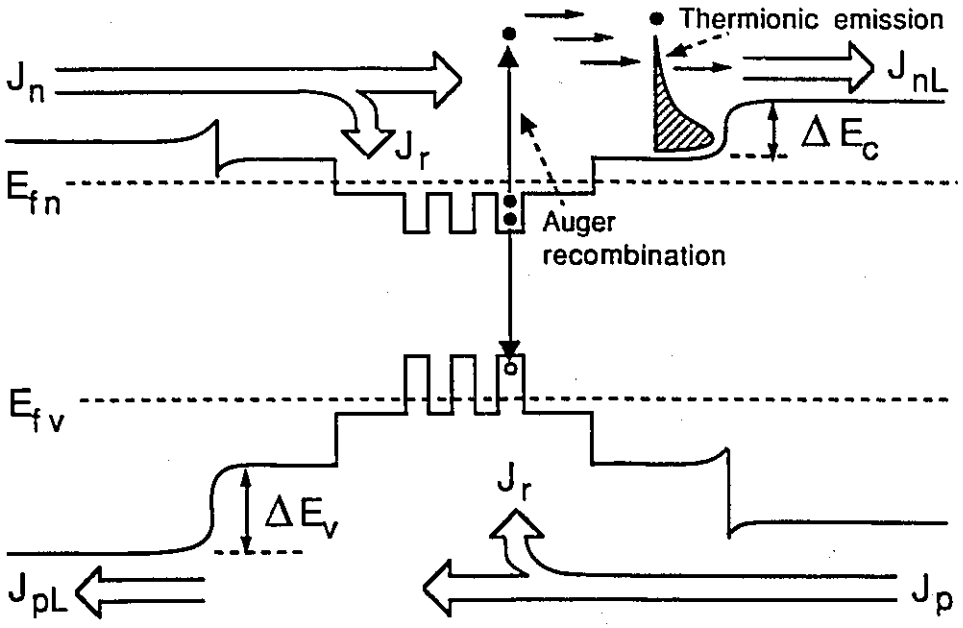

Figure 3.6: Schematic diagram showing carrier leakage over the heterojunction barrier in an InGaAsP/InP quantum well laser. Shown is leakage over the heterojunction barrier due (a) to thermionic emission also due to (b) Auger recombination induced energetic carriers (see §3.6). Efn and Efp are the quasi-Fermi levels for electrons and holes ΔE_c and ΔE_v are the conduction- and valence-band discontinuities. J_n and J_p, J_{nL} and J_{pL} are the injected and leakage current densities of electrons and holes, respectively, and J_r is the recombination current density in the active layer..

In thermionic emission, carriers which occupy energy states that have an energy greater than that of the barrier or cladding regions in the laser structure, in accordance with

Fermi-Dirac statistics, may drift or diffuse into the cladding regions. The particular transport mechanism depends on the doping of the InP cladding or barrier regions. If the doping of the InP confinement layers is relatively low ($\approx 10^{17}$ cm^{-3}), a significant field can exist in the confinement layer, in which case leakage due to drift currents dominate. However, if the doping is relatively high (>5 x 10^{17} cm^{-3}) the drift leakage is small compared to the diffusive leakage [Agrawal, 1986]. In actual devices both drift and diffusion leakage should exist [Chik, 1988]. Those carriers at the heterojunction interface (see Fig. 3.5) that do have energies excceding the barrier heights, and are able to enter into the InP cladding layer via drift or diffusion, are then lost via: recombination (either radiative or nonradiative) with majority carriers in the cladding layer; recombination in the narrow band gap capping layer (see Fig. 4.1); or at the semiconductor-metal contact.

The existence of carrier leakage in InGaAsP/InP DH lasers has been experimentally confirmed by several authors. Yamakoshi *et. al.* [1982] confirmed the existence of electron leakage by observing the 1.05 μm emission in specially designed LED structures. Chen *et. al.* [1984] and later Zhaung [1985], confirmed the existence of carrier leakage in bulk laser structures through the current dependence of 950 nm emissions caused by carriers leaking over the heterojunction barrier into the InP confinement layers.

The thermionic leakage current in DH laser structures can be estimated from a knowledge of the number of carriers, n_b, at the heterostructure boundary that have energies greater than the barrier height. This quantity can be calculated from a knowledge of the density of states for carriers in the active region and the occupation probability. It is given by the relation [Agrawal, 1986]

$$n_b = N_{cc}\frac{2}{\pi^{1/2}}\int_{E_c}^{\infty}\frac{E^{1/2}dE}{1+\exp\left[\left(\Delta E_c - E_{fc}\right)/\left(k_B T\right)\right]}, \qquad (3.6.1)$$

where E_{fc}, is the quasi-Fermi level in the conduction band, and N_{cc} is the effective density of states in the conduction band as given by:

$$N_{cc} = 2\left(\frac{2\pi m_c k_B T}{h^2}\right)^{3/2}.$$

Since n_b is the number of electrons with energy greater than the conduction-band barrier height, ΔE_c, the Boltzman approximation for the non degenerate case may be used in (3.6.1) to yield:

$$n_b = N_{cc}\exp\left(-\frac{E_1}{k_B T}\right), \tag{3.6.2}$$

where: $$E_1 = \Delta E_c - E_{fc} = \Delta E_g - \Delta E_v - E_{fc}.$$

Once n_b is known, the electron leakage current at the heterobarrier junction is then given by the relation [Agrawal, 1986], [Chik, 1988]:

$$J_L = qD_n n_b \frac{\left(q\bar{E}/k_B T - \lambda_1\right)e^{\lambda_2 W_P} + \left(\lambda_2 - q\bar{E}/k_B T\right)e^{\lambda_1 W_P}}{e^{\lambda_2 W_P} - e^{\lambda_1 W_P}}, \tag{3.6.3}$$

where D_n is the electron diffusion coefficient, W_p is the thickness of the n-type InP confinement layer, and $\lambda_{1,2}$ is given by:

$$\lambda_{1,2} = \frac{q\bar{E}/k_B T \pm \left[\left(q\bar{E}/k_B T\right)^2 + 4/L_n^2\right]^{1/2}}{2},$$

where L_n is the electron diffusion length.

In the diffusion limited case when $\bar{E} \approx 0$, (3.6.3) reduces to:

$$J_L = \frac{qD_n n_b}{L_n \tanh\left(W_p/L_n\right)}. \tag{3.6.4}$$

However, if the doping level of the confinement layer is relatively low, such that a sufficient field exists in the confinement layer, then (3.6.3) approaches the drift-limited case and J_L is given by:

$$J_L = q\mu_n n_b \bar{E} \tag{3.6.5}$$

In the above, only the electron leakage current has been considered. In reality, however, hole leakage from the active region into the n-type InP cladding layer also exists. The hole leakage current (denoted by J_{pL}) has been found to be negligible in comparison to the electron leakage current (denoted by J_{nL}) by several authors [Ishikawa, 1991], [Chik, 1988], [Yano, 1981]. However, Chen [1984] found the hole leakage current to be at least as important as the electron leakage. Similar expressions for the hole component of the leakage current as those obtained for the electron leakage can be determined in the manner above by making the appropriate variable substitutions.

The leakage current enters into the expression for the laser threshold current as an additive term so that (3.2.2) is written as:

$$J_{th} = \frac{qN_{th}d}{\tau_{th}} + J_L \tag{3.6.6}$$

From (3.6.2) it can be seen that n_b and, therefore, J_L increases rapidly with increasing temperature. This observation suggests that carrier leakage can be a major carrier-loss mechanism in InGaAsP lasers which in turn contributes significantly to the threshold current at high temperatures, especially for low heterojunction-barrier heights ΔE_c.

In addition, leakage currents will affect the external differential quantum efficiency of the laser. The external differential quantum efficiency, η_d, is affected since the internal quantum efficiency term, η_i, in (3.2.4) must include the current injection efficiency. In the case where the injection efficiency in not unity, the quantity, η_i, in (3.2.4) becomes [Horikoshi, 1982]:

$$\eta_i = \eta_{inj} \times \eta_q, \tag{3.6.7a}$$

where, η_{inj} is given by

$$\eta_{inj} = \frac{1}{1 + J_{nL}/J_r + J_{pL}/J_r} \tag{3.6.7b}$$

In (3.6.7b), J_r, is the recombination current density in the active layer (see Fig. 3.6), and η_q is the true quantum efficiency (represented by the number photons produced per electron injected into the active region without escaping over the heterojunction barrier). Thus, it is seen that, if the leakage current density is a significant fraction of the radiative current density, and if the leakage current density increases with temperature (as predicted by (3.6.3) and (3.6.2)), then the differential quantum efficiency (3.2.4) may decrease with temperature. This point was ignored by both Asada *et. al.* and Adams in their calculations of the effects of intervalence band absorption on the temperature dependence of the threshold current.

Yano *et. al.* [1981] calculated the electron and hole leakage, and the radiative current densities in InGaAsP/InP DH lasers emitting at 1.3 μm using (3.6.4), (3.3.3) and (3.6.6). They determined, as did Ishikawa [1991] for InGaAlP visible lasers, that the sharp increase in the threshold current near room temperature was caused by carrier leakage over the heterobarrier. In their calculations of the threshold current density, Yano *et. al.* assume that N_{th} in the active region is given by the commonly used relation [Agrawal, 1986]:

$$n = \left[a\left(L/\Gamma + b\right)\right]^{-1}, \tag{3.6.8}$$

where L/Γ is the total cavity loss given by (2.2.31), and a and b are the gain coefficients from the optical gain expression g = an-b [Agrawal, 1986]. They considered the temperature dependence of the band gap, the bimolecular radiative recombination

coefficient, B, the minority carrier diffusive constants, and the temperature dependence of the Fermi levels using a parabolic band model. In addition, they assumed that the temperature dependent gain coefficients a and b can be expressed as: $a \propto \exp(E_a/kT)$ and $b \propto \exp(E_b/kT)$ (showing once again the influence of Pankove's expression for the temperature dependence of laser threshold). Their results, are plotted in Fig. 3.7, where J_{th} and J_{nl} are shown as function of reciprocal temperature.

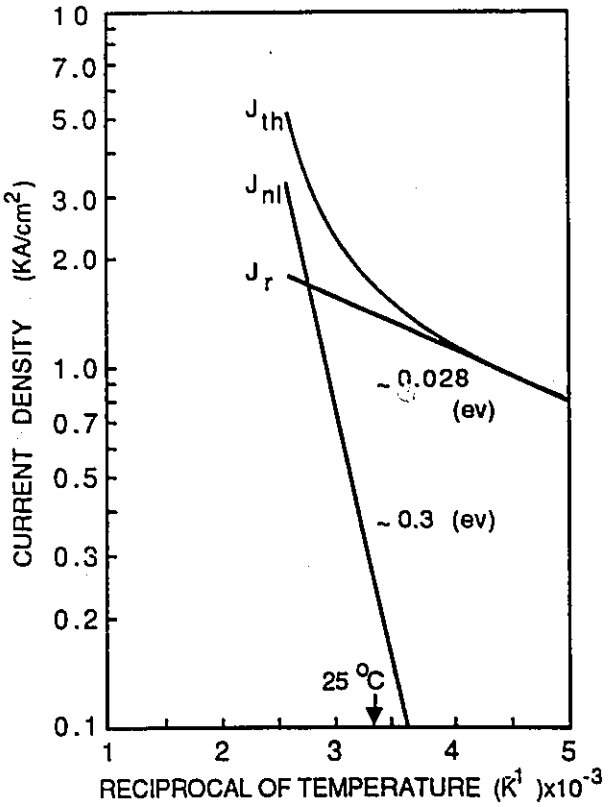

Figure 3.7: Theoretical determination of J_{Th}, J_r, and J_{nl} *vs.* reciprocal temperature according to Yano, [1981].

Yano *et. al.* found that the carrier leakage depended strongly on the active region thickness, d. For an active region thickness of d=0.13 μm they determined T_o above the break point temperature to be 75 K; however, for d=0.2 μm the calculated characteristic temperature, T_o, was 100 K. This predicted increase in T_o with an increase in the active

region thickness has not been realized since in actual devices. In addition, the leakage model above (see (3.6.2) and (3.6.3)) predicts that the electron leakage should be two orders of magnitude smaller, and therefore T_o should be much greater, for 1.55 μm devices compared to 1.3 μm devices. This prediction stems from the increase in ΔE_g and, therefore, in ΔE_c between the InGaAsP active region and the InP confinement layer in InGaAsP/InP devices emitting at 1.55 μm. However, once again, the predicted increase in T_o due to a reduced leakage current for 1.55 μm devices (which actually have a T_o similar to or less than that found in 1.3 μm devices) has not been realized empirically. In fact, it has been determined empirically that the carrier leakage in 1.55 μm devices is actually 3.6-6 times greater in 1.55 μm devices than that in 1.3 μm devices [Chik, 1988].

The effects of a larger ΔE_g in the longer-wavelength devices may be compensated for appreciably by a smaller electron mass; however, from the above results, it has been concluded [Chik, 1988], [Casey, 1984] that some other mechanism must be contributing to the carrier leakage and thereby influencing T_o. In §3.5 it was mentioned that the nonradiative Auger recombination rate increases strongly with a decrease in the band gap energy, E_q. Therefore, it has been postulated [Chik, 1990], [Zhuang, 1985] that Auger recombination induced hot carriers are the major source of carriers that participate in current leakage in InGaAsP lasers. If Auger recombination was the principal mechanism for generating energetic carriers with energies greater than the heterojunction barrier height, it could account for the increased leakage current observed in 1.55 μm devices.

3.7 TEMPERATURE DEPENDENT CARRIER LEAKAGE DUE TO AUGER RECOMBINATION INDUCED ENERGETIC CARRIERS

In Auger recombination, as illustrated in Fig. 3.4, electrons and holes may get excited to higher energy states which are well above band edge (by approximately the

energy gap, E_g). Unless the energy loss rate of these energetic carriers is extremely high, there may exist a significant concentration of energetic carriers at the InGaAsP/InP heterojunction at steady state, which have energies exceeding the InGaAsP/InP conduction- and valence-band discontinuities. Once at the heterojunction interface, these energetic carriers, as in the case of leakage due to thermionic emission, may drift and diffuse into the InP confinement layer where they recombine either radiatively or nonradiatively. The concentration of carriers that reach the heterojunction interface with energies greater than the barrier height depends upon the generation rate of energetic carriers, the heterojunction barrier height, and the relaxation rate of the energetic carriers through carrier-phonon interactions.

The generation rate of Auger induced energetic carriers can be obtained from the relations in §3.4, and are given by Chik [1988] as:

$$G_{n_{Au}} = \left(C_n + C_n^{ph}\right) n^2 (n + p_a), \quad \text{and} \quad G_{p_{Au}} = \left(C_p + C_p^{ph}\right) n (n + p_a)^2 \tag{3.7.1}$$

for electrons and holes, respectively, where C_n and C_n^{ph} are the CCHC Auger recombination coefficients of the direct and phonon-assisted band-to-band recombination processes respectively, and C_p and C_p^{ph} are the CHHS Auger recombination coefficients of the direct and phonon-assisted band-to-band recombination processes, respectively. n is the injected electron density, and p_a is the acceptor concentration in the active layer, respectively. The CHHL Auger process has been neglected as its contributions are small in comparison to the other two Auger processes [Agrawal, 1986].

Chik also calculated the energy relaxation rate of Auger recombination induced energetic (ARIE) electrons and holes due to longitudinal optical (LO) phonon emission. This relaxation rate was determined for InGaAsP by a Vegard's law interpolation (4.1.2)

between the relaxation rates for the constituent binary compounds. Since the energy relaxation rate of the energetic carriers is energy dependent, Chik defined an effective energy relaxation time, τ_{op}, which was then used to relate the energy relaxation rate of the ARIE carrier to the carrier leakage current. The magnitude of τ_{op} was determined from the statistical average of the relaxation times for the Auger excited energetic carriers with energies in the energy interval of $E_g - \Delta E$, where E_g is the band gap of the InGaAsP active region, and ΔE is the conduction- (or valence-) band discontinuity between the active layer and the InP confinement layer. The calculated value of τ_{op} was 5.2×10^{-12} s for energetic electrons, and 1.6×10^{-12} s for energetic holes. Only those ARIE electrons and holes whose energies exceed ΔE within the effective diffusion lengths given by, $L_{op}^{n} = \left(D_n \tau_{op}^{n}\right)^{1/2}$ and $L_{op}^{p} = \left(D_p \tau_{op}^{p}\right)^{1/2}$ (where D_n and D_p are the electron and hole diffusion coefficients, respectively) will reach the InGaAsP/InP heterointerface with energies exceeding the barrier heights, and therefore have the possibility of leaking out of the active layer.

In well-designed devices, the energetic carrier leakage is diffusion current dominated. By solving the rate equation describing the rate of change of the ARIE electrons and holes in the active layer (assuming diffusion dominated carrier leakage) Chik found an expression for the densities of the energetic electrons and holes in the active layer with sufficient energies to leak over the heterojunction barriers at steady state. These carrier densities are given by the following expressions:

$$n_{ex} = \frac{\tau_{op}^{n} L_{op}^{n} \tanh\left(d/L_{op}^{n}\right)\left(C_n + C_n^{ph}\right) n^2 \left(n + p_a\right)}{L_{op}^{n} \tanh\left(d/L_{op}^{n}\right) + \tau_{op}^{n} D_n \Big/ \left[L_n \tanh\left(W_p/L_n\right)\right]}, \qquad (3.7.2)$$

and

$$p_{ex} = \frac{\tau_{op}^{p} L_{op}^{p} \tanh\left(d/L_{op}^{p}\right)\left(C_p + C_p^{ph}\right) n \left(n + p_a\right)^2}{L_{op}^{p} \tanh\left(d/L_{op}^{p}\right) + \tau_{op}^{p} D_p \Big/ \left[L_p \tanh\left(W_n/L_p\right)\right]}. \qquad (3.7.3)$$

By substituting (3.7.2) into (3.6.4) with n_b replaced by n_{ex}, and substituting (3.7.3) into the equivalent expression for holes, the diffusion-limited leakage current due to ARIE electrons and holes is given by the expressions:

$$J^n_{diff} = \frac{qD_n \tau^n_{op} L^n_{op} \tanh\left(d/L^n_{op}\right)\left(C_n + C^{ph}_n\right)n^2\left(n+p_a\right)}{\tau^n_{op} D_n + L^n_{op} \tanh\left(d/L^n_{op}\right) L_n \tanh\left(W_p/L_n\right)}, \qquad (3.7.4)$$

and

$$J^p_{diff} = \frac{qD_p \tau^p_{op} L^p_{op} \tanh\left(d/L^p_{op}\right)\left(C_p + C^{ph}_p\right)n\left(n+p_a\right)^2}{\tau^p_{op} D_p + L^p_{op} \tanh\left(d/L^p_{op}\right) L_p \tanh\left(W_n/L_p\right)}, \qquad (3.7.5)$$

respectively. The leakage currents due to the drift transport mechanism can be found in Chik, [1988].

The leakage currents of (3.7.4) and (3.7.5) enter into the threshold current density expression of (3.6.6) (as $J_L = J^n_{diff} + J^p_{diff}$) in the same manner as for the case of thermionic leakage. From (3.3.4), (3.4.1), (3.4.4), (3.7.2) and (3.7.3) it can be seen that n_{ex} and p_{ex} and, therefore, J^n_{diff} and J^p_{diff}, depend exponentially on temperature and vary as the cube of the injected carrier concentration, n. The energetic hole leakage current, J^p_{diff}, has been determined to be insignificant as compared with the electron leakage current due to the higher energy loss rate of energetic holes, combined with the lower mobility of holes in InP and InGaAsP in comparison to the corresponding values found for electrons.

From the energy gap dependence of (3.4.1) and (3.4.4), the above leakage model predicts that the Auger recombination induced carrier leakage should be greater in 1.55 μm devices than in 1.3 μm devices (the theoretically estimated Auger coefficient, C_n is about 2.8-4.4 times greater in InGaAsP with compositions corresponding to 1.55 μm than 1.3 μm). In addition, Chik determined that the effective energy relaxation time for the ARIE

excited electrons in 1.55 μm InGaAsP was greater than that in 1.3 μm devices at 8.35×10^{-12} s. And, in agreement with experimental observations, Chik calculated from his leakage model that the energetic carrier leakage in the 1.55 μm devices would be on the order of 4.5-8 times higher than in 1.3 μm devices. Thus, the Auger recombination model presented above explains why no improvement in T_0 has been observed for 1.55 μm devices as predicted by the thermionic leakage model.

It was mentioned above, that for a given temperature, the diffusion-limited leakage rate of Auger recombination induced energetic carriers should have an n^3 dependence. (Drift-dominated leakage due to Auger recombination induced energetic carriers is predicted to have a functional dependence on the injected carrier density in the active layer between n^5 and n^6). Zhuang *et. al.* [1985] measured the 950 nm emission due to carriers radiatively recombining in the InP confinement layer of 1.3 μm wavelength double heterojunction stripe geometry lasers (for which it is expected that the doping profile was such that the leakage currents should be diffusion dominated). They determined that the integrated intensity of the 950 nm emission from the InP layer depended on the carrier concentration as $I_{950} \propto n^{3.1\text{-}3.3}$ for an injected carrier concentration varying from $3 \times 10^{17} < n < 1.5 \times 10^{18}$ cm^{-3}. This experimentally determined dependence is in excellent agreement with the predictions of the Auger recombination induced energetic carrier leakage model.

In addition, Zhuang *et. al.* compared the current dependence of the ratio of the intensity of the 1.3 μm laser emission to the intensity of the 950 nm emission from the InP layer, to the ratio of the nonradiative lifetime over the radiative lifetime. They found the following relation:

$$I_{1.3}/I_{950} = \tau_{Auger}/K\tau_r \qquad (3.7.6)$$

where K remained constant for the carrier concentration range $3 \times 10^{17} < n < 1.5 \times 10^{18}$. Since the ratio τ_{Auger}/τ_r represents the ratio of the radiative recombination rate to the rate of

Auger recombination relevant to current leakage, (3.7.6) provides evidence that the Auger recombination in the active layer is the physical cause of the carrier leakage. Chik [1988], determined that the quantity K, which represents the fraction of externally observed Auger recombination induced energetic carriers that leak over the heterojunction barrier, is given by the relation:

(3.7.7)

$$K = \frac{f_{950} D_n \tau_{op}^n L_{op}^n \tanh\left(d/L_{op}^n\right)}{f_{1.3} d L_n \tanh\left(W_p/L_n\right)\left\{L_{op}^n \tanh\left(d/L_{op}^n\right) + \left(\tau_{op}^n/D_n\right)/\left[L_n \tanh\left(W_p/L_n\right)\right]\right\}},$$

where, d is the active region thickness, and f_{950} and $f_{1.3}$ are the external efficiencies of the 1.3 μm and 950 nm emissions, respectively. Thus, in accordance with experimental observation, the ARIE carrier leakage model predicts that the value of K is a constant independent of the carrier concentration injected into the active layer. In addition, (3.7.7) predicts that the value of K would decrease as the active layer thickness increased. This prediction is again in agreement with the results of Zhuang *et. al.* Finally, the ARIE carrier leakage model proposed by Chik, [1988], provides excellent agreement with the empirical observations of Yamakoshi *et. al.* [1982] and of Olshansky *et. al.* [1984].

3.8 SUMMARY

In summary, in this chapter five physical mechanisms that could possibly explain the high temperature sensitivity of the threshold current in InGaAsP/InP-based materials were reviewed. Each of these physical mechanisms was suggested by different authors to be the dominant mechanism in influencing the behavior of the I_{th}-T relationship. The influence of Pankove's empirically proposed exponential relationship (1.1.1) is clear, especially, in the work of Asada *et. al.* and of Adams (where the intervalence band

absorption was determined to vary exponentially with temperature (3.2.3)), and also in the work of Su (who assumed that the linear gain parameters (3.6.8) depended exponentially on temperature as: $a \propto \exp(E_a/kT)$ and $b \propto \exp(E_b/kT)$). In fact, the results of Chapter 6 will show that the intervalence band absorption is not a strong function of temperature and may even decrease with temperature. This fact has also been noted by Leopold [1987]. The effect of the physical mechanisms proposed to be responsible for the temperature dependence of the laser threshold current were discussed primarily within the context of bulk DH lasers. The reason an emphasis was placed on DH lasers is because much of the work discussed in this chapter has not been performed for QW lasers.

Of the possible physical mechanisms responsible for the high temperature sensitivity of the threshold current in InGaAsP/InP lasers, perhaps the greatest influence on the shape of the I_{th}-T relationship stems from the combined effects of Auger recombination on the carrier lifetime, and the effects of ARIE carrier leakage. The close agreement between theory and experiment, based on the ARIE carrier leakage model [Chik, 1990], and the ability of this model to explain the results obtained by other authors, gives strong supporting evidence that this may be the case. However, Chik did not determine theoretical L-I curves as a function of temperature using his leakage model. Therefore, it is not known what values of T_o would be obtained above the break point temperature using this model.

Twenty-five years after Pankove first proposed his empirically determined exponential relationship [1968], many researchers are still attempting to clarify the physical origins of the I_{th}-T relationship [O'Gorman, 1992], [Zou, 1993], [Lui, 1993]. This research effort is clear evidence that there is still much uncertainty as to why the characteristic temperature, T_o, in InGaAsP/InP based semiconductor lasers is so low. Zou *et. al.* examined the effects of intervalence band absorption, Auger recombination, and the temperature dependence of the optical gain, and in this very recent paper states, "no final

conclusions [have] been reached regarding the temperature sensitivity of [InGaAsP/InP] lasers." Recently, O'Gorman *et. al.* [1992], pointed out that the I_{th}-T relation shows more of a super linear dependence than that given by (1.1.1); therefore, the exponential relationship proposed by Pankove may be inappropriate.

CHAPTER 4: LASER DESIGN

4.0 INTRODUCTION

For the purposes of studying the effects of strain on laser performance, two separate sets of quantum well laser structures, were designed, grown and fabricated at BNR's Advanced Technology Laboratory in Ottawa. In all, seven different laser structures were designed, each having identical graded index separate confinement (GRINSCH) regions, identical barrier heights and widths, and similar emission wavelengths. The difference between the two sets of lasers (see Table 4.1) arises from the number and the thickness of the quantum wells in the active region. In one set of lasers the active region contains three quantum wells (Fig. 4.1), whereas in the other set, the active region contains five quantum wells (Fig. 4.2). The device structures grown are listed in Table 4.1. The rational for the selection of certain design parameters, such, as the number and thickness of the quantum wells is also presented.

The comparison of the operating characteristics between the devices designed for this thesis is unique relative to other such studies that have been done to date. The device comparison within is unique in that both the strained and unstrained laser structures studied were designed to have identical well widths and similar emission wavelengths. These similarities between devices allow one to more effectively isolate the effects due to strain from those due to changes in, for example, the quantum well width. For example, as discussed in Chapter 2, the density of states for a quantum well structure may be affected by both strain and QW width. It was found in Chapter 2, and shown in Fig. 2.9 that a thicker QW can result in a lower transparency carrier density. As will be shown in

Fig. 4.8 in §4.2.1, a lower transparency carrier density can also be achieved through the appropriate application of compressive strain. Thus in studying the effects of strain, if one finds a lower threshold current density, J_{th}, for one, say compressively strained laser structure, over another, say unstrained structure, and these structures have different well widths, it cannot be certain whether the change in J_{th} is due to different QW widths or due to different strains. Thus, it is necessary to keep the well widths constant in order to ensure that any observed differences in the operating characteristics can be reasonably attributed to effects due to strain and not to effects due to changes in the QW thickness.

Table 4.1: Description of the laser structures which were processed into devices. There were seven laser structures in all. Four structures had quantum wells with a nominal thickness of 55Å (measured thickness 64 Å), and three had quantum wells with a nominal thickness of 30Å (measured thickness 38Å) The range of strains for each set of structures is indicated. Lasers having a given strain are identified by their growth number. Apart from strain and QW thickness, all structures were designed to have identical step index regions, doping profiles and emission wavelengths. Device structure R1-395 was not studied.

Set Number	Sample Number	Number of QWs	QW Thickness	Barrier Thickness	Strain
2	R1-394	5	38 Å	100 Å	-1.5 %
2	R1-395	5	38 Å	100 Å	-1.2 %
2	R1-396	5	38 Å	100 Å	Unstrained
1	R1-397	3	64Å	100 Å	+1.2 %
1	R1-398	3	64 Å	100 Å	+1.3 %
1	R1-399	3	64 Å	100 Å	-1.2 %
1	R1-400	3	64 Å	100 Å	Unstrained

A simplified block diagram of the algorithm used to design the strained MQW lasers of Fig. 4.1, and 4.2, appears in Fig. 4.3. There are essentially two stages in the design of these lasers. The first stage involves a determination of the quantum well dimensions and the material compositions required to give a desired emission wavelength while taking into consideration strain and quantum size effects.

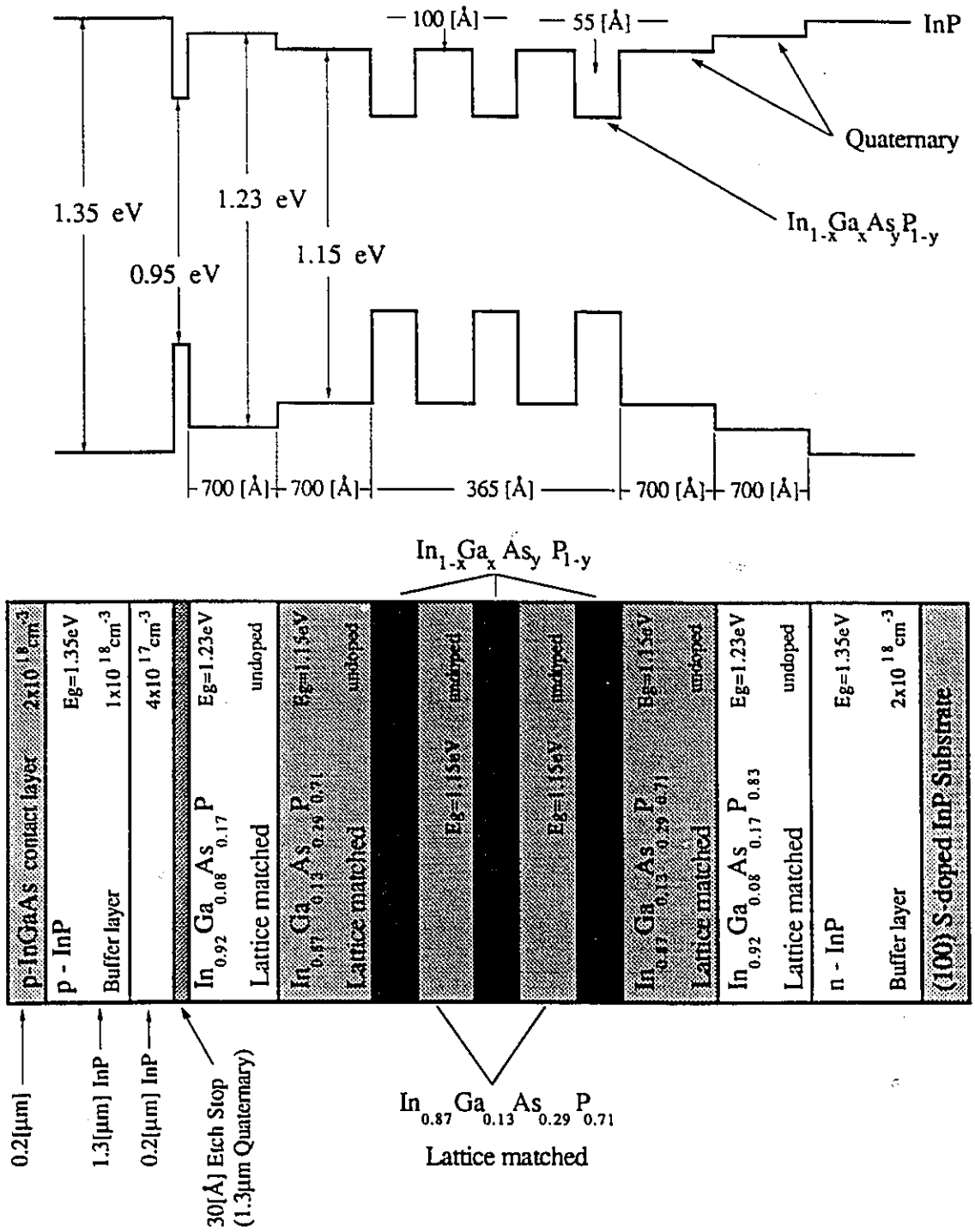

Figure 4.1: Schematic of energy band diagram and layer compositions of laser structure representative of those laser structures belonging to SET 1. The quantum well thicknesses of these structures are all 55Å and the barrier layer thicknesses are 100Å.

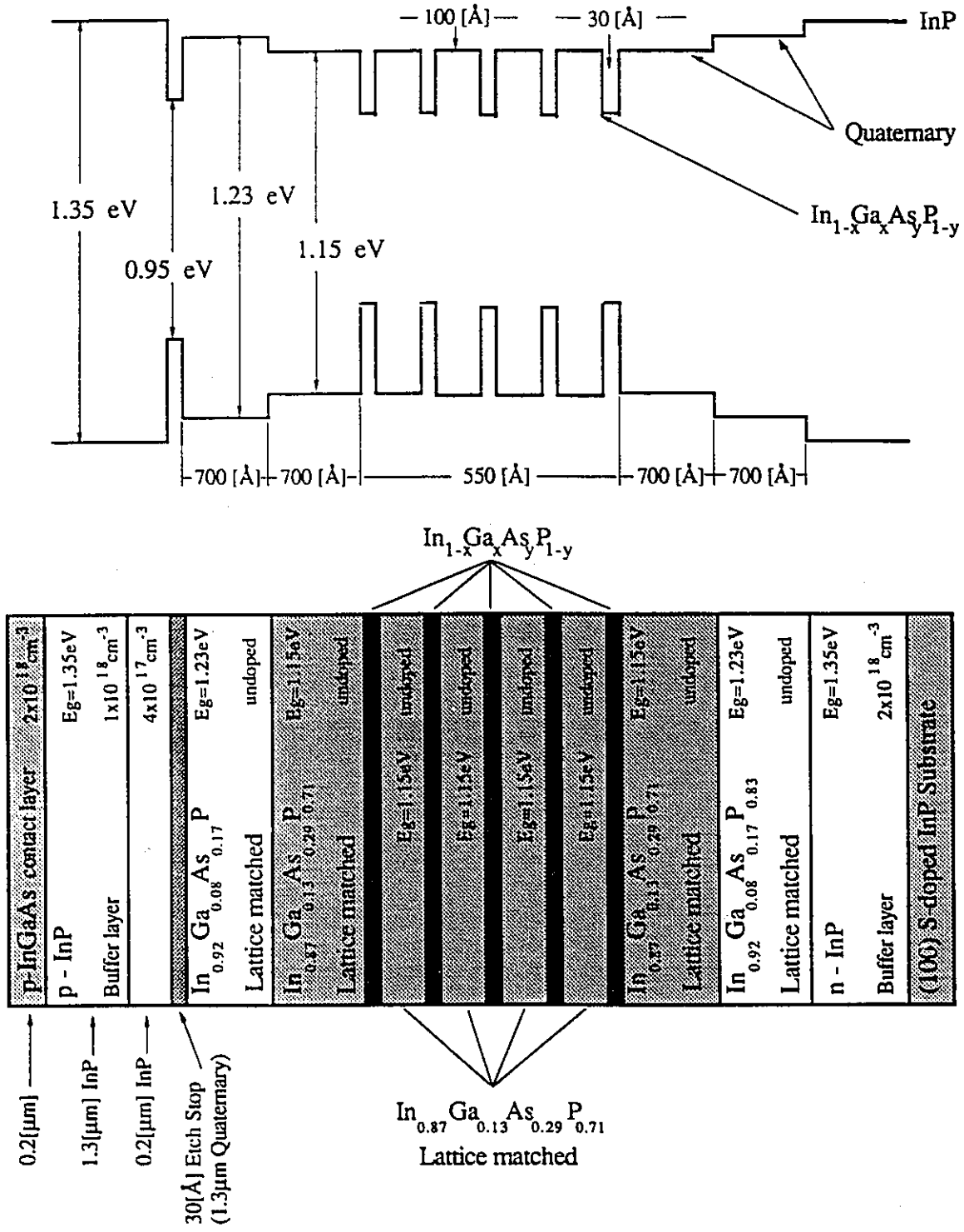

Figure 4.2: Schematic of energy band diagram and layer compositions of laser structure representative of those laser structures belonging to SET 2. The quantum well thicknesses of these structures are all 30Å and the barrier layer thicknesses are 100Å.

The second stage involves a determination of: the gain *vs.* injected carrier relation for the given quantum well material; the optical confinement factor for the proposed device structure as a function of the number of quantum wells; and, consequently, the number of quantum wells to include in the active region of the laser in order to minimize the threshold current.

4.1 DESIGN ALGORITHM: Stage 1

In the first stage of the laser design algorithm, the dimensions and material compositions of the laser active region needed to produce a specific emission wavelength are determined. The input parameters required for this stage of the laser design are: the desired emission wavelength of the laser; the desired level of strain in the quantum wells; the energy gap and thickness of the barrier layers; and estimates for the energy gap and thickness of the quantum wells needed to produce the desired transition energy. Once these parameters have been specified, stage one of the design proceeds as follows.

Firstly, the lattice constant of the well layers required to produce the desired level of strain is calculated. From the calculated lattice constant and the estimate of the unstrained bulk energy gap of the well, the composition x and y of the $In_{1-x}Ga_xAs_yP_{1-y}$ well layer is found. The material composition x and y of the barrier layer is also determined based on the reasonable assumption that this layer will be lattice matched to the InP substrate (i.e., it is assumed that the strained active region of the laser will be pseudomorphic and maintain the same biaxial lattice constant as the InP substrate).

Once the composition of the well and barrier layers have been determined, the material parameters (elastic compliance constants, deformation potentials etc.) required in order to determine the strain induced effects on the band structure of the active region are calculated.

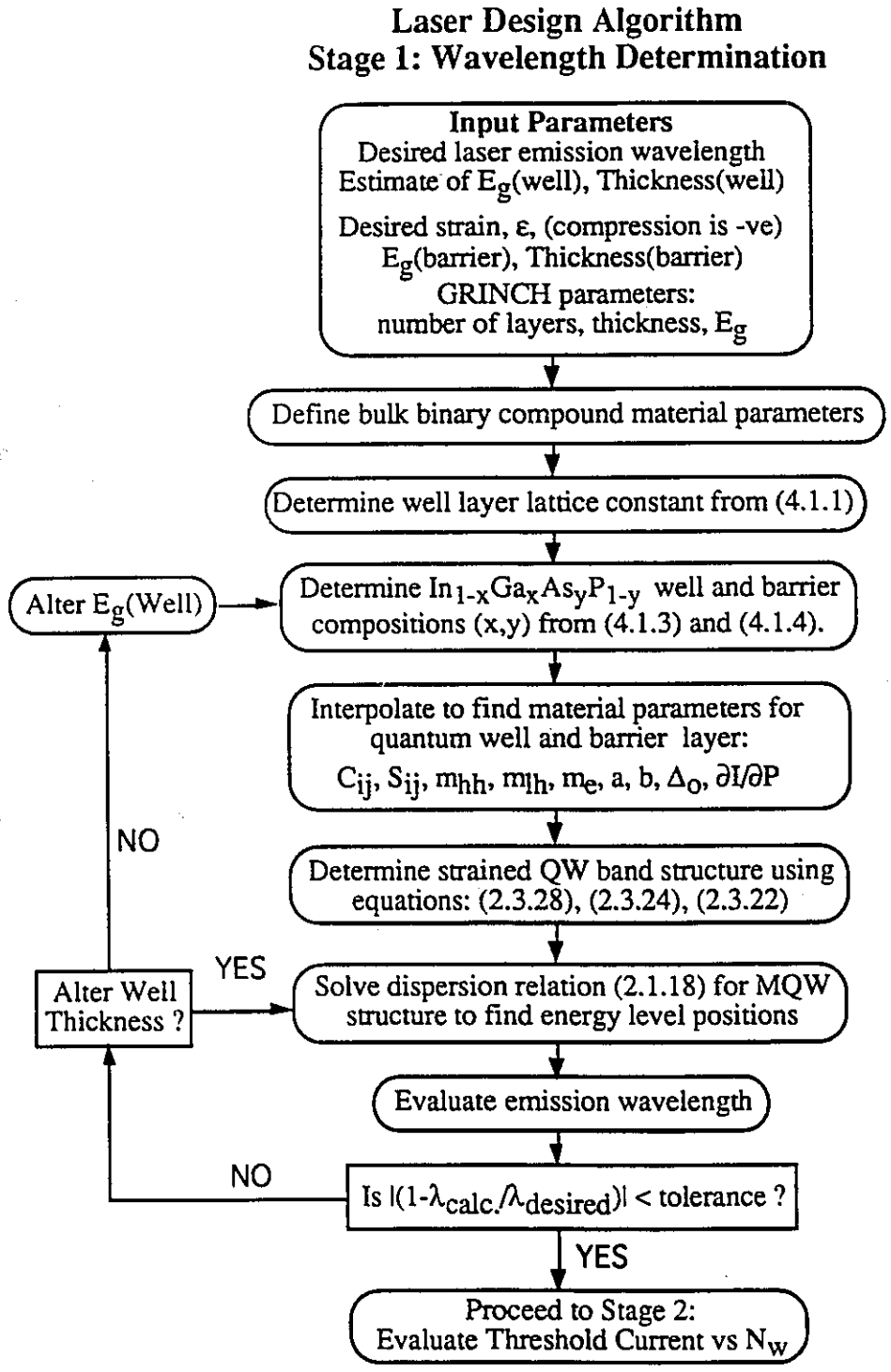

Figure 4.3(a): Algorithm used to determine the composition, band structure and emission wavelength of strained quantum well structure.

Laser Design Algorithm Stage 2: Threshold Current Calculation

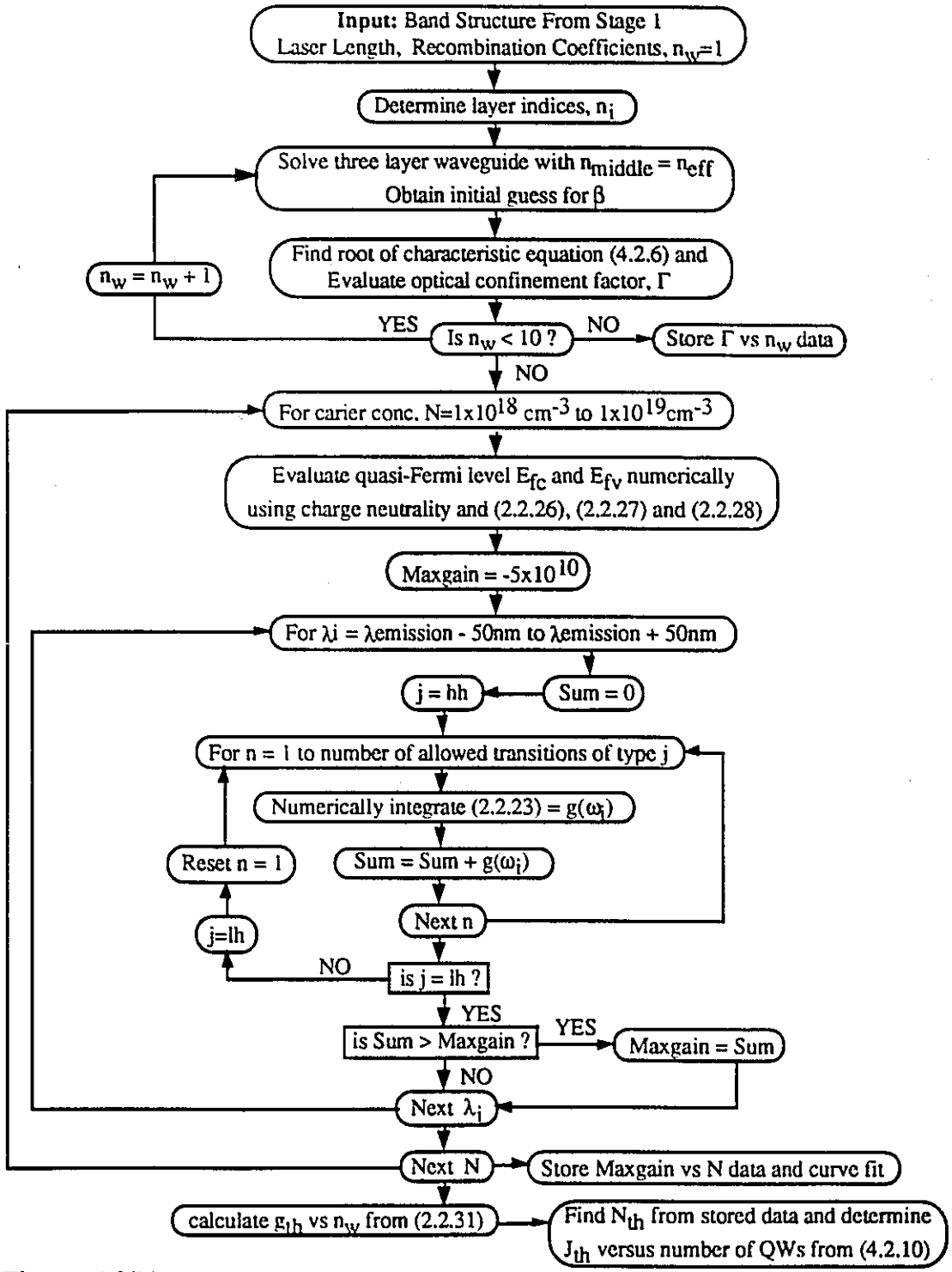

Figure: 4.3(b): Algorithm used to determine QW peak gain and J_{th} *vs.* number of quantum wells.

Using the calculated parameters, the strain induced shifts in the conduction band and the valence band are calculated along with the magnitude of the strain-induced splitting of the valence bands. The relative positions of the well and barrier energy bands after strain effects have been considered, along with the well and barrier widths, then define the quantum well structure of the active region. An envelope function approximation derived dispersion relation for this structure is then solved to give the electron and hole energy solutions (levels). Finally the emission wavelength of the laser is determined from these energy solutions. If the calculated emission wavelength is greater (less) than the desired emission wavelength, then either the original estimate of the well layer energy gap is increased (reduced), or the well width is reduced (increased), or a combination of both occurs. The procedure is then repeated until the desired transition energy is obtained. The specific mathematical calculations and approximations used in stage one of the design algorithm are presented in detail in the following.

4.1.1. Determination of the Quantum Well Lattice Constant

A determination of the well layer lattice constant required in order to produce a given level of strain is based on the premise that the entire strained-layer active region of the laser will be pseudomorphic. Such an assumption is valid since, in a quantum well laser, the thickness of the strained epilayers is much smaller than that of the substrate and the lattice-matched confinement layers. Under these conditions the strains in the substrate may be neglected [Osbourn, 1982], [Pearsall, 1990] and the lattice constant of the epilayers in the plane perpendicular to the growth direction will be identical to that of the unstrained substrate (see equation 2.3.1). As a result, the entire lattice mismatch will be accommodated as a homogeneous tetragonal distortion in the strained quantum well layers only (provided of course that their are no misfit dislocations). Under these

conditions the in-plane lattice parameter, a_W, of the unstrained (cubic) epilayer required to produce a given level of biaxial strain is given by the relation

$$a_w = \frac{a_s}{(1+\varepsilon_{\|})}, \tag{4.1.1}$$

where a_S is the lattice constant of the substrate and $\varepsilon_{||}$, is the in-plane strain in the epilayer. From (2.3.2), where $a_s = a_{//}$ and $a_w = a_A$, the in-plane strain, $\varepsilon_{||}$, is negative in the case of compressive strain, (i.e., $a_W > a_S$) and is positive in the case of tensile strain, (i.e., $a_W < a_S$).

4.1.2. Determination of the Well and Barrier Compositions

As is indicated in Fig. 4.4, both the lattice constant and the energy gap of the $In_{1-x}Ga_xAs_yP_{1-y}$ quantum well, the barrier, and the GRINSCH regions of the lasers of Figs. 4.1 & 4.2 can be controlled by varying the composition x and y of the quaternary material. Because the lattice constant of the quantum well and barrier layers are given by (4.1.1) and the lattice-matching condition, and since the energy gap of these layers is specified, all that is required in order to determine the composition of these layers is a relationship indicating how the lattice constant and energy gap vary with composition.

The lattice constant, a, of the alloy compound $In_{1-x}Ga_xAs_yP_{1-y}$ is known to vary linearly with composition [Adachi, 1982]. Therefore, if the bulk binary material lattice constants are known (see Table 4.2), the relationship between the lattice constant and the composition can be found by using Vegard's interpolation scheme:

$$a_Q(x,y) = (1-x)y \cdot a_{InAs} + (1-x)(1-y) \cdot a_{InP} + xy \cdot a_{GaAs} + x(1-y) \cdot a_{GaP}, \tag{4.1.2}$$

From (4.1.2) and (4.1.1) along with the material parameters listed in Table 4.2, one obtains the relation:

$$x = \frac{0.1895y + 5.8688 - a_w}{(0.4176 - 0.01255y)}. \tag{4.1.3}$$

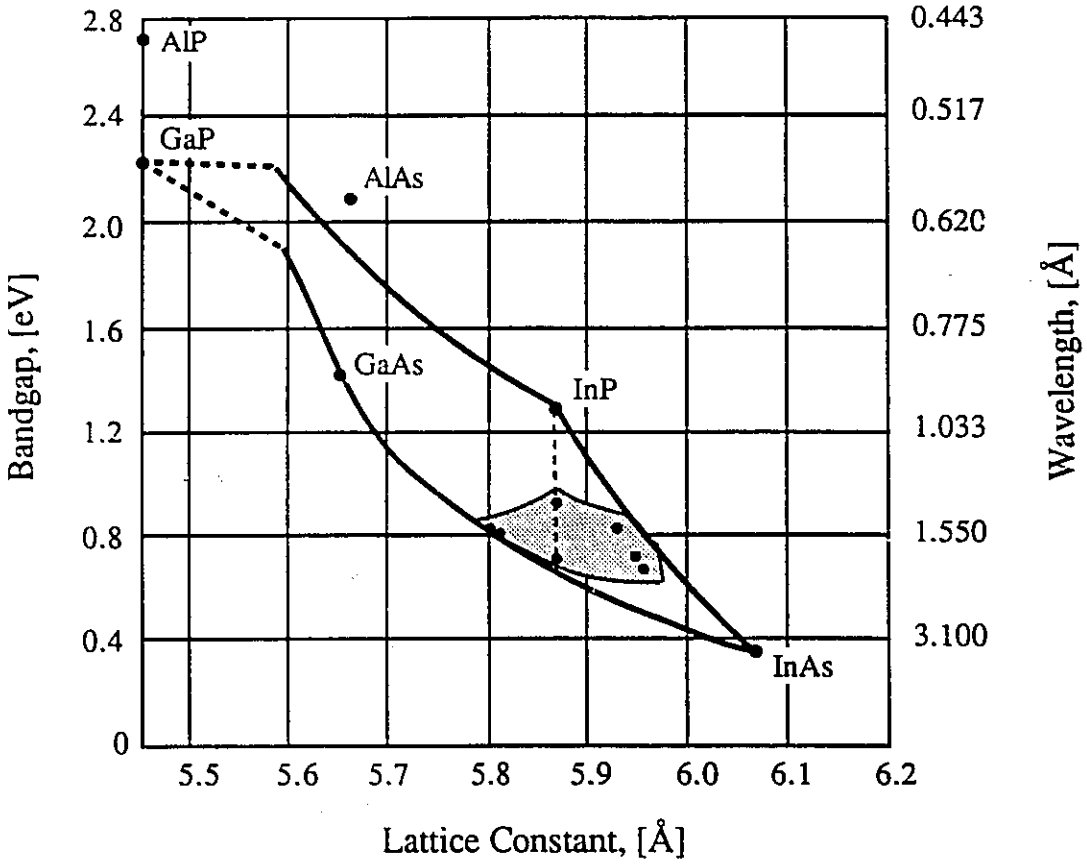

Figure 4.4: Variation of band gap and lattice constant for $In_{1-x}Ga_xAs_yP_{1-y}$ obtained by varying compositions x and y. The shaded region indicates the range of compositions used to obtain the strained epilayers of the strained MQW lasers studied in this thesis.

In contrast, the band-gap energy is known to be a nonlinear function of the material composition. In this case, the relationship between the band-gap energy and the material composition is given by the interpolation scheme [Adachi, 1982]

$$Eg(x,y)=\frac{x(1-x)[(1-y)Eg(InGaP)+yEg(InGaAs)]+y(1-y)[(1-x)Eg(InAsP)+xEg(GaAsP)]}{x(1-x)+y(1-y)} \quad (4.1.4)$$

where the relationships for the ternary band-gap parameters, (Eg(InAsP) etc.) with composition are given by:

Table 4.2: Binary compound material parameters used in the determination of the energy band structure, emission wavelength and gain characteristics of the laser structures studied in this thesis.

Parameter	InAs	InP	GaAs	GaP
Lattice Constant, [Å]	6.0583[a,b]	5.8688[a]	5.6533[a]	5.4512[c]
Eg(Γ_{8v} - Γ_{6c}), [eV]	**0.359**[c] 0.354[c]	**1.35** 1.344[a]	**1.424**[a]	**2.74** 2.780[a,c]
dI/dP, [10^{-6} eVcm^2/kg]	2.9[d]	2.3[d]	2.5[d]	2.1[d]
$dE_{g,dir}/dP$, [10^{-6} eV/bar]	**10.2**[b] 12.0 9.8[b]	**7.5** 8.0[b]	12.6 **11.1**[a] 10.6	**9.7** 9.2
m_e^*, [m_o]	**0.027**[b] 0.0219	**0.08**[e] 0.073	**0.067**[a,b,e] 0.065	0.17[e]
m_{lh}^*, [m_o]	**0.024**[b]	**0.089** 0.12	**0.068**[b] 0.076[a]	**0.14**[c] 0.12[a]
m_{hh}^*, [m_o]	**0.41**[b] 0.33 0.60[e,f]	0.85[b,e,f]	**0.50**[a,b] 0.62[f]	**0.79**[c,e,f] 0.54[c] 0.67[a]
γ_1	**19.67**[e] 20.4[b]	**6.28**[e] 5.04[b]	**7.65**[e] 6.95[b]	4.20[e]
γ_2	**8.37**[e] 8.3[b]	**2.08**[e] 1.56[b]	**2.41**[e] 2.25[b]	0.98[e]
γ_3	**9.29**[e] 9.1[b]	**2.76**[e] 1.73[b]	**3.28**[e] 2.86[b]	1.66[e]
Split off Energy, Δ_o, [eV]	0.41[b]	0.10[b]	0.384[a]	0.13[b]
C_{11} (10^{11} dyn/cm^2)	8.329[b]	**10.22**[c] 10.11[a,g]	**11.81**[b] 11.9[a,b]	**14.12**[c] 14.05[a]
C_{12} (10^{11} dyn/cm^2)	4.526[b]	**5.76**[c] 5.61[a,g]	**5.32**[b] 5.38[a,b]	**6.253**[c] 6.203[a]
C_{44} (10^{11} dyn/cm^2)	3.959[b]	**4.60**[c] 4.56[a,g]	**5.94** 5.95[a]	**7.047**[c] 7.033[a]
Hydrostatic Dfmn. Ptl., a	**-6.0**[b] -5.2	**-8.0** -5.1[g] -6.35[b]	**-9.43**[a] -9.77[b] -4.8[g]	**-9.9** -9.3[a]
Deformation Ptl., b	**-1.8**[a,b] -1.0 -2.33	**-1.55**[b,g] -2.0[b,g]	**-1.7**[a,g] -2.2[g] -2.0	**-1.5**[a,g] -1.4 -1.8[g]
Index of Refraction, n @ λ=1.3μm	3.515[b]	3.21	3.338[b]	3.1[b]

[a] Landolt-Bornstein, [1987] series III/22a, Madelung,. [b]series III/22 Harbeke, Makelung, Rossler.
[c] Landolt-Bornstein, [1987] series III/22 Kress/Grave, Hubner
[d] Champhausen, [1971]
[e]Lawaetz, [1971]
[f]Adachi, [1982]. [g][1992]

$$
\begin{aligned}
&Eg(InAsP) \Rightarrow Eg(InAs_yP_{1-y}) = 1.35 - 1.083y + 0.091y^2, \\
&Eg(InGaP) \Rightarrow Eg(In_{1-x}Ga_xP) = 1.35 + 0.643x + 0.786x^2, \\
&Eg(GaAsP) \Rightarrow Eg(GaAs_yP_{1-y}) = 2.74 - 1.473y + 0.146y^2, \\
&Eg(InGaAs) \Rightarrow Eg(In_{1-x}Ga_xAs) = 0.36 + 0.505x + 0.555x^2,
\end{aligned}
\tag{4.1.5}
$$

The coefficients of the x^2 and y^2 terms above are the nonlinear or bowing parameters. These parameters describe the deviation from linearity of the ternary compound band-gap energies with the mole fraction of the compound x or y.

For $In_{1-x}Ga_xAs_yP_{1-y}$ quaternary material which is lattice-matched to InP, an empirical relationship describing the variation of the band-gap energy with the As mole fraction, y, also, exists , [Nahory, 1978]. This relationship is given by the equation

$$Eg(y) = 1.35 - 0.72y + 0.12y^2. \tag{4.1.6}$$

Thus, with a relationship for Eg(x,y) and a(x,y), one may now determine the composition of the well and barrier layers by combining (4.1.3) and (4.1.4) [for strained epilayers] or (4.1.3) and (4.1.6) [for unstrained epilayers] and solving for x and y.

Figure 4.5 shows a comparison of the band-gap energy as a function of the y-composition parameter for $In_{1-x}Ga_xAs_yP_{1-y}$ lattice-matched to InP, as determined from (4.1.4) and (4.1.5) and the empirical relationship of (4.1.6). It should be noted from Fig. 4.5 that a discrepancy exists between the interpolated values of (4.1.4) and the experimental data. This discrepancy, which is thought to be due to the effects of quaternary-alloy disorder [Adachi, 1992] must be kept in mind when solving equations (4.1.3) and (4.1.2) for the compositions of the non-lattice matched well layer materials. Material grown to have the calculated compositions may result in the epilayers having a smaller band-gap than intended which in turn would result in a red shifting of the desired emission wavelength.

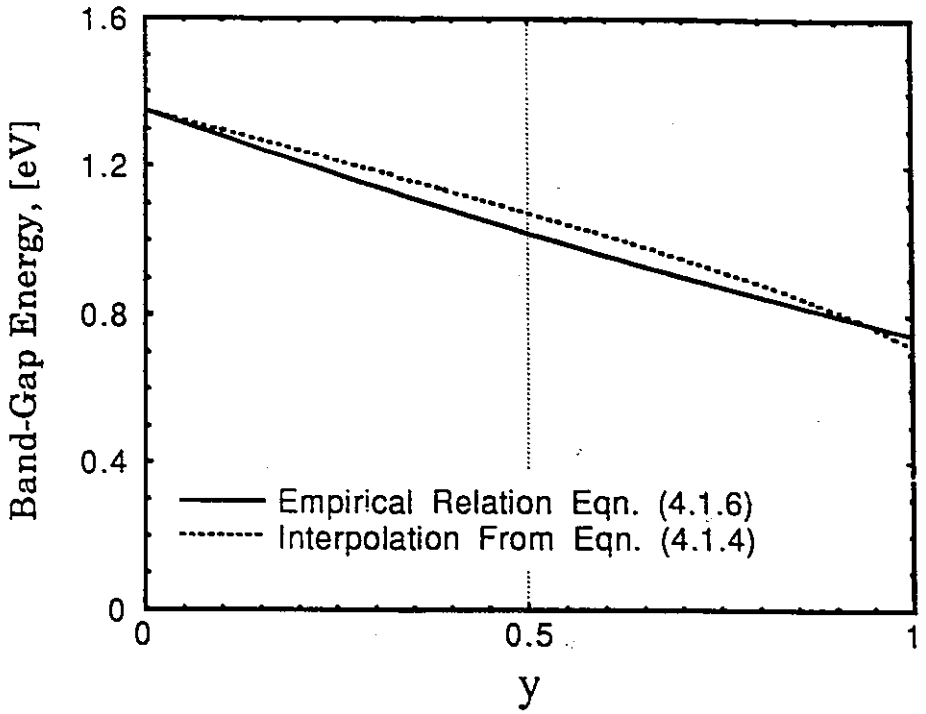

Figure 4.5: The lowest direct energy band-gap as a function of the y-composition parameter for $In_{1-x}Ga_xAs_yP_{1-y}$ lattice-matched to InP. Comparison of empirical results and those obtained from equation (4.1.4)

4.1.3. Determination of the Well and Barrier Material Parameters

Once the compositions of the active-region epilayers have been determined, it is possible, using the calculated x and y values and an appropriate interpolation scheme, to determine the well and barrier material parameters needed to determine both the strain induced effects on the active region band structure, and the discrete energy levels for electrons and holes within the wells. This information in turn allows for a determination of the emission wavelength of the given laser structure.

The important parameters for determining the effects of strain on the energy band structure of the laser active region are the elastic stiffness constants, C_{ij}, and the hydrostatic and shear deformation potentials, a and b respectively. Since the elastic

stiffness constant can be attributed to long-range Coulomb forces in solids [Nye, 1957], it has been suggested that C_{ij}, which have been extensively measured for the III-V binary compounds (Table 4.2), varies linearly with the alloy composition x and y for the quaternary material $In_{1-x}Ga_xAs_yP_{1-y}$ [Adachi, 1982]. Therefore, the linear interpolation scheme of (4.1.2), with a_Q replaced by C_{Qij}, was used to determine the elastic stiffness constants for the quaternary epilayers. Values for the deformation potentials for the quaternary epilayers were also determined via a linear interpolation between values for the binary compounds which appear in Table 4.2. The values used appear in bold type.

An important parameter for determining not only the energy levels of electrons and holes in the quantum wells, but also the quantum well density of states and leakage currents, is the carrier effective mass. The dependence on the composition of the electron effective mass in the $In_{1-x}Ga_xAs_yP_{1-y}$/InP quaternary system has been studied experimentally by many authors [Perea, 1980], [Nicholas, 1980], [Chamberlain, 1987]. In contrast to the predictions of the $\mathbf{k}\cdot\mathbf{p}$ theory (it predicts a strong bowing in m^* [Hermann, 1977]), empirical results for m_e^Γ/m_o as a function of y for $In_{1-x}Ga_xAs_yP_{1-y}$ lattice-matched to InP show a linear dependence of m_e^Γ on alloy composition. Nicholas *et al.* obtained the relation

$$\frac{m_e^\Gamma}{m_o} = 0.080 - 0.039y. \qquad (4.1.7)$$

A linear interpolation scheme [Eq. (4.1.2)] using the masses of the related binaries (Table 4.2: values in bold face) has been used to obtain effective mass values for the purpose of calculations for this thesis.

While numerous experimental data exist for the III-V binary conduction band effective masses, such is not the case for the valence-band masses. What little empirical data that is available for the heavy hole masses for $In_{1-x}Ga_xAs_yP_{1-y}$ lattice matched to InP suggests that m_{hh}/m_o may be independent of composition with a value of m_{hh}/m_o =

0.46 [Adachi, 1992]. This result is considerably smaller than those values obtained from an interpolation using the theoretically determined heavy hole masses for the binary materials given by [Lawaetz,1971] and (4.1.2). On the other hand, empirical results available for the light hole masses as a function of alloy composition for $In_{1-x}Ga_xAs_yP_{1-y}$ lattice-matched to InP are in good agreement with the theoretically calculated masses [Hermann, 1981]. For $In_{1-x}Ga_xAs_yP_{1-y}$ lattice-matched to InP the empirically determined relationship for m_{lh}/m_0 as a function of composisition is:

$$\frac{m_{lh}(y)}{m_o} = 0.120 - 0.099y + 0.030y^2. \qquad (4.1.8)$$

However, for the purpose of this thesis, and in light of the uncertainties in the values for the effective masses [Adachi 1992], both the light and heavy hole effective masses as a function of material composition x and y were determined using the interpolation scheme of (4.1.2). It should also be noted, as shown in Fig 4.6, that the effective masses are a reasonably strong function of temperature above 100K, with m^* decreasing with increasing temperature, as implied by (2.2.11).

Also important in the determination of the quantum well energy solutions for electrons and holes are the conduction and valence band offsets between the well and barrier material. The importance of this parameter (V_o) can be seen in equation (2.1.8) or (2.1.18). There is considerable controversy in the value of the conduction and valence band offsets in the InGaAsP/InP material system, with values for the ratio of the conduction-band discontinuity, ΔE_C, to the energy-gap discontinuity, ΔE_g, at the interface ranging from 0.25 to 0.65 [Nag, 1991], [Adachi, 1992], [Kazuhisha, 1990]. Band theory calculations predict that conduction-band discontinuities at heterojunctions between semiconductor alloys with common anions (e.g., GaAs and GaAlAs) are larger than the corresponding valence-band discontinuities [Forrest, 1984]. For heterojunctions between materials with dissimilar anions (e.g., InGaAs and InP) theory predicts that the valence-

band discontinuities are larger. Forrest *et. al.* determined empirically the band discontinuities for a series of compositions of $In_{1-x}Ga_xAs_yP_{1-y}$ lattice-matched to InP. They found a value for the ratio $\Delta E_C/\Delta E_g$ of 0.40. The experimental data of Kazuhisa *et. al.* indicated that $\Delta E_C/\Delta E_g$ was between 0.28 and 0.42 depending on the value of the effective mass assumed when fitting to the empirical data. Given the considerable disagreement in the values for the band offsets that appear in the literature, the offsets assumed for the purposes of calculations for this thesis were the most commonly quoted values of $\Delta E_C \approx 0.4\Delta E_g$ and $\Delta E_V \approx 0.6\Delta E_g$ [Adachi, 1992].

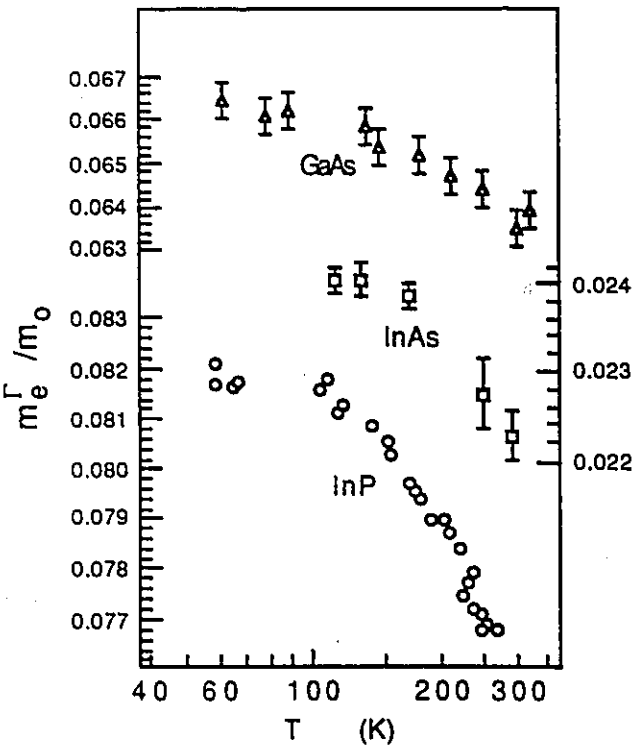

Figure 4.6: The empirically determined temperature variation of the Γ-band electron effective mass m_e^Γ/m_o for InP, InAs, and GaAs. [From Adachi, 1992].

Finally, it should be noted that the band offsets given above are for unstrained heterojunctions. The band offset for the strained-layer heterojunctions are calculated by keeping the absolute values of the valence and conduction band energies of the barrier

layers fixed. The strain induced changes in the band structure of the quantum well layers are then calculated relative to the valence band position of the barrier layer.

4.1.4 Determination of the Strained and Unstrained Quantum Well Band Edge Band Structure and Emission Wavelength.

Having determined the well and barrier material parameters from the composition x and y of the respective layers using an appropriate interpolation scheme, the strain induced shifts and splittings of the conduction and valence bands and, therefore, the quantum well band structure of the active region of the laser can be calculated. From this band structure one can in turn determine the band edge energy solutions for electrons and holes within the quantum wells and therefore the emission wavelength of the laser.

The energy band structure of the active region of the laser is calculated as follows. A reference energy band structure is initially determined from the bulk-barrier and quantum well energy band-gaps using the energy band offsets specified in §4.1.3. All energies, such as the quantum well conduction and valence band edges and the quantized energy levels, are specified with respect to the bulk valence band edge of the barrier region which is given a reference energy of zero electron volts. The hydrostatic shift in the valence band energy is then determined from the change in the ionization potential due to strain using (2.3.28). The position of the QW valence band edge, E_{v_1,v_2}, in the energy reference frame chosen, after considering the effects of the hydrostatic component of the biaxial strain, is given by:

$$E_{v_1,v_2} = \Delta E_v + \delta\Gamma_8. \tag{4.1.9}$$

The total hydrostatic shift of the energy band-gap, δE_H, due to strain is then determined using (2.3.26). The value of $\delta E_H + E_{go}$ when added to the position of the valence band as given by (4.1.9) then gives the position of the strained QW conduction band. The

splittings of the light (v_1) and heavy hole (v_2) bands due to the uniaxial component of the strain are then calculated from (2.3.22d) or (2.3.23d) such that the light and heavy hole band-gaps (E_c-E_{v1}) and (E_c-E_{v2}) are given by (2.3.25a) and (2.3.25b), respectively. The conduction and valence band offsets for the strained heterojunctions are subsequently determined from the calculated quantum well band positions relative to the well and barrier layer conduction and valence bands energies which remain unaffected by the strain.

Once the positions of the "bulk" conduction and valence bands in the quantum well region due to strain have been calculated relative to the unstrained "bulk" degenerate valence bands of the barrier region, the strained quantum well band-edge band structure as a function of position along the growth direction in the active region of the laser is known. From this band structure, the quantized energy levels for the electrons and the light and heavy holes are determined by finding the roots of the dispersion relation (2.1.18). The emission wavelength for the laser is then determined from the energy separation between the lowest lying (C_1) quantized energy level for the electrons and the highest lying quantized energy level for holes (HH_1 or LH_1). If the emission wavelength as calculated from this energy separation is not in agreement with the desired emission wavelength, then the dimensions of the quantum well (i.e., the quantum well width or depth) are adjusted iteratively until such an agreement is reached. During this procedure, the strained layer critical thickness is evaluated to ensure that the quantum well width of the final design is thin enough to avoid strain relaxation and the formation of misfit dislocations.

The outputs of the program used to determine the energy band structure and the quantized energy level positions for each of the laser structures examined in this thesis are shown in Appendix A. Figure 4.7 shows the calculated quantum well energy band

structure for three lasers belonging to Set 1. These lasers have a nominal quantum well thickness of 55Å and nominal quantum well strains of 1.2% in tension, unstrained and 1.2% in compression, respectively. From the diagram it is seen that, even though the emission wavelength is the same in all three cases, in the case of tensile strain, the lowest lying interband's, and therefore the dominant transition, is to the light hole (LH) valence band. Consequently, from the discussion of §2.2.2, this laser should emit predominantly TM polarized radiation. By contrast, the unstrained and compressively strained lasers should emit TE polarized radiation, since the dominant transition in these lasers is to the heavy hole band. This situation is particularly true for the compressively strained laser due to the large separation between the first quantized heavy hole subband and the first quantized light hole subband.

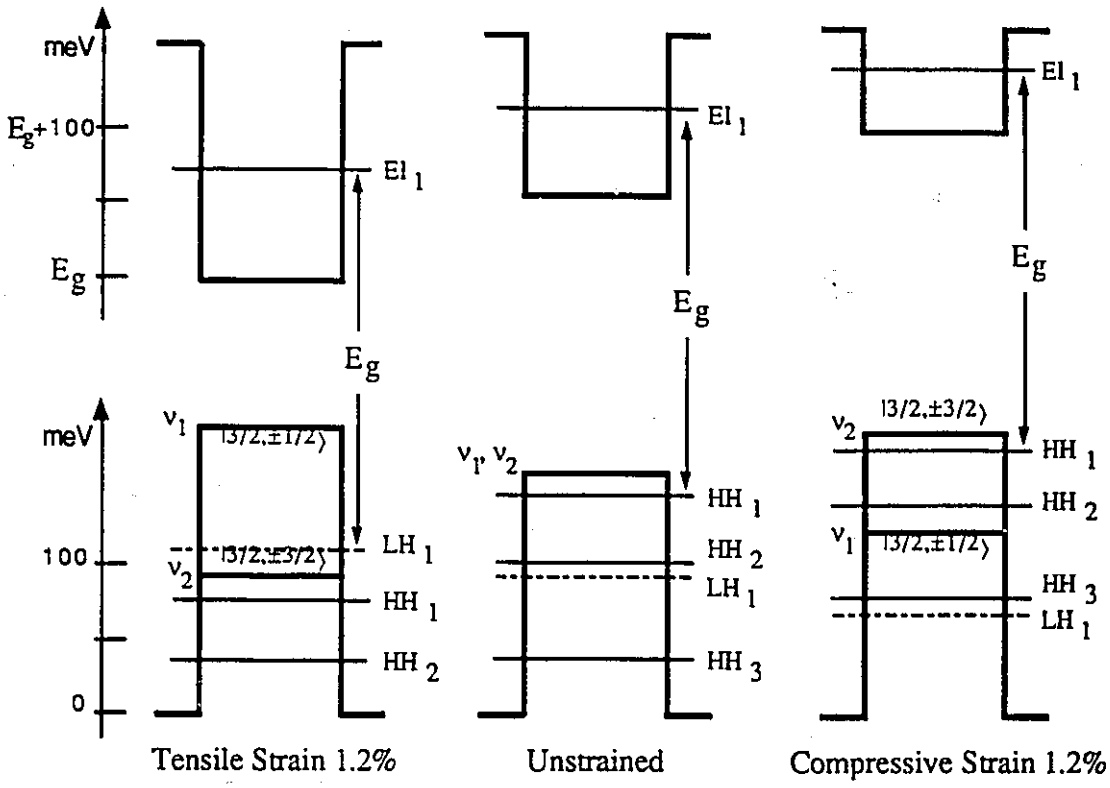

Figure 4.7: Calculated quantum well energy band structure for three lasers belonging to Set 1. Each structure has nominally 55Å thick QWs and a calculated emission wavelength of ≈1.3μm.

From Fig. 4.7 it can also be observed that, according to the model used and the assumptions made in making the calculations, strain alters the magnitude of the conduction and valence band offsets in the quantum well, such that the quantum well depths depend on the magnitude and the type of strain. In the case of tensile strain, the conduction and valence band offsets increase whereas in the case of compressive strain the offsets decrease. The strain-induced changes in the QW depth affect the energy separation between the quantized energy levels and the barrier band edge. In turn, this energy separation may have significant implications regarding the collection efficiency and the leakage rates of carriers from the quantum wells. These additional factors in turn affect laser performance, as was discussed in §3.6. Therefore, the effects of strain on the energy separation between the barrier band edge and the quantized energy levels must be kept in mind. As a final note, Takasaki et al. [1992, 1993] have empirically determined the magnitude of this energy separation for the structures belonging to Set 1 by measuring the electron and hole escape efficiencies from the QWs as a function of temperature. Their experimental results were found to be in reasonable agreement with the calculated values indicated in Appendix A.

4.2 DESIGN ALGORITHM: Stage 2

In the second stage of the laser design algorithm, the peak gain *vs.* injected carrier concentration relation is evaluated for a quantum well structure having the same dimensions and strain specified in Stage 1. Next, the optical confinement factor for the laser structure is calculated as a function of the number of quantum wells in the active region. Next the amount of gain required to reach the lasing condition is determined from (2.2.31), then, the injected carrier concentration required to produce this level of gain is found from the peak gain *vs.* carrier concentration curve. The threshold current

density as a function of the number of quantum wells in the active region is then approximately determined from (2.2.32). It should be noted that the magnitude of the threshold current density as evaluated in the manner described above is not expected, or even presumed, to produce an accurate value of the threshold current, due to the uncertainties in many of the parameters involved in the calculations. Many of these uncertainties have already been mentioned; however, other uncertainties arise, for example, in estimating τ_{th} in (2.2.32) and α_{ex} and α_{int} in (2.2.31). In addition, the above calculation assumes: one hundred percent collection efficiency of carriers by the quantum wells; that the optical confinement factor in the lateral direction is nearly unity; and ignores leakage currents which may be on the order of 7-35% of the total threshold current density for lasers fabricated from InP-based materials [Chik, 1990]. Nevertheless, the dependence of the threshold current density *vs.* the number of quantum wells in the laser active region should be described with reasonable accuracy by the above calculation; consequently, the purpose of making these calculations stems solely from a desire to optimize the laser structure for the number of quantum wells be to included in the active region.

4.2.1 Determination of the Peak Gain *vs.* Carrier Concentration Profile

The peak gain *vs.* carrier concentration profile is determined as follows. Firstly, the carrier concentration, N, injected into the quantum well is specified, then, making use of the charge neutrality condition, (2.2.26), (2.2.27) and (2.2.28) are solved numerically to obtain the position of the quasi-Fermi levels E_{fc} and E_{fv}. Next, the wavelength corresponding to the lowest energy interband transition is determined, and (2.2.23) is numerically integrated such that $g(\omega)$ is evaluated for wavelengths ranging from 50nm below the dominant transition wavelength to 50nm above it in steps of 1nm. The

intraband relaxation time, τ_{in}, used in evaluating (2.2.23) was chosen to be 0.1ps following Asada [1984], and the effective index, n_r, was evaluated as will be described in §4.2.2. The upper integration limit was chosen to be 30eV, as it was found that the

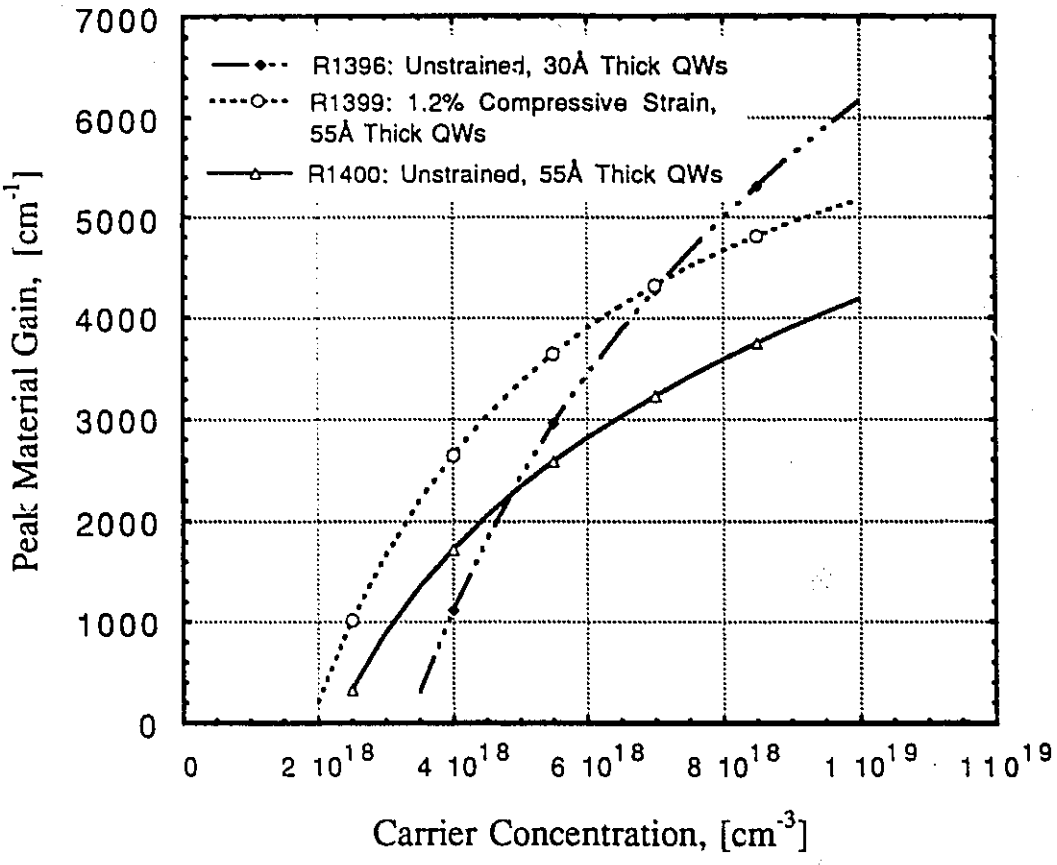

Figure 4.8: Peak material gain *vs.* carrier concentration for the 1.2% compressively strained, and the unstrained quantum well laser having 55Å thick quantum wells, and also for the unstrained quantum well lasers having 30Å thick quantum wells. All structures are calculated to have an emission wavelength near 1.3μm. The barrier layer band gap in all cases is 1.15eV.

results of the numerical integration of (2.2.23) changed by less than 1% for upper integration limit energies beyond this value. The maximum gain obtained for any wavelength in the chosen range was then stored in a file along with the corresponding

carrier concentration N. The carrier concentration was then incremented and the procedure repeated. The upper limit for the injected carrier concentration was chosen to be $1x10^{19}$ [cm^{-3}]. Examples of the calculated peak material gain *vs.* carrier concentration relation for the 1.2% compressively strained and the unstrained quantum well structures from Set 1, and the unstrained quantum well structure from Set 2, appear in Fig. 4.8.

4.2.2. Determination of the Optical Confinement Factor, Γ

The optical confinement factor for the laser structures examined in this thesis is calculated using the transfer matrix approach as outlined by Yamada [1986] and similarly, although slightly differently, by Walpita [1985]. In this approach, the optical propagation properties of a planar waveguide with a multilayer index profile are analyzed by considering the transfer matrix formed by matching the boundary conditions at each interface of the transmitted and reflected electric and magnetic fields in the multilayers. By making use of the boundary condition that the optical field must converge smoothly in substrate and superstrate cladding (InP) layers as they extend out to large distances, a characteristic equation for the waveguide may be derived and subsequently solved numerically for the propagation wave number, β, of the guided wave modes. Once β has been determined, the normalized distribution function F(y) of the optical wave, which is given as a solution to Maxwell's wave equation:

$$\left[\frac{\partial^2}{\partial y^2} - \beta^2 + n_i^2 \mu_o \varepsilon_o \omega^2\right] F(y) = 0, \qquad (4.2.1)$$

where, n_i, is the refractive index of the *i*-th region of the waveguide, may be evaluated. The optical confinement factor for the laser structure is then given by the relation:

$$\Gamma = \frac{\sum_{n_w - L_z/2}^{L_z/2} \int |F(y)|^2 \, dy}{\int_{-\infty}^{\infty} |F(y)|^2 \, dy}. \tag{4.2.2}$$

The matrix equation which one obtains from Maxwell's equation by matching the electric and magnetic fields at i-th interface of the multilayer waveguide, is:

$$\begin{bmatrix} F(y_i) \\ \dfrac{\partial F(y_i)}{\partial y} \end{bmatrix} = \begin{bmatrix} T_i(y) \end{bmatrix} \begin{bmatrix} F(y_{i-1}) \\ \dfrac{\partial F(y_{i-1})}{\partial y} \end{bmatrix}, \tag{4.2.3}$$

where, $$[T_i(y)] = \begin{bmatrix} \cos[\gamma_i(y - y_{i-1})] & (1/\gamma_i)\sin[\gamma_i(y - y_{i-1})] \\ -\gamma_i \sin[\gamma_i(y - y_{i-1})] & \cos[\gamma_i(y - y_{i-1})] \end{bmatrix}, \tag{4.2.4}$$

and where, $$\gamma_i = \sqrt{n_i^2 \mu_o \varepsilon_o \omega^2 - \beta^2}. \tag{4.2.5}$$

The characteristic equation for the waveguide which one must solve in order to obtain the propagation constant β of the guided optical mode is given by [Yamada, 1986]:

$$[|\gamma_{N+1}|, 1][T_N(y_N)][T_{N-1}(y_{N-1})] \cdots [T_{-N}(y_{-N})] \begin{bmatrix} 1 \\ |\gamma_{-N-1}| \end{bmatrix} = 0. \tag{4.2.6}$$

In order to solve (4.2.6) one requires both a knowledge of the index of refraction of the various material layers and an initial guess for the magnitude of the propagation wavenumber, β. It has been determined that the refractive index of lattice-matched $In_{1-x}Ga_xAs_yP_{1-y}$ material at the photon energy E(=hν) can be approximated by the relation [Suematsu, 1982]:

where, $$n^2 = 1 + \frac{E_d}{E_o} + \frac{E_d}{E_o^3} E^2 + \frac{\eta}{\pi} E^4 \ln\left(\frac{2E_o^2 - E_g^2 - E^2}{E_g^2 - E^2} \right), \tag{4.2.7}$$

and $$\eta = \frac{\pi E_d}{2E_o^3\left(E_o^2 - E_g^2\right)}, \tag{4.2.8}$$

$$E_o = 3.391 - 1.652y + 0.863y^2 - 0.123y^3, \tag{4.2.9a}$$

$$E_d = 28.91 - 9.278y + 5.626y^2, \tag{4.2.9b}$$

$$E_g = 1.35 - 0.72y + 0.12y^2. \tag{4..2.9c}$$

Equation (4.2.7) was used to determine the refractive indices of the lattice-matched quaternary graded-index separate confinement (GRINSCH) layers of the devices studied in this thesis. The refractive indices used for the InP cladding layers was that indicated in Table 4.2. The refractive indices for the quantum well layers in the strained devices was determined from a linear interpolation between those values for the refractive indices of the binary compounds. These values are given in Table 4.2.

The initial guess on the propagation constant, β, which was used as a starting point to solve (4.2.6), was found by solving the symmetric three layer slab waveguide problem as described in Agrawal [1986]. The index of the "active", middle layer was approximated by the weighted indices of all layers according to the relation: $n_{eff}=\Sigma n_i t_i/\Sigma t_i$, where t_i is the thickness of the *i*-th layer. The results of the optical confinement calculations for the unstrained MQW laser structures of Set 1 and Set 2, as a function of the number of quantum wells incorporated into the active region, are shown in Fig. 4.9.

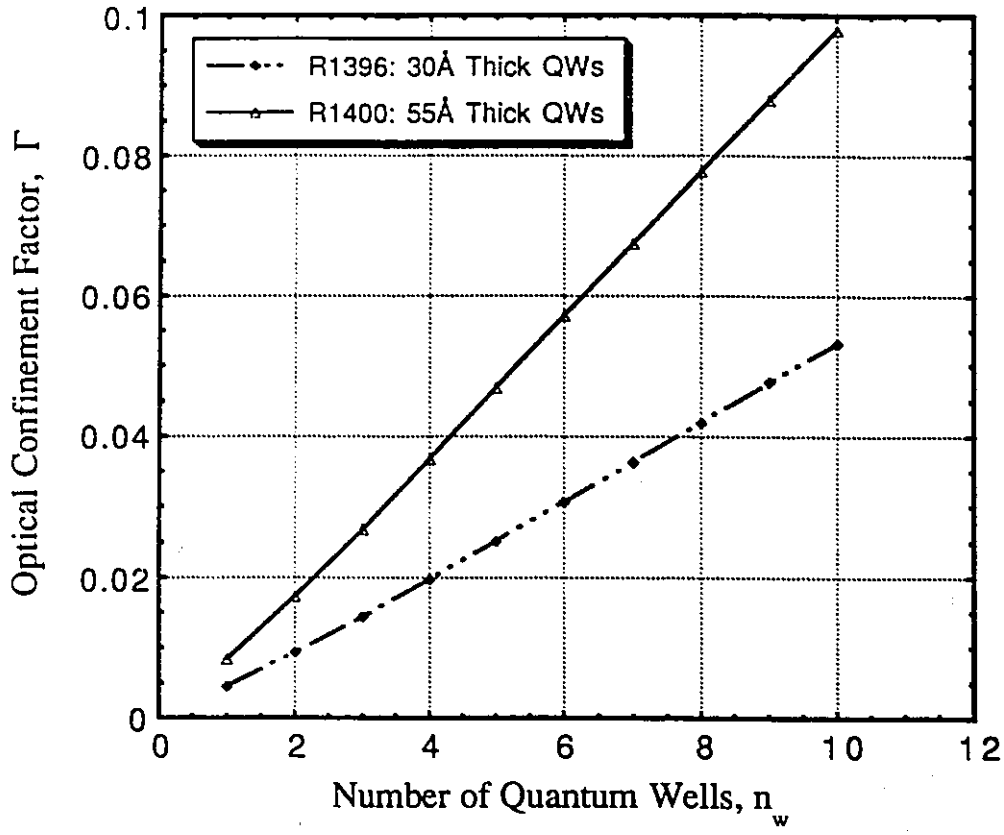

Figure 4.9: Results of optical confinement calculations *vs.* the number of quantum wells in the laser active region for unstrained quantum well lasers having quantum well thicknesses of 55Å and 30Å and graded index separate confinement structures as shown in Fig. 4.1 and Fig. 4.2 respectively.

4.2.3. Determination of the Laser Threshold Current Density

With the optical confinement data of Fig. 4.9, the laser threshold current density *vs.* the number of quantum wells in the laser active region may be determined from (2.2.31) and Fig. 4.8 along with (2.2.32), which may also be written in the form [Agrawal, 1986]:

$$J_{th} = qn_w L_z \left(AN_{th} + BN_{th}^2 + CN_{th}^3 \right) + J_L, \tag{4.2.10}$$

where A is the nonradiative recombination coefficient describing the non-radiative recombination rate of carriers due to traps and surface states etc., B is the bimolecular

radiative coefficient describing the spontaneous radiative recombination rate of carriers, and C is the Auger coefficient which characterizes the rate at which carriers recombine through non-radiative Auger processes [Olshansky, 1984]. In relating (4.2.10) to (2.2.32) the carrier lifetime, τ_{th}, is given by the relation:

$$\tau_{th}(N_{th}) = \left(A + BN_{th} + CN_{th}^2\right)^{-1}. \tag{4.2.11}$$

It should also be noted that, unlike in (2.2.32), in (4.2.10) the contribution due to leakage currents over the InP hetero-barrier, J_L, has been included.

As an example calculation, consider device structure number R1396, which has a calculated optical confinement factor of Γ=0.025. From (2.2.31), assuming α_{int} =150 cm^{-1}, α_{ext}=20 cm^{-1} [Mozer, 1985], L=500μm and R=0.28, the threshold gain, g_{th}, is 1936 cm^{-1}. From Fig. 4.8, the carrier density required to achieve this level of gain is about $4.65x10^{18}$ cm^{-3}. Using the following values for the recombination coefficients, A=$1.1x10^{8}$ s^{-1}, B=$8.6x10^{-11}$ cm^3s^{-1} and C=$4x10^{-29}$ cm^6s^{-1} [Streifer, 1979], [Agrawal, 1986], [Chik, 1990] the threshold current density from (4.2.10) is then about 1536 A/cm^2. The corresponding threshold current for the ridge waveguide structures (ridge width 2μm) studied in this thesis, assuming negligible lateral current spreading, is ≈15mA. With a 15% leakage current at room temperature, this value increases to about 17mA. The actual measured room temperature threshold current for this laser was slightly greater than this at about 22mA.

The calculated threshold current *vs.* the number of quantum wells for unstrained structures similar to those of growth numbers R1400 and R1396 is shown in Fig. 4.10. The details of these structures are described in Table 4.1 and Figs 4.1 and 4.2, where it is indicated that they have nominal quantum well widths of 55Å and 30Å, respectively. The calculations shown in Fig. 4.10 are for 500μm length laser cavities.

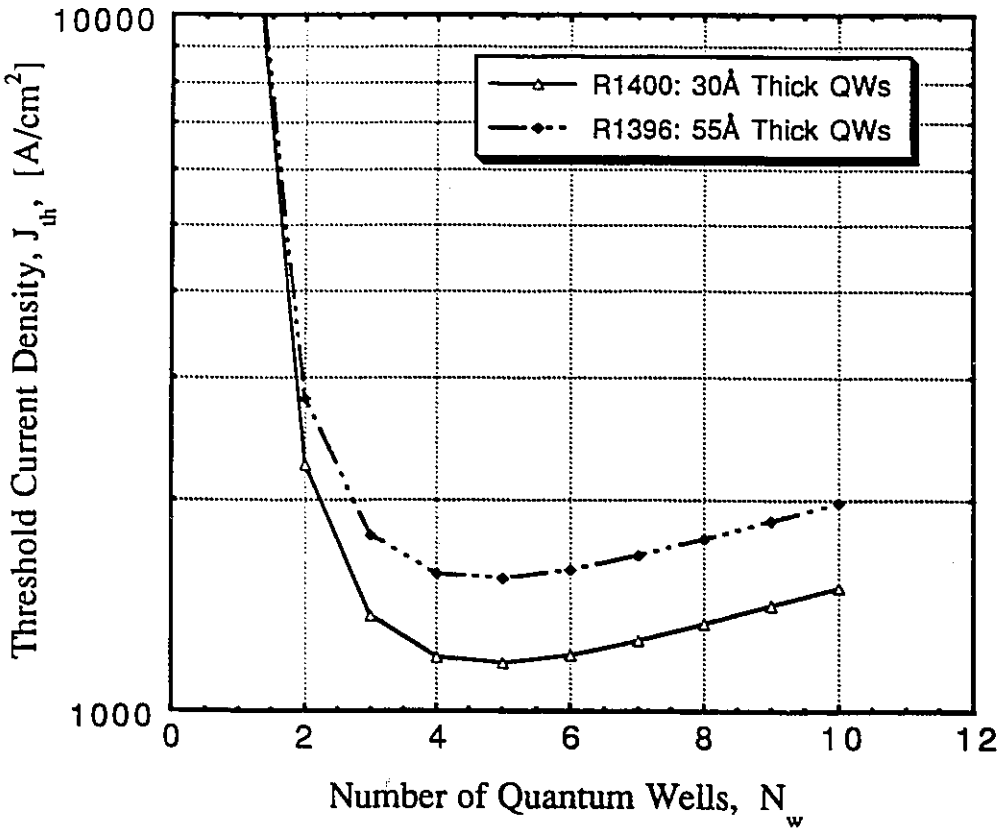

Figure 4.10: Calculated threshold current density *vs.* number of quantum wells in the active region for laser structures R1400 and R1396 and a cavity length of 500μm. The quantum well thicknesses in these structures are 55Å and 30Å respectively.

From Fig. 4.10, it can be seen that for the unstrained laser structures R1400 and R1396, the optimum number of quantum wells for a cavity length of 500μm, is five. However, laser structures R1400 having 55Å thick quantum wells were designed to have only three quantum wells in the active region. This was because of concerns about exceeding the single layer critical thickness limit in the tensile strained structures, in combination with a desire to ensure that all laser structures belonging to a given Set had similar geometries. A quantum well width of at least 55Å was necessary in the tensile strained structures in order to ensure that quantum size effects did not result in these lasers having an emission wavelength of less than 1.3μm. Those laser structures

belonging to Set 1 and having 30Å thick quantum wells, as dictated by Fig. 4.10, were designed to have five quantum wells in the active region in order to minimize the threshold current density.

Finally, the choice of the GRINSCH section of the lasers studied in this thesis was based upon an examination of laser structures reported in the literature and by correlating the geometry of these structures to laser performance. Therefore, the design of the GRINSCH structure was largely based on intuition. A band gap energy for the barrier region of the quantum wells was decided upon along with the number of graded index steps desired. The width of the step index regions was chosen to be 700Å based on structures in the literature. The band gap energy of the middle index step region was chosen to be be midway between the band gap energy of InP and the band gap energy of the barrier layer.

4.3 SUMMARY

In this chapter the method of designing the quantum well and strained quantum well laser structures for the purposes of conducting empirical work related to this thesis was discussed. The algorithm used to design the quantum well laser structures was presented in two stages. The first stage of the design algorithm involved a determination of the material compositions, strain, and quantum well dimension required to produce the desired emission wavelength for the lasers. The second stage of the design algorithm involved a determination of the optical confinement factor, Γ, for the QW laser structures as a function of the number of quantum wells in the active region of the devices. From information about the variation of Γ with the number of quantum wells, the threshold gain condition from (2.2.31), and therefore the threshold current from (2.2.32) was also determined as a function of the number of quantum wells in the laser active region. The

value for the carrier lifetime, τ_{th}, assumed in (2.2.32) was computed using values for the relevant recombination parameters found in the literature. From the above procedure then, the number of quantum wells to include in the laser active region which would result in the minimum threshold carrier density was found. The optimum number of quantum wells for a 500 μm cavity length laser, from Fig. 4.10, was found to be five. Accordingly, lasers from Set 2 have five quantum wells in the active region. However, due to a desire to ensure that the total quantum well thickness in the tensile-strained QW structures was less than the critical layer thickness, and since the quantum wells for this structure had to be at least 55 Å thick in order to obtain the desired emission wavelength, only three QWs were used in the active region for the tensile-strained lasers structures from Set 1. Since it was desirable that all laser structures belonging to a given Set had an identical number of QWs, all laser structures from Set 1 had three QWs in the active region.

In addition, within this chapter, the method for determining the various material parameters required to compute the strain and quantum sized effects in the QW structures was discussed. The uniqueness of the study of the effects of strain on laser performance presented in this thesis was also mentioned. The study within is unique in comparison to other studies of the effects of strain on laser performance in that a comparison of the effects of strain on laser performance has been conducted using quantum well laser structures in which the quantum well thickness is the same for the first time. Identical quantum well thickness were used to more effectively isolate the effects of strain on laser performance from those effects caused by a varying density of states between structures having different QW thicknesses.

CHAPTER 5: MATERIALS AND WAFER CHARACTERIZATION

5.0 INTRODUCTION

Before considering the effects of strain on the operating characteristics of processed lasers, it is vital to ensure that any differences in the observed operating characteristics can be attributed to the effects of strain, and not to differences in material quality or process variations. Therefore, prior to the processing, cleaving, bonding and testing of the laser structures designed for this thesis, the crystal quality of all laser structures was thoroughly checked using analytical tools such as, transmission electron micrography, polarization-resolved photoluminescence, scanning photoluminescence and temperature and power dependent photoluminescence. This chapter presents the findings from such examinations. These findings show that the crystal quality of all laser structures grown and tested is excellent. This excellent crystal quality ensures that any observed differences in the laser operating characteristics, for example, a poor internal quantum efficiency and high threshold current for one laser structure and not another, are **not** due to factors, such as, strain induced defects in the laser active region, but are likely due to the effects of strain on the band structure. Before presenting the findings of the analysis of the crystal quality, the laser growth sequence and doping profile are reviewed.

5.1 MATERIALS GROWTH

The laser structures studied in this thesis have been previously described in Chapter 4, Table 4.1 and are represented schematically in Fig. 4.1 and Fig. 4.2. The structures were grown by low-pressure (75 Torr) metalorganic vapor phase epitaxy (LP-MOVPE) on

(100) S-doped n-type InP substrates. The growths were carried out by N. Puetz at Bell-Northern Research (BNR) in Nepean, Ontario, and represent the first realization of high quality all-quaternary laser structures. The growth temperature in all cases was 630°C. The gas sources used were triethlygallium, trimethylindium, PH_3, and AsH_3, with dimethlyzinc and 100 ppm disilane (Si_2H_6) in H_2 being used as *p*- and *n*-type dopants, respectively. The gas flow ratios were adjusted to provide different compositions, x and y, for the $In_{1-x}Ga_xAs_yP_{1-y}$, strained and unstrained quantum well regions of the devices.

The step index, cladding region and the intended doping profile for all structures were identical. The growth sequence proceeded as follows. Firstly, a lower cladding and buffer layer was grown. This layer consisted of a 1.5-μm thickness of n-InP Si-doped to $2x10^{18}$ cm^{-3}. The lower cladding layer was followed by a nominally undoped step index waveguide and active region having dimensions as indicated in Figs 4.1 and 4.2. Next, an undoped, 30Å thick, lattice matched quaternary (λ=1.3μm) etch stop layer was grown in order to ensure reproducibility in the processing of the different wafers. This layer was followed by the upper cladding region which consisted of a 0.2μm thick, Zn-doped (to $4x10^{17}$ cm^{-3}) InP setback layer (designed to minimize the amount of Zn indiffusion into the waveguide layers), followed by a further 1.3μm thickness of p-InP Zn-doped to about $1x10^{18}$ cm^{-3}. The structure was completed with a 0.2μm thick contact layer consisting of p-InGaAs lattice-matched to InP and doped with Zn to a desired doping concentration of $1x10^{19}$ cm^{-3}.

An error occurred in the growth of sample numbers R1-394, R1-395 and R1-396 in that these samples were originally grown with the InGaAs contact layer undoped.* It was

* A regrowth of sample R1-394 without this error was performed. This regrown sample was given the identification number R1-408. Structure R1-408 was identical to sample R1-394 in design save the etch stop layer was separated from the step index region in this sample by 0.12μm of Zn doped InP. When wafer R1-408 was processed into ridge waveguide lasers and tested along with wafer R1-394, it was found that lasers from these two wafers had essentially identical characteristics. The similarity in the operating characteristics between lasers fabricated from wafer R1-394 and wafer R1-408 is an indication of the reproducibility, not only in the growth, but also in the processing of lasers from one wafer to another.

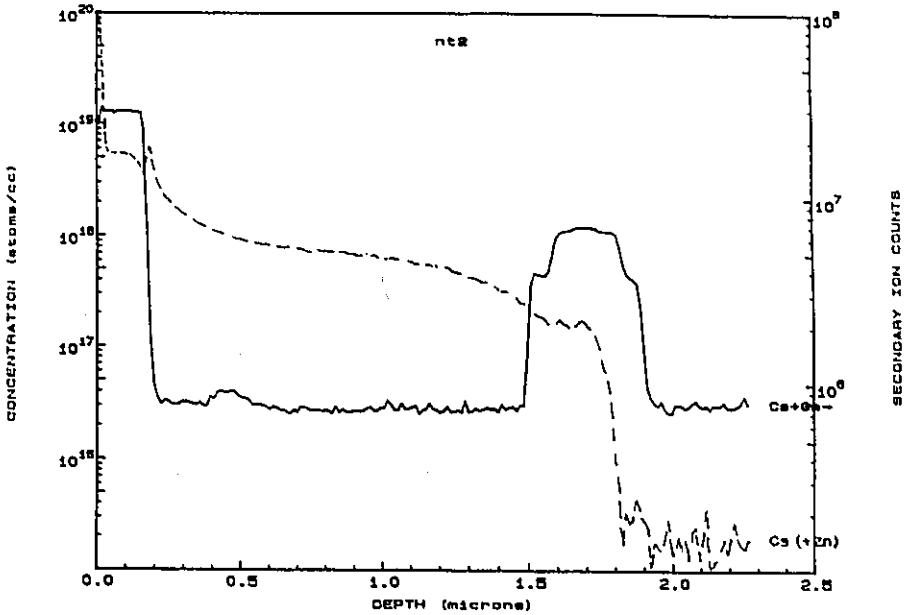

Figure 5.1(a): Secondary Ion Mass Spectrographic (SIMS) profile showing the Zn concentration as a function of depth (dotted line) for sample R1-394. The solid line represents the Ga^+ secondary ion count as a function of depth in the sample. Clearly visible from this profile are the increased Ga concentrations due to the 0.2μm thick InGaAs contact layer and the InGaAsP graded index step and barrier regions of the device structure.

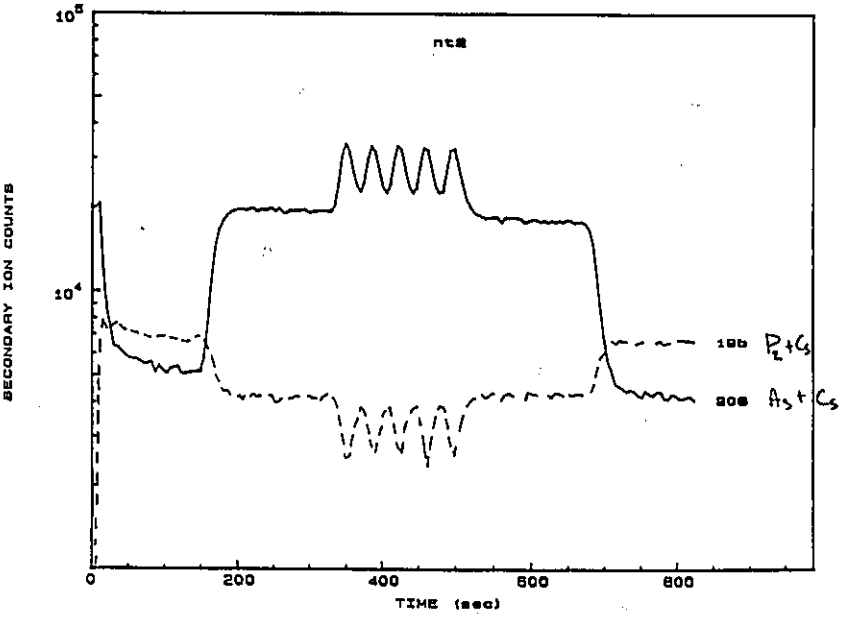

Figure 5.1(b): SIMS profile of the graded index step and MQW active region of laser structure R1-394. Shown are the P_2 and As secondary ion counts as a function of the sputtering time. The variation in the As and P counts due to the different compositions of the quaternary quantum well, barrier guiding layer and step index regions are clearly visible.

therefore necessary that these wafers undergo a Zn diffusion process in order to dope the InGaAs contact layer prior to device fabrication. To ensure that the doping in the InGaAs contact layer was sufficient to form a decent ohmic contact, and also to measure the extent to which the Zn diffusion process caused an indiffusion of Zn into the laser active region, a secondary ion mass spectrographic (SIMS) depth profile was taken of sample number R1-394. The results of this SIMS profile are shown in Fig. 5.1(a) and 5.1(b). Figure 5.1(a) shows the Zn concentration and Ga^- secondary ion counts in the sample as a function of depth from the top of the InGaAs contact layer. Figure 5.1(b) shows the P_2 and As secondary ion counts as a function of the sputtering time beginning at the top of the quaternary etch stop layer. In Fig. 5.1(b) the five 30 Å thick quantum wells in the laser active region of sample R1-394 are clearly visible as indicated by the variation in the As and P_2 counts due to the different composition of the well layers in comparison to the barrier and waveguide layers.

5.2 TRANSMISSION ELECTRON MICROGRAPHY

In order to verify well thicknesses and to ensure that the laser structures were of good crystal quality and free from defects due to possible strain relaxation, transmission electron micrographs (TEM) were taken of each sample. The samples were prepared for TEM by C. Tan at BNR. First, however, the p-InGaAs contact and p-InP cladding layers were etched off down to the etch stop layer. Cross-sectional TEM pictures of the InGaAsP step index guiding and quantum well active region of each of the samples (save sample R1-395 which was not fully tested for this thesis) appear in Figs. 5.2-5.7. Measurements from the TEM images revealed that the well widths in samples R1-398, R1-399, and R1-397 are actually 64±3Å thick instead of the specified 55Å. In sample R1-400, two of

the quantum wells were measured to have a thickness of 61±3Å, while the quantum well closest to the etch stop layer was slightly thicker with a width of 67±3Å. The measured quantum well thicknesses in samples R1-394, R1-395, and R1-396 where 38±4Å instead of the specified 30Å.

From the micrographs of Fig. 5.2-5.7., it is evident that the layer thicknesses in all samples are quite uniform and that the interfaces between the various quaternary compositions are sharp and free from visible defects. No defects due to strain relaxation were expected in the samples since the sum of the strained-layer quantum well thickness was kept below the single strained-layer critical thickness as given by (2.3.4). A plan view TEM, and a cross-sectional lattice image of sample R1-394 were taken by J. McCaffrey at the National Research Council of Canada. No defects were visible in the cross-sectional lattice image, and the plan view image showed the crystal quality to be excellent with the defect count on the order of 10^4 cm^{-2}. In addition, polarization-resolved photoluminescence scans were performed over 100µm x 100µm cross-sectional areas on sample numbers R1-397 through to R1-400 by Jian Yang in the department of Engineering Physics at McMaster University. This measurement technique has been shown to be an excellent and very sensitive means of detecting defects and dislocations in luminescent semiconductor crystals [Colbourne, 1992]. None of the polarization-resolved photoluminescence scans revealed the presence of defects. Therefore, it is concluded that all samples were of excellent crystal quality with a dislocation and defect density less than $\approx 10^4$ cm^{-2}.

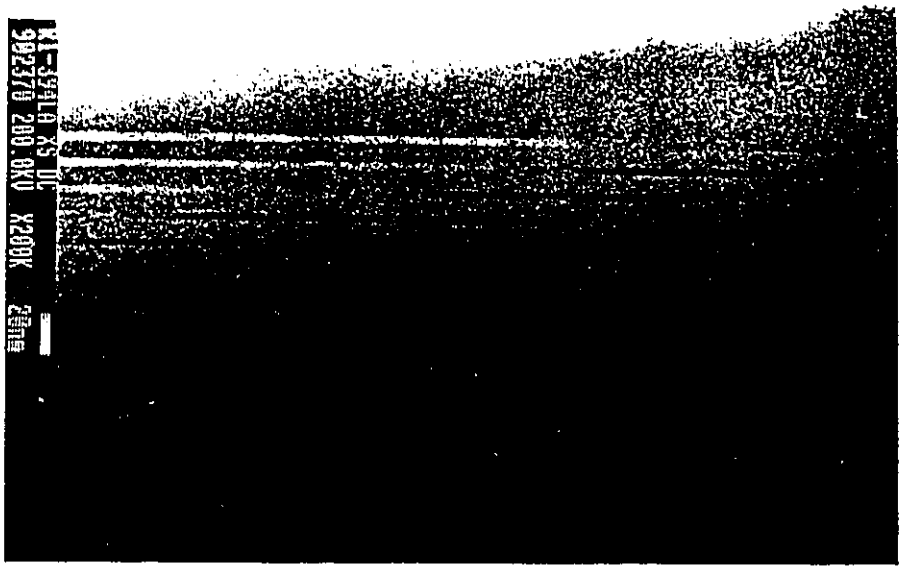

Figure 5.2: TEM photograph of sample number R1-394 (1.5% compressive strain). Measured quantum well thickness are 38±4 Å.

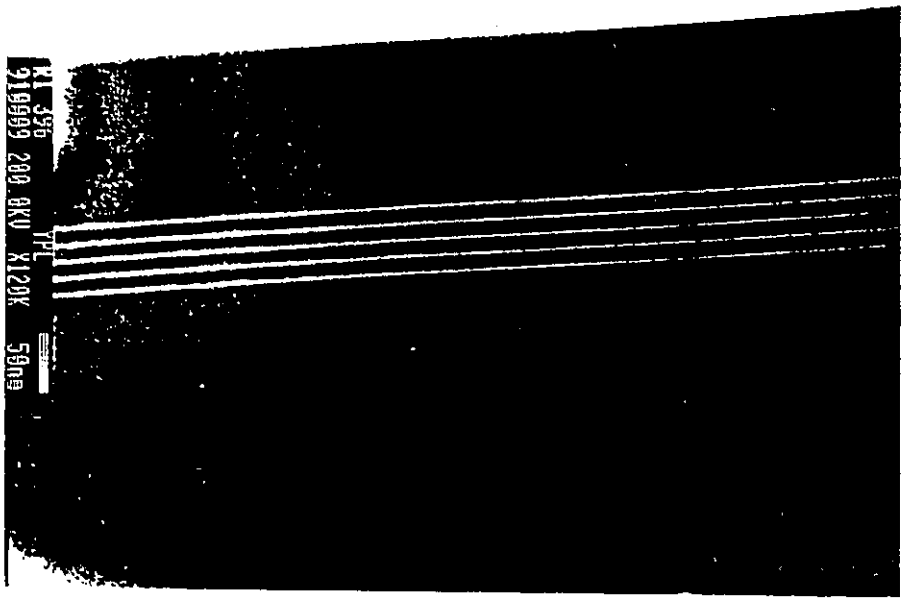

Figure 5.3: TEM photograph of sample number R1-396 (unstrained). Measured quantum well thickness are 38±4 Å.

Figure 5.4: TEM photograph of sample number R1-397 (1.2% tensile strain). Measured quantum well thickness are 64±3 Å.

Figure 5.5: TEM photograph of sample number R1-398 (1.3% tensile strain). Measured quantum well thickness are 64±3 Å.

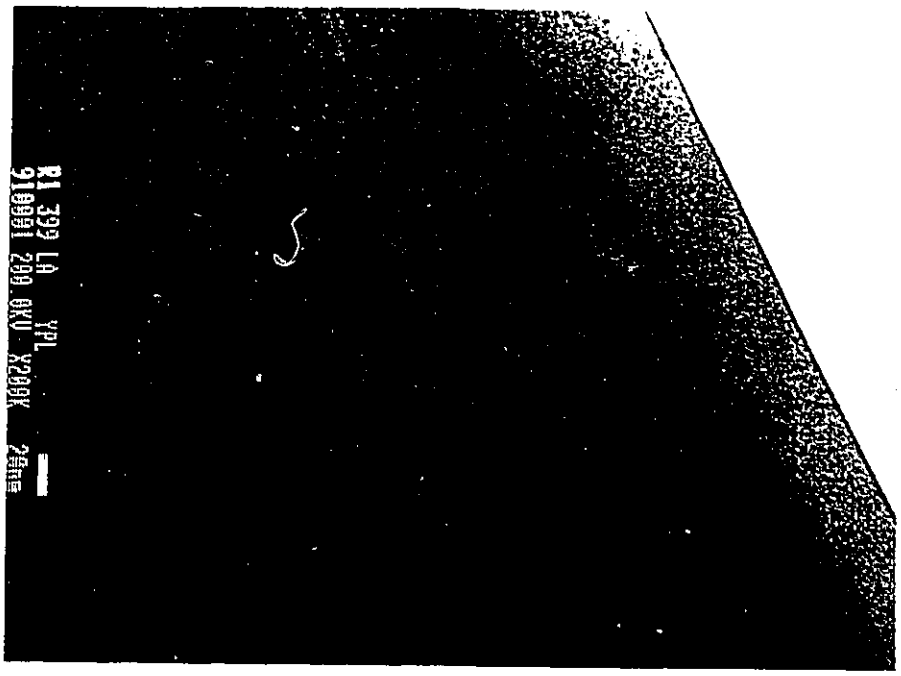

Figure 5.6: TEM photograph of sample number R1-399 (1.2% compressive strain). Measured quantum well thickness are 64±3 Å.

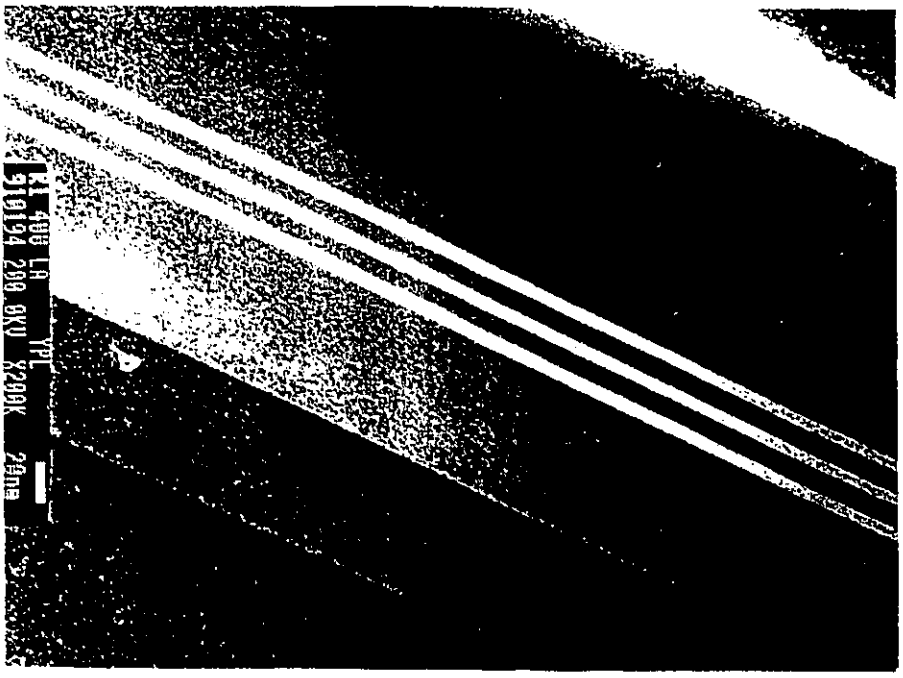

Figure 5.7: TEM photograph of sample number R1-400 (unstrained). Measured quantum well thickness are 61±3 Å for the two quantum wells closest to the substrate and 67±3 Å for the quantum well closest to the etch stop layer.

5.3 PHOTOLUMINESCENCE MEASUREMENTS

In order to check the uniformity of the quantum well layers, and the crystal quality across the wafers, a quarter of each two-inch wafer was prepared for photoluminescence (PL) and scanning photoluminescence measurements. The wafer preparation consisted of the following steps. Firstly the SiO_2 layer deposited and patterned over the entire wafer surface prior to sectioning the wafers into quarter wafer pieces had to be removed* using a 10:1 solution of Buffered:HF. Next, the InGaAs contact layer was removed using a one-minute etch in a solution of 1:5:50 H_2SO_4:H_2O_2:H_2O. The InP cladding layer was then etched off down to the etch stop layer using a solution of 2:3 HCl:H_3PO_4. This etch takes about 60 seconds and is finished when bubbling in the solution ceases. Finally, the etch stop layer was removed using a 5-second etch in 1:5:50 H_2SO_4:H_2O_2:H_2O. The motivation for etching off these top layers of the laser structure was firstly to prevent absorption of the PL and pump signal in the contact and etch stop layers, and secondly to reduce the built-in field across the quantum wells in order to limit the escape of carriers from the wells due to drift and tunneling processes [Takasaki, 1993].

5.3.1 Scanning Photoluminescence

The results of both spectrally and spatially resolved photoluminescence scans of the quarter-wafer pieces from all the grown laser structures appear in Figs. 5.8 - 5.14. Shown in these figures are wafer maps of the variation in the peak PL wavelength in nm, the variation in the full width half maximum (FWHM) of the PL signal in meV, and variations in the peak PL intensity in arbitrary calibrated units. These spectrally and spatially resolved

* The SiO_2 was originally deposited and patterned over the entire wafer surface in order to maintain the benefits of an increased processing accuracy which are achieved by patterning whole wafers instead of quarter wafer pieces.

PL scans were obtained using a Waterloo Scientific Scanning PL system at room temperature. The optical pump source was a HeNe laser emitting at 632.8 nm, and the photoluminescence signal was detected using an InGaAs detector. A summary of the data obtained from the room temperature PL measurements, including the peak emission wavelength, FWHM, and peak signal intensity is shown in Table 5.1†.

In interpreting data from Figs 5.8-5.13 it should be realized that a map of the peak PL wavelength variation across the wafer gives an indication of the uniformity of the emitting layers. An indication of the layer uniformity is given, since due to quantum size effects (2.1.8), the peak PL wavelength will be blue-shifted where the quantum wells are thinner and red-shifted were they are thicker.** The emission wavelength will also be more sensitive to microscopic thickness variations in the thinner quantum wells than in the thicker quantum wells. This result, which is again a consequence of quantum size effects, means that the FWHM of the PL signal should increase where the quantum wells are thinner. With the above information, it can be seen from Figs. 5.8-5.13 that the quantum wells tend to be thinner within a few millimeters of the edge of the wafers. In general, however, the uniformity of the quantum well thicknesses, is good to within less than ≈10 Å over essentially the entire scanned wafer surface, and less than about 3 Å over areas as large as $1cm^2$. For the 3 QW structure with 55 Å thick quantum wells, the calculated shift in the wavelength with increasing quantum well thickness is -1.16 meV/Å. For the 5 QW structures with 30 Å thick quantum wells the shift is -3.11 meV/Å.

** It should be noted that the wafer uniformity may actually be somewhat better than indicated from Figs 4.8(c)-4.13(c). The wafer uniformity may actually be better than indicated since the shallow slope at the PL peak makes it difficult to determine with high accuracy the exact location of the peak wavelength. When this inaccuracy is combined with the discreteness of having to allocate the peak wavelength into a specific bin, the wafers (quantum well thicknesses) can appear slightly less uniform than they actually are. When, instead of plotting the peak wavelength variation across the wafer, one plots variations in the half maximum wavelength (taken to the long wavelength side of the peak), where the slope of the PL signal vs wavelength curve is steep, the map of the wafer uniformity improves considerably. These images are not shown in this thesis in order to save space.

Table 5.1: Summary of the peak emission wavelength, peak PL intensity and FWHM values obtained for all wafer structure grown from photoluminescence measurements made at room temperature and taken at a location near the center of each wafer.

Device Number	Peak Emission Wavelength [μm]	Ave. Peak PL Intensity, [C.U.]	FWHM [meV]
R1-394 (1.5% Compression, 5QW)	1.391	2396	47
R1-408 (1.5% Compression, 5QW)	1.393	2117	52
R1-395 (1.2% Compression, 5QW)	1.425	2000	50
R1-396 (Unstrained, 5QW)	1.426	2519	42
R1-397 (1.2% Tension, 3QW)	1.391	1096	54
R1-398 (1.3% Tension, 3QW)	1.381	884	67
R1-399 (1.2% Compression, 3QW)	1.389	3755	37
R1-400 (Unstrained, 3QW)	1.380	3022	49

† Note: the peak emission wavelength data appearing in table 5.1, is not the average wavelength indicated in Figs. 5.8(c)-5.13(c). The average wavelength from Figs. 5.8(c)-5.13(c) is calculated including the contributions from measurements taken within a few millimeters of the wafer edges. Contributions from this data are irrelevant since only those lasers processed from material near the center of each wafer were tested. The peak emission wavelength and FWHM data appearing in table 5.1 were obtained from room temperature PL measurements taken at a location near the wafer center. These room temperature PL spectra have been published by Takasaki, [1992].

From the wavelength histograms shown in Figs. 5.8-5.13 and the data summary of table 5.1 it is seen that the wavelength corresponding to the peak in the photoluminescence signal for all samples is closer to 1.4 μm than the design wavelength of 1.3 μm. However, all structures belonging to a given design set still have similar emission wavelengths to within 10 nm†. Part of the discrepancy between the design emission wavelength and the actual emission wavelength can be attributed to the overshoot in the well thickness of the grown structures in comparison to the designed well thickness. The overshoot in the well

thickness, however, does not fully account for the extent to which the actual emission wavelength exceeds the design wavelength.

Other factors that could contribute to the greater than expected emission wavelength, which has also been observed by other authors [Tanbun-Ek, 1989], are as follows. Firstly, non-parabolicity of the band structure may have resulted in carrier effective masses that were larger than expected. A larger carrier effective mass would cause the energy levels within the quantum wells to shift toward the bottom of the quantum wells thereby producing a larger than calculated emission wavelength. Secondly, a 40/60 split in the band-gap discontinuity between the conduction and valence bands was assumed, which may not be very accurate and is difficult to determine. Work done at BNR's Advanced Technology Laboratory in Ottawa since the time these structure were grown suggests that for device structures designed to emit at a wavelength of 1.3 μm, a more appropriate ratio for the conduction and valence band-gap discontinuity may be 33/67. For device structures designed to emit at a wavelength of 1.55 μm, researchers at BNR have found a good correspondence between the calculated and the actual emission wavelengths when a conduction and valence band-gap discontinuity ratio of 25/75 is used. (The calculations done at BNR were made using the program I created to perform the calculations for this thesis). Thirdly, there may alway be some uncertaintly in the composition of the $In_{1-x}Ga_xAs_yP_{1-y}$ quantum well and barrier layers. Although, extensive calibration was performed prior to the growth of these structures.

From Fig 5.8-5.13, it can be seen that the photoluminescence intensity is reasonably uniform over the entire scanned surface of the wafers. As indicated in Table 5.1, all quantum well laser structures grown emitted strong room temerature PL signals indicating that they are of excellent crystal quality (good quality bulk lasers emit with intensities near 1500 calibrated units [Minor, 1990]). It is also seen from Table 5.1 that, for the 3QW structures belonging to Set 1 (Table 4.1), the compressively strained quantum

well structure emitted a much more intense PL signal than either the tensile-strained or the unstrained sample. The tensile-strained quantum well structures emitted the weakest PL signal. Since all structures appear to be of excellent crystal quality, possible explanations for this result are that: (1) the bimolecular recombination rate is much larger in the compressively strained over the tensile and unstrained quantum wells; (2) the non-radiative recombination processes, such as Auger recombination are reduced in the compressively strained structure, or; (3) the collection efficiency of carriers is higher in the compressively strained structure than it is in the other structures. For the 5-QW structures belonging to Set 2 (Table 4.1) both the compressively strained and unstrained structures were very efficient emitters, with the unstrained structure emitting a slightly more intense PL signal than the strained structures.

In comparing the peak PL intensity from the compressively strained and unstrained 5-QW structures to that obtained for the compressively strained and unstrained 3-QW structures with the thicker quantum wells, it is seen that the 3-QW laser structures emitted a more intense PL signal, which may be due to a greater carrier collection efficiency for the wider quantum wells. However, a greater collection efficiency by the wider quantum wells does not appear to hold true when examining the internal quantum efficiency versus temperature data shown in Fig. 6.12 and Fig. 6.13. As will be discussed in Chapter 6, for the laser structure grown for this thesis, the thinner quantum wells are predicted to be more efficient collectors of injected electrons than the thicker quantum wells.

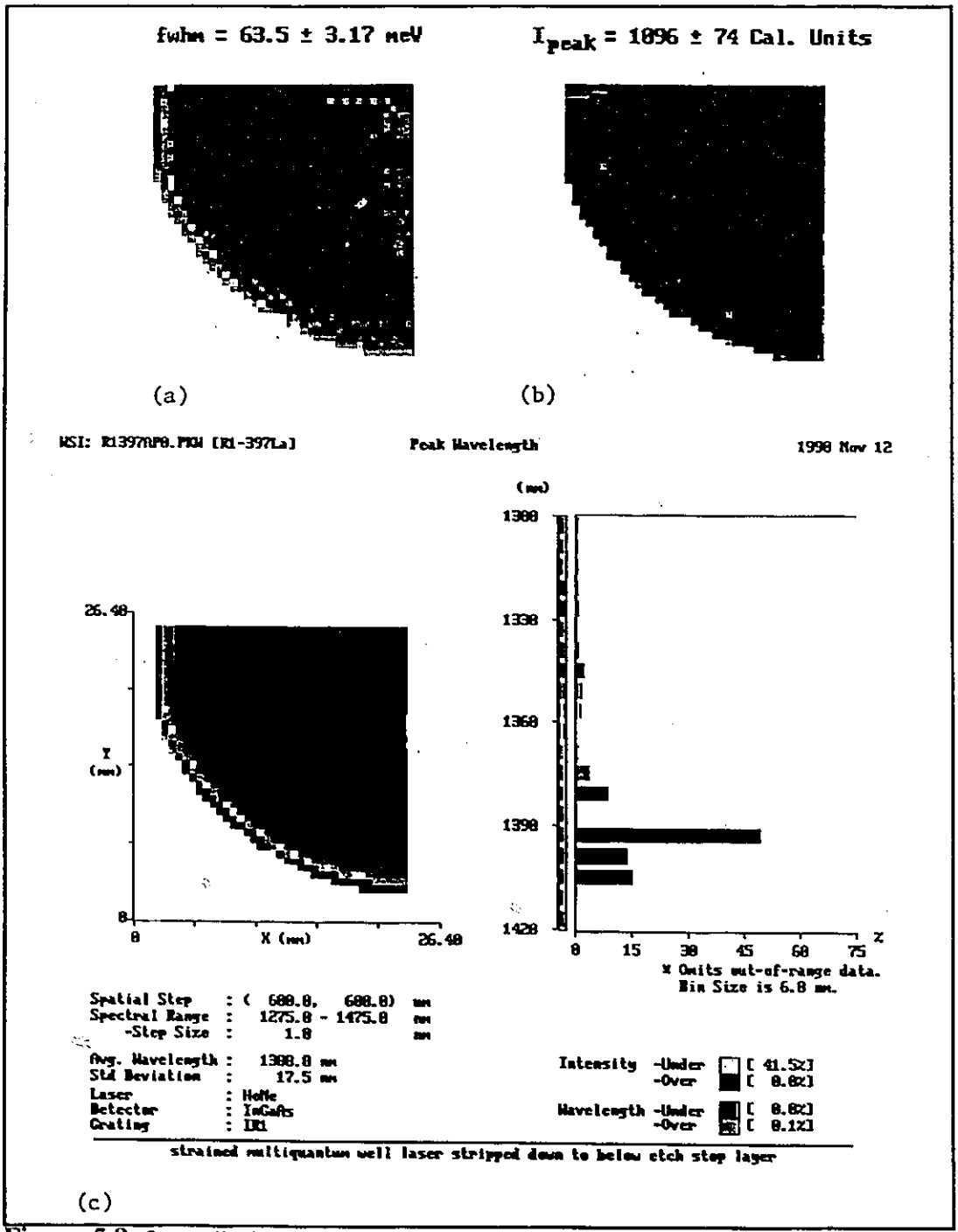

Figure 5.8: Spectrally (1 nm step size) and spatially resolved (600 µm step size) photoluminescence scan of wafer number R1-397: (a) Variation in FWHM of PL peak over the wafer surface; (b) variation in peak intensity over the wafer surface; (c) variation in peak wavelength over the wafer surface. As indicated in the histogram of (c), as the color shifts towards the red end of the color spectrum, parameter values get larger. The values for the FWHM and peak intensity, which are listed above (a) and (b) respectively, are the average values obtained from the entire quarter wafer scan plus and minus the standard deviation.

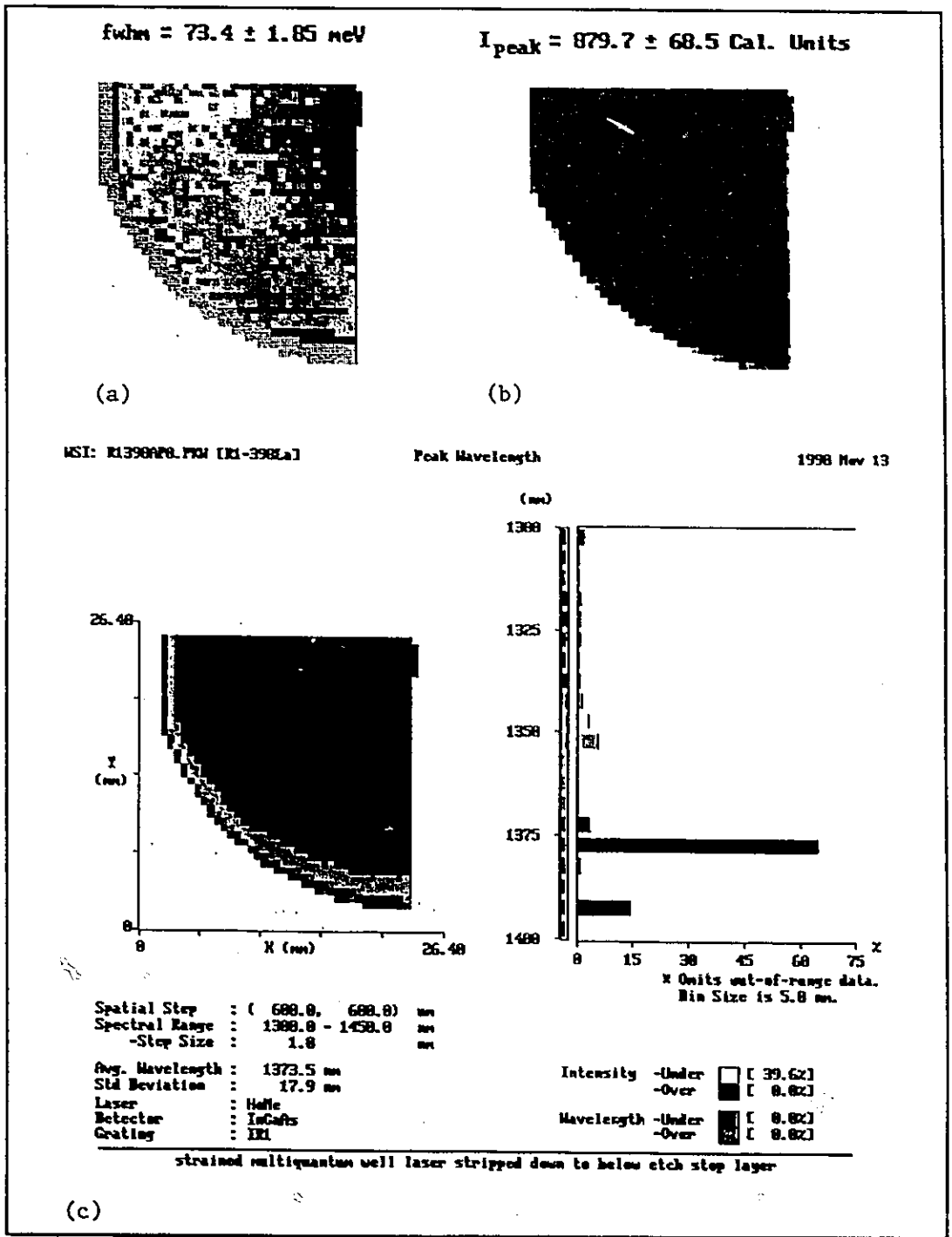

Figure 5.9: Spectrally (1 nm step size) and spatially resolved (600 µm step size) photoluminescence scan of wafer number R1-398: (a) Variation in FWHM of PL peak over the wafer surface; (b) Variation in peak intensity over the wafer surface; (c) Variation in peak wavelength over the wafer surface. As indicated in the histogram of (c), as the color shifts towards the red end of the color spectrum, parameter values get larger. The values for the FWHM and peak intensity, which are listed above (a) and (b) respectively, are the average values obtained from the entire quarter wafer scan plus and minus the standard deviation.

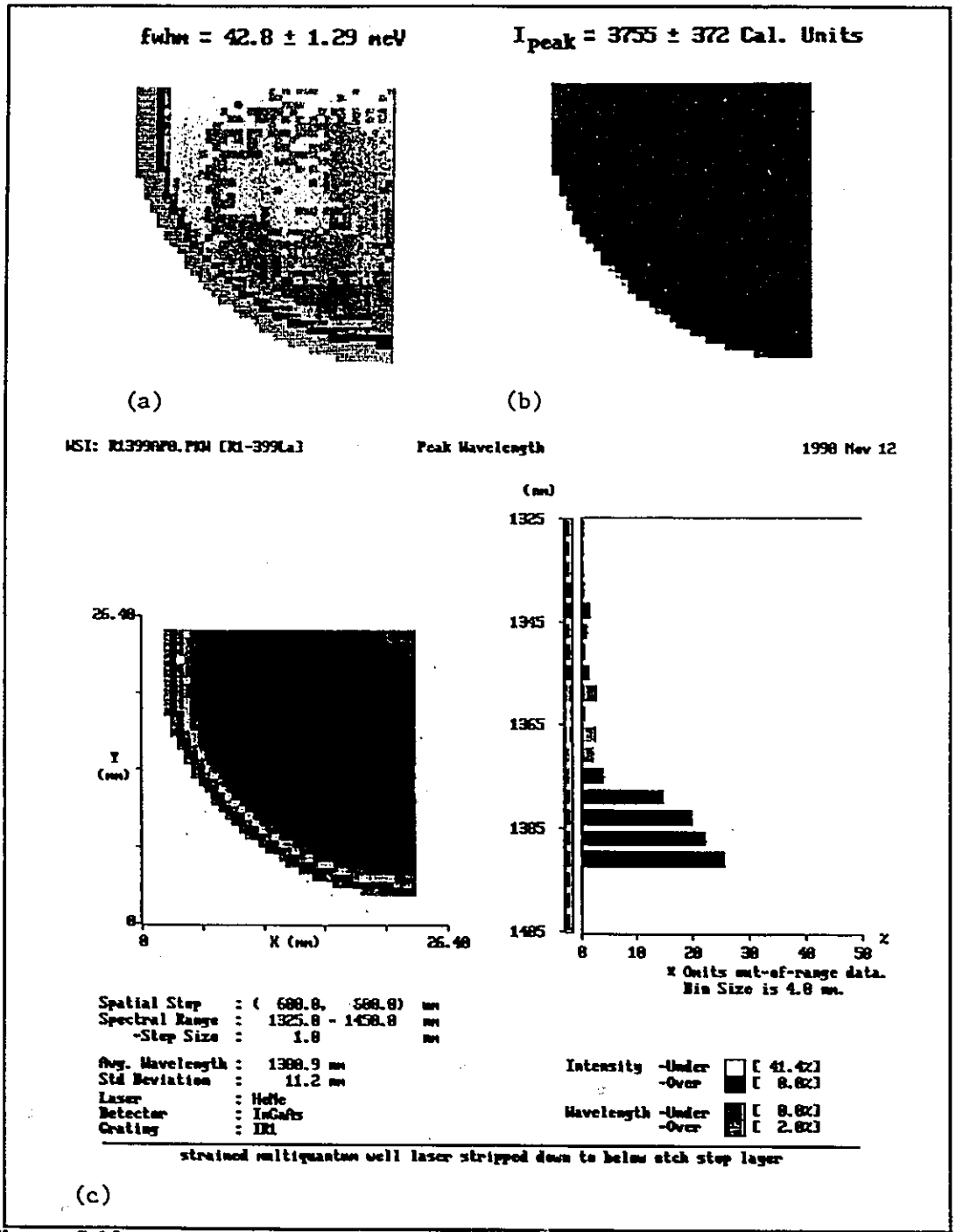

Figure 5.10: Spectrally (1 nm step size) and spatially resolved (600 μm step size) photoluminescence scan of wafer number R1-399: (a) Variation in FWHM of PL peak over the wafer surface; (b) Variation in peak intensity over the wafer surface; (c) Variation in peak wavelength over the wafer surface. As indicated in the histogram of (c), as the color shifts towards the red end of the color spectrum, parameter values get larger. The values for the FWHM and peak intensity, which are listed above (a) and (b) respectively, are the average values obtained from the entire quarter wafer scan plus and minus the standard deviation.

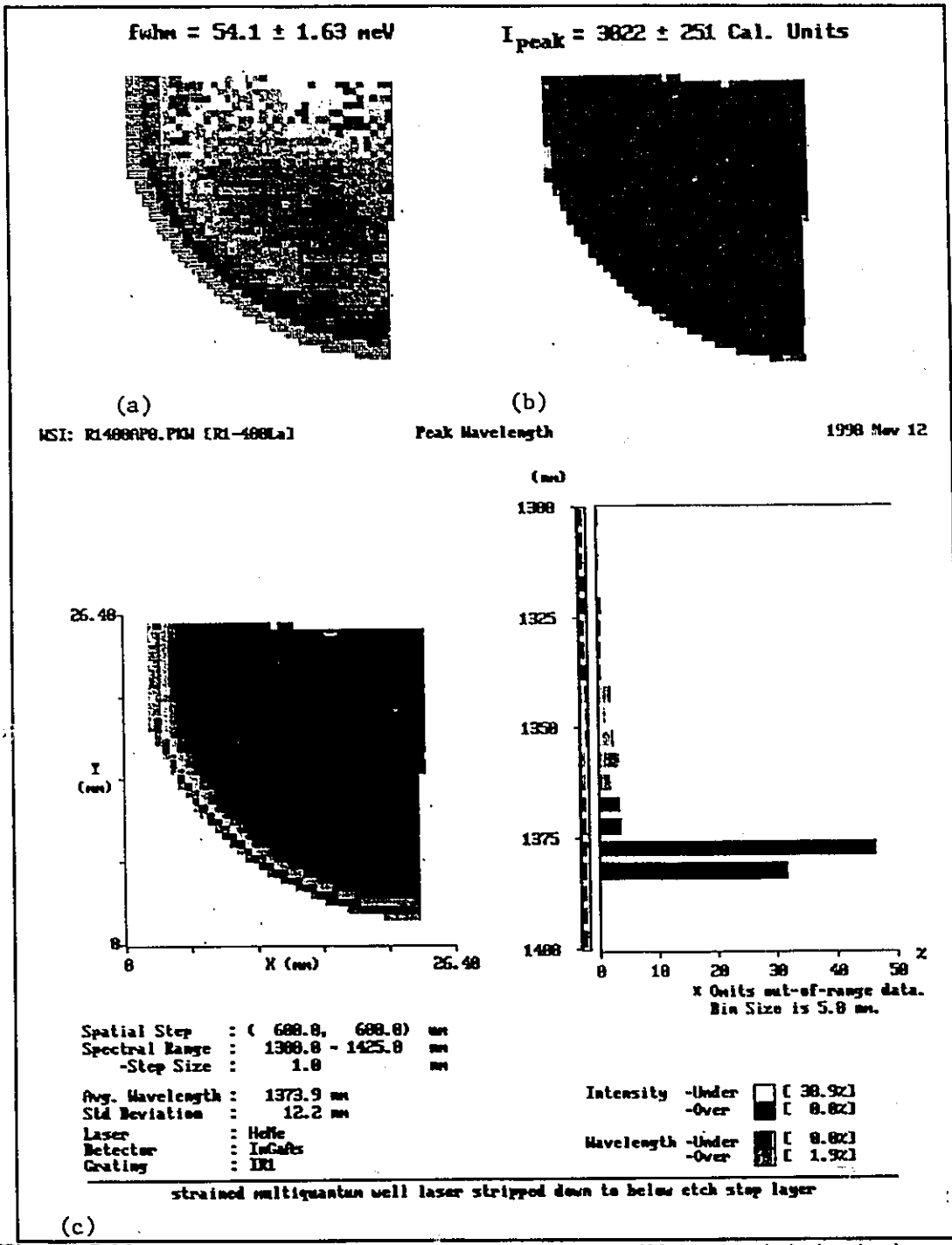

Figure 5.11: Spectrally (1 nm step size) and spatially resolved (600 μm step size) photoluminescence scan of wafer number R1-400: (a) Variation in FWHM of PL peak over the wafer surface, (b) Variation in peak intensity over the wafer surface, (c) Variation in peak wavelength over the wafer surface. As indicated in the histogram of (c), as the color shifts towards the red end of the color spectrum, parameter values get larger. The values for the FWHM and peak intensity,which are listed above (a) and (b) respectively, are the average values obtained from the entire quarter wafer scan plus and minus the standard deviation.

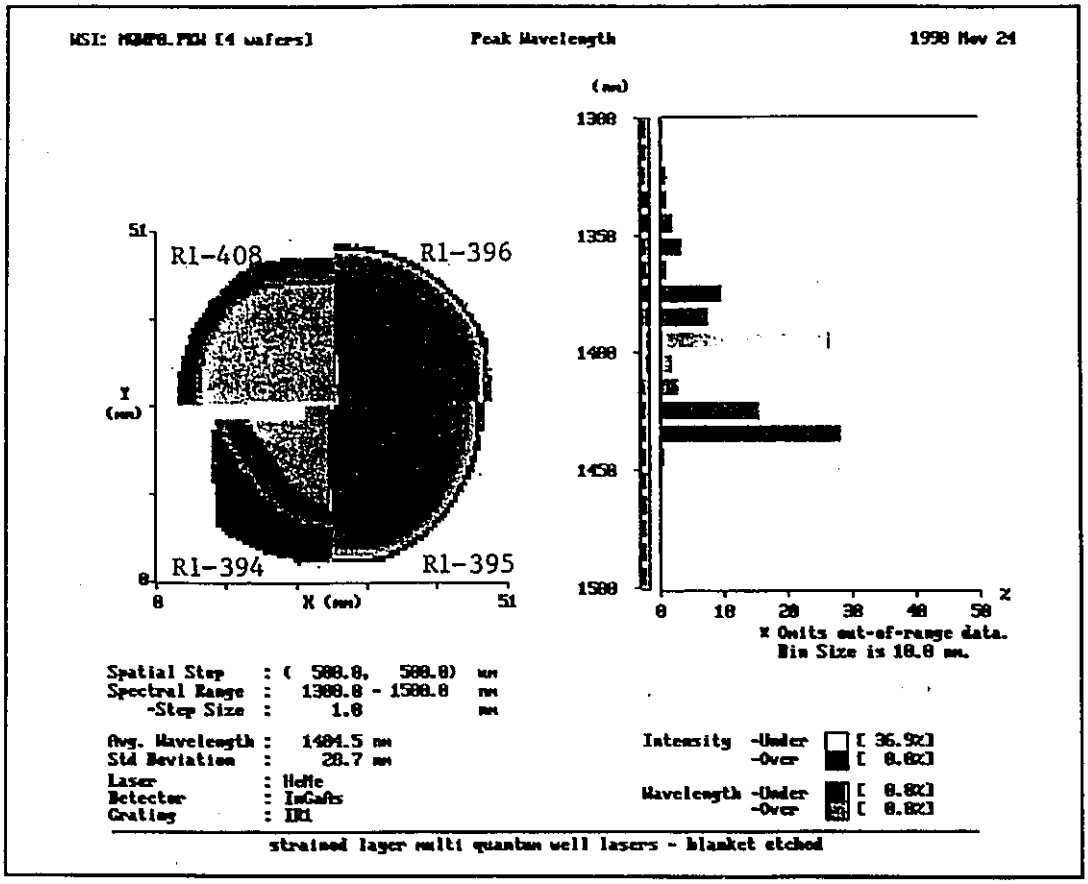

Figure 5.12: Spectrally (1 nm step size) and spatially resolved (500 μm step size) photoluminescence scans of wafer numbers R1-394, R1-395, R1-396 and R1-408. Variation in peak wavelength over the wafer surface.

The apparent contradiction between the internal quantum efficiency data, which will be seen later in Chapter 6, and the PL results shown here most likely occurs because the internal efficiency data was obtained for lasers operating just above threshold and under forward-bias, whereas the PL data were obtained at zero bias. At a forward-bias level corresponding to just above threshold, charge neutrality and, therefore, a nearly flat band condition should occur in the laser active region. For lasers under zero bias, as used for the PL data, the escape rate of electrons from the quantum wells will be largely influenced by the built-in electric field (non-flat band condition) near the active region, and will most likely be dominated by carrier tunneling [Takasaki, 1992]. In turn, the escape rate due to

tunneling depends upon the position of the electron and hole energy levels with respect to the top of the barrier layer band edge [Takasaki, 1992]. Since the energy separation between the barrier conduction band edge and the n=1 electron level in the quantum wells is smaller in the thinner quantum wells than the thicker quantum wells (see Appendix A), under the influence of the built in field, the electron escape rate due to tunneling and thermionic emission is expected to be greater. Therefore, under zero bias conditions, the net collection efficiency will be smaller for the thin quantum well structures than for the thick quantum well structures.

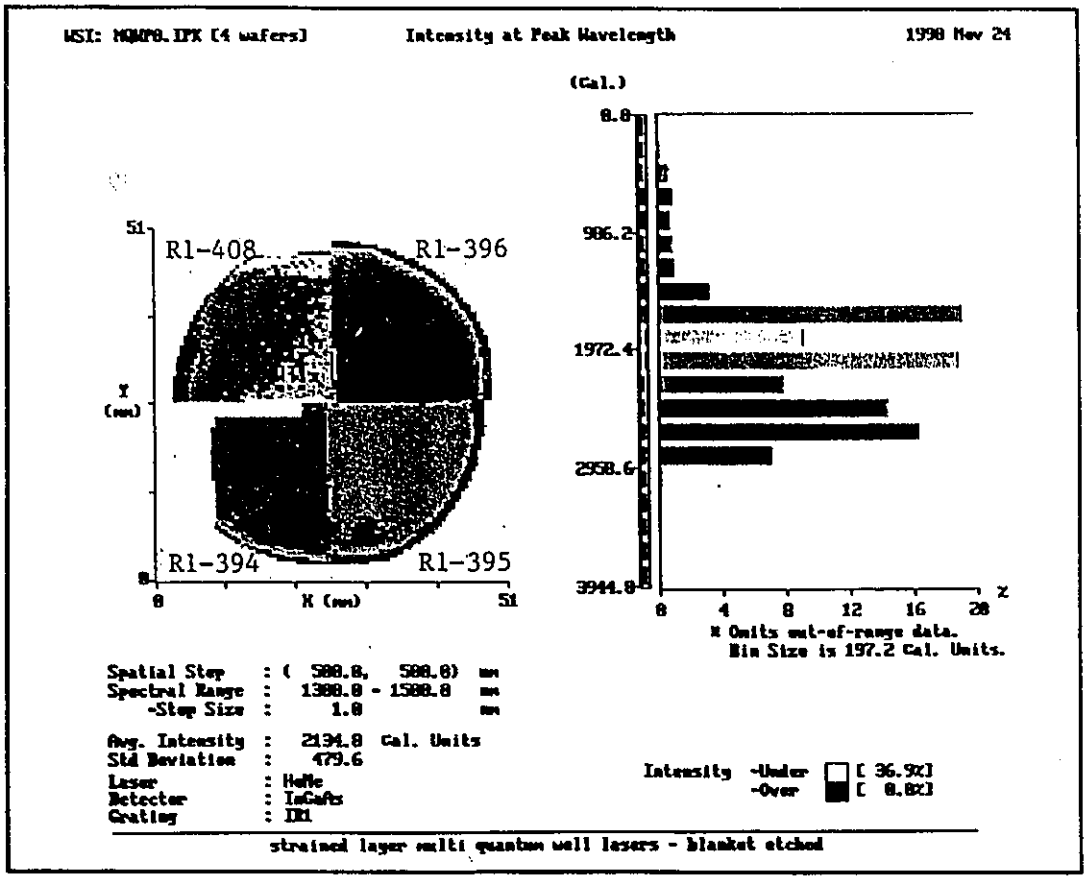

Figure 5.13: Spectrally (1 nm step size) and spatially resolved (500 μm step size) photoluminescence scans of wafer numbers R1-394, R1-395, R1-396 and R1-400. Variation in peak intensity over wafer surface.

5.3.2 Temperature and Power Dependent Photoluminescence

Temperature and power dependent photoluminescence measurements were also made on quantum well laser structures belonging to Set 1 comprising sample numbers R1-397, R1-398, R1-399 and R1-400. The samples were prepared as described in §5.3, then mounted in a cryostat (they were pasted to the cold head using Wakefield Thermal Compound) for temperature variation. The measurements were made using the experimental set-up shown in Fig. 5.14.

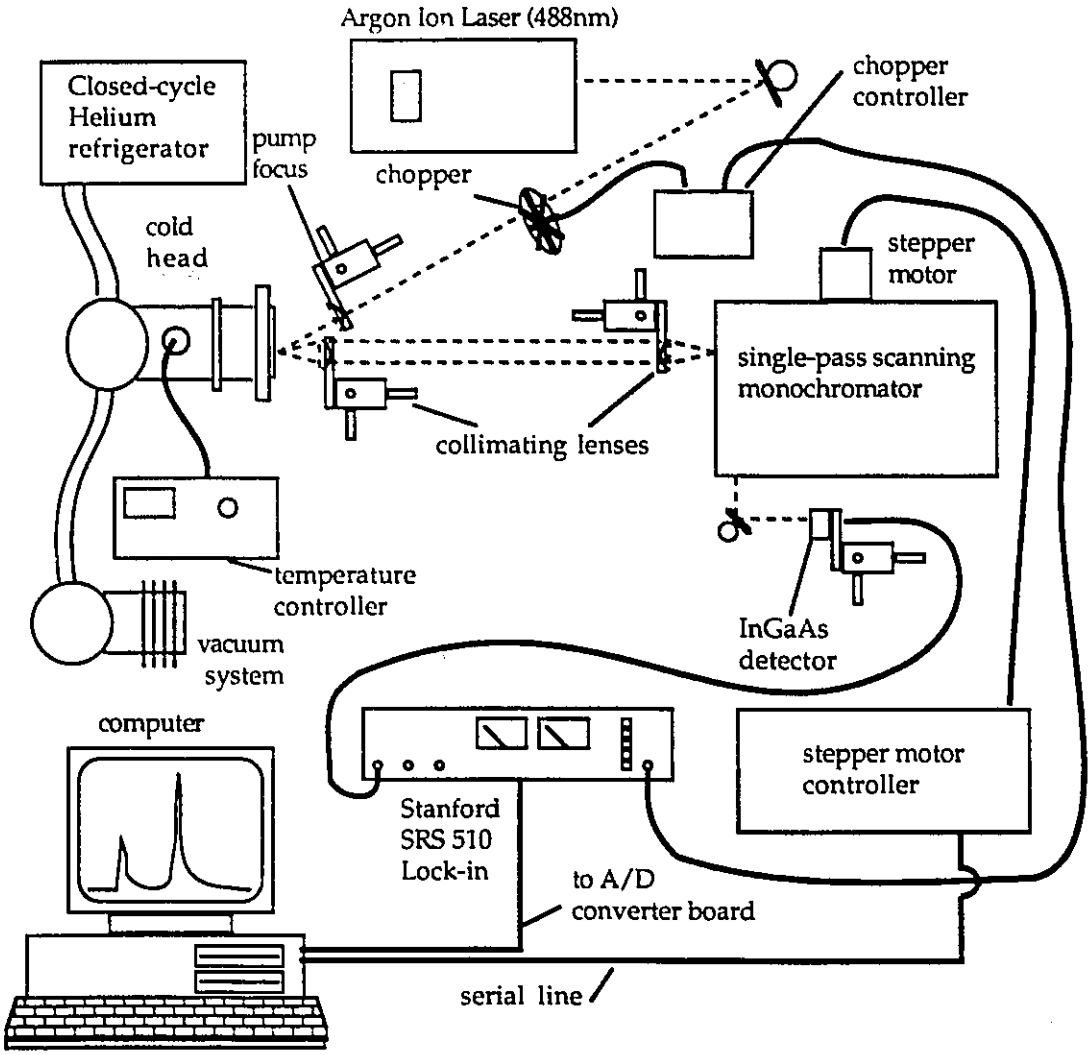

Figure 5.14: Schematic diagram of the experimental photoluminescence set-up.

The excitation source for these measurements was a CW Ar^{++} ion laser, emitting at a wavelength of 488 nm, and the incident power was variable from zero to 20.6 mW. The incident light was focused onto the sample by a 10 cm focal length lens at an angle of incidence of approximately 30°. The luminescence was collected and focused onto the entrance slit of an f/7.5, 0.64 meter, coma-corrected Czerny-Turner type scanning monochromator. The second-order spectrum was measured at the output of the monochromator by an InGaAs detector. The slit width for the power dependent measurements was set at 250μm for all samples, except for R1-398 for which the slits were set at 500μm. For the temperature-dependent measurements, the slit widths were set at 500 μm for samples R1-397 and R1-398, and 250μm for samples R1-399 and R1-400. The monochromator dispersion was 12 Å/mm. The incident light was chopped for phase-sensitive detection by an SRS 510 lock-in amplifier whose output voltage was monitored by computer.

The results of the power-dependent PL measurements, which were made at a temperature of 13K, are shown in Figs. 5.15-5.18. From these figures, as in Table 5.1, it is seen that the peak PL intensity is much greater for the compressively strained structure (R1-399) and the unstrained structure (R1-400) than it is for the tensile-strained structures (R1-397 and R1-398). It is also quite clear that the FWHM of the PL signal for the tensile-strained structures (the FWHM is 21 meV for sample R1-397, and 16 meV for sample R1-398 at a pump power of 10.7 mW) is approximately twice that of the compressively strained and unstrained structures, which have FWHMs of 8.8 meV and 10 meV, respectively, at an equivalent pump power. More interesting is the observation that the peak PL wavelength from the tensile-strained structures shifts noticeably to shorter wavelengths with increasing pump power, as shown in Fig. 5.19. There is a much smaller shift to shorter wavelengths of the peak PL signal from the unstrained and compressively

strained structures with increasing pump power. However, the peak intensity for all samples increases slightly sub-linearly with increasing pump power and a plot of the normalized peak intensity versus pump power for all structures is nearly identical. This sub-linear increase in the PL intensity with pump power, as shown in Fig. 5.20, could possibly indicate that the PL efficiency is decreasing due to heating by the incident beam, or that the carrier density being generated at the higher power levels is large enough to cause band filling.

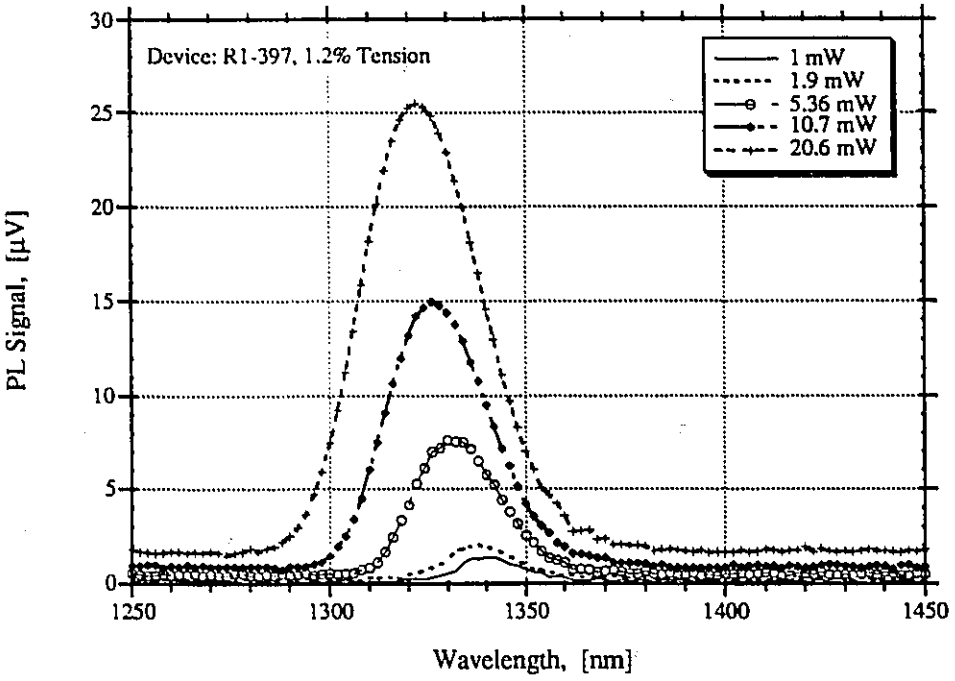

Figure 5.15: Photoluminescence spectrum of sample number R1-397 at 13 K as a function of the incident pump intensity.

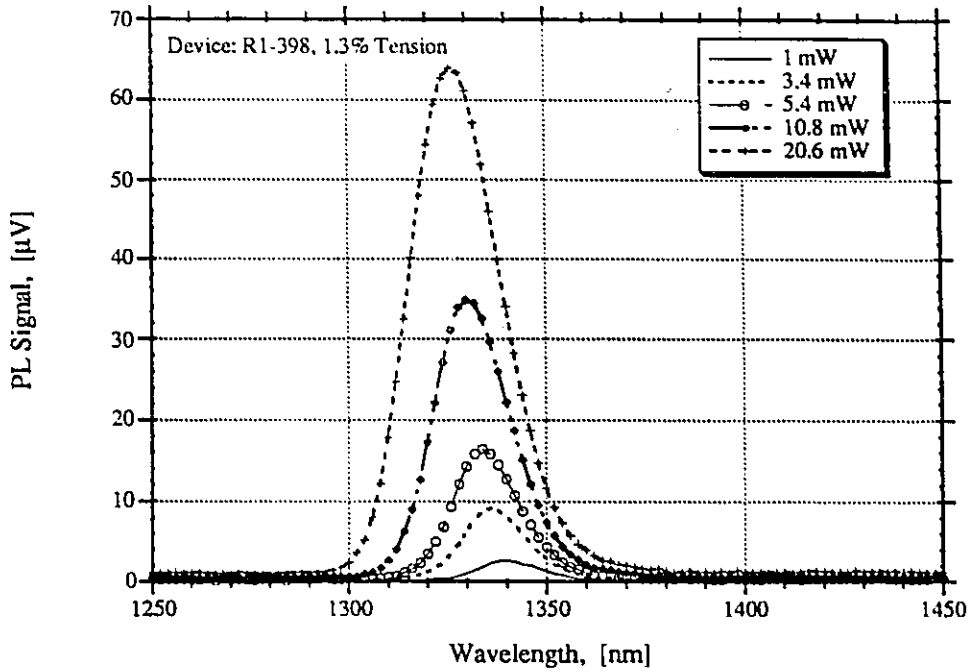

Figure 5.16: Photoluminescence spectrum of sample number R1-398 at 13 K as a function of the incident pump intensity.

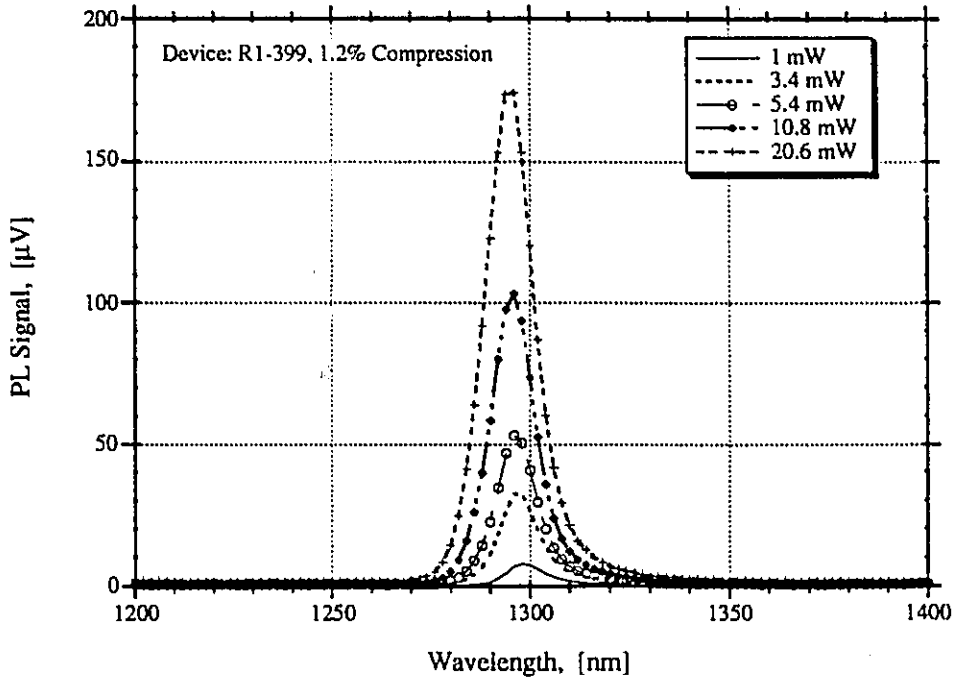

Figure 5.17: Photoluminescence spectrum of sample number R1-399 at 13 K as a function of the incident pump intensity.

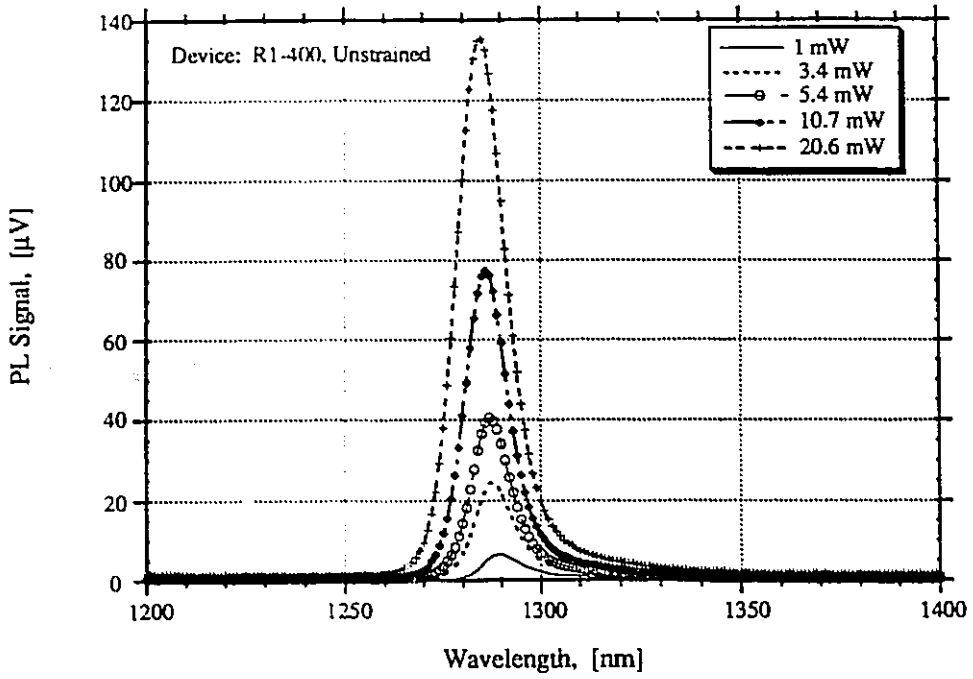

Figure 5.18: Photoluminescence spectrum of sample number R1-400 at 13 K as a function of the incident pump intensity.

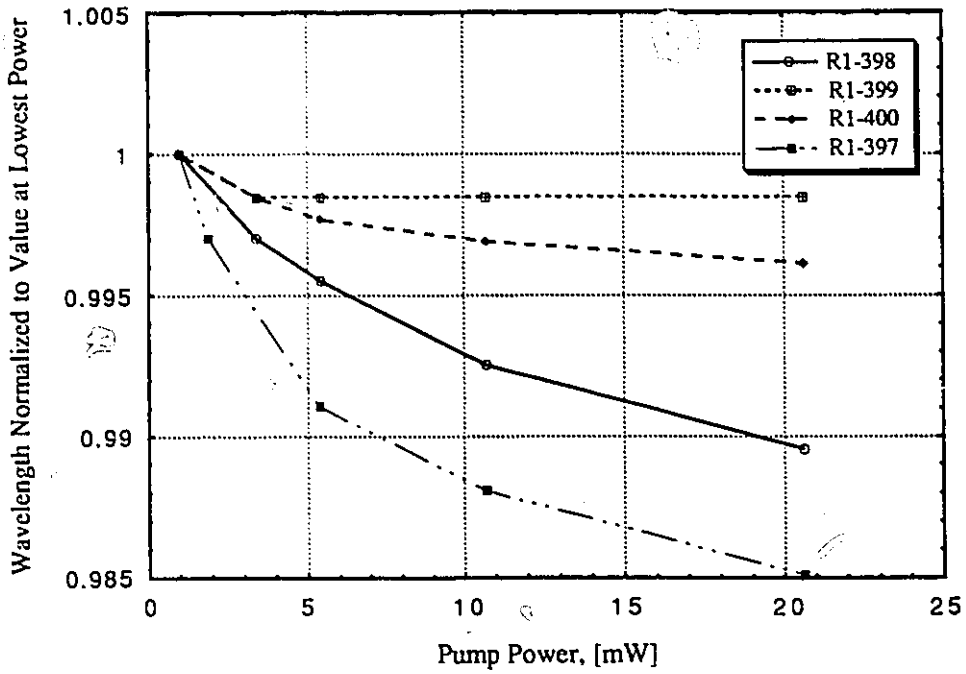

Figure 5.19: Normalized peak wavelength (to λ at the lowest pump power) *vs.* incident pump intensity for strained and unstrained MQW structures from Set 1..

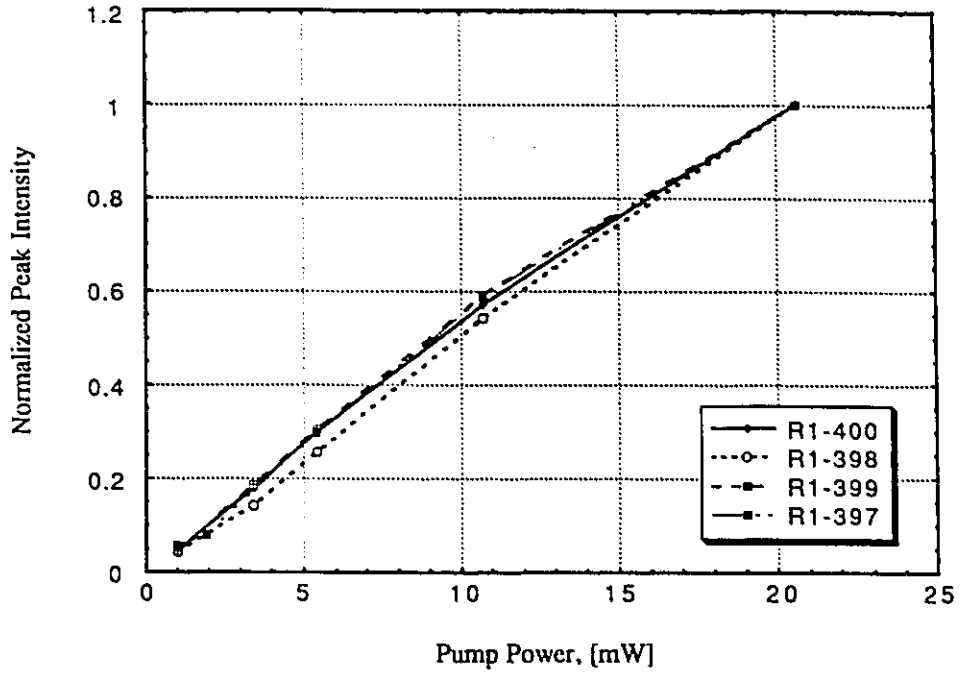

Figure 5.20: Normalized peak PL intensity*vs.* incident pump intensity for strained and unstrained MQW structures from Set 1.

The noticeable shift in the peak PL wavelength with pump power for the tensile-strained structures, in comparison to the strained and unstrained structures, would tend to suggest that the energy bands in the quantum wells are indeed being pumped to degeneracy at the higher pump powers, and that the reduced density of states for the tensile-strained samples is much smaller than that for the other samples. Due to a smaller reduced density of states in the tensile strained structures, the quasi-Fermi levels move much more rapidly into the energy band, or bands, with increasing pump intensity in these samples than in the other samples. This more rapid increase in the quasi-Fermi level separation with increasing incident power is in turn being reflected by a more rapid change in the peak emission wavelength with increasing incident power for the tensile-strained samples.

The broader FWHM of the PL signal in the tensile-strained structures is a consequence of the fact that the electron energy distribution is greater in these structures than it is in the unstrained and compressively strained structures. The broader electron energy distribution may be a reflection of energy state broadening in the quantum wells of these structure which, in turn, could be attributed to a greater degree of fluctuation in the quantum well thickness. Although this interface roughness is not evidenced in the TEM pictures of Figs. 5.4 and 5.5, there is strong evidence that for tensile-strained quaternary quantum wells, the observation of interface roughness depends strongly on the crystal plane being observed in the TEM cross-section [Okada, 1993]. For example, when TEM images are taken of a $[\bar{1}10]$ cross-section, a rough, faceted, quantum well-barrier interface is seen; however, when TEM images are taken of a [110] cross-section, only a smooth flat interface, such as that seen in Figs. 5.4 and 5.5, is seen. An example of a rough, faceted quantum well interface is seen in Fig. 5.21. Figure 5.21 shows a TEM image of a tensile strained quantum well structure (sample number R1-381) which was grown for calibration purposes prior to the growth of samples R1-397 and R1398. The tensile strain in this sample, whose geometry was essentially identical to structure R1-398, was estimated at 1.3%, and the quantum well thickness at the widest points was measured to be about 60Å. From Fig. 5.21 it can also be seen that the interface roughness becomes larger as the quantum well layer number increases. The differences between structure R1-381 and R1-398 are that structure R1-381 was grown on a semi-insulating InP substrate, the entire structure was grown undoped, and the gas flow was a slightly too Ga rich.

The results of the temperature dependent PL measurements, which were made for a pump power of 5.4 mW, are shown in Figs. 5.22-5.25. In comparing Figs. 5.22 and 5.23 with Figs. 5.24 and 5.25, it is clear that the shift of the peak PL wavelength with temperature is much smaller for the tensile-strained structures than it is for the compressively strained and the unstrained structure. In fact, the rate of change of the peak

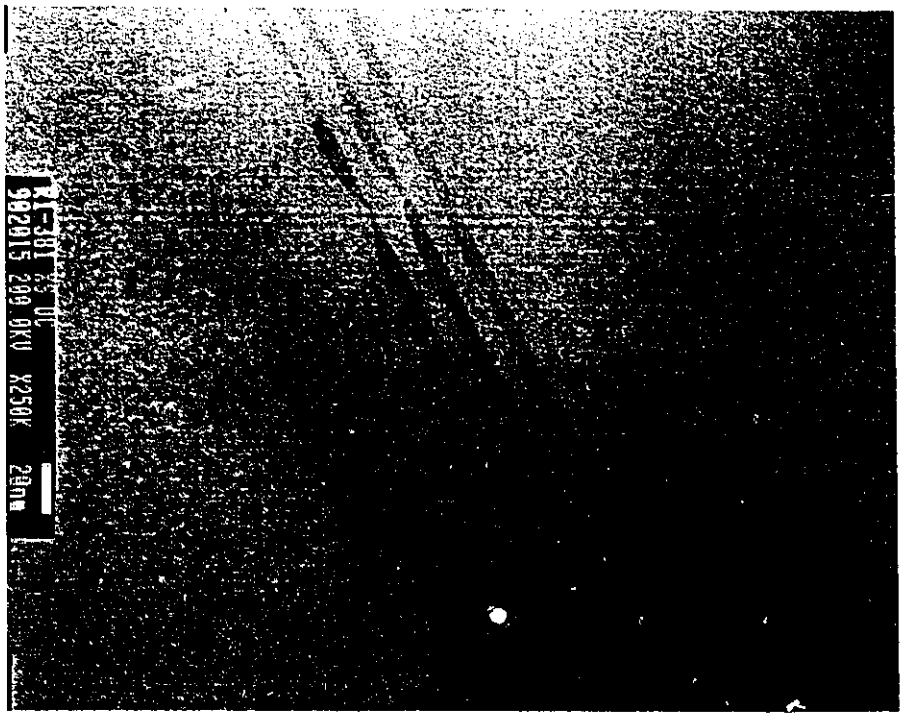

Figure 5.21: TEM photograph of sample number R1-381 (1.3% tensile strain) showing interface roughness and faceting which has been observed for tensile strained quaternary quantum well material grown on InP substrates for $[\bar{1}10]$ TEM cross-sections but not for [110] cross-sections [Okada, 1993]. The measured quantum well thickness for this sample was 60±4 Å at the thickest points.

PL wavelength for the tensile strained structures is half as large as that for the compressively strained structure and nearly one third of that for the unstrained structure. The difference in the rate of change of the peak PL wavelengths with temperature of the different structures is significant, as this phenomena may be partially responsible for the improved (less sensitive) temperature dependence of I_{th} of the tensile-strained structures (see results of Chapter 6) over that of the other structures. This possibility is explored further in the discussion of the results of Chapter 6.

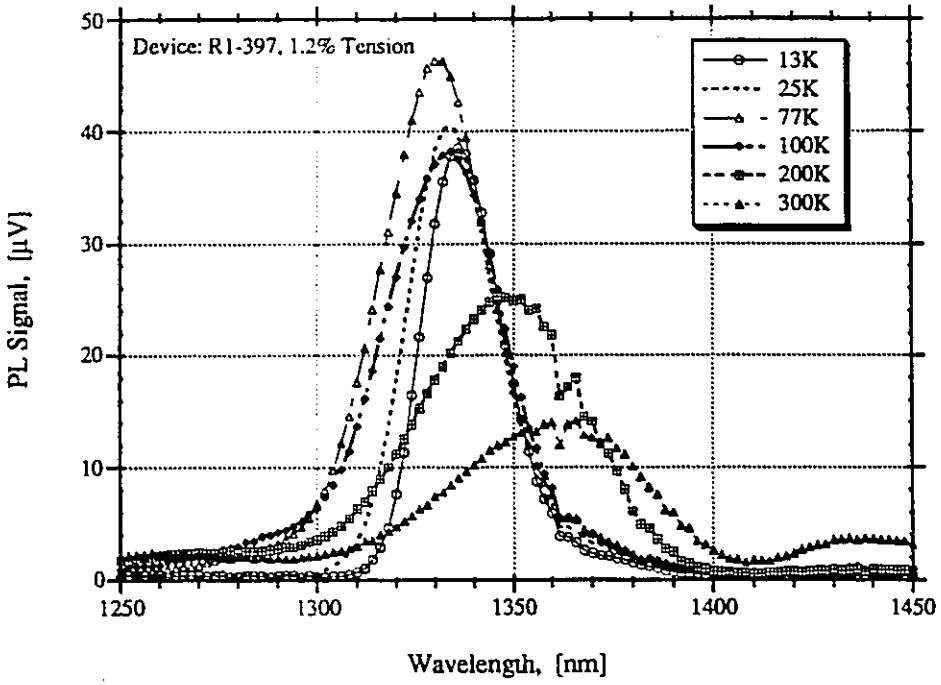

Figure 5.22: Photoluminescence spectrum of sample number R1-397 (1.2% tensile strain) as a function of temperature with a pump power of 5.4 mW.

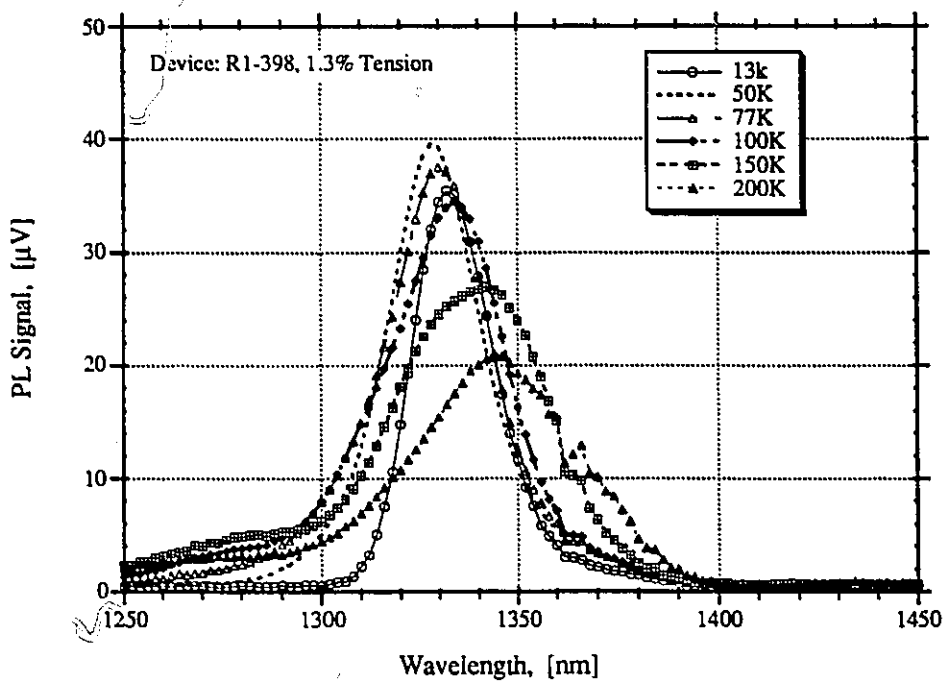

Figure 5.23: Photoluminescence spectrum of sample number R1-398 (1.3% tensile strain) as a function of temperature with a pump power of 5.4 mW.

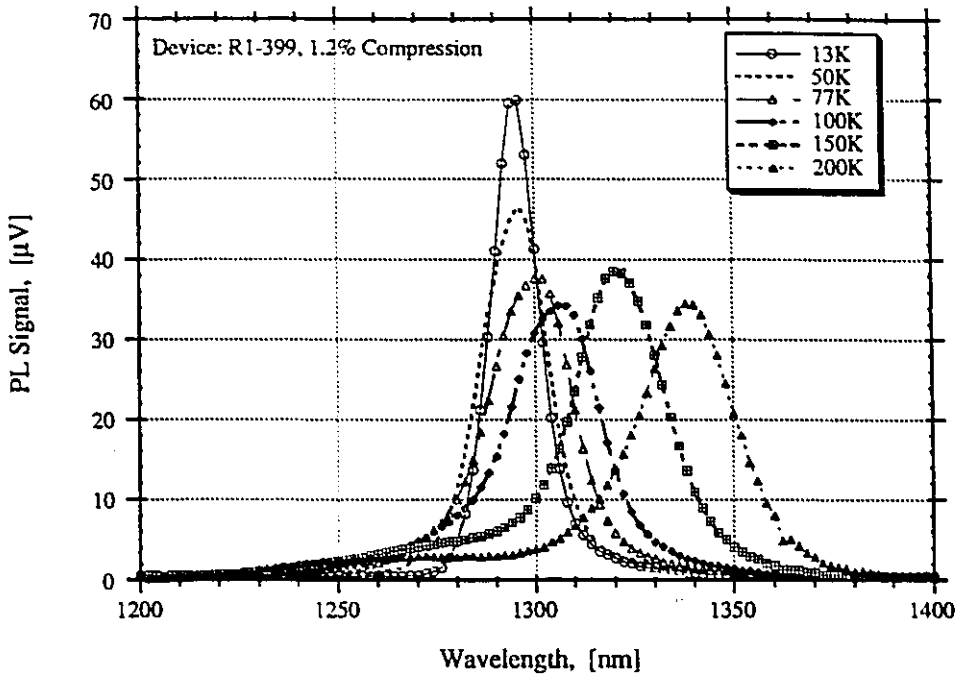

Figure 5.24: Photoluminescence spectrum of sample number R1-399 (1.2% Compressive strain) as a function of temperature with a pump power of 5.4 mW.

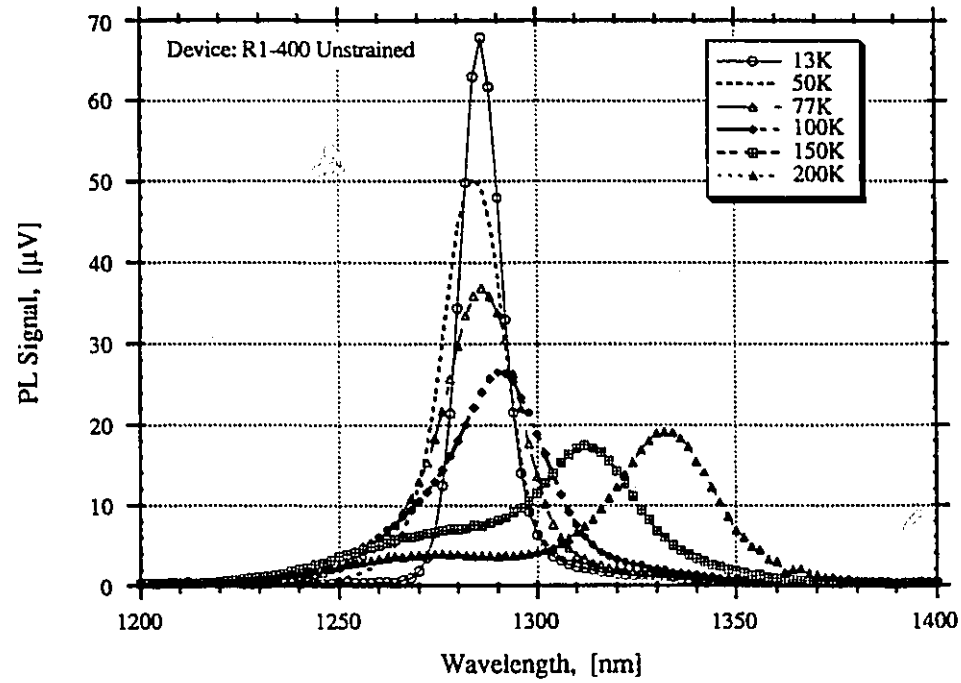

Figure 5.25: Photoluminescence spectrum of sample number R1-400 (Unstrained) as a function of temperature with a pump power of 5.4 mW.

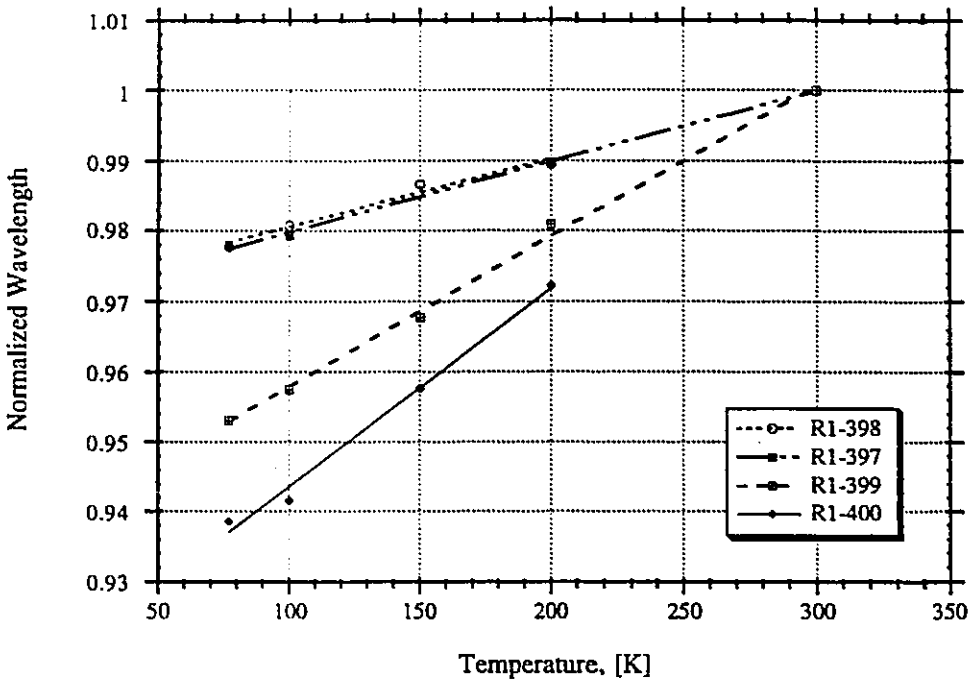

Figure 5.26: Plot of the shift of the normalized peak PL wavelength (to λ @ 300K) *vs.* temperature for strained and unstrained MQW structures from Set 1.

One factor that would contribute to the change in the peak PL wavelength of all quantum well structures with temperature is the difference in the thermal expansion coefficient between the barriers and the quantum wells which would cause an additional strain component as the temperature of the samples increases for the PL measurements.

The thermal expansion coefficients, α, for the binary materials at 300K are as follows: 4.56×10^{-6}/°C for InP, 5.16×10^{-6}/°C for InAs, 6.40×10^{-6}/°C for GaAs, and 5.91×10^{-6}/°C for GaP [Adachi, 1992]. Using Vegard's linear interpolation, (4.1.2), the thermal expansion coefficients of the well and barrier layer materials have been determined, and it has been found that the thermal expansion coefficient of the quantum well material is greater than that of the barrier material [Adachi, 1992]. Therefore, as the sample temperature increases (and band-gap decreases) the compressive strain in the QW material increases. This increasing compressive strain with temperature would act to *decrease* the

tensile strain induced shift of the quantum well band edge to longer wavelengths thereby partially compensating for the decrease in the band-gap with increasing temperature. However, the difference in the thermal expansion coefficients, $\Delta\alpha$, between the well and barrier material will only be on the order of 10^{-6}/°C. From (2.3.23), such a small difference in the thermal expansion coefficient between the well and barrier material could only account for an increase in the quantum well band-gap with temperature on the order of 10 μeV/°C or less. This is greater than two orders of magnitude smaller than the shift in the energy band-gap due to temperature, which is on the order of -4×10^{-4}eV/°C [Adachi, 1992]. Therefore, there must be other reasons why the peak PL wavelength of the tensile strained quantum well structures changes more slowly with temperature than the peak PL wavelength of the compressively strained and unstrained structures.

5.4 SUMMARY

In summary, transmission electron micorgraphs were taken of all the structures studied in this thesis. From the TEM images, it was found that the grown quantum well thicknesses were between 8 Å and 10 Å greater than the design quantum well widths. No visible defects were seen in the TEM images. From these observations, as well as results from polarization resolved photoluminescence scans, it was determined that the crystal quality of all structures was excellent and that the defect count was on the order of 10^4 cm^{-2}.

In order to check wafer uniformity and emission wavelengths, scanning PL measurements were performed. These measurements showed that the quantum well thickness was uniform to within 10 Å over the entire wafer surface, and was uniform to within about one atomic layer over the area from which most devices were fabricated. The peak emission wavelength was also found to be closer to 1.4 μm than the design emission

wavelength of 1.3 μm. Part of this wavelength overshoot was accounted for by the greater than expected quantum well widths.

Power dependent PL measurements showed that the peak emission wavelength of the tensile-strained QW structures shifted noticeably to shorter wavelengths with increasing pump power. This trend, which was not observed for the compressively strained and unstrained QW structures, indicated that the tensile strained quantum well structures may have a much smaller reduced density of states than the other structures. The full width half maximum of the PL signal from the tensile strained QW structures was also much greater than that of the compressively strained and unstrained structures. This wider FWHM was attributed to possible directional interface roughness which is only observable in $[\bar{1}10]$ TEM cross-sections.

Temperature dependent PL measurements showed that the peak PL emission wavelength of the tensile strained QW structures changes less with temperature than it does for the other structures. It was shown that the differences in the linear thermal expansion coefficient between the well and barrier layer material could not account for this result. However, it was postulated that a reduced temperature dependence of the peak PL wavelength could be reflected in a lower temperature dependence of the threshold current for lasers fabricated from the tensile strained quantum well structures.

CHAPTER 6: STRAINED QUANTUM WELL LASER DEVICE PROCESSING AND CHARACTERIZATION

6.0 INTRODUCTION

Laser structures representative of those which were grown and studied in this thesis were shown in Fig. 4.1 and 4.2. The growth sequence for these structures was described in §5.1. This chapter describes the processing of these structures, how they were configured for testing, and the experimental apparatus and configuration used to test both the continuous wave (CW), and spectral characteristics of these lasers. Finally this chapter presents and discusses the empirical results and analysis obtained from a determination of the CW light-current device characteristics as a function of both device length and temperature.

A comparison of the temperature sensitivity of the laser threshold current, I_{th}, for both strained and unstrained MQW laser structures from Set 1 and Set 2 (Table 4.1) is made. From these results it is found that both strain and QW width can be adjusted to improve the temperature sensitivity of I_{th} (increase T_o). In the course of the investigations into the effects of strain and QW width on the laser I_{th}-T relation, it is found that T_o depends on the laser cavity length. Two explanations for the length dependence of T_o are proposed. One of these explanations is based on the premise that the variation of the peak optical gain *vs.* current relation with temperature is primarily responsible for the temperature sensitivity of I_{th}. The other explanation is based on the premise that the

temperature dependence of the leakage currents is primarily responsible for the I_{th} dependence on temperature.

By measuring the temperature dependence of the inverse differential efficiency, η_d^{-1} *vs.* cavity length the internal device efficiency, η_i, and the internal optical absorption loss, α_{loss}, are determined in order to establish if there is a correlation between differences in the temperature dependence of these parameters and differences in T_o. From an examination of the variation of η_i with temperature in relation to the I_{th}-T dependence, it is shown that the temperature dependence of η_i and, therefore, leakage currents from (3.6.7), cannot be primarily responsible for the low T_o of InGaAsP based QW lasers. From an examination of the variation of α_{loss} with temperature in relation to the I_{th}-T dependence, it is also shown that the temperature dependence of α_{loss} is not a major factor in determining the I_{th}-T sensitivity of InGaAsP/InP based lasers. Additionally, it is found that compressive strain results in an increased η_i, while tensile strain results in a decreased η_i.

Next, the peak optical gain as a function of temperature is measured using the commonly employed Hakki and Paoli [1973] technique. It is found from these measurements that the rate of change of the peak optical gain, g_p, with temperature ($d(dg_p/dI)/dT$) strongly influences the I_{th} temperature sensitivity for InGaAsP/InP based QW lasers, even above room temperature. Accordingly, an inverse correlation between the magnitude of $d(dg_p/dI)/dT$ and T_o was found. However, an inverse correlation was also found between T_o and the shift in the peak PL wavelength with temperature, (i.e., dE_g/dT (from §5.3.2)) and between T_o and the change in the wavelength corresponding to the peak gain, λ_p, with injected current, $d\lambda_p/dI$. Based on these observations it is determined that there is an intimate cyclical relationship between the temperature dependence of: the current leakage; dE_g/dT; the peak optical gain; and, the shift in λ_p with current. From this cyclical relationship it is determined that the root of T_o is more complicated than can be explained by a single physical mechanism.

In the final section of this chapter additional effects of strain and QW width on laser performance, apart from those mentioned above, are illustrated. It is found that apart from an improved η_i, the application of compressive strain results in a reduced I_{th}, an increased maximum output power (140 mW), and a reduced linewidth-power product. It is found that the application of tensile strain is found to result in an increased I_{th} and a lower maximum output power, but that tensile strain can be used to reduce the laser linewidth-power product. Additionally it is found that there may be substantial advantages in using thinner QWs (<50Å) in the laser active region than thicker QWs due to an increased density of states. This idea is illustrated further in Chapter 7.

Finally, achieved from the devices designed and fabricated for this thesis are the highest ever reported CW characteristic temperature (T_0 = 88 K) for all quaternary (InGaAsP) lasers with uncoated facets, and the highest reported CW maximum operating temperature of 140°C. In addition all laser structures emitted a circular far field pattern with an angular divergence of ≈25°. This circular far field pattern is beneficial for the efficient coupling of laser light into optical fibers for optical communications purposes.

6.1 DEVICE FABRICATION

The lasers studied in this thesis were ridge waveguide lasers. Both the ridge depth and width have dimensions of 2 μm. The fundamental fabrication steps used to process these lasers are shown in Fig. 6.1. The processing sequence was identical for all structures, apart from the Zn diffusion which was required for lasers R1-394, R1-395 and R1-396, and is described as follows:

(1) Following a cleaning process which involved an oxygen plasma descum and 10:1 buffered-HF acid etch, the entire surface of each wafer was coated with a 3000 Å thick layer of SiO_2.

(2) Ridges were then patterned over the entire wafer surface using positive photolithography. The orientation of the ridges was such that they were perpendicular to the major wafer flat (i.e., in the [110] direction).

(3) Windows for the ridge channels were then opened in the oxide layer and the photoresist was removed.

(4) The ridge structures were then formed by etching the InP cladding layer down to the etch stop layer using a combination of reactive ion etching (RIE), using CH_4/Ar, and wet chemical etching (using 2:3 HCl:H_3PO_4) processes.

(5) Next the remaining oxide was removed and the wafer was blanket coated with a 2000 Å thick layer of silicon nitride.

(6) A via was then etched through the SiN_x layer to the ridge surface using a second photolithographic and RIE process.

(7) The photoresist from this process was removed and the p-contact layer was formed by a blanket deposition of Ti/Pt/Au. The p-contact metalization was annealed at 400°C for 120 seconds.

(8) The wafer was then thinned to a thickness of ≈ 150 μm by lapping and polishing the substrate side.

(9) Finally, the n-type contact was formed by blanket coating the substrate side of the wafer with Ni/Ge/Au followed by Ti/TiNi/Ti/Au and a 400°C anneal for 15 seconds.

Subsequent to processing individual laser die were cleaved from the wafer. The device lengths of these lasers ranged from 250 μm to 1500 μm, in 250 μm increments. Devices with lengths of 250 μm from wafer numbers R1-397, R1-398, and R1-400, did not lase. Therefore, only devices of lengths 500 μm and up were tested for the 3-QW laser structures. Once cleaved several devices of each length, and from each wafer, were tested at BNR in the p-side down configuration using 7 μs pulses at a repetition rate of 215 Hz. From the results of these tests, a minimum of five working devices of each length, and

a) Patterning of SiO_2 by photolithography

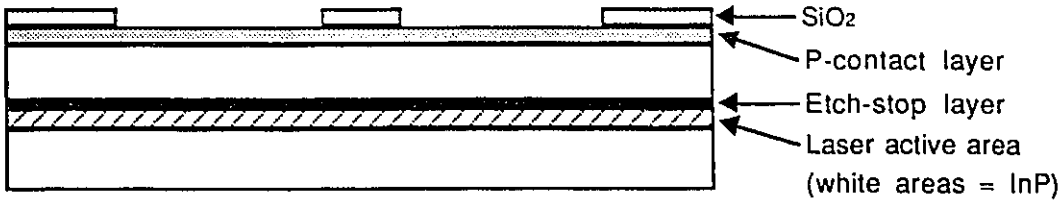

b) Reactive Ion Etching, wet etching, removal of SiO_2

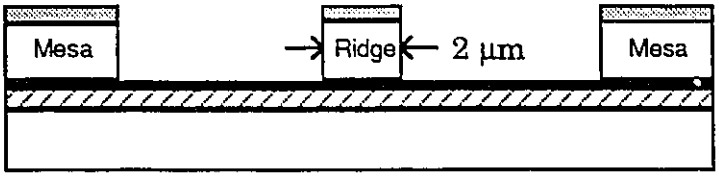

c) Blanket SiO_2/SiN_x, via to ridge by photolithography and wet etch.

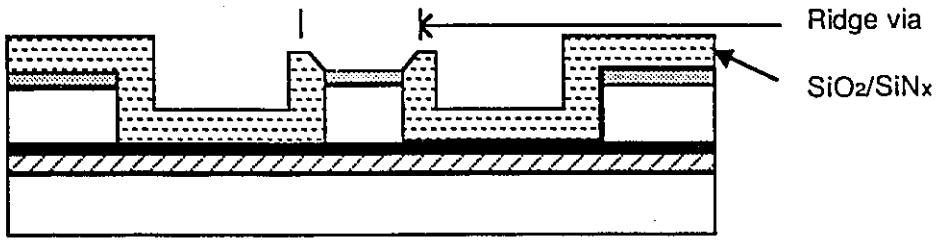

d) Deposition of p metal contact, substrate lap and polish, n metal contact

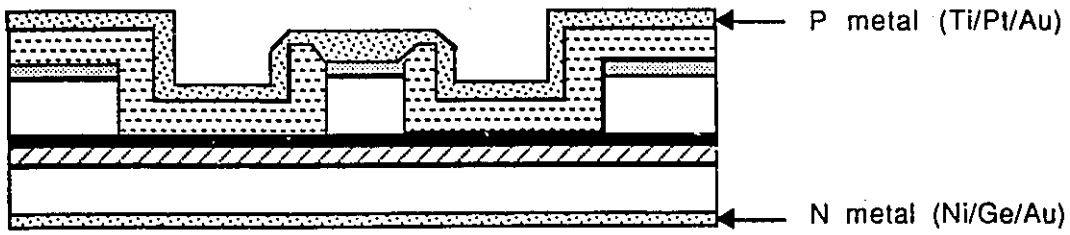

Figure 6.1: Schematic illustration of the laser fabrication process.

from each wafer, were mounted for further testing. The devices were mounted by bonding them p-side up onto gold-plated SiC heat sinks (using 80% Au / 20% Sn solder), which were, in turn, die bonded onto Au-plated copper blocks. The copper blocks were then cemented (using thermally conducting epoxy) onto thermally conducting ceramic sub-carriers. These ceramic subcarriers had Au bonding pads on them to which the p- and n-side contacts of the laser were wire bonded, as shown in Fig. 6.2. Once mounted, CW light-current (L-I), spectral and leakage properties of the devices were measured as a function of temperature, as described in the following sections.

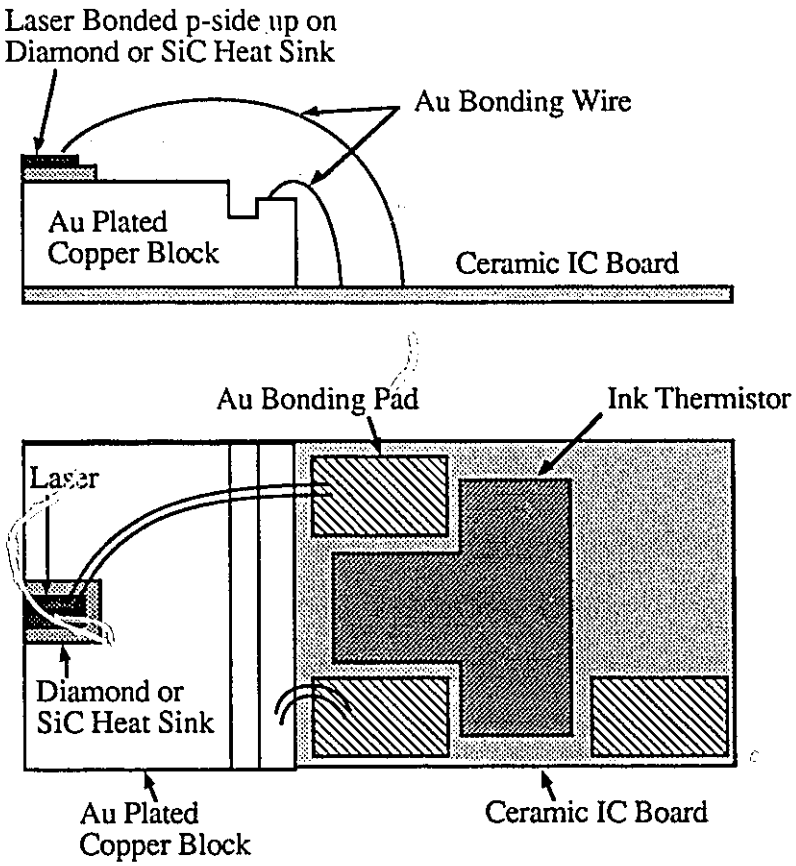

Figure 6.2: Schematic diagram of mounted laser. Lasers were dibonded onto gold plated SiC or Diamond heat sinks which were in turn bonded onto gold plated copper blocks. The copper block was mounted using thermally conducting epoxy onto a ceramic sub-carrier with Au pads for wire bonding. Wire bonds were then made between the laser p- and n-side contacts and the Au bonding pads. During testing contact was made to the Au bonding pads with copper beryllium springs.

6.2 EXPERIMENTAL SET-UP FOR LIGHT-CURRENT MEASUREMENTS

The experimental set-up used to measure the CW L-I characteristics of the lasers as a function of temperature is shown in Fig. 6.3. The lasers were mounted inside a specially designed vacuum chamber to prevent condensation from forming on the devices at the lower temperatures. The base pressure inside this vacuum chamber was about 15 millitorr and was monitored with a convectron vacuum guage. A two stage thermoelectric cooling/heating stage was assembled inside the vacuum chamber to allow for temperature control of the lasers. A photograph of this cooling/heating stage is shown in Fig. 6.4 and the details of it's construction are given below.

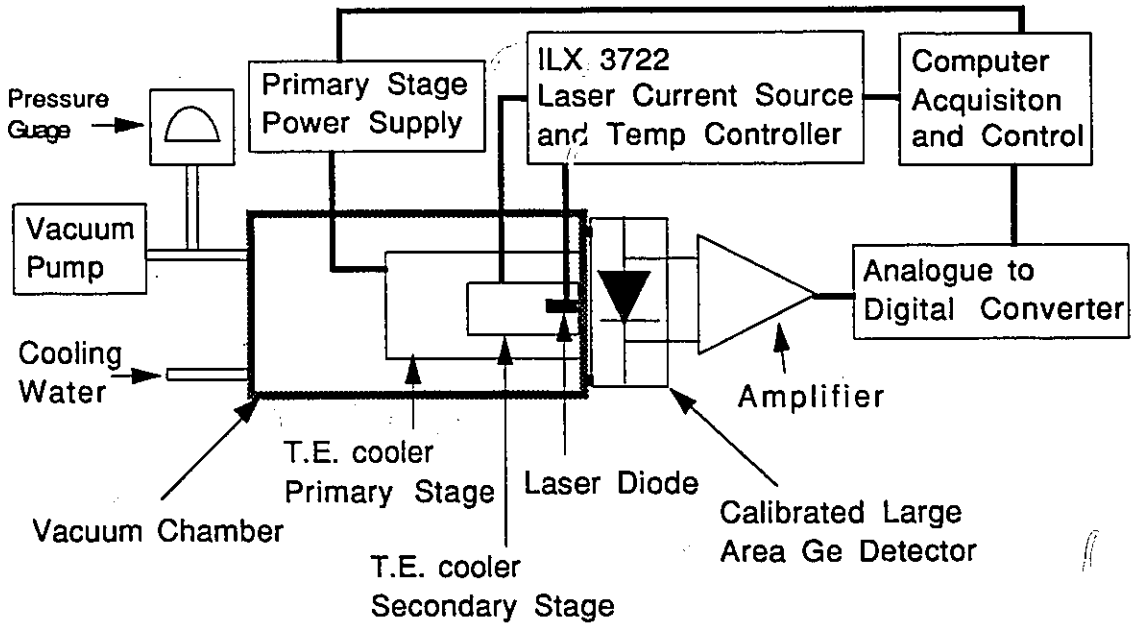

Figure 6.3: Schematic diagram of the experimental set-up used to measure the CW light-current characteristics of the strained and unstrained MQW ridge waveguide lasers.

The primary stage of the two stage cooling/heating apparatus consisted of two thermoelectric coolers mounted in series. One of these coolers had surface dimensions of

20mm x 20mm and a heat pump capability of 16.8 Watts. This thermoelectric (TE) cooler was mounted on top of second TE cooler which had a surface area of 30mm x 30mm and a heat pump capability of 38.5 Watts. One side of this TE stack was contacted to the vacuum chamber base (which was cooled with flowing water) using Wakefield Thermal Compound. The other side of the TE stack was contacted to a copper plate, on top of which was mounted the thermoelectric cooler of the second stage followed by the laser diode mount.

The function of the primary cooling/heating stage was to assist in obtaining low temperature measurements without having the delay times associated with changing the temperature of a large thermal mass. This was accomplished in the following manner. The primary cooling stage kept the copper plate at a constant base temperature. The TE cooler of the second stage was then used to rapidly change the temperature of the laser diode and mount (which has a small thermal mass) over a range of temperatures, ΔT, about the base temperature. The primary cooling/heating stage had an applied current limit of 8.5 Amps and was driven by a Xantrex HPD 15-20 power supply whose output was remotely controlled by applying an analog signal to the back panel. The analog signal was applied to the HPD 15-20 from the digital to analog converter of an SR510 lock-in amplifier, which in turn was connected to the data acquisition computer via an IEEE 488 interface. The temperature of the copper plate was monitored using an AD590 linear thermal sensor. For the low temperature measurements the temperature of the copper plate was maintained at about -38°C.

The secondary cooling/heating stage, which was mounted on top of the copper plate in contact with the primary cooling stage, consisted of a smaller (dimensions ≈ 11mm x 11mm) thermoelectric cooler on top of which was mounted a copper block and the laser diode. The copper block was machined such that the bonded laser and ceramic sub-carrier

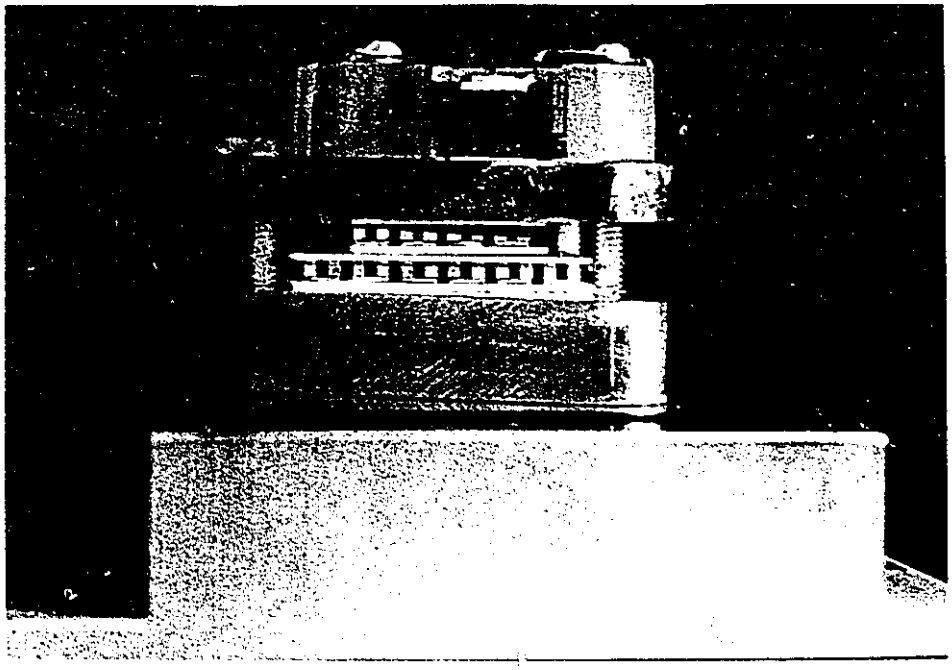

Figure 6.4a: Photograph of the two stage heating/cooling apparatus for controlling the laser temperature.

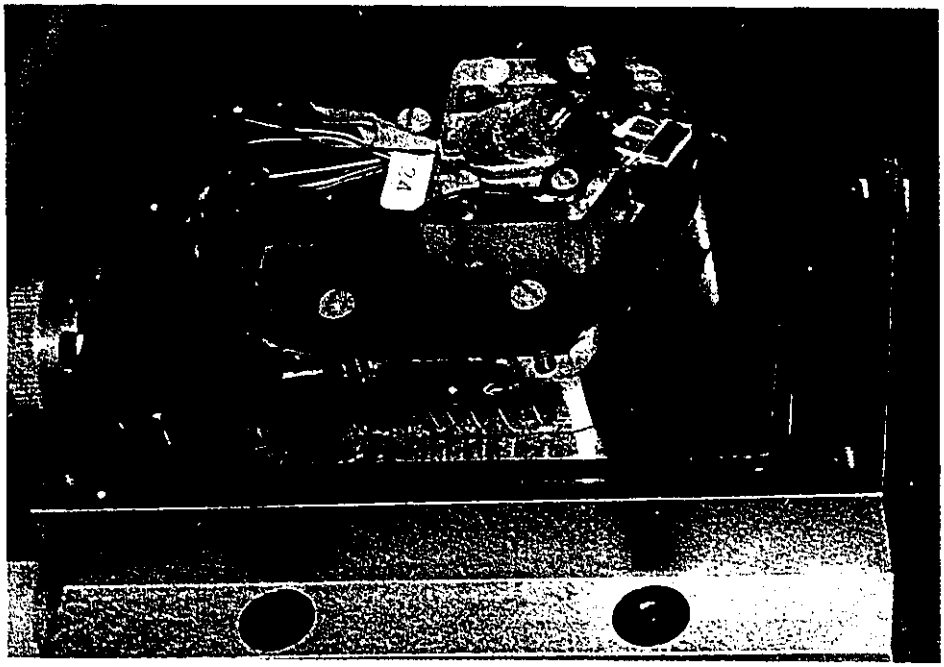

Figure 6.4b: Photograph of the vacuum chamber base with two stage heating/cooling apparatus laser diode and electrical connections shown.

could be accurately positioned with reproducibility inside the vacuum chamber. The TE cooler of the second stage had a current limit of 1.2 Amps, a heat pump capability of 6.67 Watts and a ΔT of 67°C, with the hot side of the TE cooler at 300K. The power to this device was controlled via the ILX 3722 laser driver temperature controller, which was also connected to the data acquisition computer using an IEEE 488 interface.

The combined primary and secondary thermoelectric cooling stage allowed for a minimum laser temperature of ≈-55°C. The temperature of the laser diode heat sink was monitored using a calibrated 10 Kohm thermistor in the temperature range from -10°C to 130°C, and a calibrated 2.252 Kohm thermistor in the temperature range -60°C to -10°C. These thermistors were situated about half a millimeter beneath the laser diodes ceramic carrier. The laser diode and it's ceramic carrier mount were contacted to the copper block in which the thermistors were mounted using Wakefield Thermal Compound.

The current was applied to the lasers using an ILX 3722 laser diode and temperature controller, which was controlled by computer using the IEEE 488 interface. Before making an L-I measurement the laser temperature was held stable to within 0.1°C of the target temperature for at least 10 minutes. The accuracy of the temperature measurement was ± 0.2°C.

The light output from the laser diode was collected by a large area ($1cm^2$), calibrated, germanium detector (Germanium Power Devices Corp. GM10HS08) which was situated within 3 mm of the laser diode facet. The detector had a responsivity of 0.6077 A/W at a wavelength of 1370 nm, and was connected across the input terminals of an LF357 OP amp configured to have a gain variable from $1x10^2$ to $2x10^6$ V/A. The output voltage from the detector circuit was digitized using the analog to digital (ADC) converter of an SR510 lock-in amplifier, the output of which was read by computer over the IEEE 488 interface. The ADC used 13-bit quantization and had a maximum input voltage of 10.24V. These specifications translate into a voltage resolution of 2.5mV, and

with the gain of the detector circuit set at 2 V/mA, a laser diode output power resolution of ≈1 μW. The maximum current that could be applied to the laser diodes was limited to 400 mA; however, once the laser output power (≈9mW) was sufficient to create a detector voltage at the inputs of the ADC of 10 V, the current to the device was shut off. The current to the diode was shut off at this point since the voltage input limit for the ADC was only 10 V. In addition, the detector circuit saturated at only a few volts above this value.

6.3 EXPERIMENTAL SET-UP FOR SPECTRAL AND LEAKAGE CURRENT MEASUREMENTS

Since the peak output wavelength of the laser diode changes as a function of temperature, in order to obtain a calibrated L-I characteristic (using the calibrated Ge detector), it was necessary to know the dominant emission wavelength of the laser as a function of temperature. Therefore, the output spectrum of each laser was measured as a function of temperature. The experimental set-up used to perform these measurements is shown in Fig. 6.5.

The experimental set-up shown in Fig. 6.5 is fundamentally similar to that shown in Fig. 6.3 save for the following differences. The light output from the laser diode, instead of being directly detected by a Ge detector, was collimated using a laser diode collimating lens and focused onto the entrance slit of an f/8.6, 0.5 meter, Jarrell-Ash Monospec 50 scanning monochromator with a dispersion of 3.2 nm/mm. The light at the output slit of the monochromator (which was calibrated using a mercury vapor lamp) was then detected using an InGaAs photodiode. The InGaAs detector had a responsivity of about 0.84 A/W, and the gain in the detector circuit could be adjusted from $1x10^2$ to $2x10^7$ V/A. In order to obtain a good signal to noise ratio, the light output from the laser diode was chopped for phase sensitive detection by an SR510 lock-in amplifier. Finally, the

laser diode was not mounted inside a vacuum chamber for the spectral measurements; consequently, the base temperature of the laser diode heat sink was limited to about 10°C. Due to this limitation, the dominant emission wavelengths of the laser diodes below 10°C had to be obtained by interpolation using a least squares linear fit to the wavelength *vs.* temperature data above 10°C.

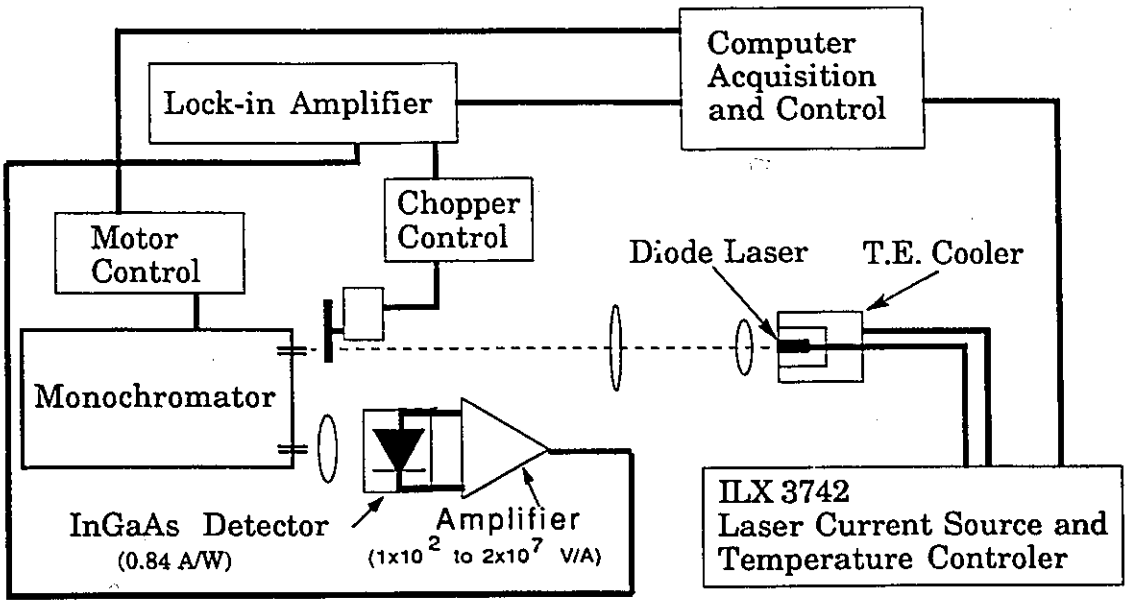

Figure 6.5: Schematic diagram of experimental set-up used to perform spectral measurements. In this figure an ILX 3742 laser driver and temperature controller is shown in place of the ILX 3722. The ILX 3742 is similar to the ILX 3722, save the maximum output current is 3 Amps instead of 500 mA, and current steps are limited to 0.1 mA.

As with the L-I characterization facility, the measurement of the laser diodes spectral characteristics was fully automated. Monochromator control was accomplished using an RS-232 interface connected to an SX Series Compumotor stepping-motor. This stepping motor had a resolution of 25000 steps/revolution, or 2500 steps/nm, which allowed for fine wavelength control.

6.4 EXPERIMENTAL RESULTS: CW L-I AND RELATED CHARACTERISTICS

From the measurement of the CW light-current characteristics of a laser diode as a function of temperature one can obtain information on the temperature sensitivity of the threshold current (T_o) and the external quantum efficiency of the device. By measuring these properties as a function of device length it is then possible to determine, not only the length dependence of these quantities, but also to extract information about how the internal quantum efficiency, η_i, and the internal absorption loss, α_{loss}, change as a function of temperature.

In this thesis, the CW L-I characteristics as a function of temperature for devices of various lengths, strain, and quantum well width were measured in order to determine how quantum well dimensions and, in particular, strain can affect the temperature dependence of both α_{loss} and η_i (and therefore leakage currents as explained in §3.4). The effects of strain and quantum well width on the α_{loss}-T and η_i-T relations were then correlated to any observed changes in the temperature sensitivity of the device threshold current (i.e., T_o).

One of the objectives of this research was to attempt to reduce the temperature sensitivity and to increase the maximum operating temperature of long wavelength laser diodes through the application of strain. Another objective was to attempt to gain further insight, through empirical examinations, into the physical mechanisms primarily responsible for the temperature sensitivity of these devices.

6.4.1 Effects of Strain on Temperature Sensitivity of Laser Threshold Current

As discussed in Chapter 3, the threshold current of long wavelength lasers is very sensitive to temperature, and this temperature sensitivity can be problematic when these

lasers are used in optical communications systems. Therefore, it is desirable to decrease this temperature sensitivity as much as possible. It is predicted that the use of strained quantum wells may be one means of improving the temperature sensitivity of the laser threshold current; however, to date there have been few reports of such improvement. An example of the temperature variation of the light-current characteristics of long wavelength lasers, specifically of a 250 μm cavity length strained quantum well laser from structure R1-394, is shown in Fig. 6.6.

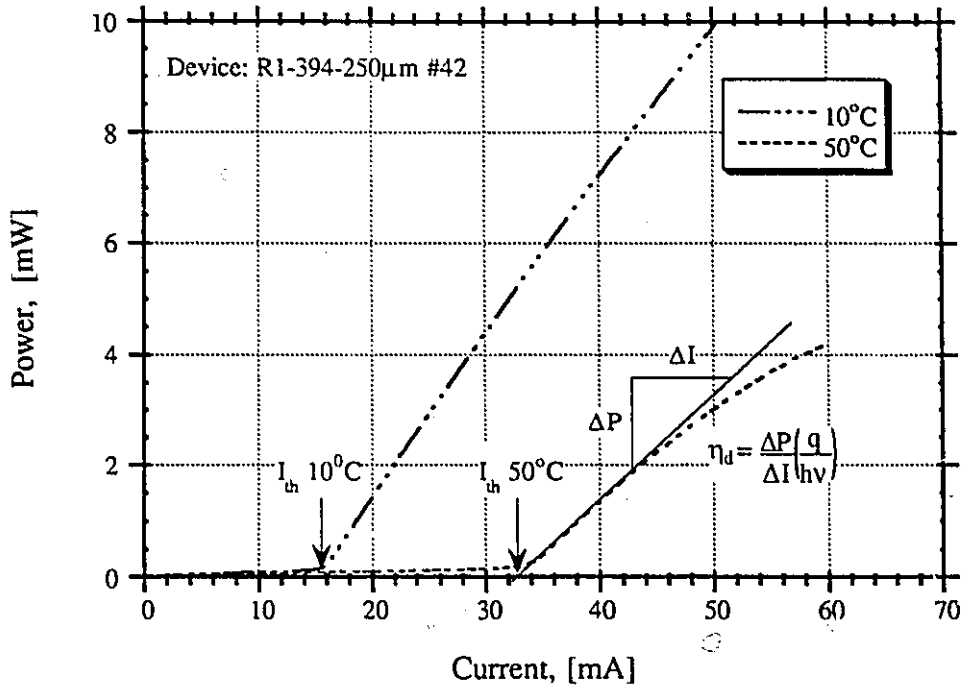

Figure 6.6: L-I characteristics at 10°C and 50°C for strained quantum well laser structure R1-394, which has five-38 Å thick QWs in the active region. The cavity length of this device was 250 μm. Shown in the figure are the determination of the differential quantum efficiency and the laser threshold current.

Figures 6.7 and 6.8 show a comparison of the temperature sensitivity of the laser threshold current between unstrained and strained quantum well lasers. The threshold current for the devices shown in these figures, as indicated in Fig. 6.6, was found by performing a least squares linear fit over the linear region of the L-I curves (between 0.22

mW output power and ≈2 mW output power) and finding the intercept of the best fit line on the current axis.

Fig. 6.7 illustrates the I_{th}-T relations obtained for the unstrained (R1-396) and the 1.5% compressively strained (R1-394) lasers structures, both of which have five 38 Å thick quantum wells. Also shown in the Fig. 6.7 are the I_{th}-T relations obtained for two device lengths from each structure (250 μm and 1000 μm). Listed by each curve is the characteristic temperature, T_o, as obtained from a fit of (1.1.1) to the data over the temperature range from 10 to 50°C. The error in these T_o values is ≈± 2 K.

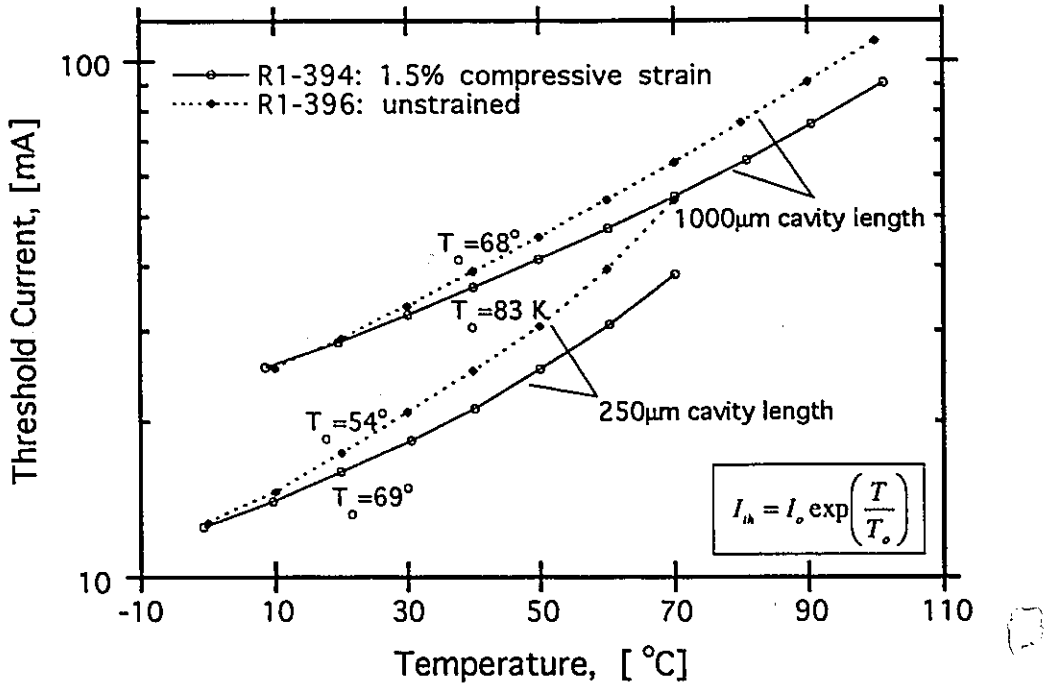

Figure 6.7: Threshold current as a function of heat sink temperature and strain for lasers from Set 2 (five 38 Å thick quantum wells). Shown are the I_{th}-T characteristics for devices with cavity lengths of 250 μm and 1000μm. The 1.5% compressively strained structure has an improved T_o over that of the unstrained structures by ≈ 15 K. In addition, it is seen that the characteristic temperature increases with device length.

From Fig. 6.7, it is clear that the temperature sensitivity of the threshold current of the 1.5%, compressively strained MQW structure is less than that of the unstrained MQW structure indicating improved temperature characteristics for this device. The 1.5%

compressively strained structure has a T_0 (between 10 and 50°C) that is ≈15 K larger than that of the unstrained structure. Since the optical confinement factor, quantum well widths, doping profiles, and GRINSCH regions of these lasers are identical, this improved temperature sensitivity has been attributed to the effects of strain.

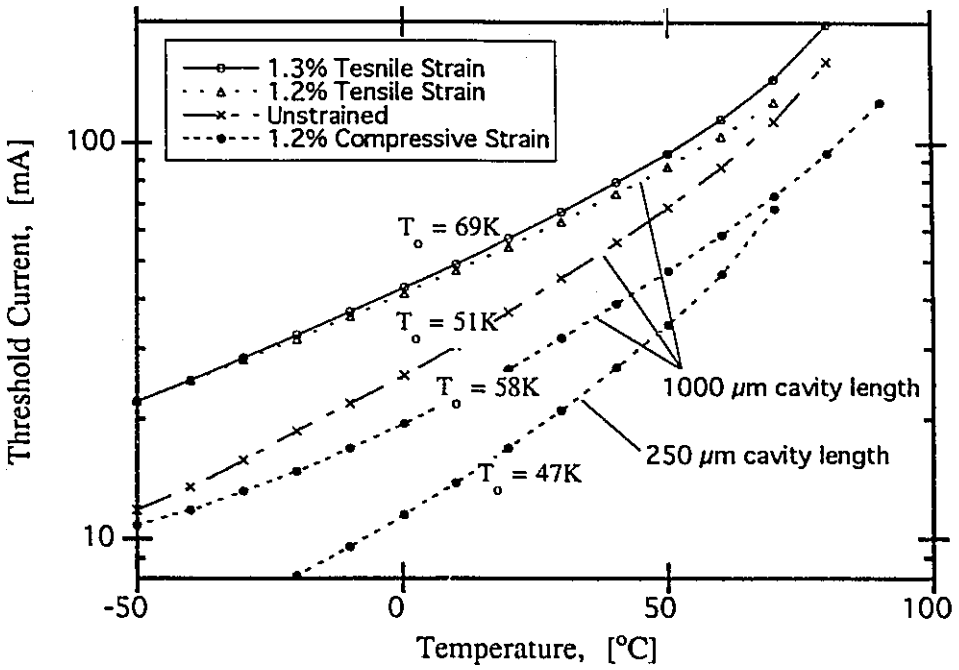

Figure 6.8: Threshold current as a function of heat sink temperature and strain for 1000 μm lasers from Set 1 (three 68 Å thick quantum wells). The 1.2% and 1.3% tensile-strained structures have an improved T_0 (between 0°C and 40°C) over that of the unstrained structure of ≈ 18 K, and a improved T_0 over that of the 1.2% compressively strained structure of ≈11 K. In addition, it is seen that the characteristic temperature increases with device length. Shown for comparison is the I_{th}-T characteristics for a 1.2 % compressively strained devices with a cavity length of 250 μm.

Figure 6.8 illustrates the I_{th}-T relation obtained for the 1.2% and 1.3% tensile-strained (structures R1-397 and R1-398 respectively), the unstrained (R1-400), and the 1.2% compressively strained (R1-399) laser structures with device lengths of 1000 μm. All of these structures, which are from Set 1 (see Table 4.1), have three 64 Å thick quantum wells. Listed by each curve in Fig. 6.8 is the characteristic temperature, T_0, as obtained from a least squares fit of (1.1.1) to the data over the temperature range from 0°C

to 40°C. Also shown in Fig. 6.8 is the I_{th}-T relation for a 1.2% compressively strained structure with a cavity length of 250 μm. As in the case of Fig. 6.7, the error in the T_o values indicated in Fig. 6.8 is approximately ± 2 K.

From Fig. 6.8, it is clear that the characteristic temperature is greater and, therefore, the temperature sensitivity of the threshold current is smaller for the tensile strained laser structures (R1-397 and R1-398) over that of both the unstrained (R1-400) and the compressively strained (R1-399) laser structures. A small improvement in T_o is observed for the 1.2% compressively strained laser structure over that of the unstrained laser structure. This observation is consistent with the observations of an improved T_o of compressively strained over unstrained devices, as shown in Fig. 6.7 for the case of the five QW devices. However, the improvement in T_o for the compressively strained over the unstrained lasers is not as marked for the three QW lasers as it is for the five QW lasers. As for the case of the five QW lasers, since all of the laser structures with three QWs have similar quantum well widths, doping profiles and GRINSCH structures, the improved temperature sensitivity of the tensile strained over the unstrained and compressively strained laser structures is again attributed to the effects of strain.

6.4.2 Threshold Current Density and T_o Dependence on Cavity Length.

Apart from the improvement in T_o for the strained over the unstrained structures, it can also be seen from Fig. 6.7 and Fig. 6.8, that the characteristic temperature and, therefore, the temperature sensitivity of the laser threshold current depends on the cavity length of the device. From Fig. 6.9, it is seen that the characteristic temperature, T_o, increases with cavity length. This observation is contrary to the observations of Zou *et. al.* [1993], but is consistent with those of Leopold [1987], and Hagen *et. al.* [1990]. However, it should be noted that T_o does not increase indefinitely with an increase in cavity

length but becomes essentially constant once the device length exceeds between 750 μm and 1000 μm. Note also from Fig. 6.9, that an improved T_o for the strained over the unstrained laser structures is clearly evident for all device lengths, for laser structures belonging to a given Set (see Table 4.1).

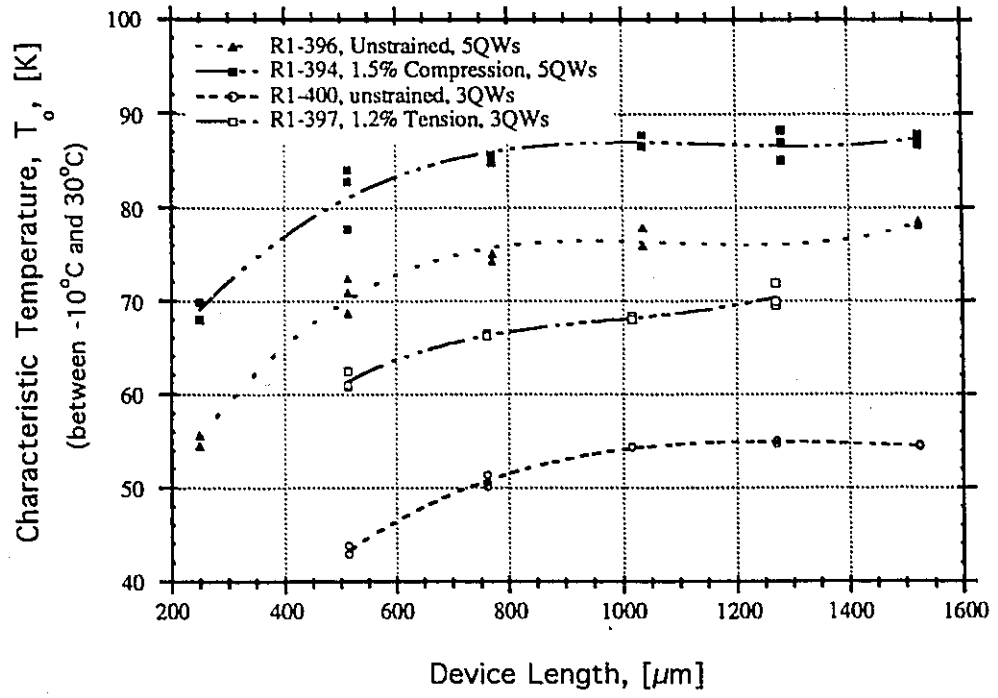

Figure 6.9: Dependence of the characteristic temperature, T_o, on cavity length for device numbers R1-394, R1-396, R1-397 and R1-400. The characteristic temperature is seen to noticeably increase with device length for device length less than between 750 μm and 1000 μm. The curves drawn through the data points are shown only to aid the eye. The increase in T_o as a result of the application of strain is clearly evident in this figure.

Although Leopold did offer an explanation for the T_o dependence on cavity length, his explanation was based on the premise that the optical gain varied linearly with injected current density and that the loss term, α_{loss}, of (3.2.1) decreased with temperature. As will be shown in this Chapter, neither of these premises can be assumed to be strictly valid for quantum well lasers. Therefore, no reasonable explanation for the T_o dependence on the cavity length has been given to date. I now propose two possible explanations for the

cavity length dependence of T_o. One of these explanations is based on the premise that (i) the temperature dependence of the optical gain is primarily responsible for the I_{th} dependence on temperature. The other is based on the premise that (ii) the leakage currents are primarily responsible for the temperature dependence of I_{th}.

(i) **The role of optical gain in the T_o *vs.* Length Dependence:** If the temperature dependence of the optical gain contributes significantly to the temperature sensitivity of the laser threshold current (as discussed in §3.1), then this sensitivity could be reduced, and T_o increased, by decreasing the threshold gain condition, by reducing optical losses. From (2.2.31) one way to reduce the optical losses, and therefore to reduce the threshold gain, g_{th}, (and the temperature sensitivity of I_{th}), is to reduce the distributed mirror losses (as described by the term $[2\Gamma L]^{-1}\ln(1/R_1R_2)$ in (2.2.31)). From (2.2.30) the distributed mirror losses, and therefore the temperature sensitivity of I_{th}, can be decreased by increasing the cavity length, L. However, since the contributions of the distributed mirror losses to g_{th} decrease with increasing L, these losses become less important in comparison to the contributions of the other loss terms, α_{int} and $\alpha_{ext}(1-\Gamma)/\Gamma$ as the cavity length increases. So no further improvements in T_o should be observed for an increase in the cavity length beyond a certain value, as observed in Fig. 6.9.

(ii) **The role of leakage currents in the T_o *vs.* length Dependence:** If the primary cause of the high temperature sensitivity of the laser threshold current in long wavelength lasers is due to leakage currents, as proposed in §3.6 and §3.7, then another possible explanation for the increase in T_o with cavity length could be as follows: It has commonly been observed that the threshold current density of semiconductor lasers is a strong function of the device length, L [Osinski, 1992], [Beernink, 1989], [Coleman, 1992],[Zhang, 1992]. Using the theoretical dependence of the optical gain *vs.* current density [McIlroy, 1985],[Makino,1990], [Rozenzweig, 1991]:

$$g = \beta J_o Ln(J/J_o) \tag{6.4.1}$$

where, β is the gain coefficient and J_0 is the transparency current density, it may be shown that the threshold current dependence on cavity length for quantum well lasers is given by [Coleman, 1992], [Rozenzweig, 1991]

$$J_{th} = \frac{J_o}{\eta_i} \exp\left(\frac{\alpha + L^{-1} \ln(1/R)}{\Gamma \beta J_o} \right) \tag{6.4.2}$$

where, η_i is the internal efficiency and Γ is the optical confinement factor. Therefore, as the cavity length increases the threshold current decreases and asymptotically approaches a constant value. This trend is shown in Fig. 6.10 where the threshold current density for lasers fabricated from the unstrained MQW device structure R1-396 is plotted *vs.* cavity length. The dashed curve in Fig. 6.10 is from a fit of (6.4.2) to the data where α_{loss} has been taken to be 15 cm^{-1}, J_o/η has been determined to be 1030±18 A/cm^2, and $\Gamma\beta J_o$ has been determined to be 403±7 cm^{-1}.

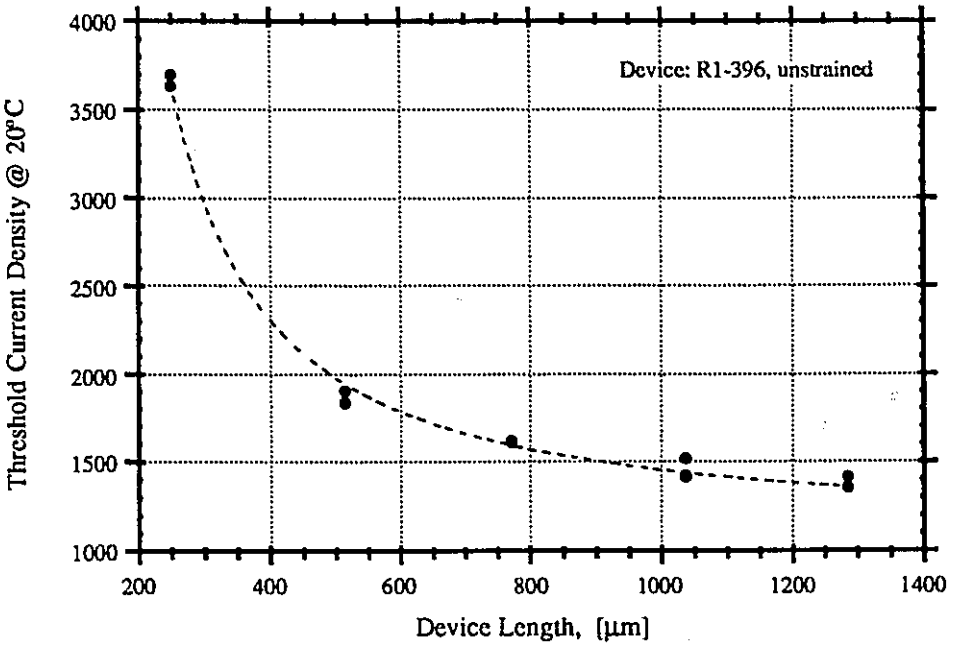

Figure 6.10: Threshold current density at 20^0C vs. cavity length for unstrained MQW laser R1-396. The dashed curve is a fit to (6.4.2) where α= 15 cm^{-1}, J_o/η = 1030 A/cm^2 and $\Gamma\beta J_o$ = 403 cm^{-1}.

As shown in Fig. 6.10, the threshold current density approaches a constant value as the cavity length increases. From (2.2.32) this requires the carrier density, N_{th}, and thus, the quasi-Fermi levels to approach limiting values as the cavity length increases. Also, the quantities n_b in (3.6.4) and n_{ex} in (3.7.2) approach constant values. Since the thermionic leakage current, as given by (3.6.4), and the Auger recombination induced energetic carrier leakage, as given by (3.7.4), are directly proportional to n_b and n_{ex}, respectively, it is expected that the magnitude of the leakage currents, and also their temperature dependence at a given N_{th}, should approach limiting values as the cavity length increases. Since from Fig. 6.10, (2.2.32) and the above arguments, the threshold carrier density, N_{th}, decreases as the cavity length increases, the contribution of the leakage current, and therefore the temperature dependence of the leakage current, to the total threshold current density, and its temperature dependence, will be reduced as the cavity length increases.

6.4.3 Determination of the Strain and Temperature Dependence of α_{loss} and η_i.

It is commonly accepted that the external differential quantum efficiency, η_d, for a laser just above threshold is given by the relation of (3.2.4) [Agrawal, 1986], [Temkin, 1990, 1993],[Tsang, 1992], [Matsumoto, 1991] and [Zou, 1993]. By inverting (3.2.4) one obtains the relation:

$$\eta_d^{-1} = \eta_i^{-1}\left[1+\frac{\alpha_{loss}L}{\ln(1/R)}\right]. \tag{6.4.3}$$

From (6.4.3), it can be seen that if one plots the external differential quantum efficiency above laser threshold *vs.* cavity length, it is then possible to obtain the internal quantum efficiency, η_i, from the y-intercept, and the losses, α_{loss}, from the slope. If this procedure is followed for devices at various temperatures, one may then also determine the

temperature dependence of the quantities α_{loss} and η_i. The absorption losses, α_{loss}, and the laser internal efficiency, η_i, are commonly obtained following this procedure by many authors. However, it should be noted that the validity of this procedure for determining α_{loss} and η_i depends on the common assumption that α_{loss} and η_i are independent of device length. The length dependence of these quantities is rarely, if ever, mentioned in the literature [Agrawal, 1986], [Temkin, 1990, 1993],[Tsang, 1992], [Matusmoto, 1991] and [Zou, 1993]. However, in Fig. 6.10, it was seen that the threshold current density, and therefore N_{th}, are quite strongly dependent on device length for device lengths less than ≈700 μm. With J_{th} and, therefore, N_{th}, increasing with decreasing cavity length for short cavity lasers (Fig. 6.10), it is only reasonable to assume that the optical absorption losses (whether they be by free carrier or intervalence band absorption) should depend on the device length. This assumption is reasonable since for the larger values of N_{th} associated with the shorter length devices there will be a greater density of states available in the valence band to participate in intervalence band absorption processes, (i.e., the quantity E_1 in Fig. 3.2 will move further into the valence band). Similarly, it is reasonable to assume that η_i depends on N_{th} and, therefore, device cavity length. This assumption is also reasonable since, from (3.6.7), η_i depends on the leakage current density. The leakage current density, as discussed in §3.6 and §3.7, in turn increases with N_{th}. Therefore, it is expected that η_i should decrease with increasing N_{th} and, consequently, with decreasing cavity length for devices with cavity lengths less than ≈ 700 μm (since from Fig. 6.10 the threshold current density increases dramatically with decreasing device lengths less than 700μm).

Koren *et. al.* [1987] described the dependence of the total internal loss on the carrier density, N, by the relation

$$\alpha_{loss} = \alpha_{sc} + (1-\Gamma)\alpha_{ext} + \Gamma(\alpha_{int} + bN), \qquad (6.4.4)$$

where the active layer loss term in (3.2.1) has been replaced by the quantity, $\Gamma(\alpha_{int}+bN)$, and the term α_{sc} has been added to (3.2.1) to account for additional scattering losses. By assuming the linear gain relation,† commonly given by (cf. (3.6.8)) [Agrawal, 1986] :

$$g = \Gamma a(N - N_t), \tag{6.4.5}$$

where N_t is the transparency carrier density and a is the linear gain coefficient, Koren *et. al.* arrived at the expression:

$$\eta_d^{-1} = \tilde{\eta}_i^{-1}\left[1 + \frac{\tilde{\alpha}_{loss} L}{\ln(1/R)}\right], \tag{6.4.6}$$

where $\tilde{\alpha}_{loss}$ and $\tilde{\eta}_i$ (termed the apparent internal loss, and the apparent quantum efficiency, respectively) are, as given by [Koren *et. al.*, 1987]:

$$\tilde{\alpha}_{loss} = \alpha_{sc} + (1-\Gamma)\alpha_{ext} + \Gamma(\alpha_{int} + bN_t), \tag{6.4.7}$$

and

$$\tilde{\eta}_i = \eta_i(1 - b/a). \tag{6.4.8}$$

From the above relations, Koren *et. al* then determined that the true internal loss is then given by the relation:

$$\alpha_{loss} = \frac{\tilde{\alpha}_{loss} + (b/a)L^{-1}\ln(1/R)}{1 - b/a}. \tag{6.4.9}$$

The "apparent" internal loss, $\tilde{\alpha}_{loss}$ and the "apparent" internal efficiency, $\tilde{\eta}_i$, were determined for the devices studied in this thesis as a function of temperature using (6.4.6). The linear gain relation, as shown by the results of §6.4.6 and (6.4.1), is not valid for quantum well lasers; hence, the shortest cavity length devices were neglected in fitting (6.4.6) to the data, depending on the temperature. They were neglected because it was felt

† This assumption is approximately valid for quantum well lasers only as long as g_{th} is small

that with the higher current densities for these devices, α_{loss} and η_{int} must depend on device length. Therefore, neglecting the short cavity length devices gives some assurance that the threshold current density and, thus, α_{loss} and η_{int}, for all devices from a given structure do not differ over too wide a range. Thus in fitting (6.4.6) to the data, the effects due to variations in device length on the measured internal loss and quantum efficiency are minimized. It is in turn hoped that the "apparent" values obtained for $\tilde{\alpha}_{loss}$ and $\tilde{\eta}_i$ more closely resemble the true loss, α_{loss} and internal efficiency, η_i. Figure 6.11 shows an example of the least squares fit of (6.4.6) to the η_d^{-1} *vs.* cavity length data obtained from the unstrained, five-38 Å thick quantum well, laser structure R1-396 at various temperatures.

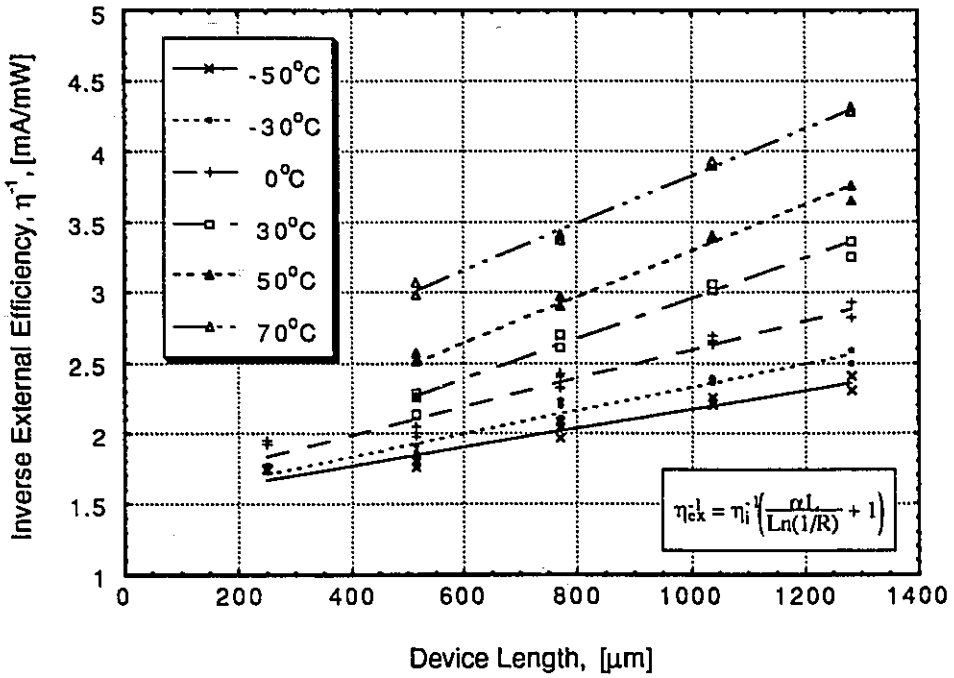

Figure 6.11: Example of the variation of the inverse external differential quantum efficiency, η_d^{-1}, *vs.* device cavity length, L, as a function of temperature. The results shown are for unstrained MQW laser structure R1-396. From the fit of (6.4.6) to the data, the internal device efficiency, η_i, is obtained from the y-intercept, and the absorption loss, α_{loss}, is determined from the slope.

6.4.4 Strain and Temperature Dependence of The Internal Efficiency, η_i.

The internal efficiency, η_i, as a function of temperature was determined for laser structures R1-394, R1-396, R1-397, R1-398, R1-399 and R1-400 using the method described in §6.4.3. The results obtained for structures R1-394 (1.5% compressive strain) and R1-396 (unstrained), which both have five-38Å thick quantum wells, are shown in Fig. 6.12. The results obtained for structures R1-397 (1.2% tension), R1-399 (1.2% compression), and R1-400 (unstrained), which have three-64 Å thick quantum wells are shown in Fig. 6.13. The data from the 1.3% tensile strained device R1-398 was equivalent to that of device R1-397 within experimental error and so the data from this device is not shown in Fig. 6.13 for reasons of clarity.

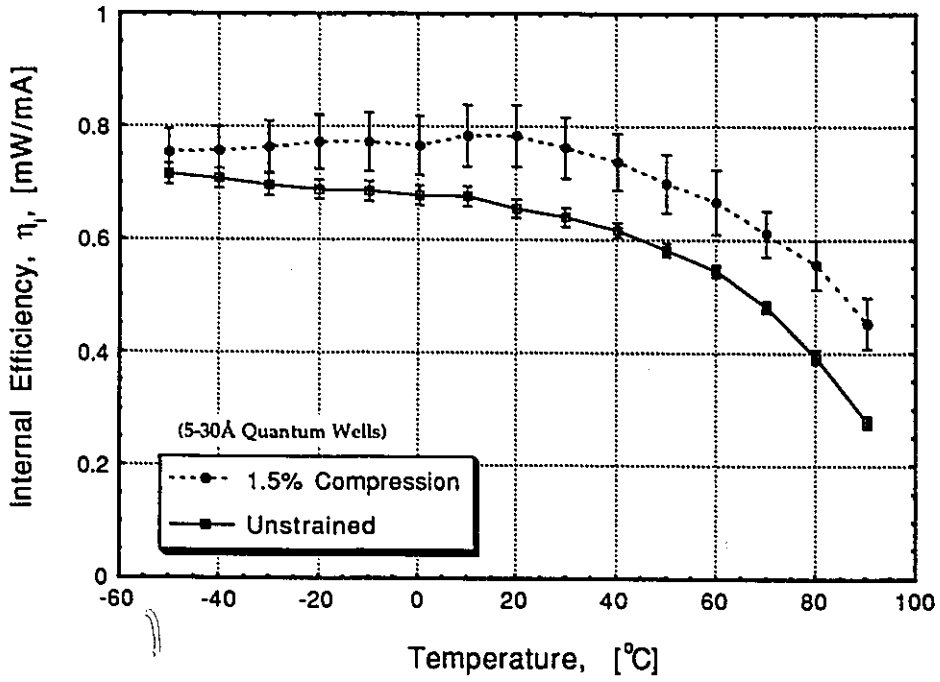

Figure 6.12: Internal efficiency, η_i, *vs.* temperature for 1.5% compressively strained MQW laser structure R1-394 and unstrained MQW laser structure R1-396 as obtained from a fit of (6.4.6) to the η_d^{-1} *vs.* temperature data. Results show that the compressively strained lasers have an improved internal efficiency over the unstrained lasers.

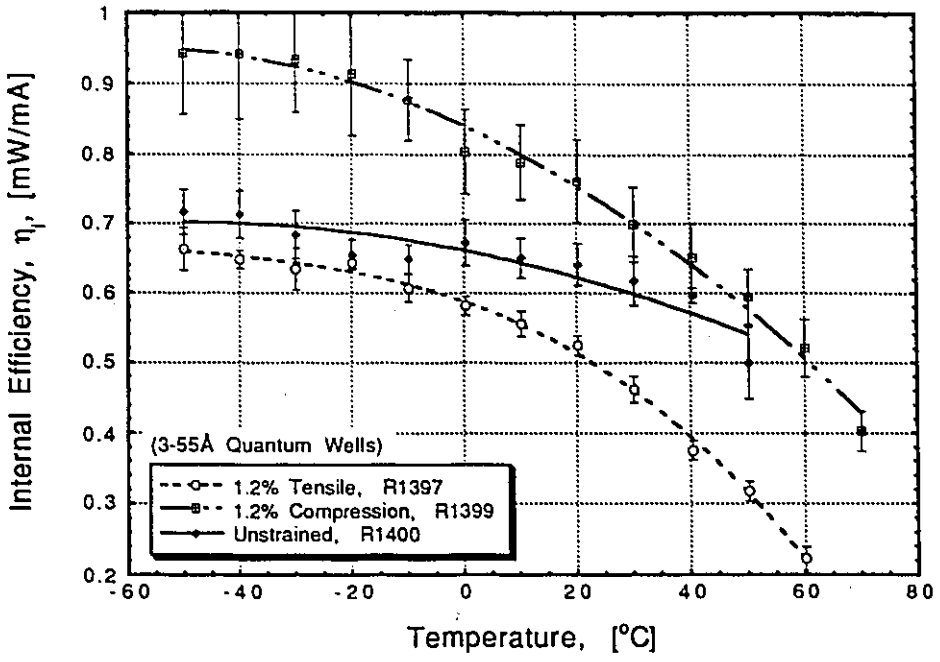

Figure 6.13: Internal efficiency, η_i, *vs.* temperature for 1.2% tensile-strained MQW laser structure R1-397, 1.2% compressively strained MQW lasers structure R1-399 and unstrained MQW laser structure R1-400 as obtained from a fit of (6.4.6) to the η_d^{-1} *vs.* temperature data. As for Fig. 6.12, results show that the compressively strained lasers have an significantly improved internal efficiency over that of the unstrained lasers. The tensile-strained lasers are shown to have the poorest internal efficiency.

From both Fig. 6.12 and Fig. 6.13, it is clear that compressive strain results in an improved internal device efficiency, η_i. At 20°C, the internal efficiency of both the compressively strained devices having 5-38 Å thick QWs, and the compressively strained device having 3-64 Å thick quantum wells was greater than 75%, while that of the unstrained QW lasers having similar geometry was only about 65%. The tensile-strained MQW laser structures having 3-64 Å thick quantum wells had the worst internal efficiency with η_i at 20°C being only about 53% for both device numbers R1-397 and R1-398.

In comparing the temperature dependence of the internal efficiency obtained for devices R1-394 and R1-396 (Fig. 6.12), the internal efficiency of the unstrained device

decreases more rapidly with temperature than that of the compressively strained device below 20°C. However, above 20°C there is no noticeable difference in the rate of change of the internal efficiency with temperature. In comparing the temperature dependence of η_i obtained for devices R1-397, R1-399 and R1-400 (Fig. 6.13), it is clear that the temperature dependence of η_i for the 1.2% compressively strained and the 1.2% tensile-strained MQW lasers is much greater than that for the unstrained laser.

The internal efficiency plotted in Fig. 6.12 and Fig. 6.13 was obtained for devices that are operating just above threshold; therefore, as discussed in §3.2, the radiative lifetime in (3.2.5) will be that of stimulated emission. Since spectral hole burning has been observed in InGaAsP/InP semiconductor lasers [Huang, 1993], [Hayward, 1993] the stimulated radiative lifetime is expected to be on the order of that of the intraband relaxation time (i.e., < 1 ps). The nonradiative lifetime in (3.2.5) has been determined to be on the order of 1 ns [Olshansky, 1984]; therefore, the internal quantum efficiency, η_q, appearing in (3.6.7a), and as given by (3.2.5) is expected to be unity. This result means that the non-unity internal efficiencies seen in Fig. 6.12 and Fig. 6.13 must be a result of leakage currents according to (3.6.7b), and therefore of a non-unity current injection efficiency, η_{inj}. Consequently, the decrease in the internal efficiency, η_i, with temperature must be caused by an increase in the leakage of carriers out of the laser active region with temperature. Therefore, the η_i *vs.* temperature curves of Fig. 6.12 and Fig. 6.13 give an indication of the variation of the leakage currents with temperature.

From the above postulate and Fig. 6.13, it is clear that the magnitude of the carrier leakage, and its temperature dependence, is greater for the tensile strained laser structures R1-397 and R1-398 than for the unstrained laser structure R1-400†. If carrier leakage

† An increased carrier leakage for the tensile strained QW laser structures may be due to a reduced conduction band effective mass (and therefore, ρ_{red}) in these structures which, from (2.2.27), would result in the Fermi level being situated higher up in the conduction band for a given injected carrier density, and also a greater carrier mobility, therefore a greater carrier leakage from (3.4.2) and (3.4.4).

variations with temperature are the primary cause of the low T_0 in InGaAsP lasers, then it follows from the above that the tensile strained quantum well lasers should have an inferior temperature characteristic (low T_0) in comparison to the other devices.

Contrary to the above prediction, from Fig. 6.8 and Fig. 6.9, the characteristic temperature of the tensile strained devices, at all temperatures, is almost 20 K larger (about 35% greater at room temperature) than that of the unstrained devices which show a more gradual variation of η_i with temperature. The temperature variation of η_i (and therefore the leakage current from the above postulate) is also much greater for the 1.2% compressively strained laser structure R1-399 than the unstrained laser structure R1-400. From Fig. 6.8, lasers from structure R1-399 were also found to have a slightly larger T_0 than that found for lasers from the unstrained structure R1-400.

Additionally, the variation of η_i with temperature between -50°C and 40°C, and thus carrier leakage, is almost identical for unstrained lasers R1-400 and R1-396. Yet, from Fig. 6.9, the T_0 values observed for lasers from structure R1-396 (which has five, 38Å thick QWs in comparison to three, 63 Å thick QWs for laser structure R1-400) are much greater than the T_0 values obtained for lasers from structure R1-400 (by ≈17 K). From these results it is *unlikely* that the temperature dependence of the carrier leakage is the primary cause of the low T_0 found in InGaAsP lasers. Although, clearly leakage currents contribute significantly to the value of the threshold current.

It will be recalled from §3.2 that leakage currents can be up to 35 per cent of the total threshold current. Typical values for the carrier leakage have been theoretically and experimentally determined to be between 10 and ≈35 per cent of the threshold current [Chik, 1990], [Chen, 1983]. These observations are consistent with those of Fig. 6.12 and Fig. 6.13 in the context of (3.6.7a).

6.4.5 Strain and Temperature Dependence of The Internal Absorption, α_{loss}.

The results of the variation of the internal optical absorption losses, α_{loss}, as a function of temperature obtained for laser structures R1-394 and R1-396 using the method described in §6.4.3, are shown in Fig. 6.14. Similar results are shown for laser structures R1-397, R1-398, R1-399 and R1-400 in Fig. 6.15.

From Fig. 6.14, and Fig. 6.15, it can be seen that the application of compressive strain has resulted in an increased internal optical absorption loss, α_{loss}, (over the temperature range from -50°C to 30°C) than that found for the unstrained lasers. This observation is contrary to that of some authors [Zou *et. al.*, 1993] but in agreement with that of others [Temkin, 1991],[Mathur, 1993]. From Fig. 6.15, the application of tensile strain has resulted in a reduced α_{loss}, over that found for the unstrained lasers above room temperature.

For laser structures R1-396 and R1-394 from Set 2, α_{loss} increases linearly with temperature between -50°C and 40°C. It is found from a least squares linear fit to the data from Fig. 6.14 over this same temperature range, that the rate of increase of α_{loss} with temperature is greater for the 1.5% compressively strained structure than that for the unstrained structure. (The equations from the least squares fit to the α_{loss}-T data over the temperature range from -50°C to 40°C for the strained and unstrained lasers appears above the respective curves in Fig. 6.14). If the temperature dependence of the optical absorption loss is primarily responsible for the low T_o of long wavelength lasers, as proposed by Asada [1981] and Adams [1980], then it would be expected from the results of Fig. 6.14 that the 1.5% compressively strained laser would have a lower T_o than the unstrained lasers

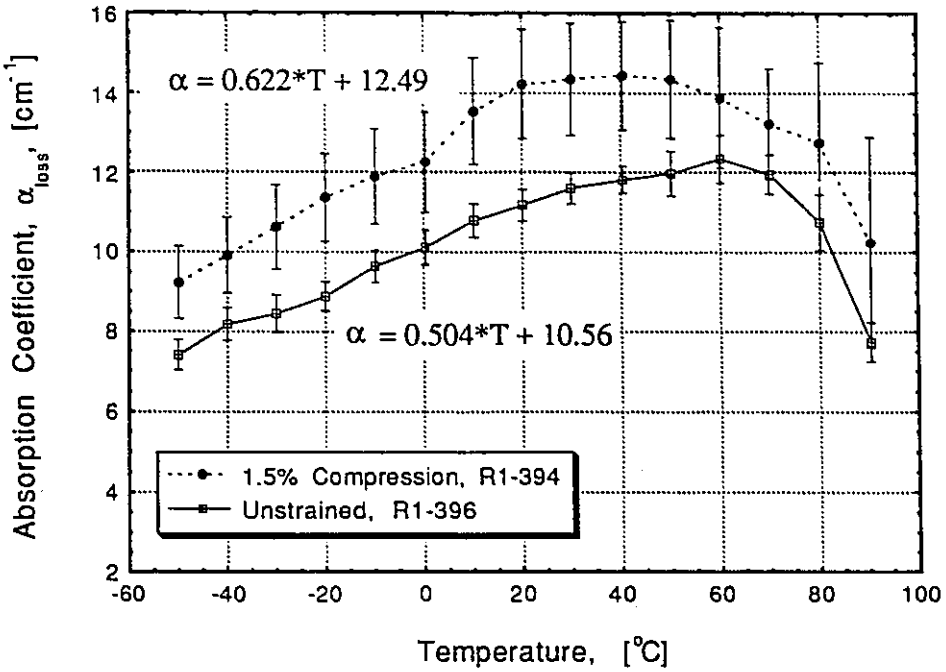

Figure 6.14: Internal absorption coefficient, α_{loss}, *vs.* temperature for strained and unstrained MQW lasers R1-394 and R1-396 from Set 2. Results show that the compressively strained lasers from this set have a higher absorption coefficient which increases more rapidly with temperature than that for unstrained lasers.

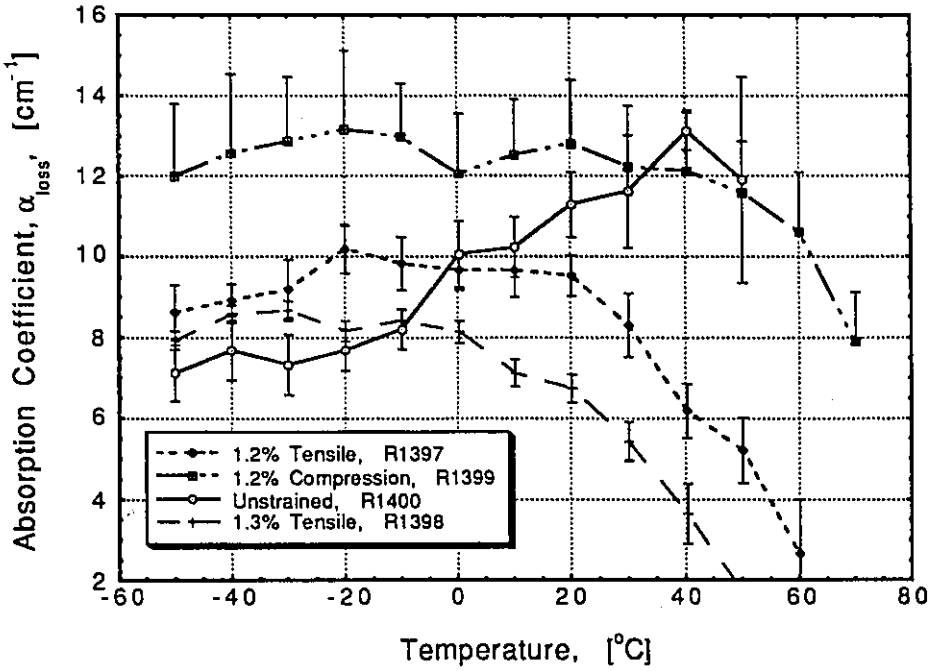

Figure 6.15 Internal absorption coefficient, α_{loss}, *vs.* temperature for laser structures R1-397, R1-398, R1-399 and R1-400 from Set 1. Again, the compressively strained lasers have a higher absorption coefficient; however, in this case, its temperature dependence is less than that for unstrained lasers.

due to the greater temperature dependence of α_{loss} for this structure. In fact the T_o value observed at all temperatures for the compressively strained laser structure R1-394 is much greater than that observed for the unstrained laser structure R1-396 (as discussed in §6.4.3 and shown in Fig. 6.9).

Additionally, from Fig. 6.14 it is seen that beyond 40°C, α_{loss} decreases with an increase in temperature for both the strained and the unstrained lasers. A decrease in α_{loss} with temperature is also seen for the tensile- and compressively-strained laser structures above 0°C in Fig. 6.15. From the I_{th} *vs.* T data of Fig. 6.8 it is seen that the temperature sensitivity of the laser threshold current actually gets worse (T_o decreases) with an increase in temperature above 0°C. If an increase in α_{loss} with temperature was primarily responsible for causing the temperature sensitivity of I_{th}, then from the observations of Fig. 6.15, one would expect T_o to get larger, not smaller as the temperature increased. Therefore, from these observations it is *unlikely* that the temperature dependence of α_{loss} is a major factor in determining the temperature sensitivity of the laser threshold current in long wavelength lasers.

It should be noted that ,while a decrease in α_{loss} with temperature in QW lasers has been observed by other authors [Leopold], it is possible that the observed decrease in α_{loss} with temperature in Fig. 6.14 and Fig. 6.15 is a result of the short cavity effects discussed in §6.4.1 and shown in Fig. 6.10: For short cavity lasers, the larger N_{th}, as discussed §6.4.1, may cause a decreased injection efficiency and increased absorption in these lasers. An increase in these parameters would in turn cause η_d to decrease, and therefore η_d^{-1} to increase for the short cavity length devices. As a result, the slope of the η_d^{-1} *vs.* L curve may tend to get shallower and, therefore, the measured α_{loss} to be smaller than would otherwise be the case if α_{loss} and η_i were truly cavity length independent. However, as mentioned in §6.2.1, precautions were taken to eliminate these effects by not including the

data for the shortest length devices in the fit to the η_d^{-1} *vs.* L curves at the higher temperatures. It should also be mentioned that the results of other authors are obtained using the same method as that used to determine α_{loss} and η_i in this thesis, as described in §6.4.3. Therefore, data appearing in other publications will suffer from the same possible sources of error.

6.4.6 Strain and Temperature Dependence of The Peak Material Gain *vs.* Current Relation.

The peak material gain of the quantum well laser structures studied in this thesis was determined using the method of Hakki and Paoli [1973,1975],[Agrawal, 1986]. This technique, which is widely used [Westbrook, 1986], [Tanbun-Ek, 1991], [Zou, 1993], involves measuring the depth of modulation of the Fabry-Perot modes in the sub-threshold emission spectra of the laser which are caused by the laser cavity resonances. A simple mathematical relationship exists between the single-pass optical gain of the laser medium and the ratio of the emission intensities measured at the optical frequencies which satisfy the resonant and antiresonant conditions of the laser cavity (i.e., the maximum and minimum intensities of the Fabry-Perot modes). This relationship is given by the equation:

$$\Gamma\bar{g} = \frac{1}{L}\ln\left(\frac{r^{1/2}-1}{r^{1/2}+1}\right) + \frac{1}{L}\ln\left(\frac{1}{R}\right), \tag{6.4.10}$$

where, R is the facet reflectivity, L is the cavity length of the laser, and r is the depth of modulation given by:

$$r = \frac{P_i^+ + P_{i+1}^+}{2P_i^-}, \tag{6.4.11}$$

where P_i^+ and P_{i+1}^+ are the intensities of the i^{th} and the $(i+1)^{th}$ cavity resonances, respectively, and P_i^- is the measured intensity at the i^{th} antiresonance (i.e., valley) between P_i^+ and P_{i+1}^+.

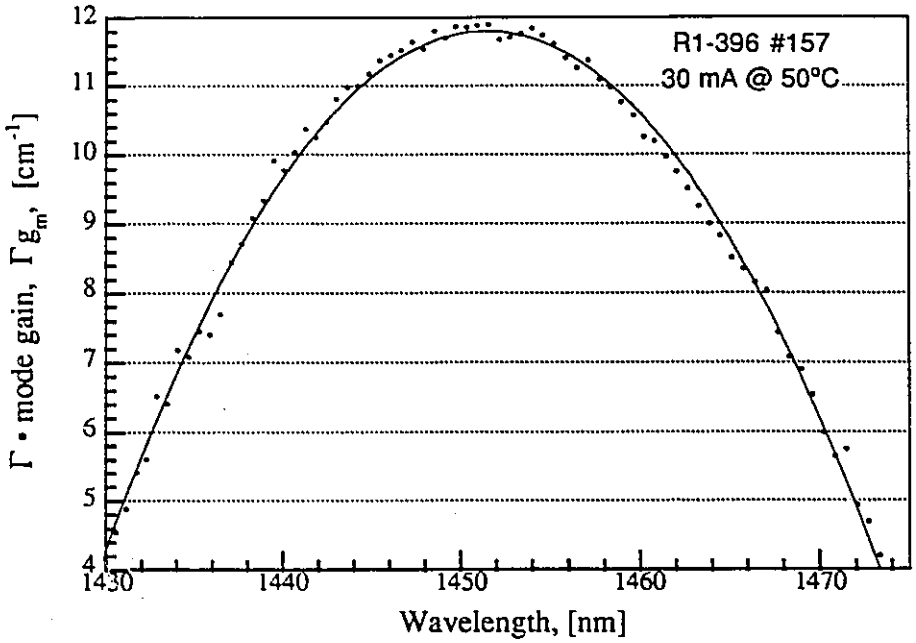

Figure 6.16: Example of Γ x mode gain, g_m, *vs.* wavelength as obtained for 500 μm length unstrained laser structure R1-396 at a drive current of 30 mA and a temperature of 50°C

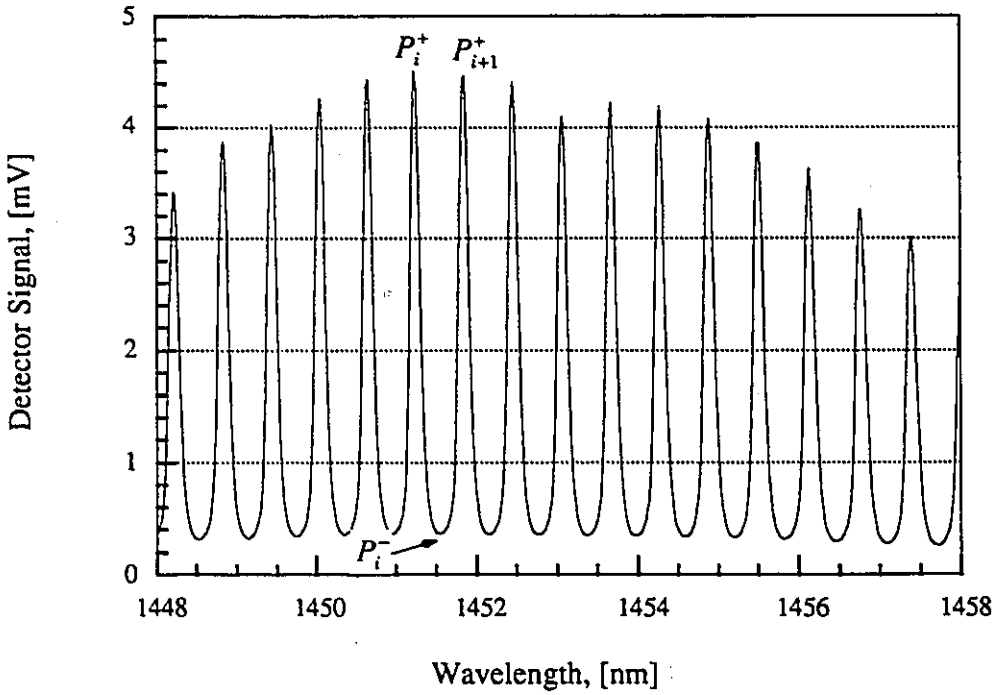

Figure 6.17: Example of the output spectrum of 500 μm length laser structure R1-396 used to determined the $\Gamma \cdot g_m$ *vs.* λ data of Fig. 6.16. Labeled are the peak of the i^{th} and $(i+1)^{th}$ Fabry-Perot resonance and the i^{th} antiresonance.

Before presenting the results of the peak gain *vs.* current measurements, it should be noted that Cassidy [1984] has determined that improvements could be made to the Hakki and Paoli measurement technique and, thereby, a more accurate measurement of the gain of a given laser mode could be made. These improvements involve, firstly, taking the ratio, not of the peak mode intensity to the intensity at the anitresonant minimum of the spectrum, but by taking the ratio of the integrated intensity over a region corresponding to one free spectral range to the minimum intensity. A second improvement involves measuring and deconvolving the monochromator response from the measured spectrum. Neither of these techniques was implemented for the measurements taken for this thesis. The result of these omissions will be to underestimate the peak material gain by about 14%, [Cassidy, 1984]. Nevertheless, a comparison of the peak material gain *vs.* injection current and temperature is still valid for the structures studied in this thesis since the above omissions result in a systematic error which is equivalent from measurement to measurement.

The gain measurements for this thesis were taken using the experimental apparatus shown in Fig. 6.5. The detector gain for all measurements was $\approx 1.7 \times 10^4$V/mW, and the monochromator slits were set at 40 μm. Temperature control was achieved as described in §6.2 and the temperature was varied between 10°C and 90°C depending on the laser structure. An example of the calculated mode gain *vs.* wavelength curve for a 500 μm length device from laser structure R1-396, and the spectrum used to obtain this curve are shown in Fig. 6.16 and 6.17 respectively.

The position (wavelength) of the antiresonance (minimum intensity) of the Fabry-Perot modes shown in Fig. 6.17, due to noise considerations, was obtained by finding the wavelength of the resonance modes (peak intensity) on either side of the minimum and dividing by two. The wavelength corresponding to the peak intensity was obtained by fitting a quadratic to the spectrum about the peak intensity and taking the position of the

maximum. The value of the peak material gain was obtained by fitting a quadratic to the mode gain *vs.* wavelength data, as shown in Fig. 6.16, and finding the maximum.

Figures 6.18-6.23 show the measured peak material gain *vs.* sub-threshold drive current for lasers R1-394 through to R1-400 respectively. To accurately determine the effects of strain on the gain relation for these lasers it would be necessary to determine the injected carrier concentration by determining the carrier lifetime at a given injection level. Unfortunately, facilities to perform these measurements were not available. Nevertheless, the rate of change of the peak gain with current, dg/dI, at a measured peak gain of 15 cm^{-1} was determined as a function of temperature and correlated with the temperature sensitivity of the threshold current.

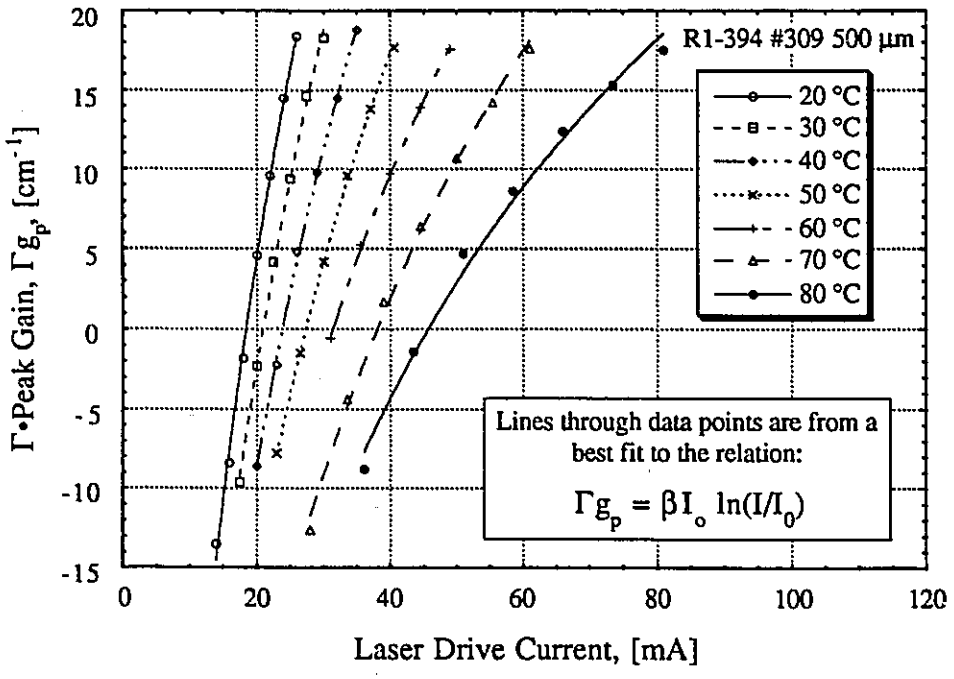

Figure 6.18: Measured Γ x peak material gain, g_p, *vs.* injection current, I, for 1.5% compressively strained QW laser structure R1-394, as obtained from the Fabry-Perot resonances, (6.4.10) and (6.4.11). The cavity length was 500 µm. Best fit line is obtained by fitting data to (6.4.1).

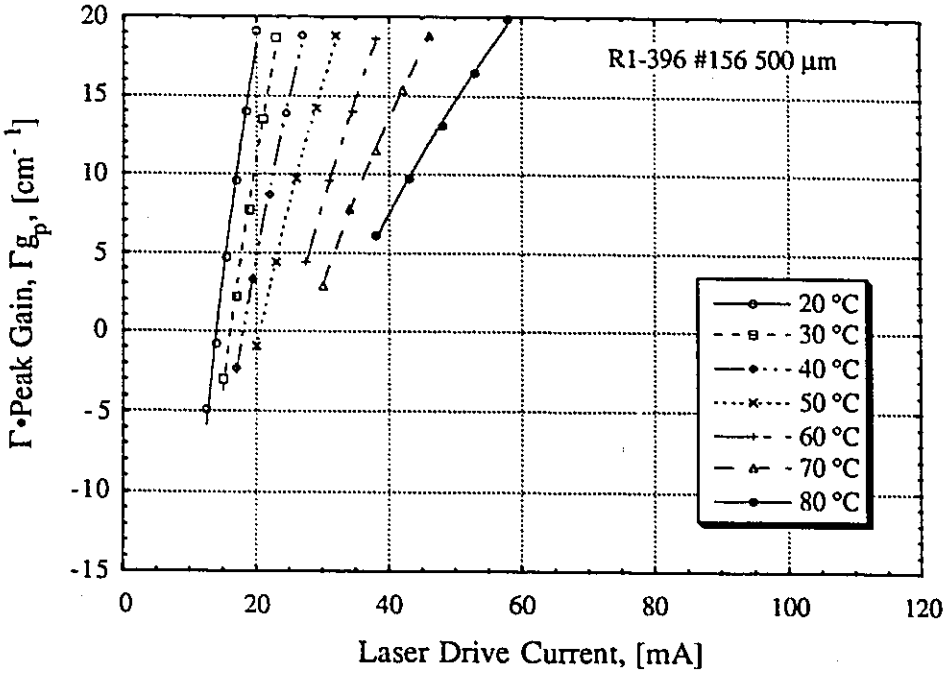

Figure 6.19: Measured Γ x peak material gain, g_p, *vs.* injection current, I, for unstrained QW laser structure R1-396.

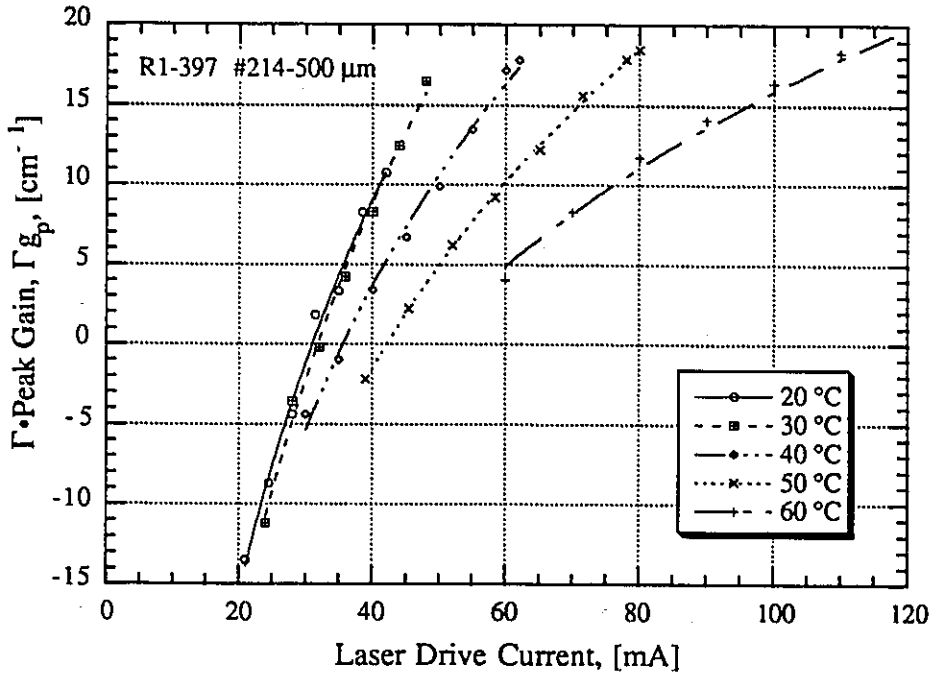

Figure 6.20: Measured Γ x peak material gain, g_p, *vs.* injection current, I, for 1.2% tensile-strained QW laser structure R1-397.

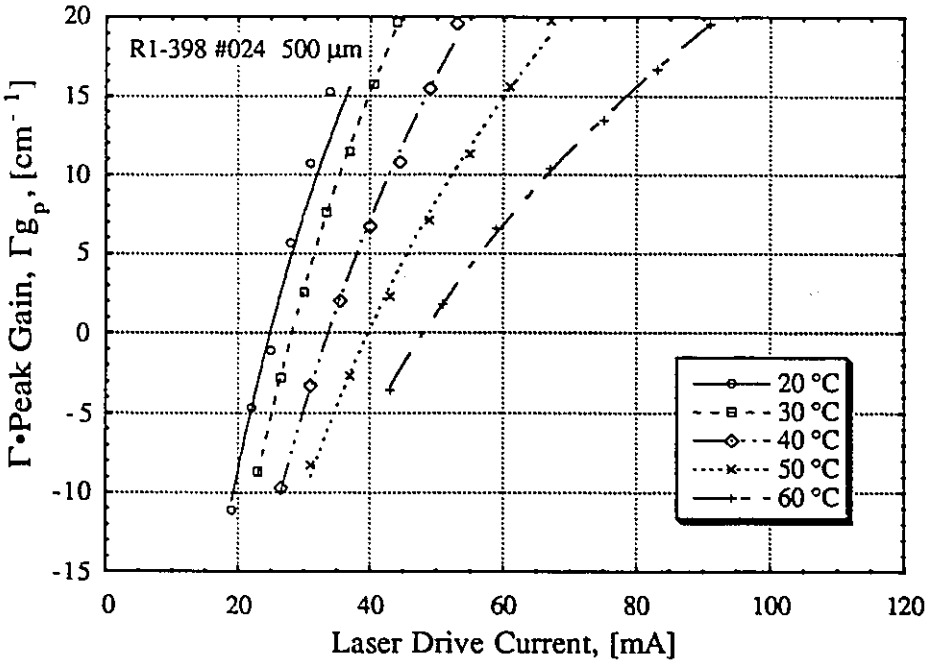

Figure 6.21: Measured Γ x peak material gain, g_p, *vs.* injection current, I, for 1.3% tensile-strained QW laser structure R1-398.

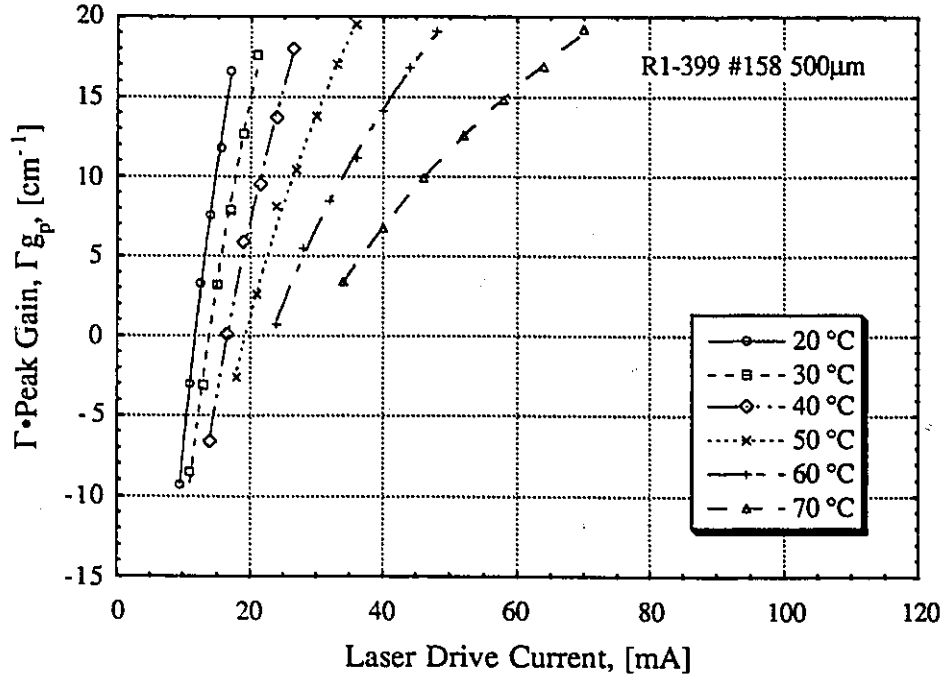

Figure 6.22: Measured Γ x peak material gain, g_p, *vs.* injection current, I, for 1.2% tensile-strained QW laser structure R1-399.

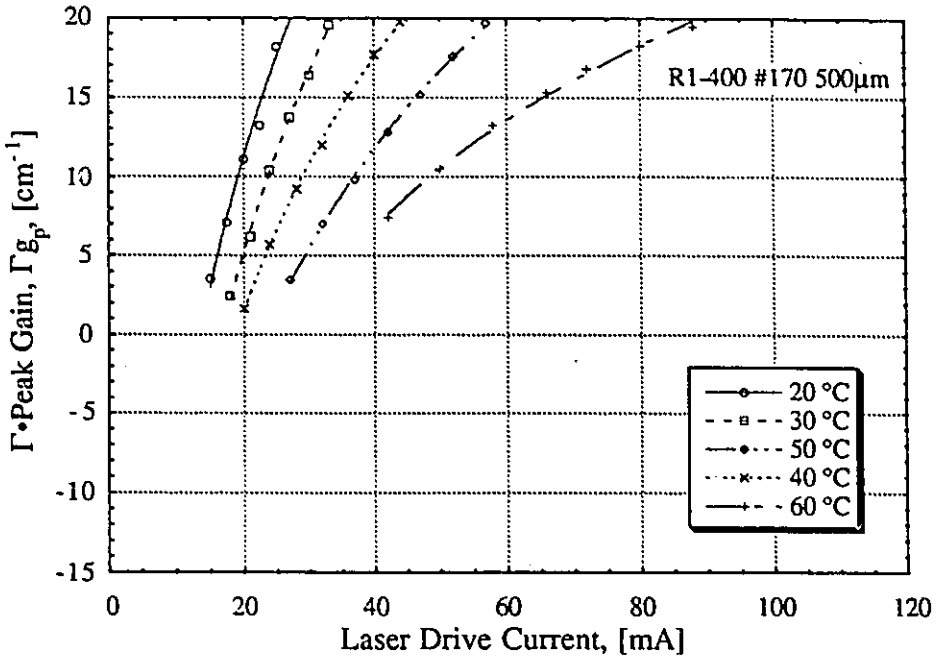

Figure 6.23: Measured Γ x peak material gain, g_p, *vs.* injection current, I, for unstrained QW laser structure R1-400.

Figure 6.24 shows a comparison of the rate of change of dg_p/dI with temperature, $d\left(dg_p/dI\right)/dT$, for the compressively strained and unstrained laser structures R1-394 and R1-396, respectively. Figure 6.25 shows a comparison of the rate of change of dg_p/dI with temperature for laser structures R1-397, R1-399, and R1-400. From Fig. 6.24 and Fig. 6.25, it is clear that strain affects the rate of change of the peak gain with current (dg_p/dI) and the rate of change of dg_p/dI with temperature, ($d\left(dg_p/dI\right)/dT$). This is contrary to the observations of Zou *et. al.* [1993] who determined that strain had no affect on dg_p/dI; however, Zou *et. al.* compared the effects of strain on dg_p/dI for structures with different quantum well thicknesses. From (2.2.23) it is clear that the quantum well thickness will affect the slope of the gain *vs.* carrier concentration profile, and therefore dg_p/dI; consequently, Zou *et. al.* may not have observed any affects on dg_p/dI due to strain as a result of compensating effects due to different QW thicknesses.

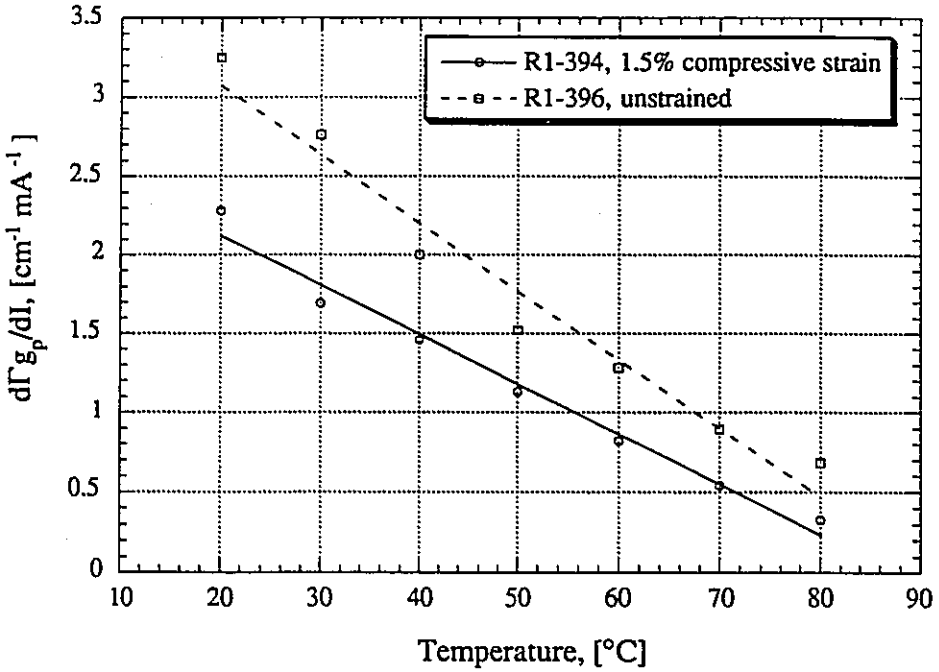

Figure 6.24: Comparison of rate of change dg_p/dI *vs.* Temperature about a peak gain, Γg_p, of 15 cm^{-1} for strained and unstrained lasers structures R1-394 and R1-396, respectively, having active regions containing five 38Å thick QWs.

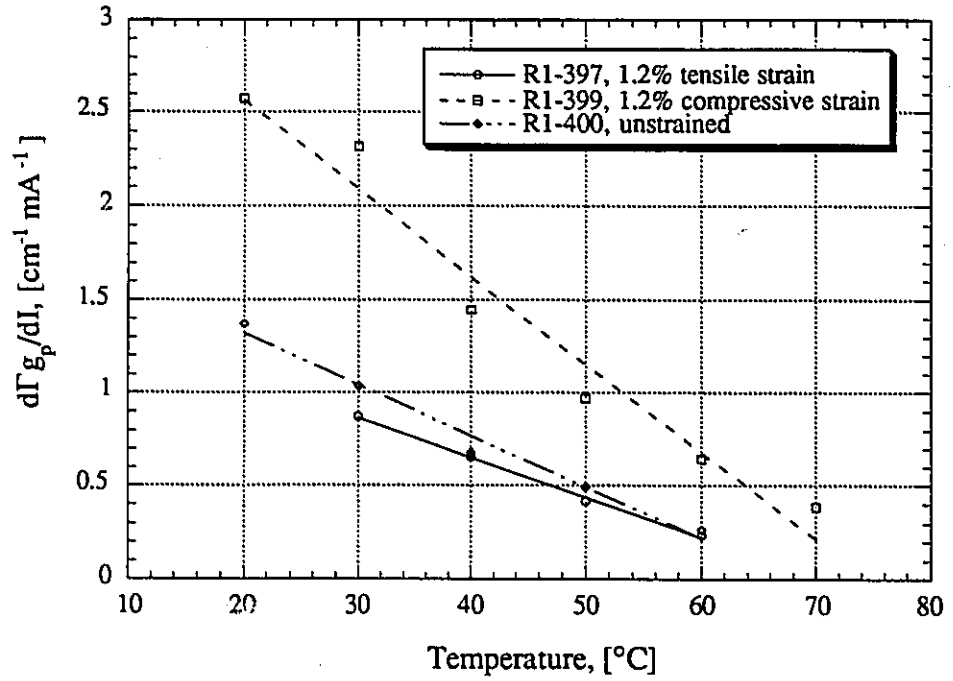

Figure 6.25: Comparison of rate of change dg_p/dI *vs.* Temperature about a peak gain, Γg_p, of 15 cm^{-1} for strained and unstrained lasers structures R1-397, R1-399, and R1-400, having active regions containing three 64Å thick QWs.

Table 6.1: Summary of computed values for: T_o (between 0°C and 40°C); the gain coefficient, β, and transparency current, I_o, (from a fit of (6.4.1) to the Γg_p *vs.* I data); $d\left(dg_p/dI\right)/dT$ (at Γg_p=15 cm^{-1}); and, $d(\lambda_p/\lambda_{max})/dI$ (at 60°C).

Device Structure	T_o (0 - 40°C) for 1000μm device	Gain coeff. β @ 30°C [cm-mA]$^{-1}$	Transparency current I_o @ 30°C, [mA]	$\frac{d\left(d\Gamma g_p/dI\right)}{dT}$ [mA-cm-°C]$^{-1}$	$\frac{d}{dI}\left(\frac{\lambda_p}{\lambda_{max}}\right)$ [mA]$^{-1}$
R1-394 (-1.5%, 5QWs)	88±2K	2.494±.038	20.91±.08	-3.147×10^{-2}	-2.986×10^{-4}
R1-396 (0%, 5QWs)	70±2K	3.169±.112	16.12±.14	-4.339×10^{-2}	-4.369×10^{-4}
R1-397 (+1.2%, 3QWs)	68±2K	1.209±.038	31.8±.27	-2.154×10^{-2}	-2.695×10^{-4}
R1-398 (+1.3%, 3QWs)	69±2K	1.548±.013	28.2±.07	-2.475×10^{-2}	-2.272×10^{-4}
R1-399 (-1.2%, 3QWs)	57±2K	2.925±.078	13.82±.10	-4.697×10^{-2}	-3.805×10^{-4}
R1-400 (0%, 3QWs)	51±2K	1.701±.020	16.68±.14	-2.758×10^{-2}	-3.651×10^{-4}

A summary of the computed values for $d\left(dg_p/dI\right)/dT$, T_o, the gain coefficient, β, and the transparency current (as obtained from a fit of (6.4.1) to the Γg_p *vs.* I data) appears in Table 6.1. In comparing the slope of the dg_p/dI *vs.* temperature relations of Fig. 6.24 and 6.25 with laser structure, and the respective T_o values for these structures, there appears to be an inverse correlation between $d\left(dg_p/dI\right)/dT$ and T_o for laser structures from a given Set. Both laser structures R1-394 and R1-397 have much higher characteristic temperatures in comparison to similar laser structures belonging to the same set. The $d\left(dg_p/dI\right)/dT$ for laser structure R1-394 is ≈30 per cent less than that of laser structure R1-396 and its characteristic temperature is between 20 and 30 per cent larger. This result suggests that the rate of change of material gain with temperature, $d\left(dg_p/dI\right)/dT$, strongly influences the temperature sensitivity of quantum well lasers,

even above room temperature, and that this temperature dependence can be improved through the use of strain.

The rate of change of dg/dI with temperature, $d\left(dg_p/dI\right)/dT$, for laser structure R1-397 is ≈60 per cent less than that of laser structure R1-399 and its characteristic temperature is ≈20 percent larger. Thus, again there is an inverse correlation between the magnitude of $d\left(dg_p/dI\right)/dT$ and the temperature sensitivity of the laser threshold current above room temperature. However, $d\left(dg_p/dI\right)/dT$ is only about 20 per cent less for laser structure R1-397 in comparison to that for laser structure R1-400. Yet, laser structure R1-397 has a T_0 that is about 35 per cent greater than that obtained for laser structure R1-400. The reduced temperature dependence of the internal efficiency (and hence carrier leakage) for laser structure R1-400 in comparison to structures R1-397 and R1-399 (Fig. 6.13), could possibly account for the smaller difference in $d\left(dg_p/dI\right)/dT$ between structures R1-397 and R1-400 than that between R1-397 and R1-399. However, the reduced temperature dependence of the carrier leakage for structure R1-400 in comparison to structure R1-397 (see Fig. 6.13) would also suggest that laser structure R1-400 should have a larger T_0. From this observation, combined with the observed small difference in $d\left(dg_p/dI\right)/dT$ relative to the improvement in T_0 between devices R1-397 and R1-400, it is postulated that there are other factors that contribute to the temperature sensitivity of laser threshold current, apart from the temperature dependence of the optical gain and carrier leakage.

In §5.3.2, it was observed that the shift in the peak PL wavelength, and therefore the bandgap, E_g, with temperature was much smaller for the tensile-strained laser structures than for the other structures. It was also postulated that this observation may be related to an improved T_0 for these structures. This observation is now correlated with those observations regarding the rate of change of dg/dI with temperature, $d\left(dg_p/dI\right)/dT$.

From (2.2.11), the carrier effective mass is proportional to the energy gap of the material. From (2.2.23) the effective mass, through the term ρ_{red} (which is assumed constant for QWs), is also a multiplier that affects the slope of the gain *vs.* injected carrier relation for a quantum well structure. Therefore, as observed in §5.3.2, if the bandgap, and thus the effective mass change more slowly with temperature, then the slope of the gain *vs.* injected carrier density (and therefore current) curve should change more slowly with temperature (i.e., $d\left(dg_p/dI\right)/dT$ should be reduced), resulting in a larger characteristic temperature, T_0. This prediction is in accordance with the experimental observations of Fig. 6.25, and Table 6.1. In addition, from Fig. 5.26 and Fig. 6.8, there is an inverse correlation between the rate of change of the peak PL wavelength and T_0. (The reasons why the change in the bandgap with temperature was less for the tensile strained QW structures in comparison to that of the other structures is not yet clear).

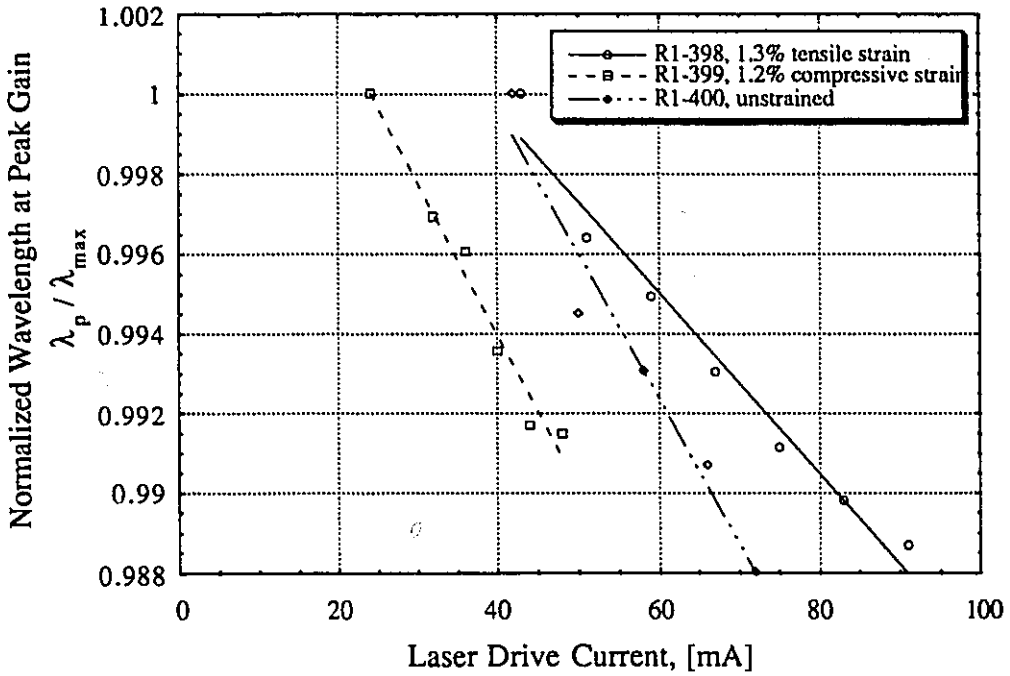

Figure 6.26: Plot of the variation of the wavelength, λ_p, (corresponding to the peak material gain) *vs.* injected current density at a temperature of 60°C for strained and unstrained MQW laser structures R1-398, R1-399 and R1-400. Wavelengths are normalized to λ_p at the lowest current level.

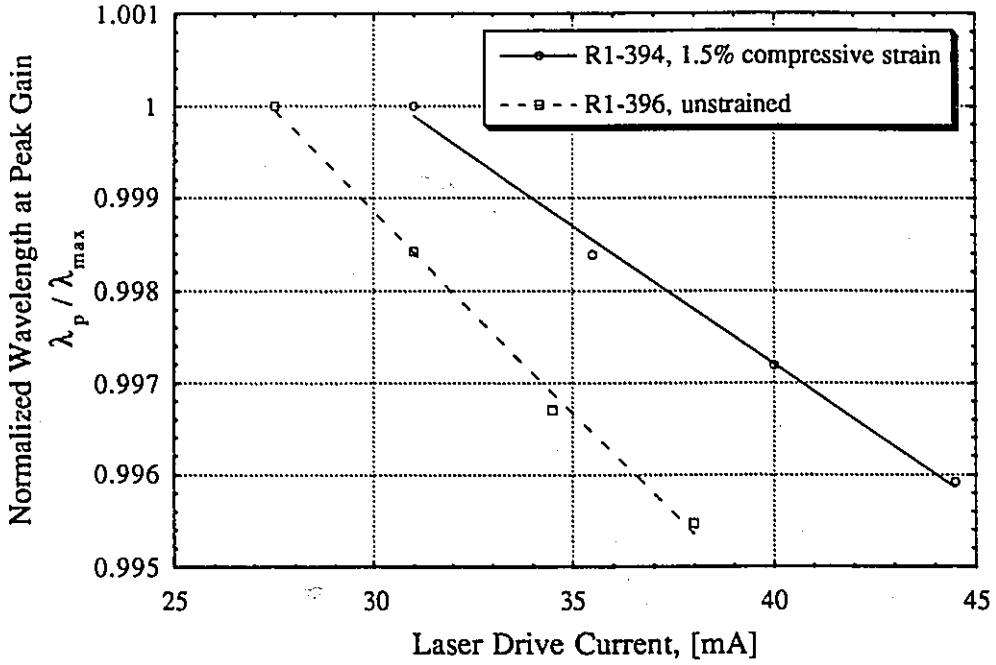

Figure 6.27: Plot of the variation of the wavelength, λ_p, (corresponding to the peak material gain) *vs.* injected current density at a temperature of 60°C for strained and unstrained MQW laser structures R1-394 and R1-396, respectively. Wavelengths are normalized to λ_p at the lowest current level.

Figures 6.26 and 6.27 show plots of the variation of the normalized wavelength corresponding to the peak material gain, λ_p, at 60°C *vs.* injected current for the QW laser structures from Set 1 and Set 2, respectively. Values obtained from the slope, $(d(\lambda_p/\lambda_{max})/dI)$, of the curves in these figures appear in Table 6.1. From Fig. 6.26, Fig. 6.27 and Table 6.1, an inverse correlation is also observed between $d(\lambda_p/\lambda_{max})/dI$ and the laser characteristic temperature, T_o. The rate of change of λ_p with injected current, $d(\lambda_p/\lambda_{max})/dI$, is about 30 per cent less for the compressively strained laser structure R1-394 than for the unstrained laser structure R1-396. In contrast, laser structure R1-394 has a T_o that is between 20 and 30 per cent larger than that of laser structure R1-396. $d(\lambda_p/\lambda_{max})/dI$ is about 37 per cent less for the tensile-strained laser structure R1-398 than it is for the unstrained laser structure R1-400. The T_o for the tensile-strained structure R1-

398 is about 35 per cent larger than that for laser structure R1-400. Therefore, the correlation between the rate of change of λ_p with injected current, $d(\lambda_p/\lambda_{max})/dI$, and T_o is remarkable.

From the above analysis there is an intimate cyclical relationship between the parameters: dE_g/dT; $d(\lambda_p/\lambda_{max})/dI$; T_o, and therefore dI_{th}/dT; and $d\left(dg_p/dI\right)/dT$. This may be seen as follows.

(i) By definition, a smaller T_o indicates a larger dI_{th}/dT

(ii) An inverse correlation has been shown to exist between dE_g/dT and T_o, and hence dI_{th}/dT. (see §5.3.2)

(iii) An inverse correlation has also been shown to exist between $d(\lambda_p/\lambda_{max})/dI$ and T_o, and hence dI_{th}/dT. (see Table 6.1)

(iv) Thus, from (ii) and (iii), $d(\lambda_p/\lambda_{max})/dI$ and dE_g/dT are correlated.

(v) From (2.2.2) and (2.2.15) the effective density of states ρ_{rcd}, is directly correlated to the effective mass, m^*, which is in turn directly correlated to E_g by (2.2.11).

(vi) $d\left(dg_p/dI\right)/dT$ is directly correlated to ρ_{rcd} (see (2.2.23)) and, hence, from (v) dE_g/dT is directly correlated to $d\left(dg_p/dI\right)/dT$.

(vii) $d\left(dg_p/dI\right)/dT$ has been shown to be inversely correlated to T_o (see Table 6.1) and, therefore, directly correlated to dI_{th}/dT from (i).

(viii) From (ii) and (iii) a larger dI_{th}/dT results in a larger value for $d(\lambda_p/\lambda_{max})/dI$ and dE_g/dT, which from (v) and (vi) causes a larger $d\left(dg_p/dI\right)/dT$, which from (vii), again causes a larger dI_{th}/dT. Hence, the cyclical relationship is complete.

In addition, current leakage enters into the above cyclical relationship as follows. If I_{th} (and therefore J_{th}) increases more rapidly with temperature, so does the position of the quasi-Fermi level, E_f, within the conduction- and valence-bands. The increase in the

temperature sensitivity of the position of E_f within the energy bands, in turn leads to an increase in the leakage current and, also, the rate of change of the leakage current with temperature. Also (from (3.6.4) and (3.6.7)) a reduction in η_i, and the rate of change of η_i with temperature are associated with greater leakage currents, and a greater rate of change of leakage current with temperature, respectively. From (6.4.2) these factors, in turn, lead to a more rapid change of dI_{th}/dT with temperature and, therefore, from (ii) and (iii) above larger values for $d(\lambda_p/\lambda_{max})/dI$ and dE_g/dT; consequently, current leakage is also involved in the cyclical relationship described above.

From the above results it is clear that the root of the temperature dependence of the laser threshold current is much more complicated than any explanation based simply on the variation of carrier leakage, Auger recombination, or optical gain with temperature. In Chapter 7, a previously un-mentioned strong correlation between the threshold current density, J_{th}, and the temperature sensitivity of the laser threshold current, $\nabla_T J_{th}$, is explored to illustrate this point.

6.5 ADDITIONAL OBSERVATION REGARDING THE EFFECTS OF STRAIN AND QW WIDTH ON THE OPERATING CHARACTERISTICS OF QW LASERS.

In this section additional observations regarding the effects of strain and quantum well width on laser performance are presented. The additional properties considered include: the effects of quantum well width on the characteristic temperature, T_o; the effects of strain and QW width on the maximum output power; the effects of strain on the laser threshold current, I_{th}; and, the effects of strain on laser linewidth.

6.5.1 Observations Regarding the T_o Dependence on Quantum Well Width.

From Fig. 6.9 and Table 6.1, it is clear that the characteristic temperature, T_o, obtained for the laser structures having five-38 Å thick quantum wells is substantially larger

than that obtained for the laser structures having three-64 Å quantum wells. For the unstrained laser structure having 38 Å thick QWs, the room temperature T_o was 68 K, while that for the structure having 64 Å thick QWs was only 51 K. For the compressively strained QW laser structure having 38 Å thick quantum wells, the room temperature T_o was 83 K, while that for the structure having 64 Å thick quantum wells was only 69 K. Thus, for both strained and unstrained laser structures, the structure having the thinner quantum wells had a T_o that was about 15 K larger than that obtained for the structure with the thicker quantum well. Since from Fig. 4.9 the optical confinement factor is approximately equivalent for both laser structures, the improvement in T_o for the laser structures having the thinner quantum wells is probably related to a larger density of states for these structures (see (2.2.2)). (This concept is discussed further in the context of the results of Chapter 7). Thus it appears that the characteristic temperature for long wavelength, MQW semiconductor lasers may be improved by decreasing the quantum well width.

It should be noted that most studies of long wavelength MQW laser structures have involved structures with quantum well thicknesses greater than 55 Å and less than about 100 Å [Zou, 1993],[Mathur, 1993],[Osinski, 1992],[Temkin, 1990], and no great improvements in T_o have been obtained from these structures. However, one report (apart from the results presented in this thesis) of an increased T_o of 97 K for long wavelength MQW lasers has been obtained for a structure that had 30 Å thick QWs [Thijs, 1989]. This result is consistent with those of this thesis.

The reason why thicker quantum wells are generally used in MQW laser designs is because it is believed that the carrier collection efficiency (and therefore η_i) is greater for larger quantum wells. In addition, the transparency current density decreases with increasing well width for quantum well laser structures which have a QW thickness less than 100 Å because it is easier to achieve the Bernard-Duraffourg (2.2.24) condition for a smaller density of states [Lau, 1993]. Kolbas [1990] has shown that the carrier collection

efficiency of quantum well structures actually increases with decreasing QW width for quantum wells that have a thickness less than 50 Å. This result has been attributed to an increase in the spatial extent of the carrier wavefunction as the QW width decreases, which in turn leads to an increase in the capture probability due to an increased interaction distance between carriers in the barrier and the QW carrier wavefunction.

From Fig. 6.9 it can be seen that a characteristic temperature of 88 K between -10°C and 30°C was obtained for device structure R1-394. Apart from the results of Thijs [1991], this is the highest reported characteristic temperature ever achieved for long wavelength semiconductor lasers, and the largest ever reported for CW operation. Thijs reported a T_o value of 97 K for long wavelength (1.5 μm), 1000 μm cavity length lasers having four 30 Å thick, 1.8% compressively strained, $Ga_{0.2}In_{0.8}As$ quantum wells, with three 200 Å thick InGaAsP barriers lattice matched to InP. However, the T_o reported by Thijs was for lasers operating under pulsed conditions (200 ns at 500 Hz), and for devices with a 90% high reflectivity (HR) coating on the back facet and a 60% HR coating on the front facet. In addition, the T_o value of 97 K reported by Thijs was quoted as being valid for the temperature range between 20°C and 50°C; however, from an examination of Thijs' original data [1989], the $T_o$value of 97 K was actually obtained from the asymptote of the I_{th}-T curve at 20°C. Thus the characteristic temperature T_o of 88 K reported in this thesis is the largest ever T_o to be obtained for long wavelength semiconductor lasers operating under CW conditions without the benefit of high reflection coatings. Also obtained from laser structure R1-394, as shown in Fig. 6.28, was the highest CW operating temperature (of 140°C) reported to date for a long wavelength InGaAsP/InP laser.

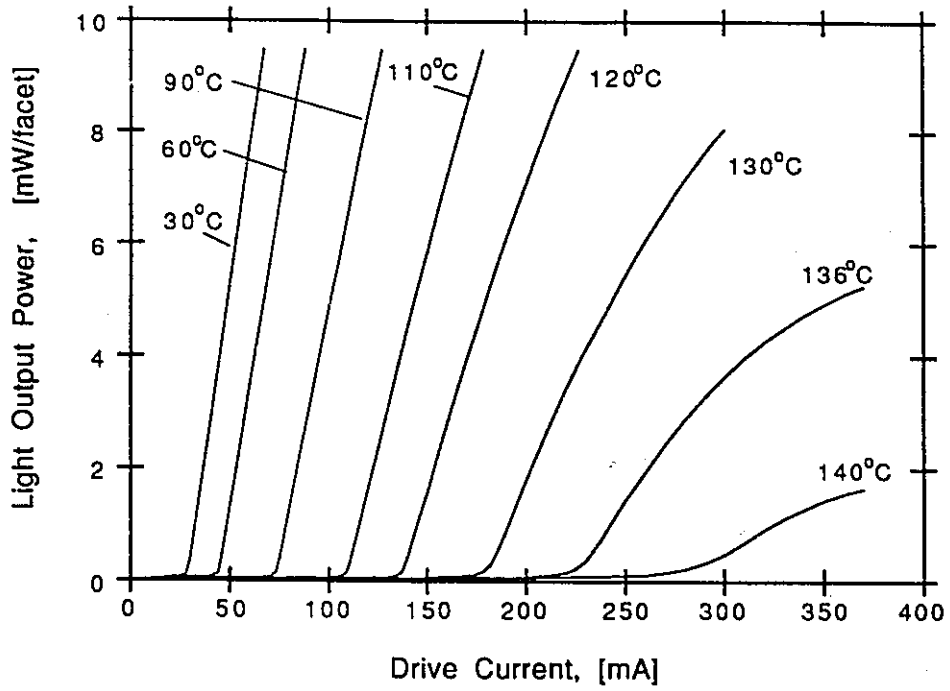

Figure 6.28: L-I characteristics as a function of temperature for 1.5 % compressively strained laser structure R1-394 from Set 2 with a cavity length of 1000 μm. This data shows CW operation at a temperature of 140°C which is the highest ever observed operating temperature for an all quaternary long wavelength semiconductor laser.

6.5.2 Effects of Strain on Laser Threshold Current.

From Fig. 6.8 it can be seen that the room temperature threshold current of the 1.2% compressively strained QW laser structure R1-399 is significantly smaller than that of the unstrained QW structure R1-400. The magnitude of threshold current for laser structure R1-399 is only two thirds of that obtained for laser structure R1-400. From Fig. 6.7, I_{th} for the 1.5% compressively strained structure R1-394 is also less than that for the unstrained structure R1-396 at room temperature; however, the reduction in I_{th} is not as significant as that found in the case of the laser structures having three-64 Å thick QWs. From these observations it is clear that the use of compressive strain results in a reduced I_{th} for lasers with a similar QW thicknesses in accordance with the theoretical predictions of

Chapter 2. However, from Fig. 6.8, it can be seen that the use of tensile-strained QWs has resulted in an increase in I_{th}, even though T_o is improved. The I_{th} of the tensile-strained QW structures R1-397 and R1-398 is about 50 per cent larger than that of the unstrained QW structures.

The increase of the threshold current for the tensile strained QW structures is consistent with the reduced internal efficiency, η_i, found for these structures as illustrated in Fig. 6.13. Part of the reason for the higher threshold current for the tensile strained structures may be due to a smaller optical confinement factor and, therefore, a larger threshold gain condition, g_{th}, from (2.2.31). The smaller optical confinement factor, Γ, for these structures is in part due to the fact that these lasers emit TM polarized light as a result of the dominant electron transition being from the conduction band to the light-hole band (see (2.2.14b). It is well-known that TM polarized radiation has a smaller optical confinement factor in slab waveguides [Agrawal, 1986]. In addition, from a comparison of spatially and polarization resolved electroluminescence measurements from the facets of the strained and unstrained QW laser structures, there are indications that the stress distribution due to the ridge structure in the tensile-strained laser structure is causing some lateral mode anti-guiding [Cassidy and Elenkrig, 1993]. This anti-guiding would further reduce Γ for these structures. Nevertheless, an examination of the far field pattern for all laser structures showed a circular beam profile as shown in Fig. 6.29.

The far field pattern shown in Fig. 6.29 for laser structure R1-397 is typical of that measured for all laser structures. The singly peaked profile indicates that the lasers are operating in a single lateral mode. Also noted from Fig. 6.29 is the fact that the angular divergence of the beam, as measured at the full width half maximum, is only about 25° in both the lateral (horizontal) and transverse (vertical) directions. The angular width of the far field pattern for typical semiconductor lasers is much larger in the vertical direction ($\theta_\perp \approx 65°$) than that in the horizontal direction ($\theta_\parallel \approx 33°$) [Agrawal, 1986]. The circular far

field pattern obtained for the structures designed for this thesis is a result of the profile of the graded index step region [Li, 1992]. The circular beam emission obtained from these MQW GRINSCH lasers is also highly advantageous for the efficient coupling of light into optical fibers for optical communications purposes.

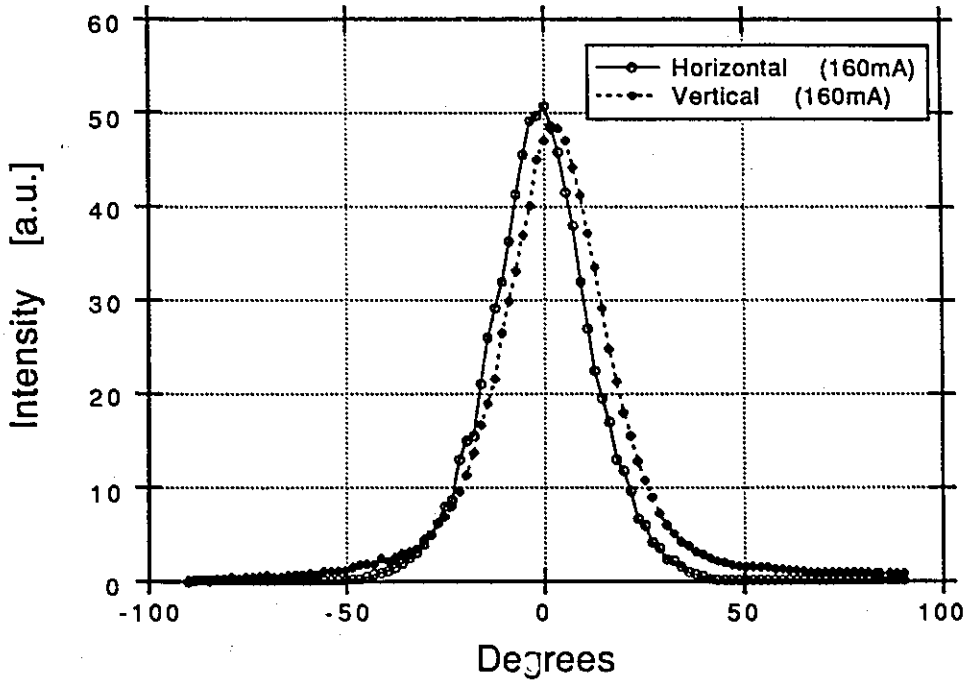

Figure 6.29: Far field pattern as measured for tensile strained laser structure R1-397, having three-64 Å thick QWs. The full width half maximum for both the lateral and transverse directions is about 25°.

6.5.3 Effects of Strain and QW Width on Maximum Output Power.

Apart from having lower threshold currents, the compressively strained QW laser structures R1-394 and R1-399, as shown in Fig. 6.30 and Fig 6.31, have a significantly higher maximum optical output power than that found for the unstrained QW structures R1-396 and R1-400, respectively. As shown in Fig. 6.31, the maximum optical output power

for laser structure R1-394 (1.5% compression, 5-38 Å thick QWs) is also significantly larger than that of laser structure R1-399 (1.2% compression, 3-64 Å thick QWs). The maximum output power of laser structure R1-394 was 70 mW/facet, or 140 mW total, in comparison to 43 mW/facet for laser structure R1-399. It will be recalled that the R1-394 lasers have a much higher T_0 than the R1-399 lasers with the thicker QWs. Therefore, the above result illustrates another ostensible advantage of using thinner quantum wells in the laser active region over thicker quantum wells.

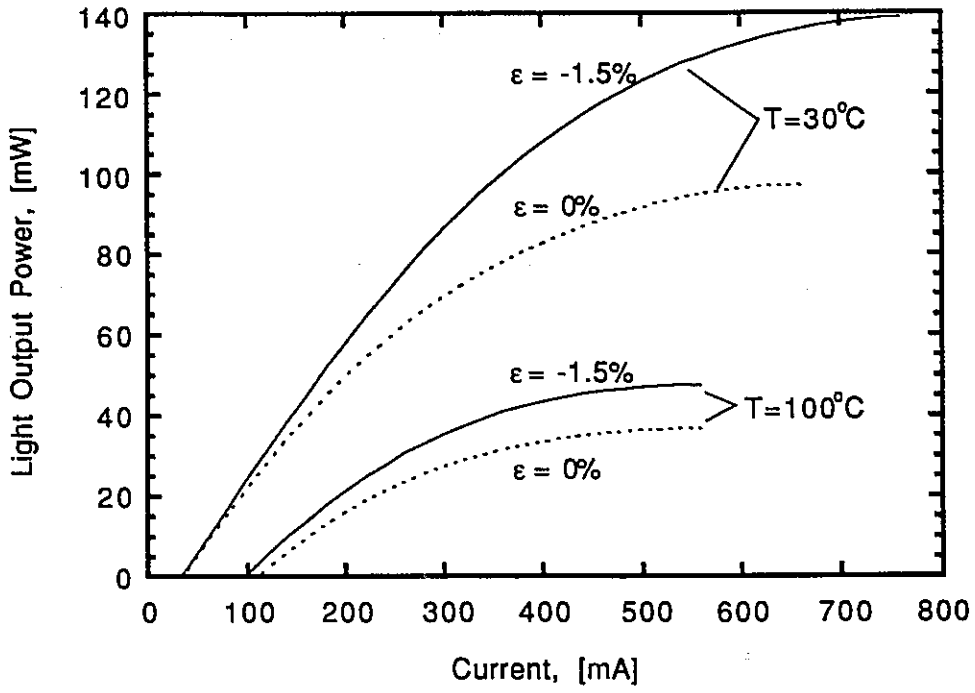

Figure 6.30: Light output power *vs.* current for 1000 μm cavity length, uncoated, 1.5% compressively strained and unstrained MQW lasers R1-394 and R1-396, respectively. Both lasers have five 38 Å thick QWs and are from Set 2. The measurements were made under pulsed conditions (pulse length 7 μs, 215 Hz repetition rate), and show that the use of compressive strain significantly increases the maximum optical output power.

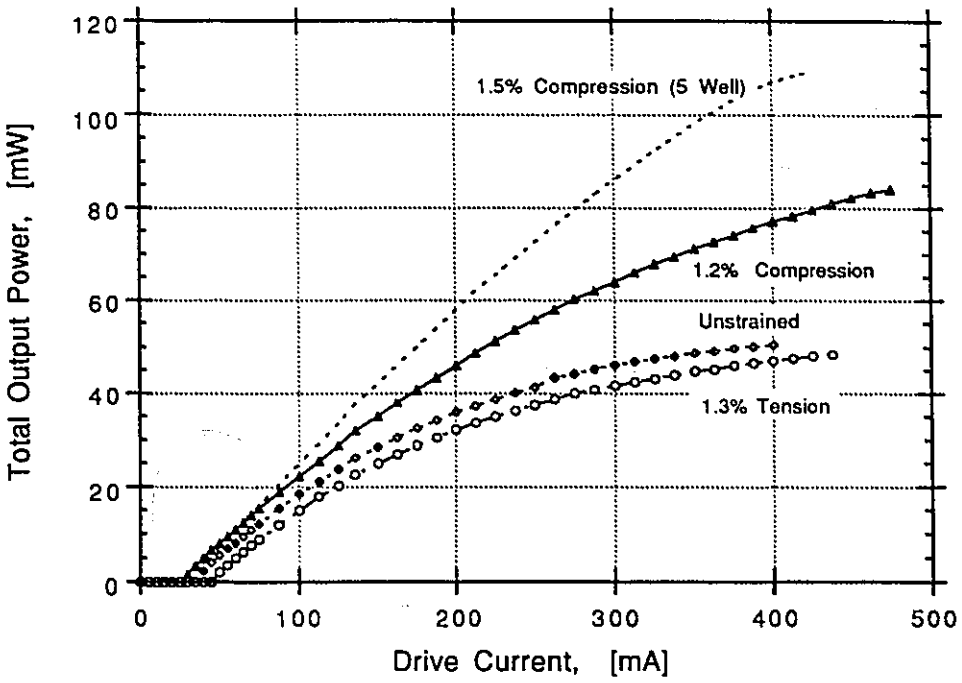

Figure 6.31: Light output power *vs.* current strained and unstrained MQW lasers R1-398 (1.3% tension), R1-399 (1.2% compression), and R1-400 (unstrained). These lasers have three-64 Å thick QWs and are from Set 1. The measurements were made under pulsed conditions (pulse length 7 μs, 215 Hz repetition rate), and once again show that the use of compressive strain significantly increases the maximum optical output power. Shown for comparison is the optical output power *vs.* current relation for laser structure R1-394. The data shows that the use of thinner QWs in the laser active region can result in an increased maximum optical output power.

6.5.4 Effects of Strain on Laser Linewidth.

A narrow linewidth for long wavelength lasers, particularly at 1.55 μm, is essential for long-haul optical communications due to the wavelength dispersion in the optical fibers which spatially broadens out the laser pulses. One of the proposed advantages of using strained QW lasers for optical communications systems is that strain is predicted to cause a reduction in the laser linewidth for these lasers relative to that found for unstrained, quantum well, and bulk lasers [Ohtoshi, 1989], [Thijs, 1991], [Zah, 1991], [Tiemeijer, 1991], [Dutta, 1990]. The linewidth of a single laser mode from laser structures R1-394,

R1-397, R1-398, R1-399 and R1-400 as a function of the lasers' optical output power was measured by Woodside [1992]. Fig. 6.32 shows the linewidth *vs.* optical power relation obtained for 500 μm length lasers from structures R1-397, R1-399 and R1-400. From this figure, it can be seen that both the compressively strained (R1-399) and tensile-strained (R1-397) QW lasers have a reduced linewidth-power product (as determined from the slope of the linewidth $\Delta\nu$ *vs.* inverse optical power, P^{-1}, relation) in comparison to that obtained for unstrained laser structure R1-400. The linewidth-power product for the compressively strained laser structure R1-399 was found to be 21.7±0.4 MHz-mW in comparison to 28.2±0.6 MHz-mW for the unstrained laser structure R1-400. The corresponding result for tensile-strained laser structure R1-397 was 20.5±0.2 MHz-mW and only 18.0 ±0.5 MHz-mW for laser structure R1-398. Woodside attributed the reduction in the linewidth-power product for the strained QW lasers in comparison to that obtained for the unstrained QW lasers to strain.

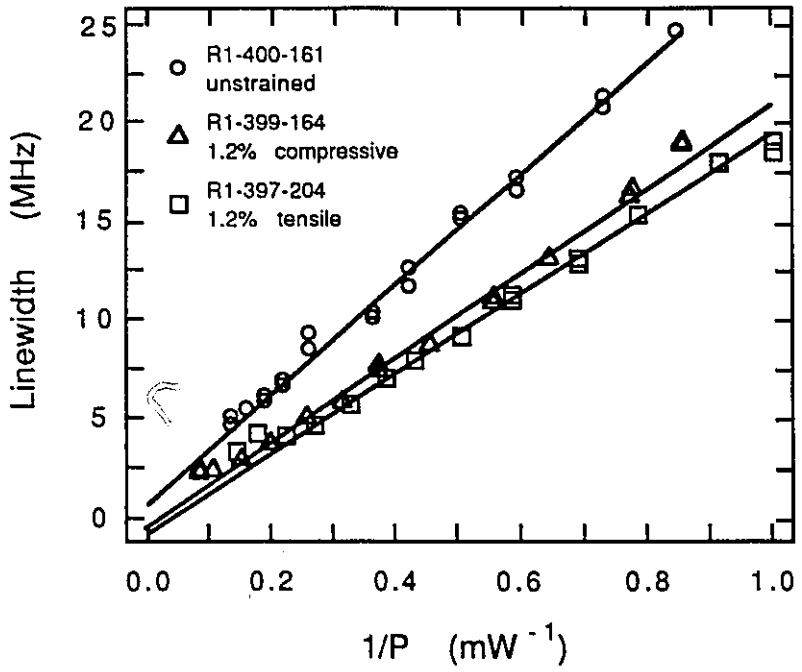

Figure 6.32: Measurement of the linewidth-power product (MHz-mW) for strained and unstrained laser structures R1-397, R1-399, and R1-400 as obtained from the slope of the linewidth *vs.* inverse optical power curve. All laser cavity lengths were 500 μm. [Woodside, 1992].

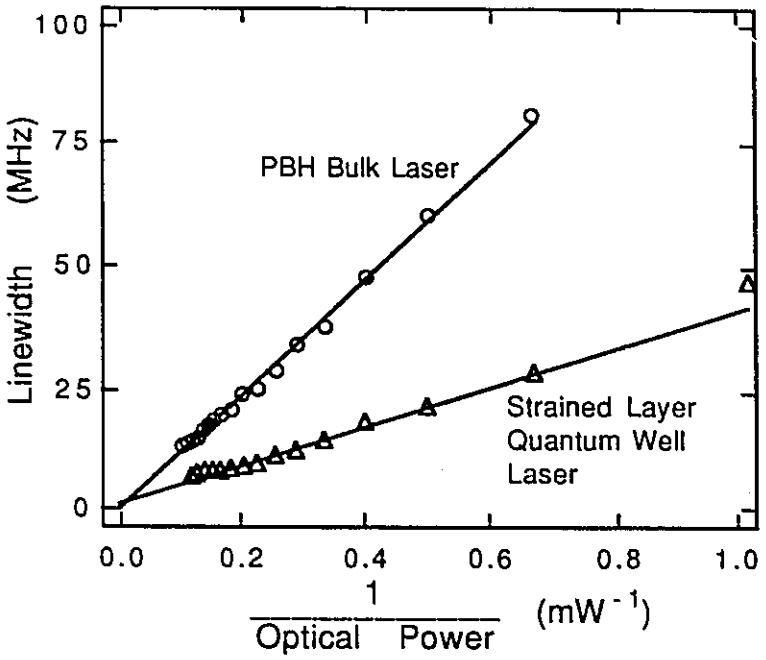

Figure 6.33: Comparison of the linewidth vs. inverse power relation for a 250 μm cavity length, bulk PBH laser and a 250 μm cavity length laser from MQW laser structure R1-394. The linewidth power product is obtained from the slope of the best fit line to the data and for the strained MQW laser is only one-third the value of that obtained for the bulk PBH laser. [Woodside, 1992].

Data on the linewidth-power product for the unstrained laser structure R1-396 was not obtained for a comparison of the linewidth power product between the compressively strained (R1-394) and unstrained laser structures with active regions containing narrower quantum wells. However, Woodside did measure the linewidth-power product for a 250 μm cavity length laser from structure R1-394. The linewidth-power product obtained for this laser is compared with that obtained for an unstrained bulk, planar buried heterostructure (PBH) laser, with the same cavity length, in Fig. 6.33. From this figure it is clear that the linewidth-power product (slope of the $\Delta\nu$ *vs.* P^{-1} relation) of the strained MQW laser is markedly reduced in comparison to that of the PBH laser. The linewidth-power product for laser structure R1-394 was determined by Woodside to be 36.8 ± 0.9 MHz-mW, while that of the PBH laser was found to be 111±1 MHz-mW. This distinct

reduction in the linewidth-power product for the strained QW laser in comparison to the PBH laser is in accordance with theoretical predictions as observed by other authors [Thijs, 1991], [Dutta, 1990]. The reduction in the measured linewidth-power product for the three QW laser structures relative to that obtained for the five quantum well laser structure (R1-394), was attributed by Woodside to the longer cavity length (500 μm *vs.* 250 μm) of the three QW laser structures. A summary of the observed effects of strain and device structure on: the linewidth-power product; the threshold current, I_{th}; the maximum output power; the characteristic temperature, T_o, and the lasing mode appears in Table 6.2.

Table 6.2: Summary of the results of the effects strain and device structure on: T_o (between 0 and 40°C); I_{th} at 30°C; the maximum lasing temperature for 1000 μm length devices; the maximum output power; lasing mode; and, linewidth-power product.

	R1-394	R1-396	R1-397	R1-398	R1-399	R1-400	RWG Typical Values
T_o (0-40°C) @ 1000μm	88 ±2K	70 ±2K	68 ±2K	69 ±2K	57 ±2K	51 ±2K	40 - 70K
I_{th} @ 30°C, 250μm	17mA	20mA	49mA	53mA	21mA	33mA	22 - 27mA
Max. Lasing Temp. @ 1000μm	140°C	>110°C	>80°C	>80°C	>110°C	>80°C	70 - 90°C
Max. O/P Power/Facet @ 1000μm	70mW	48mW	25mW	26mW	43mW	28mW	25 - 35mW
Wavelength [nm] @ 30°C	1391	1426	1391	1381	1389	1380	1300
Lasing mode	TE	TE	TM	TM	TE	TE	TE
LW-Power Product [MHz·mW]	36.8 250μm	N.A.	20.5 500μm	18.0 500μm	21.7 500μm	28 500μm	>110 250μm

6.6 SUMMARY

In this chapter the fabrication procedure used to process the MQW laser structures designed for this thesis into ridge waveguide lasers was described along with the empirical apparatus and configuration used to test both the CW light-current and spectral characteristics of these devices.

A comparison of the effects of both tensile and compressive strain, and QW width, on the temperature sensitivity of the laser threshold current, I_{th}, was made. It was found that both strain and QW width can be adjusted to produce an increase in T_o. Additionally, T_o was found to depend on the device cavity length, and two possible explanations for this behavior were proposed. One of these explanations was based on the premise that the temperature variation of the peak optical gain *vs.* current relation is primarily responsible for the I_{th}-T dependence of long wavelength semiconductor lasers. The other explanation was based on the premise that the I_{th}-T behavior of InGaAsP/InP based lasers is primarily governed by the temperature dependence of the leakage currents.

The temperature dependence of the internal efficiency, η_i, and the internal optical absorption losses, α_{loss}, were determined from measurements of the inverse external differential quantum efficiency of the lasers, η_d^{-1}, *vs.* cavity length as function of temperature. From an examination of the temperature dependence of η_i and α_{loss} in relation to the temperature sensitivity of I_{th}, it was determined that neither the temperature variation of η_i and, therefore, leakage currents, nor the temperature variation of α_{loss} could be major factors contributing to the low T_o of InGaAsP/InP based long wavelength semiconductor MQW lasers.

The peak optical gain as a function of temperature was measured using the Hakki and Paoli [1973] technique. From these measurements it was found that the rate of change of the peak optical gain, g_p, with temperature ($d(dg_p/dI)dT$) was inversely correlated with

T_o and that $d(dg_p/dI)dT$ strongly influences the temperature sensitivity of the laser threshold current with temperature. An inverse correlation was also found between T_o and the shift in the peak PL wavelength with temperature, (i.e., dEg/dT (from §5.3.2)) and between T_o and the change in the wavelength corresponding to the peak gain, λ_p, with injected current, $d\lambda_p/dI$. A cyclical relationship between these parameters and the magnitude of $1/T_o$, or equivalently of dI_{th}/dT was determined. From this cyclical relationship it was in turn proposed that the root cause of the temperature sensitivity of the laser threshold current in InGaAsP/InP based MQW lasers is much more complicated than can be explained by a single dominant physical mechanism as proposed by many authors and discussed in Chapter 3.

In the final section of this chapter additional effects of strain and QW width on laser performance, apart from those mentioned above, were illustrated. It was found that apart from an improved η_i, the application of compressive strain resulted in a reduced I_{th}, an increased maximum output power (140 mW), and a reduced line-width power product. It was found that the application of tensile strain results in an increased I_{th} and a lower maximum output power, but that tensile strain can be used to reduce the laser linewidth-power product. Additionally it was found that there may be substantial advantages in using thinner QWs (<50Å) in the laser active region than thicker QWs due to an increased density of states.

Achieved from the devices designed and fabricated for this thesis were the highest ever reported CW characteristic temperature (T_o = 88 K) and CW maximum operating temperature (of 140°C) for all quaternary (InGaAsP) lasers with uncoated facets. In addition all laser structures were found to emit a circular far field pattern with an angular divergence of ≈25° which is beneficial for the efficient coupling of laser light into optical fibers for optical communications purposes.

CHAPTER 7: NEW INSIGHT INTO THE TEMPERATURE SENSITIVITY OF THE THRESHOLD CURRENT OF LONG WAVELENGTH SEMICONDUCTOR LASERS

7.0 INTRODUCTION

From Fig. 6.9 it is clear that the characteristic temperature, T_o, varies with cavity length, L. Also from the J_{th} *vs.* L characteristics, shown in Fig. 6.10 and (6.4.2), it is clear that the J_{th} varies with L in an opposite manner to T_o. Therefore, it is reasonable to suspect that there should be a correlation between the temperature sensitivity of the laser threshold current density and the magnitude of J_{th}. Horikoshi [1982] examined the relationship between T_o and J_{th} and concluded that there was "no distinct correlation between T_o and J_{th}." Horikoshi most likely did not observe a correlation between these parameters because he based his observations regarding T_o *vs.* J_{th} on data published in the literature which was for a number of different devices structures. Yano *et. al.* also looked for a correlation between T_o and J_{th}/d (d is the stripe width of the laser). They found a slight inverse correlation between these parameters; however, there was a very large degree of scatter in their data which made any conclusive observations difficult.

The discussion of the results of §6.4.6 indicated that the cause of the temperature dependence of I_{th} is much more complicated than can be explained simply on the basis of the temperature dependence of a single physical phenomena, such as the temperature dependence of carrier leakage, Auger recombination, optical gain or intervalence band absorption. It was also discussed in Chapters 1 and 3 that the commonly used I_{th}-T relation proposed by Pankove [1968] is inappropriate to describe the temperature sensitivity

of the laser threshold current, and that the proposed relationship was without any physical basis. Nevertheless, for the past twenty-five years much of the work published with regard to the temperature sensitivity of I_{th} has been based on trying to explain this exponential relationship. In addition, it has been noted by many authors (see Chapter 1) that the characteristic temperature, T_o, used to describe the temperature sensitivity of the laser threshold current is not a constant but is actually dependent on temperature. Also, a high value for the T_o does not necessarily have much bearing on the ultimate maximum operating temperature of a laser. And, in the search for a coolerless laser, i.e., one that can operate in telecommunications systems without the need for costly and bulky thermoelectric coolers, it is the maximum possible operating temperature of the lasers which is of primary concern. Consequently, the meaning and usefulness of the T_o parameter must be called into question.

In the following work, the concept of the characteristic temperature, T_o, has been discarded and the true temperature sensitivity of J_{th}, in terms of the temperature rate of change of J_{th}, as given by

$$\nabla_T J_{th} \cong \frac{J_{i+1} - J_i}{T_{i+1} - T_i} \equiv \frac{\partial J}{\partial T} \tag{7.0.1}$$

is examined in relation to the threshold current density, J_{th}. A strong correlation is found between $\nabla_T J_{th}$ and J_{th}, where $\nabla_T J_{th}$ is found to be related to J_{th} by a power law expression. This power law relationship is seemingly universal for all the lasers studied for this thesis, including a bulk InGaAs/InP, gain-guided, Zn-diffused oxide stripe laser emitting at 1.3 μm.

The power law expression derived from empirical data is given by the relation:

$$\frac{J^m}{\nabla_T J_{th}} = C \tag{7.0.2}$$

where C is a constant, and is found to depend upon device structure (i.e., strain and quantum well thickness). The power m has a value of $\approx 3/2$ for all devices.

By integrating (7.0.2) an entirely new expression for the variation of the threshold current density with temperature is arrived at. The constant of integration is given the label T_{max}, and represents a new and more useful parameter with which to describe the temperature sensitivity of the laser threshold current than T_o. The constant T_{max}, physically represents the maximum ideal operating temperature of the laser (i.e., the point where J_{th} asymptotically approaches infinity). From the variation of J_{th} with cavity length, an expression relating the maximum operating temperature of the laser, T_{max}, with cavity length is derived. The predicted variation of T_{max} with cavity length is found to be in accordance with experimental data. Therefore, based on the derived relationship, it should be possible to optimize the laser cavity length against such parameters as the device capacitance (and therefore operating speed), and the external differential efficiency, in order to achieve the best possible compromise between the maximum operating temperature of the laser and these other parameters.

7.1 EMPIRICAL OBSERVATIONS REGARDING THE $\nabla_T J_{th}$ DEPENDENCE ON J_{th}

Figures 7.1 to 7.6 show the quantity $1/(\nabla_T J_{th})$ plotted against the threshold current density, J_{th}, for laser structures R1-394 to R1-400, and also for a bulk gain-guided semiconductor laser emitting at 1.3 μm. The data shown in each of these figures was obtained from measurements of devices from a given structure as a function of length and temperature. Each figure contains the data from at least 12, and up to 30, devices of various lengths from each structure. The line through the data points is obtained from the best fit of (7.0.2) to the data.

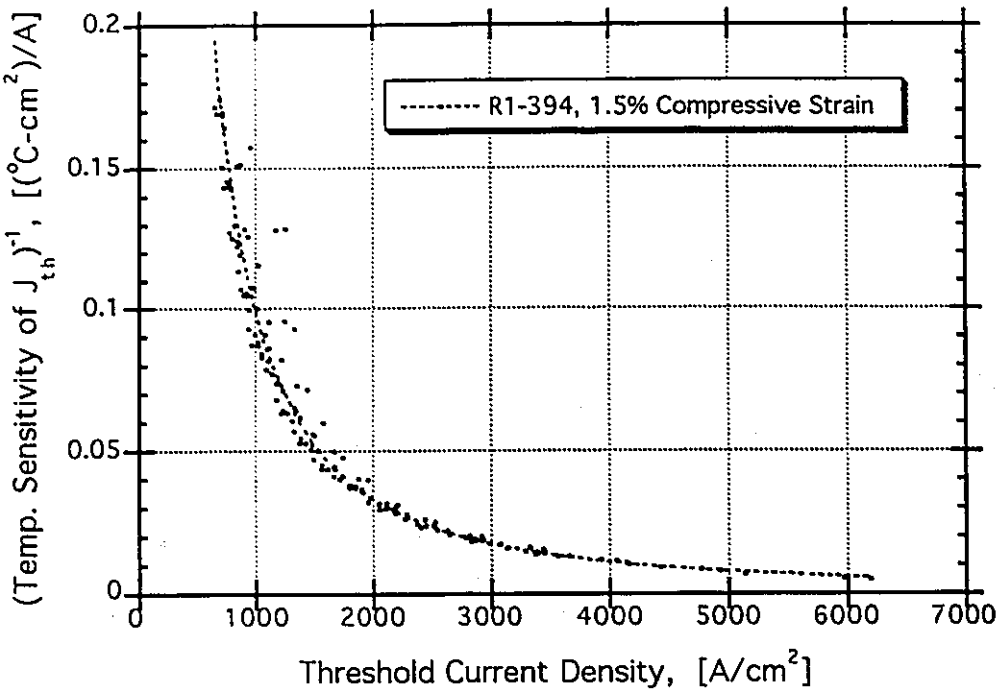

Figure 7.1: Inverse temperature sensitivity of threshold current density *vs.* J_{th} for compressively strained MQW laser R1-394, 5QWs.

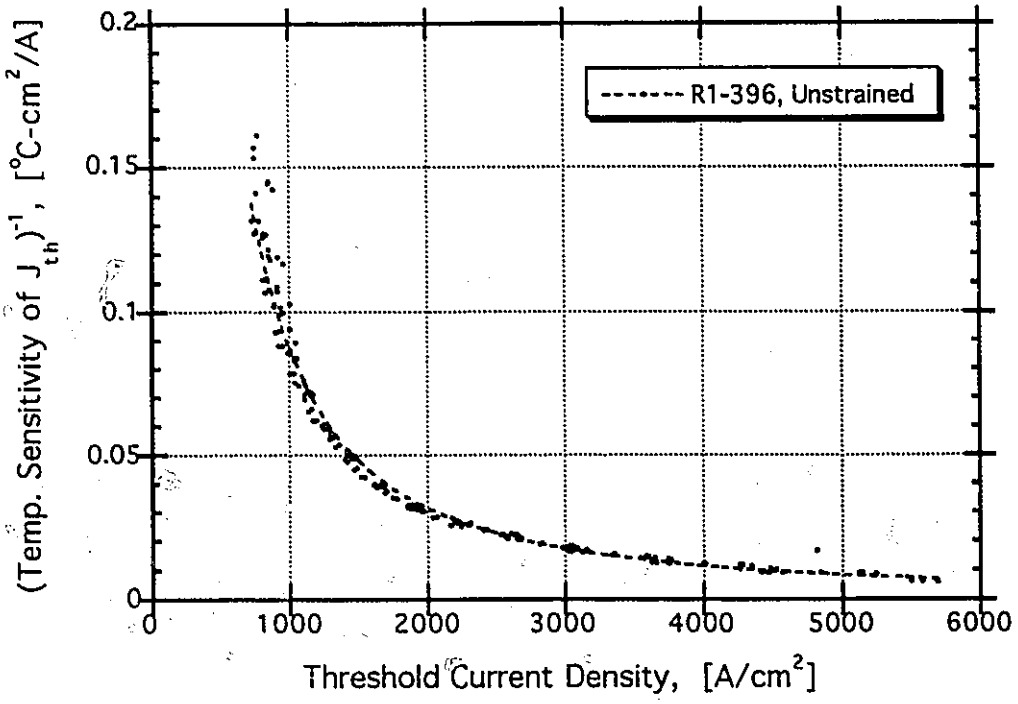

Figure 7.2: Inverse temperature sensitivity of threshold current density *vs.* J_{th} for unstrained MQW laser R1-396, 5QWs.

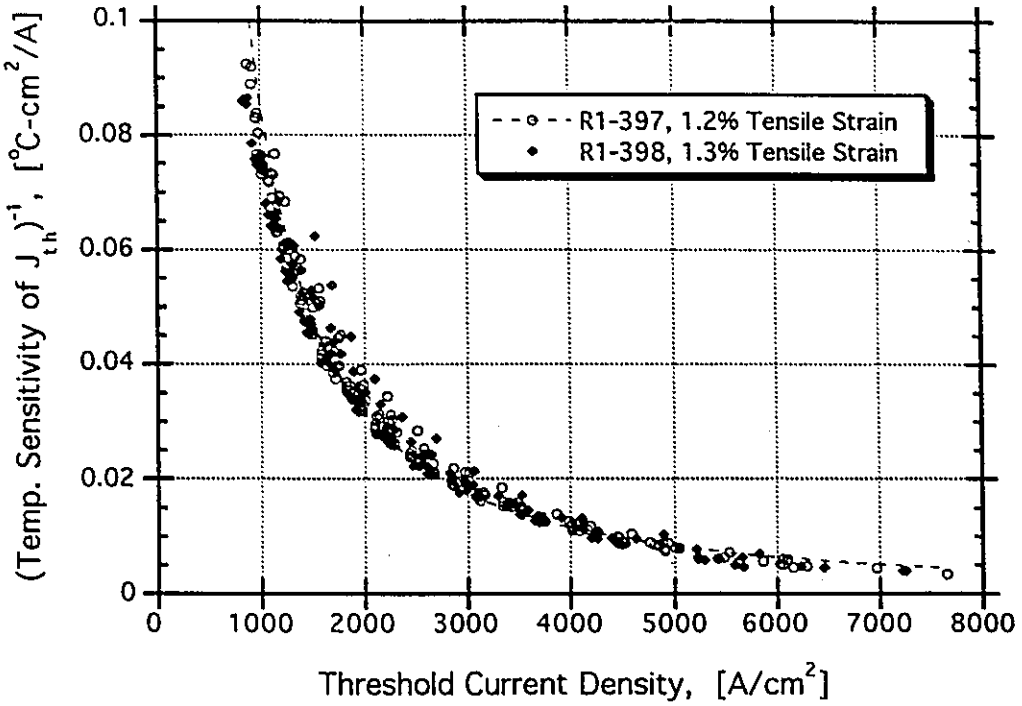

Figure 7.3: Inverse temperature sensitivity of threshold current density *vs.* J_{th} for tensile strained MQW lasers R1-397 and R1-398, 3QWs.

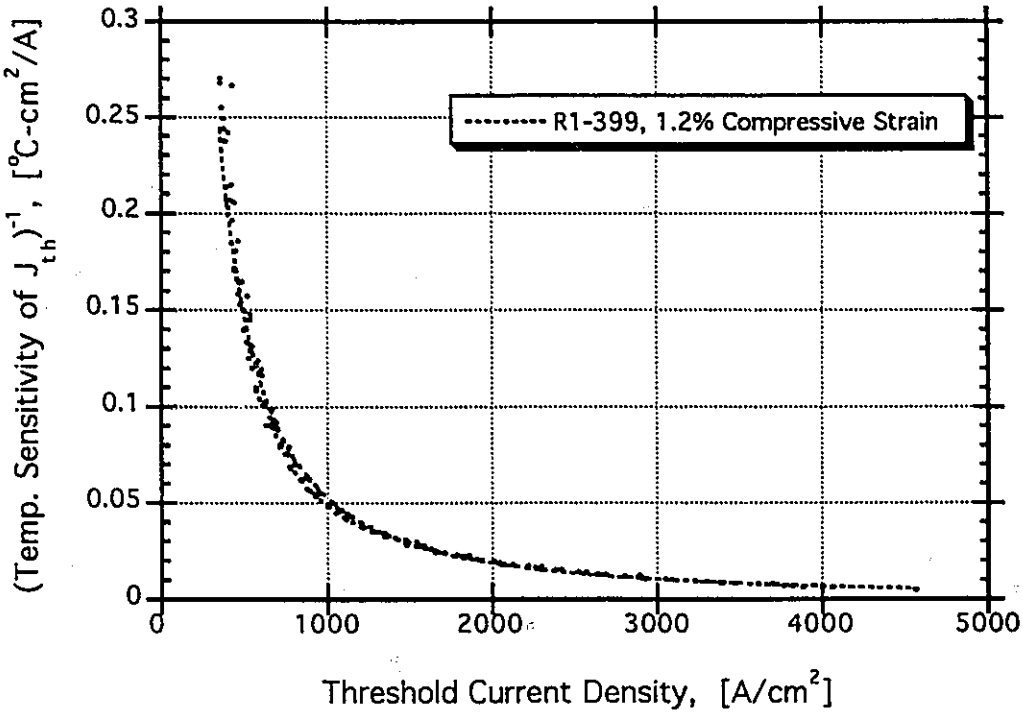

Figure 7.4: Inverse temperature sensitivity of threshold current density *vs.* J_{th} for tensile strained MQW lasers R1-399, 3QWs.

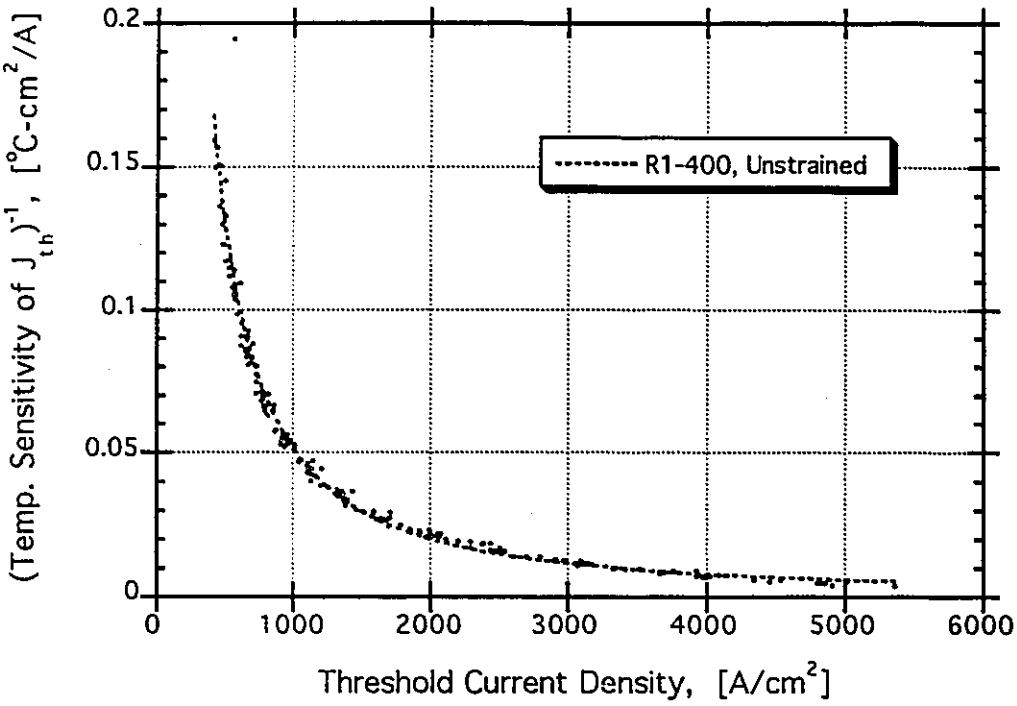

Figure 7.5: Inverse temperature sensitivity of threshold current density vs. J_{th} for unstrained MQW lasers R1-400, 3QWs.

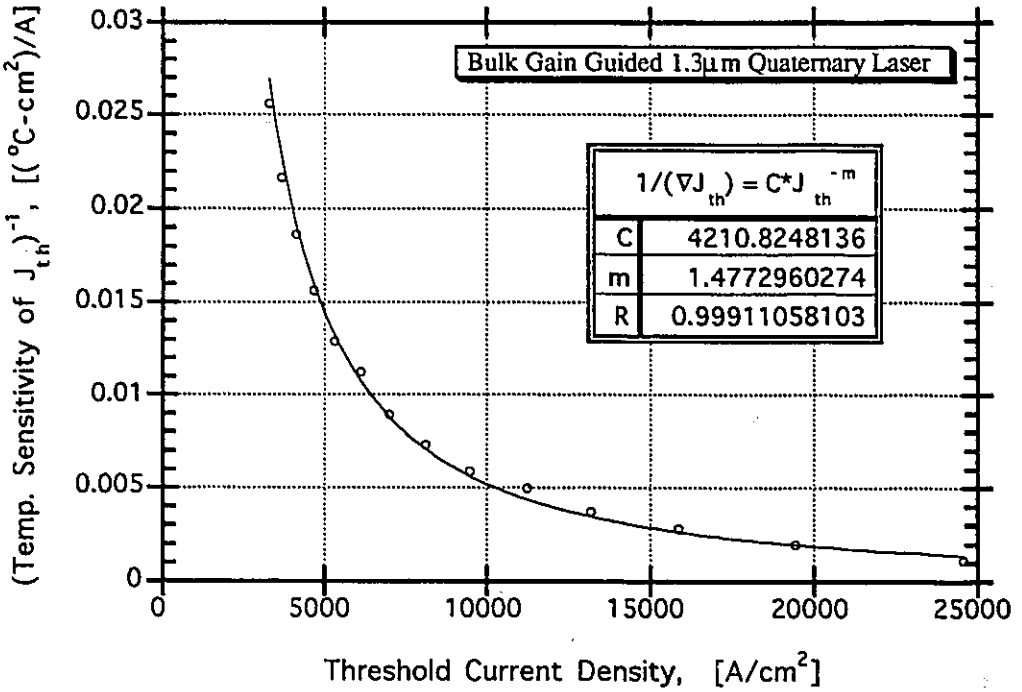

Figure 7.6: Inverse temperature sensitivity of threshold current density vs. J_{th} for a bulk gain guided laser structure emitting at 1.3 µm.

Clearly from Figs. 7.1 to 7.6 there is a very strong correlation between the temperature sensitivity of the laser threshold current density and J_{th}. In interpreting the data from these figures, it should be realized that the magnitude of J_{th} for any given structure may be altered by changing either the temperature of the device (Fig. 6.7) or by changing its length (Fig. 6.10). *However, regardless of how the threshold current density is changed, the value of* $1/(\nabla_T J_{th})$ *falls about the best fit line as determined from* (7.0.2). This result is extremely significant as it indicates that two lasers of different lengths may have the same temperature sensitivity of the laser threshold current density (here-in referred to as $\nabla_T J_{th}$) at vastly different temperatures, (ΔT >60°C from the data analyzed). For example, a laser with a cavity length of 250 μm may have the same value of $\nabla_T J_{th}$ at -40°C as a 2000 μm cavity length device operating at 40°C. In other words the following relation (from (3.2.2)) holds

$$\frac{\partial}{\partial T}\left(\frac{N_{th,1}}{\tau_{th,1}}\right)\Bigg|_{T=T_1}^{L=L_1} = \frac{\partial}{\partial T}\left(\frac{N_{th,2}}{\tau_{th,2}}\right)\Bigg|_{T=T_2}^{L=L_2} \tag{7.1.1}$$

as long as the quantity (N_{th}/τ_{th}) is identical regardless of the values of L and T.

If the effects of Auger recombination on τ_{th} (3.2.2), or the effects of Auger-recombination-induced energetic carrier leakage on η_i (3.5.7a) were the primary cause of the temperature sensitivity of I_{th}, then this observation should not hold true. This is because Auger recombination is thought to be negligible at -40°C due to its exponential temperature dependence (Fig. 3.5 and (3.3.5)). Therefore, τ_{th1} at T_1 and τ_{th2} at T_2 in (7.1.1) will be determined by different physical processes with a different temperature dependence (i.e., radiative recombination or Auger recombination from (3.3.2)); consequently, Auger recombination cannot be primarily responsible for the temperature dependence of the laser threshold current. Furthermore, as shown in Fig. 7.7 and 7.8 for the data from device structures R1-394 and R1-397, respectively, the constant C in (7.0.2) is independent of temperature over a measured temperature range of 140°C; therefore, once

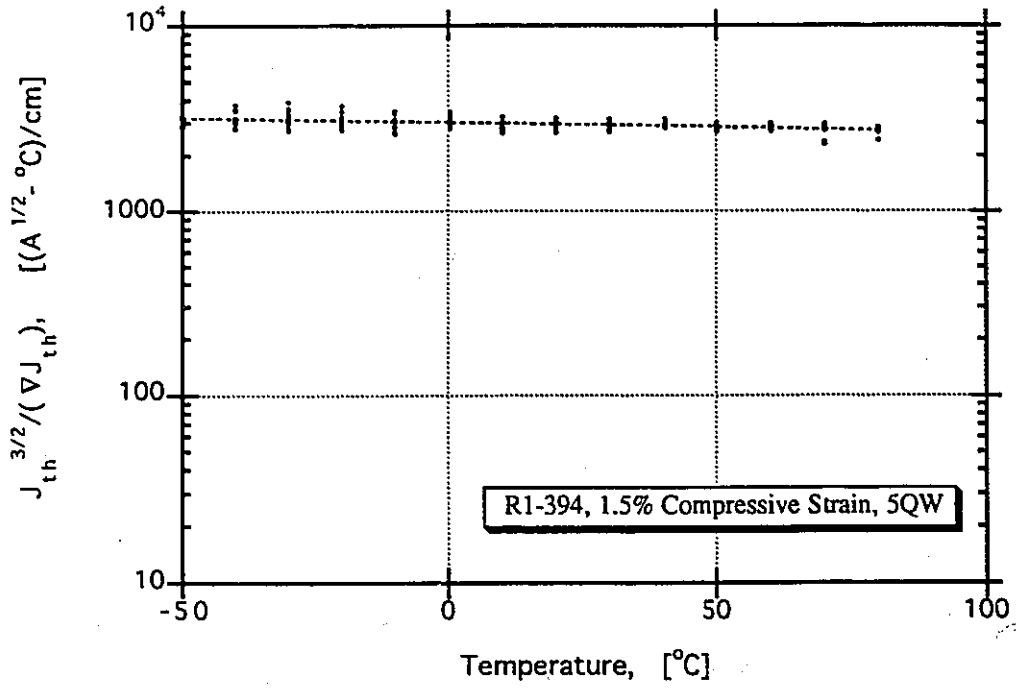

Figure 7.7: Plot of the constant C [$=J_{th}^{3/2}/(\nabla J_{th})$] as a function of temperature for laser structure R1-394. The constant C, unlike the parameter T_o, is found to be independent of temperature.

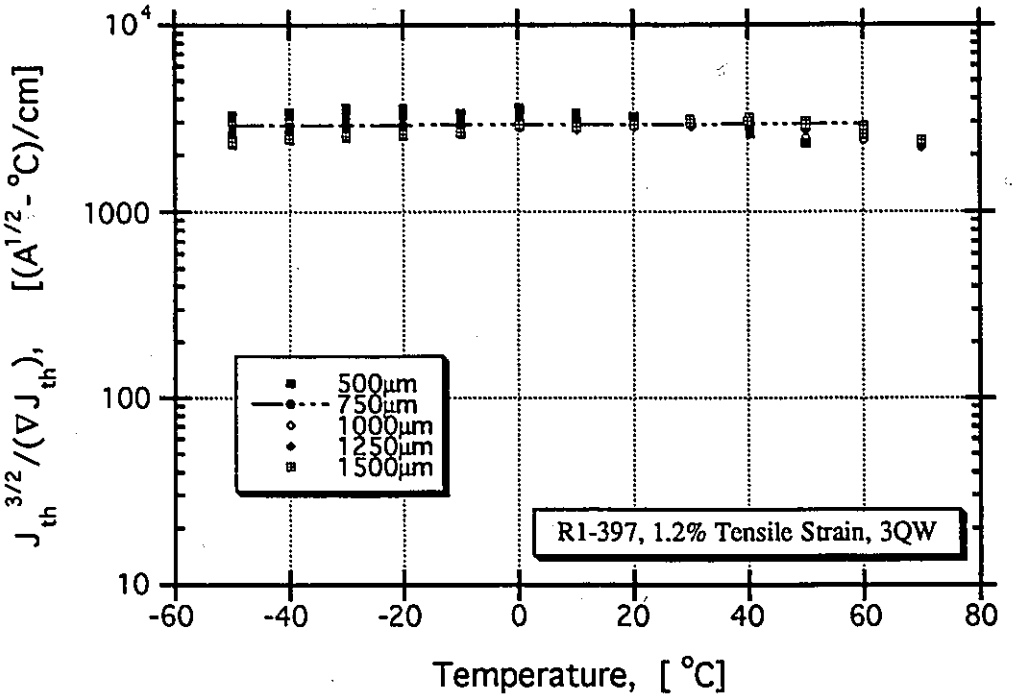

Figure 7.8: Plot of the constant C [$=J_{th}^{3/2}/(\nabla J_{th})$] as a function of temperature for laser structure R1-397.

again Auger recombination cannot be the primary cause of the low T_o in InGaAsP laser structures because the quantity $\nabla_T J_{th}$ would have a different mathematical form, and thus, probably magnitude relative to J_{th}, at -50°C than at 90°C if this were the case.

However, the results of Figs. 7.1-7.6 suggest that carrier leakage, and therefore its temperature sensitivity, is extremely relevant to the temperature sensitivity of I_{th}, and therefore J_{th}. One arrives at this conclusion from the data of Figs. 7.1-7.6 because, as J_{th} increases so should N_{th}, and thus, from (2.2.27), the position of the quasi-Fermi levels within the conduction- and valence-bands, and the increase in these parameters corresponds to an increase in $\nabla_T J_{th}$ (see Figs. 7.1-7.6). If the position of the quasi-Fermi levels is increasing within the bands, then it is reasonable to assume from (3.4.2) and (3.4.3) that the carrier leakage should also increase. To support this possibility, it has commonly been observed, that the carrier leakage increases superlinearly with injected current density [Zhaung, 1985], [Chik,1990], [Chiu, 1983], [Yamakoshi, 1982], [Chen,1983].

The results of Figs. 7.1-7.6 also indicate that, in addition to an increased carrier leakage with an increase in J_{th}, the incremental increase in the peak optical gain with current, and also with temperature, decreases as the average energy of the electrons increases. The average energy of the electrons increases with the position of the quasi-Fermi levels within the bands (and therefore with J_{th}) and also with temperature. If a decrease in the rate of increase of gain with injected carrier density were to occur as the average electron energy increased, either due to an increase in temperature or to an increase in current (i.e. an increase in the quasi-Fermi levels), it would require more injected carriers in order to achieve enough gain to overcome the sum of the cavity losses with an increase in either of these parameters. This increase in the required number of carriers would in turn cause a further reduction in the rate of change of gain with injected carrier density and again require additional carriers in order to support lasing. At the same time carrier leakage will be increasing, further compounding the problem. This cyclical process will proceed until a

steady state is reached and, once again, (as discussed in §6.4.6) illustrates the intimate relationship between the temperature and current dependence of the optical gain, carrier leakage and threshold current. It also suggests that in order to fully understand the physics behind the temperature dependence of I_{th}, I_{th} is probably be related to the temperature through a transcendental equation. However, the use of such a transcendental equation for laser design and optimization purposes would not be as clear as a relationship between I_{th} and temperature through some material constants. Such a relationship is presented in §7.2.

With regard to a decrease in the rate of change of the gain with an increase in the average electron energy, and therefore J_{th} or temperature, the observations of Figs. 6.18 to 6.25 indicate that this decrease does indeed occur. In addition, a decrease in the rate of change of the peak gain with increasing electron energy is supported by the theory of Chapter 2. In Chapter 2, the probability of optical emission due to the transition of an electron between the conduction band and the valence band was found to depend on the electron **k**-vector and therefore, the energy through (2.2.14). As the electron energy, and, thus, **k** increases the probability of optical emission into radiation modes of a different polarization to that of the operating lasing modes increases since the product $\hat{\mathbf{k}}\cdot\hat{\mathbf{e}}$ has a component normal to the heterojunction plane (for lasers operating in the TE mode). The component of $\hat{\mathbf{k}}\cdot\hat{\mathbf{e}}$ normal to the heterojunction plane arises because, as the electron energy increases (for a quantum well), $\hat{\mathbf{k}}$ has components normal to $\hat{\mathbf{k}}_z$: $\hat{\mathbf{k}}_z$ is the electron momentum vector when the electron is at the minimum band edge energy and $\mathbf{k}^2 = \mathbf{k}_z^2 + \mathbf{k}_{\|}^2$. As the electron energy increases **k** increases and so $\mathbf{k}_{\|}\neq 0$.

Having radiation go into optical modes of a different polarization than the main lasing modes reduces the coherency of the optical field and, therefore, reduces the optical gain of the main lasing modes. In addition, as the electron energy increases, from (2.1.11) and (2.1.12) intervalence band mixing effects occur; therefore, the valence band wavefunction has both light and heavy hole components. As discussed by Corzine [1993],

the consequence of this band mixing is to cause transitions that are forbidden (see §2.2.2) when the electron energy is small, such as a transition from the first quantized electron subband to the third quantized heavy hole band, to have a finite probability. Thus, band-mixing causes certain "forbidden" transitions to become observable due to a redistribution of the transition strength among the various subband transitions. Optical transitions between subbands other than those primarily responsible for optical gain at the dominant lasing wavelength (i.e., $\lambda_{(E11\text{-}HH1)}$ for TE polarized lasers) contribute photons to the photon flux which have a different wavelength than that of the peak gain wavelength. These photons with a wavelength different than that of the dominant optical mode also reduce the coherency of the optical field and rob the dominant transition of available electrons, and therefore photons that can contribute to gain in the main lasing mode. Consequently, as the electron energy increases, due to either an increase in temperature or an increase in the threshold current density, the rate of change of the peak gain with injected carrier density (i.e., current) will decrease supporting the above hypothesis.

7.2 A NEW RELATION TO DESCRIBE THE TEMPERATURE SENSITIVITY OF THE LASER THRESHOLD CURRENT.

Figures 7.1 to 7.5 showed the quantity $1/(\nabla_T J_{th})$ plotted against the threshold current density, J_{th}, for laser structures R1-394 to R1-400. A best fit line to the data using (7.0.2) was found to be very good. Although $1/(\nabla_T J_{th})$ *vs.* J_{th} is an empirically determined relationship, it may, nevertheless, be treated as a mathematical relationship. This being the case we may integrate (7.0.2) to get the following expression describing the threshold current density dependence upon temperature:

$$J_{th} = \frac{1}{\left[\frac{n}{C}\left(T_{max} - T\right)\right]^{1/n}}, \tag{7.2.1}$$

where $n = m-1$, and T_{max} is the constant of integration. A fit of (7.2.1) to the J_{th} *vs.* T data for two devices of different lengths from laser structure R1-399 is shown in Fig. 7.9. Also shown in Fig. 7.9, for comparative purposes, is the fit of Pankove's equation (1.1.1) to the data between -50°C and -30°C. Clearly (7.2.1) gives a much better fit (correlation factor R=0.9999) to the data than does Pankove's exponential relationship which is in terms of the parameter T_o.

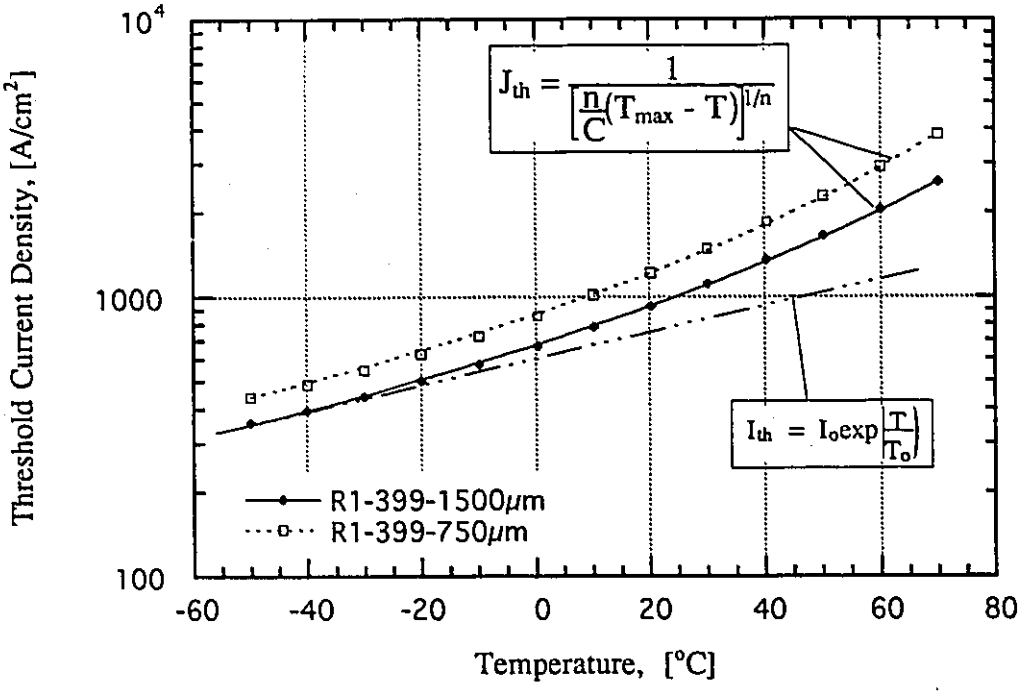

Figure 7.9: J_{th} *vs.* Temperature data for two devices from laser structure R1-399, one 750 μm cavity length device and one 1500 μm cavity length device, and a comparison of the best fit lines as obtained from (7.2.1) over all data and Pankove's relation (1.1.1) between -50°C and -30°C. Equation (7.2.1) fits to the data over the entire temperature range with a correlation factor R of 0.9999.

By fitting (7.2.1) to the J_{th} *vs.* temperature data (using the values of n ($=m-1$) and C as obtained from a fit of (7.0.2) to the $1/(\nabla_T J_{th})$ *vs.* J_{th} data as initial starting values) values of T_{max} *vs.* cavity length and refined values of n and C were obtained for each device from all the device structures grown for this thesis. Table 7.1 shows the mean values of n and C obtained for each device structure. Figs. 7.10 and 7.11 in §7.3 show

the variation of T_{max} *vs.* cavity length, L, for device structures R1-394 and R1-396, and R1-397 to R1-400, respectively.

Table 7.1: Summary of the mean values of n and C obtained for all the MQW laser structures studied in this thesis. These values of n and C were obtained by fitting a best fit line of (7.2.1) to the J_{th} *vs.* T data for each individual device using the values of n and C obtained from a fit of (7.0.2) to the $1/(\nabla_T J_{th})$ *vs.* J_{th} data as starting values. The mean values were determined statistically from the data obtained for all devices (from 11 to 22 in number) from a given structure. The data summarized for laser structure R1-397 was obtained excluding the values of n and C obtained for the shortest cavity length devices.

Device Number	Mean Value of n	Std Deviation in n	Mean Value of C	Std Deviation in C
R1-394 (-1.5%, 5QW)	.508	.010	3572	529
R1-396 (Unstrained, 5QW)	.509	.012	3249	362
R1-397 (+1.2%, 3QW)	.501	.009	3353	322
R1-398 (+1.3%, 3QW)	.507	.011	3449	452
R1-399 (-1.2%, 3QW)	.517	.001	2312	38
R1-400 (Unstrained, 3QW)	.506	.015	2347	266
Bulk Gain Guided λ=1.3 μm	.48	N.A.	4210	N.A.

The mean values of n and C that appear in Table 7.1 were obtained by fitting (7.2.1) to the J_{th} *vs.* temperature data for at least 11, and up to 22, devices from each laser structure. From this data it is found that the value of n is $\approx 1/2$ for all device structures within at most a 3 per cent error. The error in the value of C was at most 15 per cent. The mean values of n and C that were obtained by fitting (7.2.1) to the J_{th} *vs.* temperature data were in agreement with those obtained by fitting (7.0.2) to the $1/(\nabla_T J_{th})$ *vs.* J_{th} data. This point is significant since (7.0.2) represents an empirically derived relationship; however, (7.2.1) is a mathematical relationship which, though derived from the empirical relationship

of (7.0.2) is completely independent from it. Therefore values of n and C obtained from both an empirical fit to the data and a mathematical fit to different data agree, thereby confirming the self-consistency of the relations proposed, and indicating that both n and C should have some physical significance.

The consistency of the values for n (and therefore m in (7.0.2)) that appear in Table 7.1, as well as the fact that n has a seemingly universal rational value of 1/2 (m =3/2 in (7.0.2)) may provide for further insight into the physics behind the temperature sensitivity of the laser threshold current in long wavelength semiconductor lasers. This insight is expected to be more useful than that provided from Pankove's commonly used exponential relationship for two reasons. Firstly, since the parameter m in (7.0.2) has a seemingly constant value of 3/2 for all device structures, (7.0.2) relates the temperature sensitivity of the laser threshold current to J_{th} (and therefore the quasi-Fermi levels, and possibly the density of states, the effective mass, and the barrier heights) by only a single parameter, C. Secondly, from Fig. 7.7, Fig. 7.8 and Table 7.1, this parameter, unlike T_0 or I_0 in (1.1.1), is truly a constant independent of temperature. In addition, the parameter T_{max} obtained by integrating (7.0.2), unlike T_0, has some physical meaning as it represents the maximum possible operating temperature for the laser.

It is found by comparing the value of C obtained for the MQW laser structures studied in this thesis, that there is a correlation between the magnitude of C and the temperature sensitivity of the laser threshold current. The largest value obtained for C [3572±529 ($A^{1/2}$-^oC)/cm] was for laser structure R1-394. The threshold current density of this laser structure was also the least sensitive to temperature variations (T_0>80K at 30°C). In addition, in comparing the laser structures that had three quantum wells in the active region, the smallest temperature sensitivity of I_{th} was observed for laser structures R1-397 and R1-398. The characteristic temperature for the unstrained laser structure R1-400 was found to be only ≈74±8 per cent of the T_0 obtained for the tensile-strained laser structure

R1-397. The constant C for laser structure R1-400 was also only about 72±16 per cent of that of laser structure R1-397.

In addition, it appears as though there is a correlation between the magnitude of the constant C and the density of states at the quasi-Fermi level. Due to the thinner quantum wells in the unstrained laser structure R1-396 in comparison to the unstrained laser structure R1-400, the quantum well density of states for laser R1-396 is much larger than that of laser structure R1-400. Laser structure R1-396 also has a much larger value of C [3249±362 ($A^{1/2}$-^oC)/cm] than that of laser structure R1-400 [C=2347±266 ($A^{1/2}$-^oC)/cm]. Also, the bulk gain-guided laser, due to the $E^{1/2}$ dependence of the density of states (see (2.2.1) and Fig. 2.6), is expected to have a larger density of states than the quantum well structures for energies larger than the quantum well band edge. Since under lasing conditions the Bernard-Durafforg condition (2.2.24) must hold true, the Fermi-level will indeed be above the quantum well band edge. The value of the constant C for the bulk gain guided device [C=4210 ($A^{1/2}$-^oC)/cm] was larger than that obtained for any of the MQW device structures.

7.3 THE DEPENDENCE OF T_{max} ON DEVICE PARAMETERS

By relating (7.2.1) to (6.4.2) an expression relating the parameter representing the maximum operating temperature of the laser, T_{max}, to the cavity length of the laser was obtained. The parameter T_{max} is found to increase with laser cavity length according to the relation:

$$T_{max}(L) = \frac{C\xi}{n \cdot \exp\left(\frac{nD}{L}\right)} + T_{ref}, \tag{7.3.1}$$

where
$$\xi = \frac{(\eta/J_\circ)^n}{\exp\left(\frac{\alpha n}{\Gamma\beta J_\circ}\right)}, \tag{7.3.2}$$

and
$$D = \frac{\ln(1/R)}{\Gamma\beta J_\circ}. \tag{7.3.3}$$

In the above relationships, the parameters C and n (=m-1) are the constants arrived at either by fitting (7.0.2) to the $1/(\nabla_T J_{th})$ *vs.* J_{th} data, or by fitting (7.2.1) to the J_{th} *vs.* temperature data. The parameter Γ is the optical confinement factor, β is the gain coefficient appearing in (6.4.1), η is the internal device efficiency, R is the facet reflectivity, α is the optical loss parameter, and J_o is the transparency current density (i.e., the current density at which the net gain inside the laser cavity, neglecting mirror losses, is zero). The parameter T_{ref} is the temperature at which Γ, β, α, η and J_o are measured. The quantities $\Gamma\beta J_o$ and η/J_o at a given temperature can be determined by fitting (6.4.2) to the J_{th} *vs.* cavity length data as was done in Fig. 6.10.

Equation (7.3.1) also relates the maximum operating temperature of the laser to adjustable device parameters (unlike Pankove's relation) such as: the facet reflectivity, R; the internal efficiency, η; the gain coefficient β, and the transparency current density. As was found in Chapter 6 and Chapter 4, all of these parameters are adjustable by changing quantum well thickness, the number of quantum wells, the constant C, and material strain. For example, in §6.4.4 it was found that compressive strain resulted in a larger internal efficiency, η_i. Therefore, it is expected from (7.3.1) that the compressively strained laser structures R1-394 and R1-399 should have a higher T_{max} than their unstrained counterparts (device structures R1-396 and R1-400, respectively). Indeed, as shown in Fig. 7.10 and 7.11, the compressively strained lasers do have a larger T_{max} than their unstrained counterparts.

Figures 7.10 and 7.11 show the variation of T_{max} with cavity length for the MQW laser structures from Set 1 (3-64Å QWs) and Set 2 (5-38Å QWs), respectively. The value of T_{max} can be determined by fitting (7.2.1) to the J_{th} *vs.* T data directly, or by plotting the quantity $J_{th}^{-1/2}$ *vs.* T and finding the intercept along the temperature axis as indicated by (7.3.4):

$$J_{th}^{-1/2} = \frac{1}{2C}(T_{max} - T). \tag{7.3.4}$$

Equation (7.3.4) is obtained by inverting (7.2.1) and setting n=1/2. Figure 7.12 shows the $J^{-1/2}$ *vs.* T for lasers having three different cavity lengths from device structure R1-399; the excellent correlation is also noted. The method of determining T_{max} from the intercept on the temperature axis is clearly illustrated in this figure.

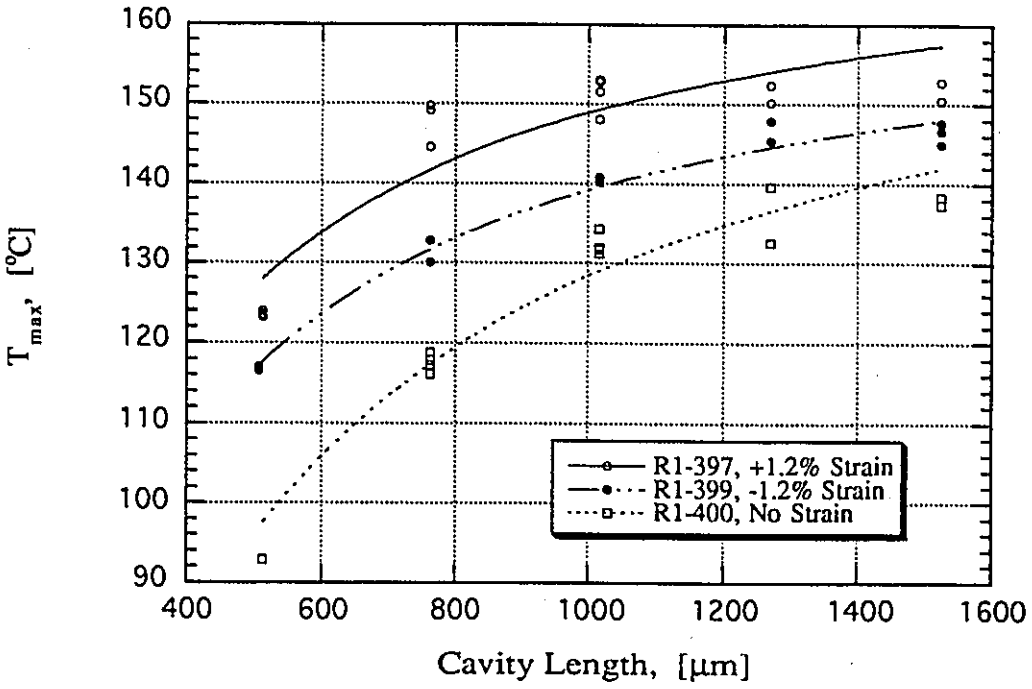

Figure 7.10: T_{max} *vs.* cavity length, L, for lasers from device structures R1-397, R1-399 and R1-400 from Set 1. These devices have active regions containing three 64Å thick QWs.

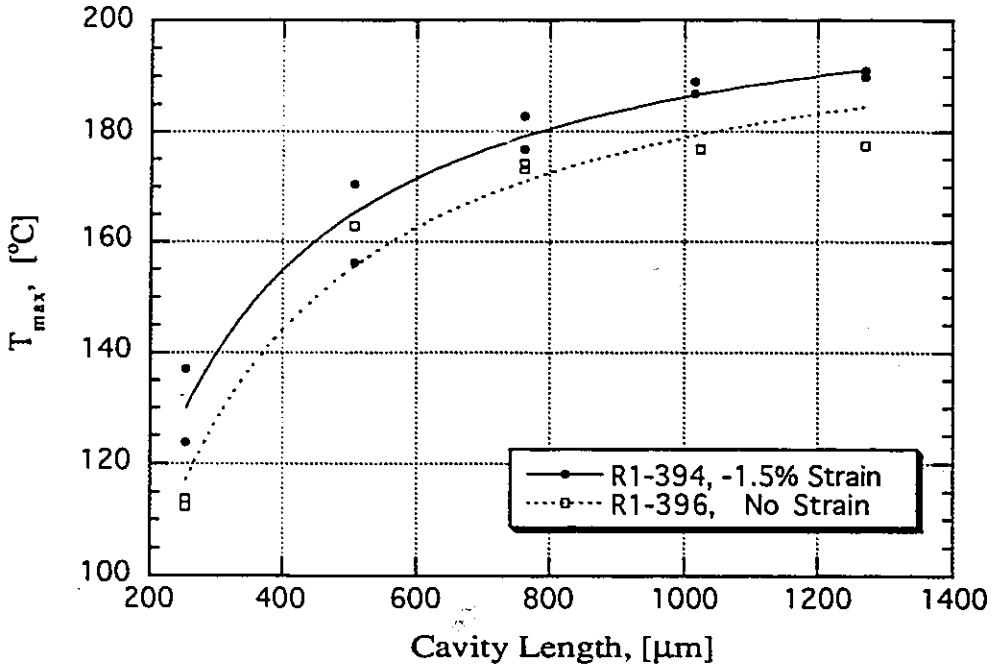

Figure 7.11: T_{max} *vs.* cavity length, L, for lasers from device structures R1-394 and R1-396 from Set 2. These devices have active regions containing five 38Å thick QWs.

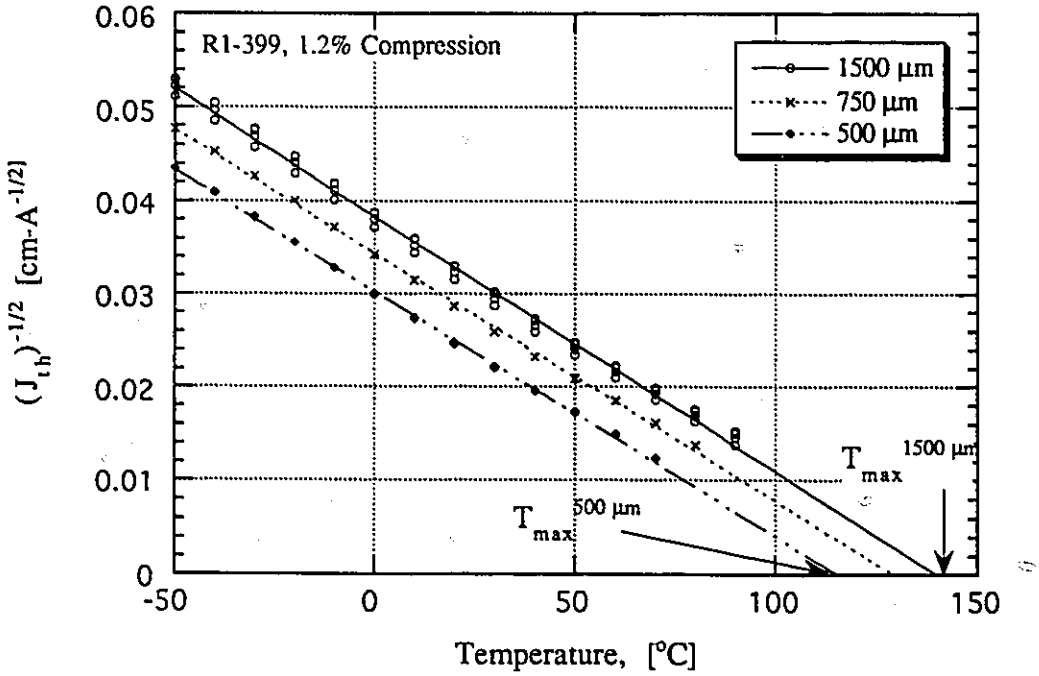

Figure 7.12: Plot of $J_{th}^{-1/2}$ *vs.* temperature for devices with three different cavity lengths from laser structure R1-399. T_{max} is determined by finding the intercept of the best fit line to the data for n=1/2 and C=2312, as indicated in Table 7.1.

Because (7.3.1) relates the laser maximum operating temperature to adjustable device parameters other than the length, it should then be possible to optimize the maximum operating temperature of the laser against these parameter, and therefore, other device characteristics. The following illustrates just a few examples of such parameter adjustment.

Semiconductor lasers used for optical communications purposes often have a high reflectivity coating on the back facet to increase the output power from the front facet and also (from (6.4.3)) to increase the external differential efficiency of the device to improve speed. From (7.3.1) it is seen that increasing the facet reflectivity, R, also results in an increased maximum operating temperature T_{max} for the laser.

The maximum operating temperature may also be increased by increasing the gain constant, β. From (2.2.23) this can be accomplished by using thinner quantum wells and thereby increasing the reduced density of states, ρ_{red}. A larger β found for thinner QWs, as indicated by a comparison of data obtained for the unstrained MQW laser structures R1-396 and R1-400 in Table 6.1 and Fig. 6.24 and Fig. 6.25, respectively, also results in a larger $d\Gamma g_p/dI$ and therefore device speed (and possibly a reduced laser linewidth). The larger $d\Gamma g_p/dI$ for laser structure R1-396 over that found for laser structure R1-400, can be attributed to a larger β for device structure R1-396 since the internal efficiency, η (Fig. 6.12 and Fig. 6.13), the optical confinement factor, Γ (Fig. 4.9), internal absorption, α (fig. 6.14 and 6.15), and the facet reflectivity for laser structures R1-396 and R1-400 are identical. From a comparison of Fig. 7.10 and Fig. 7.11, T_{max} is about 40°C larger for laser structure R1-396 than it is for laser structure R1-400. As discussed in §6.5.1, QWs less than 50 Å thick are rarely used in the active region of semiconductor laser structures as the use of thin QWs increases the transparency current density, J_o. A large J_o is avoided because it is thought that by reducing J_o and, therefore, J_{th} as much as possible one can avoid excess device heating, due to ohmic losses, and increase T_{max}.

However, as indicated by (7.3.1) a larger transparency current density, J_o, also leads to an increased T_{max}. The increase in T_{max} due to a larger transparency current density is supported by the data of Fig. 7.10: laser structures R1-398 and R1-397 had threshold currents, and transparency currents at 30°C that were ≈50 per cent larger than that the values obtained for the unstrained QW structure R1-400, as indicated in Table 6.1 and Table 6.2. From Fig. 7.10, the T_{max} for the tensile-strained laser structure R1-397 is significantly larger than that for the unstrained laser structure R1-400. The tensile strained laser structures were also found to have a larger value for C in (7.3.1) and this could also contribute to a larger T_{max} for theses structures.

Finally, it can be seen that by increasing the optical confinement factor (i.e., by adding more QWs to the active region of the laser), T_{max} can also be improved. It should be noted, however, that from (6.4.7) a larger optical confinement factor also increases the contributions due to intervalence band and free-carrier absorption in the laser active region. And an increase in the internal absorption coefficient, α, will tend to decrease T_{max}. Nevertheless, using the relation of (7.3.1) it should be possible to do a multi-variable analysis of laser design parameters appearing in (7.3.1) in relation to device structure in order to optimize laser performance against the maximum operating temperature, T_{max}.

7.4 SUMMARY

In this chapter a strong correlation between the temperature sensitivity of the laser threshold current (in terms of the temperature rate of change of J_{th}, as given by $\nabla_T J_{th}$ and not T_o) and the laser threshold current density, J_{th}, was observed for the first time. The quantity $\nabla_T J_{th}$ was found to be related to J_{th} by the power law expression:

$$\frac{J^m}{\nabla_T J_{th}} = C \qquad (7.0.1)$$

where m was determined to have a value of 3/2 for all devices studied, and the parameter C was thought to be related to the density of states in the laser active region. In Chapter 1, Chapter 3 and Chapter 6 it was mentioned that the exponential relationship (1.1.1) proposed by Pankove in 1968, and used since to describe the temperature sensitivity of the laser threshold current, is inappropriate. From (7.0.1) a new expression to describe the temperature sensitivity of the laser threshold current was derived mathematically. This expression, as given by

$$J_{th} = \frac{1}{\left[\frac{n}{C}\left(T_{max} - T\right)\right]^{1/n}}, \tag{7.2.1}$$

where $n=m-1$, was found to fit to the I_{th}-T characteristics of a laser much better than Pankove's exponential relationship over a wide range of temperatures. In addition, unlike in the case of Pankove's exponential relationship, the constants appearing in (7.2.1) were found to be truly constant independent of temperature. The constant T_{max} in (7.2.1) was found to have physical significance as it represents the maximum operating temperature of a laser. This is a useful parameter, since, in the search for lasers which can operate without the benefit of thermoelectric coolers, it is the maximum operating temperature which is important, and not necessarily T_o.

Equation (7.0.1) was empirically derived; however, by treating this expression as a mathematically one and integrating it, the mathematical relationship of (7.2.1) was found. When a best fit of (7.0.1) was made to the $\nabla_T J_{th}$ *vs.* J_{th} data, and a best fit of (7.2.1) was made to the J_{th} *vs.* T data, similar values of m and C were obtained, thereby indicating the self consistency of these expressions. By setting $n = 1/2$ in (7.2.1) and then inverting and squaring this equation, a linear relationship between $J^{-1/2}$ and T was obtained in terms of T_{max}. T_{max} was then obtained from the intercept on the temperature axis from a best fit

line to a plot of the $J^{-1/2}$ *vs.* T data for lasers of varying cavity lengths, L. A plot of T_{max} *vs.* L showed that the maximum operating temperature of a laser depends on cavity length, especially for short length devices. In Chapter 6 a relationship between J_{th} and laser cavity length was also noted. By further relating the J_{th}-T relation of (7.2.1) to the J_{th}-L relation of (6.4.2) at a given temperature, an explicit relationship, (7.3.1), between T_{max} and device cavity length was obtained. A best fit line of (7.3.1) to the T_{max} *vs.* cavity length data for each device structure was found to fit reasonably well.

The expression relating T_{max} to the device cavity length, L, arrived at in the above manner also contained the device parameters: η (internal efficiency); J_o (transparency current density); α (optical absorption loss); Γ (optical confinement factor); β (gain coefficient); and, R (facet reflectivity). The parameters Γ, R, and L are related to device structure and can be adjusted easily. The parameters η, J_o and β reflect not only device structure, but also material properties, such as the density of states and QW strain. In Chapter 6, the effects of QW width and strain on the parameters η, J_o and β were noted, and it was found that these parameters can be increased by adjusting both strain and QW width. By increasing these parameters it was seen from (7.3.1) that the maximum operating temperature of a laser could also be increased. In addition from (7.3.1) it is shown that T_{max} can also be increased by increasing the magnitude of Γ, R and L. Thus, for the first time, a relationship between a lasers maximum operating temperature and easily adjustable device parameters has been obtained. The existence of such a relationship will henceforth allow for the optimization of T_{max} (by adjusting the above device parameters) against other device characteristics such as speed and external differential efficiency.

CHAPTER 8: CONCLUSIONS

8.0 LASER STRUCTURE AND DESIGN

In this thesis an extensive study of multiple quantum well (MQW) and strained MQW graded index separate confinement (GRINSCH), ridge waveguide laser structures fabricated in the InGaAsP/InP material system was reported. For the purposes of this thesis two sets of laser structures were designed, grown and fabricated. In one set of laser structures (Set 1) the laser active regions contained three-64 Å thick quantum wells (QWs) with the material strain in the QWs ranging from 1.3 per cent in tension to 1.2 per cent in compression. Unstrained QW structures were also fabricated. In the other set of laser structures (Set 2), the laser active region contained five-38 Å thick quantum wells with the material strain in the QWs ranging from no-strain to 1.5 per cent compressive strain. Laser structures from both sets were designed to have identical GRINSCH waveguiding regions and similar emission wavelengths. The study conducted using these laser structures was unique in comparison to those studies performed by other authors in that, for the first time, an emphasis was placed on comparing the temperature performance, of strained and unstrained QW laser structures having the *same* QW thickness, in addition to similar emission wavelengths. By maintaining an identical QW width in the active region for laser structures belonging to a given set, the effects due to strain on device performance could be more effectively isolated.

To set the stage for this thesis the theoretical concepts of energy level quantization, and the effects of quantization on the density of states for carriers in a quantum well were presented. The effects of material strain on the quantum well band structure were also

discussed. By relating strain and quantization effects on the quantum well band structure to the theoretical optical gain in a quantum well laser, the implications of quantization and strain effects with regards to laser performance, specifically the laser threshold current, I_{th}, and rate of change of gain with injected carrier concentration were illustrated.

Next, the procedure used to design the MQW and strained MQW laser structures for this thesis was presented along with the results from some example calculations. In addition, the methodology for determining the magnitude of the $In_{1-x}Ga_xAs_yP_{1-y}$ material parameters required to perform the design calculations was discussed.

To ensure that any observed differences in the operating characteristics between the strained and unstrained MQW laser structures studied in this thesis could be attributed to strain effects, and not due to variations in material quality, an extensive investigation into the crystal quality and consistency of the grown laser structures was performed. The analytical techniques used for these investigations included: cross-sectional and plan view transmission electron microscopy; polarization resolved photoluminescence (PL); scanning PL; and power and temperature dependent PL measurements. From these investigations the crystal quality of all the device structures studied was found to be excellent.

8.1 LASER TEMPERATURE PERFORMANCE

The laser threshold current, I_{th}, for InGaAsP/InP based semiconductor lasers for optical communications purposes suffers from a high temperature sensitivity in comparison to lasers fabricated in the AlGaAs/GaAs material system. The objectives of the experimental investigations of this thesis were to determine if strain could be used to decrease the temperature sensitivity of I_{th} for InGaAsP/InP based lasers and, also, to determine if strain could be used to increase the maximum operating temperature of these lasers. Given these objectives, the physical mechanisms proposed by other authors to be

responsible for the temperature sensitivity of I_{th} in InGaAsP/InP based lasers were presented. It was found that the physical explanations proposed by other authors to be primarily responsible for the I_{th}-T characteristics of InGaAsP/InP based lasers were largely influenced by the existence of an exponential relationship proposed by Pankove in 1968 to describe this temperature sensitivity; even though, in his original manuscript Pankove [1968] suggested that "there [was] no explicit demonstration that an exponential dependence of I_{th} on temperature should be obtained". Since Pankove first proposed the exponential relationship

$$I_{th} = I_o \exp(T/T_o), \tag{1.1.1}$$

in 1968, the temperature sensitivity of the laser threshold current has been described in terms of the characteristic temperature parameter, T_o. From an examination of (1.1.1) it is seen that a small value for T_o indicates a large I_{th}-T sensitivity.

From the experimental investigations of this thesis it was found that the temperature sensitivity of I_{th} in InGaAsP/InP based lasers is much more complicated than can be described by a single dominant physical mechanism as proposed by other authors. It was found that the I_{th}-T relation for InGaAsP lasers is governed by an intimate cyclical relationship between; the temperature rate of change of the peak optical gain *vs.* current relations; the change in the energy band-gap with temperature and injected current; and, current leakage out of the laser active region. It was also found that (1.1.1) is inappropriate to describe the temperature sensitivity of the laser threshold current and an alternate relationship was proposed.

The relationship proposed in this thesis to describe the temperature sensitivity of I_{th} of InGaAsP/InP based lasers was arrived at mathematically from an empirically observed power law relationship between the temperature rate of change of the threshold current

density, $\nabla_T J_{th}$, and the threshold current density, J_{th}. This empirically observed power law relationship was found to be:

$$\frac{J^m}{\nabla_T J_{th}} = C, \tag{7.0.2}$$

where m was found to have a value of 3/2 for all device structures studied, and C was found to be related to the carrier density of states in the laser active region.

The alternate relationship proposed to describe the temperature sensitivity of I_{th} was found to fit to the empirical I_{th}-T data much more accurately than the relationship proposed by Pankove. The alternate mathematical expression proposed to describe the I_{th}-T relationship for InGaAsP based QW lasers in this thesis was:

$$J_{th} = \frac{1}{\left[\frac{n}{C}(T_{max} - T)\right]^{1/n}}, \tag{7.2.1}$$

were n was found to have a value of 1/2 for all device structures studied in this thesis (including a gain-guided Zn diffused oxide stripe laser emitting at 1.3 μm), and the parameter T_{max} was found to have much more physical significance than the characteristic temperature parameter T_o proposed by Pankove. The parameter T_{max} represents the maximum possible operating temperature of a laser (i.e., that temperature at which the threshold current density asymptotically approaches infinity). In the search for long wavelength semiconductor lasers which are capable of operating at high temperatures (so that costly thermoelectric coolers with a large power requirement can be eliminated in the packaging of these devices) it is this maximum operating temperature that is important.

Additionally, by relating (7.2.1) to the theoretically arrived at and experimentally confirmed relationship between the threshold current density, J_{th}, of a QW laser and the device cavity length, an expression relating T_{max} to adjustable device parameters, such as:

the internal efficiency, η; the transparency current density, J_0; the optical absorption loss, α; the optical confinement factor, Γ; the gain coefficient, β; and, the facet reflectivity, R, was arrived at for the first time. This expression is given by:

$$T_{max}(L) = \frac{C\xi}{n \cdot \exp\left(\frac{nD}{L}\right)} + T_{ref}, \tag{7.3.1}$$

where

$$\xi = \frac{(\eta/J_o)^n}{\exp\left(\frac{\alpha n}{\Gamma\beta J_o}\right)}, \tag{7.3.2}$$

and

$$D = \frac{\ln(1/R)}{\Gamma\beta J_o}. \tag{7.3.3}$$

Equation (7.3.1) indicates that it could be possible to optimize the maximum operating temperature of a long wavelength semiconductor QW laser for use in optical communications systems against other important device characteristics, such as the maximum operating speed and external differential efficiency, by adjusting the appropriate material parameters. In (7.3.1) the parameters Γ, R, and L are related to device structure and can be easily adjusted. The parameters η, J_0 and β reflect not only device structure, but also material properties, such as the density of states and QW strain. Through the course of the investigations performed for this thesis, it was found that compressive strain can be used to increase η, β, C and J_0 in (7.3.1) and, therefore, to increase the maximum operating temperature of a QW laser. Accordingly, for a 1.5 per cent compressively strained QW laser structure containing five 30 Å QWs in the active region, the highest ever reported maximum operating temperature of 140°C for an InGaAsP based laser was observed. In terms of the old characteristic device parameter T_0, for reference, this device was also found to be characterized by the largest ever reported characteristic temperature

(T_o= 88 K) measured for an InGaAsP based laser without the benefits of high reflectivity (HR) coatings on the facets, and under continuous wave (CW) operating conditions.

8.2 EFFECTS OF STRAIN ON LASER OPERATING CHARACTERISTICS

Apart from an improvement in the maximum operating temperature, it was also found that quantum well material strain affects other device characteristics. It was found that the use of compressive strain results in; a higher maximum output power (140 mW for the 1.5 per cent compressively strained MQW laser having five-38 Å thick QWs); a higher internal efficiency, η_i; a smaller threshold current, I_{th}; and, a smaller laser linewidth-power product, in comparison to unstrained structures. The use of tensile strain was also found to result in a beneficial smaller linewidth-power product and reduced internal optical absorption; however, tensile strain was also associated with a smaller gain coefficient, β; a larger threshold current, I_{th}; a larger transparency current; and, a reduced internal efficiency.

8.3 RECOMMENDATIONS FOR FUTURE WORK

In the course of the investigations for this thesis a number of questions regarding the effects of strain on laser performance and laser performance in general arose. Since carrier leakage into the InP cladding regions of an InGaAsP/InP laser structure is theoretically strongly dependent on temperature, and since above threshold the internal quantum efficiency of the laser should be ≈1, due to a much smaller stimulated radiative lifetime in comparison to the non-radiative lifetime, it is surprising that the measured internal device efficiency does not approach unity at low temperatures. To investigate this phenomena further, it is suggested that the measurements of this thesis be extended down to cryogenic temperatures and that broad area device structures be investigated to determine

if the internal efficiency in these devices approaches unity when the importance of lateral current spreading is reduced. In addition, it is suggested that spatially resolved electroluminescence measurements be made from the laser facets to clarify the role of lateral carrier diffusion within the active region of ridge waveguide lasers. By extending the measurements of the operating characteristics of these lasers down to cryogenic temperatures it will be possible to eliminate the effects of Auger recombination on the non-radiative lifetime and thereby isolate the effects of Auger recombination on laser device performance.

All the measurements performed in this thesis were made under CW conditions; therefore, it is also suggested that investigations undertaken be performed for lasers operating under pulsed conditions. By performing low duty cycle high speed pulsed measurements, internal device heating effects could be eliminated. Therefore the effects of internal device heating on the I_{th}-T relation proposed in this thesis under CW operating conditions, and, therefore, the constants, n, C and T_{max} could be determined.

Theoretical laser device models could also be developed with the objective of explaining the apparent universality of the value of 3/2 for the constant m in (7.0.2). Through such theoretical analysis it may be possible to gain further insight into the physics responsible for the high temperature sensitivity of I_{th} for InGaAsP/InP based semiconductor lasers. O'Gorman *et. al.* [1992] have recently suggested a possible connection between the I_{th}-T characteristics of a laser and thermodynamic second order phase transitions. In addition by developing theoretical device models which include the effects of strain and QW width on the device parameters appearing in (7.3.1), the optimization of the maximum operating temperature of InGaAsP/InP based lasers against other device characteristics, such as, the maximum operating speed and differential efficiency, could possibly be performed.

APPENDIX A

Calculations: R1-394

Bulk Material Parameters at Temperature [K] = 300
Barrier Composition: x = 0.134 y = 0.292
Well Composition: x = 0.105 y = 0.697

	InGaAsP (well)	InGaAsP (Barrier)
S11 [cm^2/10^11 dyne]	0.1777	0.1641
S12 [cm^2/10^11 dyne]	-0.0625	-0.0580
S44 [cm^2/10^11 dyne]	0.2334	0.2172
Lattice Constant [A]	5.9582	5.8688
Heavy Hole Mass (Mh)	-0.5480	-0.7194
In-plane mass (Mh)	-0.0484	0.0000
Light Hole Mass (Ml)	-0.0504	-0.0773
In-plane mass (Ml)	-0.1153	0.0000
Eff. Electron Mass (Ml)	0.0470	0.0739
Hydrostatic Cons. [eV]	-6.8802	-7.6218
Deformation Potnl. [eV]	-1.7153	-1.6144
Valence Band [eV]	0.2400	0.0000
Conduction Band [eV]	0.9900	1.1500
Band Gap [eV]	0.7500	1.1500

Superlattice Parameters
Fractional relaxation from substrate = 0

	Well Layer	Barrier Layer
Stress [10^11 dyne/cm^2]	-0.1301	0.0000
Biaxial Strain	-0.0150	0.0000
Critical Layer Thickness	134.719	
Lattice Const [A]	5.8688	5.8688
Layer Thickness [A]	30.0	100.0
Heavy Hole Band [eV]	0.2703	0.0000
Light Hole [eV]	0.1815	0.0000
Conduction Band [eV]	1.0612	1.1500
Band Gap [eV]	0.7910	1.1500

ENERGY SOLUTIONS

Heavy Hole Band [eV]	Energy Spread	Light Hole Band [eV]	Energy Spread
0.22569312	0.00000000	0.05126729	0.00980331
0.10517009	0.00000000		

Electron Band [eV]	Energy Spread
1.13913992	0.07031523

EL1-HH1 Transition Energy = 0.905447[eV]
EL1-HH1 Transition Wavelength = 1.369490[um]

Calculations: R1-396

Bulk Material Parameters at Temperature [K] = 300
Barrier Composition: x = 0.134 y = 0.292
Well Composition: x = 0.419 y = 0.898

	InGaAsP (well)	InGaAsP (Barrier)
S11 [cm^2/10^11 dyne]	0.1596	0.1641
S12 [cm^2/10^11 dyne]	-0.0543	-0.0580
S44 [cm^2/10^11 dyne]	0.2141	0.2172
Lattice Constant [A]	5.8688	5.8688
Heavy Hole Mass (Mh)	-0.4860	-0.7194
In-plane mass (Mh)	-0.0523	0.0000
Light Hole Mass (Ml)	-0.0509	-0.0773
In-plane mass (Ml)	-0.1211	0.0000
Eff. Electron Mass (Ml)	0.0501	0.0739
Hydrostatic Cons. [eV]	-7.5267	-7.6218
Deformation Potnl. [eV]	-1.7348	-1.6144
Valence Band [eV]	0.2100	0.0000
Conduction Band [eV]	1.0100	1.1500
Band Gap [eV]	0.8000	1.1500

Superlattice Parameters
Fractional relaxation from substrate = 0

	Well Layer	Barrier Layer
Stress [10^11 dyne/cm^2]	0.0000	0.0000
Biaxial Strain	0.0000	0.0000
Critical Layer Thickness	0.000	
Lattice Const [A]	5.8688	5.8688
Layer Thickness [A]	30.0	100.0
Heavy Hole Band [eV]	0.2100	0.0000
Light Hole [eV]	0.2100	0.0000
Conduction Band [eV]	1.0100	1.1500
Band Gap [eV]	0.8000	1.1500

ENERGY SOLUTIONS

Heavy Hole Band [eV]	Energy Spread	Light Hole Band [eV]	Energy Spread
0.16335000	0.00000000	0.06455000	0.00739999
0.04805000	0.00000000		

Electron Band [eV]	Energy Spread
1.11405000	0.01440001

EL1-HH1 Transition Energy = 0.942700[eV]
EL1-HH1 Transition Wavelength = 1.315371[um]

Calculations: R1-397

Bulk Material Parameters at Temperature [K] = 300
Barrier Composition: x = 0.134 y = 0.292
Well Composition: x = 0.640 y = 1.000

	InGaAsP (well)	InGaAsP (Barrier)
S11 [cm^2/10^11 dyne]	0.1453	0.1641
S12 [cm^2/10^11 dyne]	-0.0480	-0.0580
S44 [cm^2/10^11 dyne]	0.1987	0.2172
Lattice Constant [A]	5.7992	5.8688
Heavy Hole Mass (Mh)	-0.4676	-0.7194
In-plane mass (Mh)	-0.0605	0.0000
Light Hole Mass (Ml)	-0.0532	-0.0773
In-plane mass (Ml)	-0.1347	0.0000
Eff. Electron Mass (Ml)	0.0522	0.0739
Hydrostatic Cons. [eV]	-8.1946	-7.6218
Deformation Potnl. [eV]	-1.7360	-1.6144
Valence Band [eV]	0.1224	0.0000
Conduction Band [eV]	1.0684	1.1500
Band Gap [eV]	0.9460	1.1500

Superlattice Parameters
Fractional relaxation from substrate = 0

	Well Layer	Barrier Layer
Stress [10^11 dyne/cm^2]	0.1234	0.0000
Biaxial Strain	0.0120	0.0000
Critical Layer Thickness	179.114	
Lattice Const [A]	5.8688	5.8688
Layer Thickness [A]	55.0	100.0
Heavy Hole Band [eV]	0.1029	0.0000
Light Hole [eV]	0.1951	0.0000
Conduction Band [eV]	0.9907	1.1500
Band Gap [eV]	0.7957	1.1500

ENERGY SOLUTIONS

Heavy Hole Band [eV]	Energy Spread	Light Hole Band [eV]	Energy Spread
0.08650931	0.00000000	0.11149302	0.00160062
0.04217892	0.00000000		

Electron Band [eV]	Energy Spread
1.06591351	0.00300130

EL1-LH1 Transition Energy = 0.946420[eV]
EL1-LH1 Transition Wavelength = 1.310200[um]

Calculations: R1-398

Bulk Material Parameters of Temperature [K] = 300
Barrier Composition: x = 0.134 y = 0.292
Well Composition: x = 0.654 y = 1.000

	InGaAsP (well)	InGaAsP (Barrier)
S11 [cm^2/10^11 dyne]	0.1442	0.1641
S12 [cm^2/10^11 dyne]	-0.0476	-0.0580
S44 [cm^2/10^11 dyne]	0.1975	0.2172
Lattice Constant [A]	5.7935	5.8688
Heavy Hole Mass (Mh)	-0.4689	-0.7194
In-plane mass (Mh)	-0.0614	0.0000
Light Hole Mass (Ml)	-0.0538	-0.0773
In-plane mass (Ml)	-0.1363	0.0000
Eff. Electron Mass (Ml)	0.0528	0.0739
Hydrostatic Cons. [eV]	-8.2427	-7.6218
Deformation Potnl. [eV]	-1.7346	-1.6144
Valence Band [eV]	0.1122	0.0000
Conduction Band [eV]	1.0752	1.1500
Band Gap [eV]	0.9630	1.1500

Superlattice Parameters
Fractional relaxation from substrate = 0

	Well Layer	Barrier Layer
Stress [10^11 dyne/cm^2]	0.1346	0.0000
Biaxial Strain	0.0130	0.0000
Critical Layer Thickness	161.796	
Lattice Const [A]	5.8688	5.8688
Layer Thickness [A]	55.0	100.0
Heavy Hole Band [eV]	0.0912	0.0000
Light Hole [eV]	0.1918	0.0000
Conduction Band [eV]	0.9902	1.1500
Band Gap [eV]	0.7985	1.1500

ENERGY SOLUTIONS

Heavy Hole Band [eV]	Energy Spread	Light Hole Band [eV]	Energy Spread
0.07538624	0.00000000	0.10958364	0.00160049
0.03326599	0.00010005		

Electron Band [eV]	Energy Spread
1.06490830	0.00290142

EL1-LH1 Transition Energy = 0.947325[eV]
EL1-LH1 Transition Wavelength = 1.308949[um]

Calculations: R1-399

Bulk Material Parameters at Temperature [K] = 300
Barrier Composition: x = 0.134 y = 0.292
Well Composition: x = 0.117 y = 0.629

	InGaAsP (well)	InGaAsP (Barrier)
S11 [cm^2/10^11 dyne]	0.1749	0.1641
S12 [cm^2/10^11 dyne]	-0.0615	-0.0580
S44 [cm^2/10^11 dyne]	0.2300	0.2172
Lattice Constant [A]	5.9401	5.8688
Heavy Hole Mass (Mh)	-0.5771	-0.7194
In-plane mass (Mh)	-0.0519	0.0000
Light Hole Mass (Ml)	-0.0552	-0.0773
In-plane mass (Ml)	-0.1223	0.0000
Eff. Electron Mass (Ml)	0.0519	0.0739
Hydrostatic Cons. [eV]	-7.0274	-7.6218
Deformation Potnl. [eV]	-1.6978	-1.6144
Valence Band [eV]	0.1920	0.0000
Conduction Band [eV]	1.0220	1.1500
Band Gap [eV]	0.8300	1.1500

Superlattice Parameters
Fractional relaxation from substrate = 0

	Well Layer	Barrier Layer
Stress [10^11 dyne/cm^2]	-0.1058	0.0000
Biaxial Strain	-0.0120	0.0000
Critical Layer Thickness	178.579	
Lattice Const [A]	5.8688	5.8688
Layer Thickness [A]	55.0	100.0
Heavy Hole Band [eV]	0.2158	0.0000
Light Hole [eV]	0.1432	0.0000
Conduction Band [eV]	1.0805	1.1500
Band Gap [eV]	0.8648	1.1500

ENERGY SOLUTIONS

Heavy Hole Band [eV]	Energy Spread
0.20041570	0.00000000
0.15530091	0.00000000
0.08477779	0.00000000
0.00655215	0.00100033

Light Hole Band [eV]	Energy Spread
0.07446581	0.00320068

Electron Band [eV]	Energy Spread
1.12292965	0.01130850

EL1-HH1 Transition Energy = 0.914514[eV]
EL1-HH1 Transition Wavelength = 1.355912[um]

Calculations: R1-400

Bulk Material Parameters at Temperature [K] = 300
Barrier Composition: x = 0.134 y = 0.292
Well Composition: x = 0.346 y = 0.745

	InGaAsP (well)	InGaAsP (Barrier)
S11 [cm^2/10^11 dyne]	0.1749	0.1641
S12 [cm^2/10^11 dyne]	-0.0553	-0.0580
S44 [cm^2/10^11 dyne]	0.2153	0.2172
Lattice Constant [A]	5.8688	5.8688
Heavy Hole Mass (Mh)	-0.5400	-0.7194
In-plane mass (Mh)	???????	0.0000
Light Hole Mass (Ml)	-0.0579	-0.0773
In-plane mass (Ml)	???????	0.0000
Eff. Electron Mass (Ml)	0.0575	0.0739
Hydrostatic Cons. [eV]	-7.4608	-7.6218
Deformation Potnl. [eV]	-1.7061	-1.6144
Valence Band [eV]	0.1620	0.0000
Conduction Band [eV]	1.0420	1.1500
Band Gap [eV]	0.8800	1.1500

Superlattice Parameters
Fractional relaxation from substrate = 0

	Well Layer	Barrier Layer
Stress [10^11 dyne/cm^2]	0.0000	0.0000
Biaxial Strain	0.0000	0.0000
Critical Layer Thickness	0.000	
Lattice Const [A]	5.8688	5.8688
Layer Thickness [A]	55.0	100.0
Heavy Hole Band [eV]	0.1620	0.0000
Light Hole [eV]	0.1620	0.0000
Conduction Band [eV]	1.0420	1.1500
Band Gap [eV]	0.8800	1.1500

ENERGY SOLUTIONS

Heavy Hole Band [eV]	Energy Spread
0.14635000	0.00000000
0.10125000	0.00000000
0.03515000	0.00000000

Light Hole Band [eV]	Energy Spread
0.09085000	0.00220000

Electron Band [eV]	Energy Spread
1.09735000	0.00540000

EL1-HH1 Transition Energy = 0.943000[eV]
EL1-HH1 Transition Wavelength = 1.314952[um]

REFERENCES

Adachi, S., (1992), Physical Properties of III-V Semiconductor Compounds, InP, InAs, GaAs, GaP, InGaAs, and InGaAsP. John Wiley & Sons, Toronto.

Adachi, S., (1982), "Material parameters of $In_{1-x}Ga_xAs_yP_{1-y}$ and related binaries." J. Appl. Phys. **53**(12) pp.8775-8792.

Adams, A.R., Asada, M., Suematsu, Y., and Arai, A., (1980), "The temperature dependence of the efficiency and threshold current of $In_{1-x}Ga_xAs_yP_{1-y}$ lasers related to intervalence band absorption." Japanese J. Appl. Phys. **19**(10), pp.L621-L624.

Agrawal, G.P., and Dutta, N.K., (1986), Long-Wavelength Semiconductor Lasers. Van Nostrand Reinhold, New York.

Ahn, D., and Chuang, S-L., (1990), "Optical gain and gain suppression of quantum-well lasers with valence band mixing." IEEE J. Quantum Electron. **26**(1), pp.13-24.

Anderson, T.G., Chen, Z.G., Kulakovskii, V.D., Uddin, A., and Vallin, J.T., (1987), "Variation of the critical layer thickness with In content in strained $In_xGa_{1-x}As$-GaAs quantum wells grown by molecular beam epitaxy." Appl. Phys. Lett. **51**(10), pp.752-754.

Asada, M., and Suematsu, Y., (1983), "The effects of loss and nonradiative recombination on the temperature dependence of threshold current in 1.5-1.6 μm GaInAsP/InP lasers." IEEE J. Quantum Electron, **19**(6), pp.917-923.

Asada, M., Adams, A.R., Stubkjaer, K.E., Suematsu, Y., Itaya, y., and Arai, S., (1981), "The temperature dependence of the threshold current of GaInAsP/InP DH lasers." IEEE J. Quantum Electron. **17**(5), pp.611-618.

Asada, M., Kameyama, A., and Suematsu, Y., (1984), "Gain and intervalence band absorption in quantum-well lasers." IEEE J. Quantum Electron. **20**(7), pp.745-753.

Asai, H., and Oe, K., (1983), "Energy band-gap shift with elastic strain in $Ga_xIn_{1-x}P$ epitaxial layers on (001) GaAs substrates." J. Appl. Phys. **54**(4), pp.2052-2056.

Bastard, G. (1981), "Superlattice band structure in the envelope-function approximation." Phys. Rev. B, B**24**, No.10, pp.5693-5697.

Bastard, G. (1982), "Theoretical investigations of superlattice band structure in the envelope-function approximation." Phys. Rev. B, B**25**, No.12, pp.7584-7597.

Beernink, K.J., York, P.K., and Coleman, J.J. (1989), "Dependence of threshold current density of quantum well composition for strained-layer InGaAs-GaAs lasers by metalorganic chemical vapor deposition." Appl. Phys. Lett. **55**(25), pp.2585-2587.

Brennan, K.F., and Summers, C.J., (1987), "Theory of resonant tunneling in a variably spaced multiquantum well structure: An airy function approach." J. Appl. Phys. **61**(2), pp.614-623.

Briodo, D.A., and Sham, L.J., (1985), "Effective masses of holes at GaAs-AlGaAs heterojunctions." Phys. Rev. B, B**31**(2), pp.888-892.

Camphausen, D.L, Connell, N. G.A., and Paul, W., (1971), "Calculation of energy-band pressure coefficients from the dielectric theory of the chemical bond." Phys. Rev. Lett., **26**(4), pp. 184-188.

Capasso, F., Sen, S., Gossard, A.C., Hutchinson, A.L., and English, J.H., (1986), "Quantum-well resonant tunneling bipolar transistor operating at room temperature." IEEE Electron. Device Lett. EDL-**7**(10), pp.573-576.

Capasso, F., and Kiehl, R.A., (1985), "Resonant tunneling transistor with quantum well base and high-energy injection: A new negative differential resistance device." J. Appl. Phys. **58**(3), pp.1366-1368.

Casey, Jr. H.C., (1984), "Temperature dependence of the threshold current density in InP-$Ga_{0.28}In_{0.72}As_{0.6}P_{0.4}$ (λ=1.3 μm) double heterostructure lasers." J. Appl. Phys. **56**(7), pp.1959-1964.

Casey, Jr. H.C., and Panish, M.B., (1978), Heterostructure Lasers, Part A: Fundamental Principles. Academic Press, New York.

Cassidy, D.T., (1984), "Technique for measurement of the gain spectra of semiconductor diode lasers." J. Appl. Phys. **56**(11), pp.3096-3099.

Cassidy, D.T., and Elenkrig, B., (1993), private communication.

Chamberlain, J.M., Reeder, A.A., Turner, R.J., Kuphal, E., and Benchimol, J.L., (1987), "Effective masses and evidence for alloy disorder effects in $Ga_xIn_{1-x}As_yP_{1-y}$ investigated by shallow donar photoconductivity." Solid-State Electron. **30**, pp. 217.

Chandrasekar, M., and Pollak, F.H., (1977), "Effects of uniaxial stress on the electroreflectance spectrum of Ge and GaAs." Phys. Rev. B, B**15**(4), pp.2127-2144.

Chen, L-H, Mattos, J.C.V., Prince, F.C., and Patel, N.B., (1984), "Spatially resolved observation of carrier leakage in 1.3-μm $In_{1-x}Ga_xAs_yP_{1-y}$ lasers." Appl. Phys. Lett. **44**(5), pp.520-521.

Chen, T.R., Chang, B., Chiu, L.C., Yu, K.L, Margalit, S., and Yariv, A., (1983), "Carrier leakage and temperature dependence of InGaAsP lasers." Appl. Phys. Lett. **43**(3), pp. 217-218.

Chen, T.R., Margalit, S., Koren, U., Yu, K.L, Chiu, L.C., Hasson, A., and Yariv, A., (1983), "Direct measurement of the carrier leakage in an InGaAsP/InP laser." Appl. Phys. Lett. **42**(12), pp. 1000-1002.

Chen, Y., Zucker, J.E., Chiu, T.H., Marshall, J.L., and Jones, K.L., (1992), "Quantum well electroabsorption modulators at 1.55 μm using single-step selective area chemical beam epitaxial growth." Appl. Phys. Lett. **61**(1), pp.10-12.

Chik, K.D., and Richardson, B.A., (1990), "On the origin of the carrier leakage in GaInAsP/InP double-heterojunction lasers." J. Appl. Phys. **67**(5), pp. 2660-2662.

Chik, K.D., (1988) "A theoretical analysis of Auger recombination induced energetic carrier leakage in GaInAsP/InP double heterojunction lasers and light emitting diodes." J. Appl. Phys. **6**399), pp.4688-4698.

Choi, K.-K., Levine, B.F., Bethea, C.G., Walker, J., and Malik, R.J., (1987), "Multiple quantum well 10 μm GaAs/$Al_xGa_{1-x}As$ infrared detector with improved responsivity." Appl. Phys. Lett. **50**(25), pp.1814-1816.

Chong, T.C., and Fonstad, C.G., (1989), "Theoretical gain of strained-layer semiconductor lasers in the large strain regime." IEEE J. Quantum Electron,. **25**(2), pp.171-178.

Chuang, S.L. (1991), "Efficient band-structure calculations of strained quantum wells." Phys. Rev. B. B**43**(12), pp.9649-9661.

Chiu, L.C., Yu, K.L., Margalit, S., Chen, T.R., Koren, U. Hasson, A., and Yariv, A., (1983), "Field and hot carrier enhanced leakage in InGaAsP/InP heterojunctions." IEEE J. Quantum Electron. **19**(9), pp.1335-1338.

Colbourne, P.D. and Cassidy, D.T., (1992), "Observation of dislocation stresses in InP using polarization-resolved photoluminescence." Appl. Phys. Lett. **61**(10), pp.1174-1176.

Colbourne, P.D. and Cassidy, D.T., (1992), "Dislocation detection using polarization-resolved photoluminescence." Can. J. Phys. **70** pp.803-812.

Coleman, J.J, Beernink, K.J., and Givens, M.E., (1992), "Threshold Current Density in Strained Layer $In_xGa_{1-x}As$-GaAs Quantum-Well Heterostructure Lasers." IEEE J. Quantum Electron. **28**(10), pp.1983-1989.

Corzine, W.W., Yan, R.H., and Coldren, L.A., (1993), *in* Quantum Well Lasers, *edited by* P. S. Zory, Jr. Academic Press, Inc. , Toronto.

Datta, S., (1989), Quantum Phenonmena. Modular Series on Solid State Devices, Vol. VIII, Addison-Wesley Publishing Company, New York.

Dutta, N.K., Lopata, J., Sivco, D.L., and Cho, A.Y., (1991), "Temperature dependence of threshold of strained quantum well lasrs." Appl. Phys. Lett. **58**(11), pp.1125-1127.

Dutta, N.K., Temkin, H., Tanbun-Ek, T., and Logan, R., (1990), "Linewidth enhancement factor for InGaAs/InP strained quantum well lasers." Appl. Phys. Lett. **57**(14), pp.1390-1392.

Dutta, N.K., (1982), "Calculated threshold current of GaAs quantum well lasers.", J. Appl. Phys. **53**(11), pp.7211-7214.

Dutta, N.K., and Nelson, J., (1982), "The case for Auger recombination in $In_{1-x}Ga_xAs_yP_{1-y}$." J. Appl. Phys. **53**(1), pp.74-92.

Dutta, N.K., and Nelson, J., (1981), "Temperature dependence of threshold of InGaAsP/InP double-heterostructure lasers and Auger recombination." Appl. Phys. Lett. **38**(6), pp.407-409.

Evans, J.D., Makino, T., Puetz, N., Simmons, J.G., and Thompson, D.A., (1992), "Strain-induced performance improvements in long-wavelength, multiple-quantum-well ridge-waveguide lasers with all quaternary active regions." IEEE Photon. Technol. Lett., **4**(4), pp.299-301.

Forest, S.R., Schmidt, P.H., Wilson, R.B., and Kaplan, M.L., (1984), "Relationship between the conduction-band discontinuities and band-gap differences of InGaAsP/InP heterojunctions." Appl. Phys. Lett. **45**(11), pp.1199-1201.

Fritz, I.J., Picaraux, S.T., Dawson, L.R., and Drummond, T.J., (1985), "Dependence of critical layer thickness on strain form $In_xGa_{1-x}As$/GaAs strained-layer superlattices." Appl. Phys. Lett. **46**(10), pp.967-969.

Fukushima, T., Kasukawa, A., Iwase, M., Namegaya, T. , and Shibata, M., (1993), "Compressively strained 1.3 μm InAsP/InP and GaInAsP/InP multiple quantum well lasers for high-speed parallel data transmission systems." IEEE J. Quantum Electron. **29**(6), pp.1536-1542.

Fumiyoshi, K., Yamanaka, T., Yamamoto, N., Yoshikuni, Y., Mawatari, H., Tohmori, T., Yamamoto, M., and Yokoyama, K., (1993), "Reduction of linewidth enhancement factor in InGaAsP-InP modulation-doped strained multiple-quantum-well lasers." IEEE J. Quantum Electron. **29**(6), pp.1553-1558.

Guy, D.R.P., Taylor, L.L., Besgrove, D.D., Apsley, N., and Bass, S.J., (1988), "High contrast-ratio electroabsorptive GaInAs/InP quantum well modulator." Electron. Lett. **24**(19), pp.1253-1255.

Hagen, A.H., Valster, A., Boermans, M.J.B., and van der Heyden, J., (1990), "Investigation of the temperature dependence of the threshold current density of GaInP.AlGaInP double-heterostructure lasers." Appl. Phys. Lett. **57**922) pp.2291-2293.

Hakki, B.W., and Paoli, T.L., (1973), "CW degradation at 300°K of GaAs double-heterostructure junction lasers. II. Electronic gain." J. Appl. Phys. **44**(9), pp.4113-4119.

Hakki, B.W., and Paoli, T.L., (1975), "Gain spectra in GaAs double-heterostructure injection lasers." J. Appl. Phys. **46**(3), pp.1299-1306.

Hayward, J.E., (1993), Spectral Properties of 1.3 μm InGaAsP Semiconductor Diode Lasers. Ph.Eng. Thesis, McMaster University, Hamilton, Ontario.

Hermann, C., and Pearsall, T.P., (1981), "Optical pumping and the valence-band light-hole effective mass in $Ga_xIn_{1-x}As_yP_{1-y}$ (y≈2.2x)", Appl. Phys. Lett. **38(6)**, pp.450-452.

Hermann, C., and Weisbuch, C., (1977), "$\vec{k} \cdot \vec{p}$ perturbation theory in III-V compounds and alloys: a reexamination.", Phys. Rev. B. **B15**, pp.823-833.

Hess, K., Vojak, B.A., Holonyak, Jr. N., Chin, R., and Dapkus, P.D., (1980), "Temperature dependence of threshold current for a quantum-well heterostructure laser.", Solid-State Electronics, **23**, pp.585-589.

Horikoshi, Y., (1982), in GaInAsP Alloy Semiconductors. *edited by* T.P. Pearsall, John Wiley & Sons Ltd. , New York.

Houghton, D.C., Perovic, D.D., Baribeau, J.-M., and Weatherly, G.C., (1990), "Misfit strain relaxation in Ge_xSi_{1-x}/Si heterostructures: The structural stability of buried strained layers and strained-layer superlattices." J. Appl. Phys. **67**(4), pp.1850-1862.

Huag, A., (1988), "Comparison of T_o-values of bulk and quantum-well semiconductor lasers." Electron. Lett. **24**(23), pp. 1442-1443.

Huang, J., and Casperson, L.W., (1993), "Gain and saturation in semiconductor lasers." Opt. Quantum Electron. **25**, pp.369-390.

Ishikawa, M., Shiozawa, H., Itaya, K., Hatakoshi, G., and Uematsu, Y., (1991), "Temperature dependence of the threshold current for InGaAlP visible laser diodes." IEEE J. Quantum Electron. **27**(1), pp.23-29.

Ji, G., Huang, D., Reddy, U.K., Henderson, T.S., Houdré, and Morkoç, H., (1987), "Optical investigation of highly strained InGaAs-GaAs multiple quantum well", J. Appl. Phys. **62**(8), pp.3366-3373.

Kane, E.O., (1979), "Band structure of narrow gap semiconductors.", Proceedings of the International Summer School on Narrow Gap Semiconductors, Physics and Applications, Nimes France, Sept. 3-15, 1979 (Berlin, Germany: Springer-Verlag.1980), p.13-31.

Kasukawa, A., Murgatroyd, I.J., Yoshihiro, I., Matsumoto, N., Fukushima, T., Okamoto, H. , and Kashiwa, S., (1989), "High quantum efficiency, high output power 1.3 μm GaInAsP buried graded-index separate-confinement-heterostructure multiple quantum well (GRIN-SCH-MQW) laser diodes." Japanese J. Appl. Phys. **28**(4), pp.L661-L663.

Kato, H., Iguchi, N., Chika, S., Nakayama, M., and Sano, N., (1986), "Photoluminescence study of $In_xAl_{1-x}As$-GaAs strained-layer superlattices." J. Appl. Phys. **59**(2), pp. 588-592.

Kazuhisa, U., Shinji, A., Tomonobu, T., and Naoki, C., (1990), "Novel method of determining conduction-band discontinuities by using monolayer energy splitting in quantum-well structures.", J. Appl. Phys. **67**(2), pp. 904-907.

Kinch, M.A., and Goodwin, M.W., (1985), "II-VI infrared superlattices.", J. Appl. Phys. 58(11).

Kolbas, R.M., Lo, Y.C., and Lee, J-H., (1990), "Laser properties and carrier collection in ultrathin quantum-well heterostructures." IEEE J. Quantum Electron. **26**(1), pp.25-31.

Koren, U., Miller, B.I., Su, Y.K., Koch, T.L., and Bowers, J.E., (1987), "Low internal loss separate confinement heterostructure InGaAs/InGaAsP quantum well laser.", Appl. Phys. Lett. **51**(21), pp.1744-1746.

Kuo, C.P., Vong, S.K., Cohen, R.M., and Sringfellow, G.B., (1985), "Effect of mismatch strain on band gap in III-V semiconductors." J. Appl. Phys. **57**(12), pp.5428-5432.

Lau, K.Y., (1993), *in* Quantum Well Lasers. *edited by* P. S. Zory, Jr. Academic Press, Inc, Toronto.

Laude, L.D., Pollak, F.H., and Cardona, M., (1971), "Effects of uniaxial stress on the indirect exiton spectrum of silicon." Phys. Rev. B, B3(8), pp.2623-2645.

Lawaetz, P., (1971), "Valence-band parameters in cubic semiconductors." Phys. Rev. B, B4(10), pp. 3460-3467.

Leopold, M.M., and Specht, A.P., (1987), "Temperature-dependent factors contributing to T_0 in graded-index separate-confinement-heterostructure single quantum well lasers." Appl. Phys. Lett. **50**(20), pp. 1403-1404.

Levine, B.F., Bethea, C.G., Hasnain, J. Walker, and Malik, R.J., (1988), "High-detectivity $D^*=1.0x10^{10}cm\sqrt{Hz}/W$ GaAs/AlGaAs multiquantum well $\lambda=8.3$ μm infrared detector." Appl. Phys. Lett. **53**(4), pp.296-298.

Li, G.P., Makino, T., Evans, J., and Beckett, D.J.S., (1992), "Circular beam emission from 1.3 μm InGaAsP strained multiquantum-well lasers." IEEE Photon. Technol. Lett. **4**(5), pp.419-301.

Lipsanen, H., Coblentz, D.L., Logan, R.A., Yadvish, R.D., Morton, P.A., and Temkin, H., (1992), "High-speed InGaAsP/InP multiple-quantum-well laser." IEEE Photon. Tech. Lett. **4**(7), pp.673-675.

Liu, P.L., Heritage, J.P., and Martinez, O.E., (1984), "Temperature dependence of the threshold current of an InGaAsP laser under 130-ps electrical pulse pumping." Appl. Phys. Lett. **44**(4), pp.370-372.

Loehr, J.P., and Singh, J., (1991), "Theoretical studies of the effect of strain on the performance of strained quantum well lasers based on GaAs and InP technology." IEEE J. Quantum Electron. **27**(3), pp.708-716.

Lui, Q.Q., Yamanaka, T., Yoshikuni, Y., Yokoyama, K., and Seki, S., (1993), "Suppression of Auger recombination effects in compressively strained quantum-well lasers." IEEE J. Quantum Electron. **29**(6), pp.1544-1547.

Lui, W.W., Yamanaka, T., Yoshikuni, Y, Seki, S., and Yokoyama, K., (1993), "Unifying explanation for recent temperature sensitivity measurements of Auger recombination effects in strained InGaAs/InGaAsP quantum-well lasers." Appl. Phys. Lett. **63**(12), pp.1616-1618.

Luttinger, J.M., and Kohn, W. (1955), "Motion of electrons and holes in perturbed periodic fields." Phys. Rev. **97**(4), pp.869-883.

Luttinger, J.M., (1956), "Quantum theory of cyclotron resonance in semiconductors: general theory." Phys. Rev. **102**(4), pp. 1030-1041.

Lu, X.Z., Garuthara, Lee, S., and Alfano, R.R., (1988), "Gallium arsenide photoluminescence under picosecond-laser-driven shock compression." Appl. Phys. Lett. **52**(2), pp.93-95.

McIlroy, P.W.A., Kurobe, A., and Uematsu, Y., (1985), "Analysis and application of theoretical gain curves to the design of multi-quantum-well lasers." IEEE J. Quantum Electron. **21**, pp.1958-1963.

Makino, T., and Murgatroyd, I.J., (1990), "Simple approximate relations in the design of multi-quantum well lasers." Yokohama R & D Laboratories. The Furukawa Electric Co. Ltd., private communication.

Marzin, J.Y., Gérard, J.M., Voisin, P., and Brum, J.A. (1990), *in* Strained-Layer Superlattices: Physics. Semi-conductors and Semimetals. Vol. 32. Academic Press, Inc., New York.

Matsumoto, N., Kasukawa, A., Namegaya, T., and Okamoto, H., (1991), "Low threshold current, high quantum efficiency 1.5 μm GaInAs-GaInAsP GRIN-SCH single quantum well laser diodes." IEEE J. Quantum Electron. **27**(6), pp.1790-1793.

Matthews, J.W., and Blakeslee. A.E., (1974), "Defects in epitaxial multilayers I. Misfit dislocations." J. Cryst. Growth **27**, pp.118-125.

Mathur, A., Osinski, J.S., Grodzinski, P., and Dapkus, P.D., (1993), "Comparative study of low-threshold 1.3 μm strained and lattice-matched quantum-well lasers." IEEE Photon. Technol. Lett., **5**(7), pp.753-755.

Mozer, A.P., Hausser, A., and Pilkuhn, M.H., (1985), "Quantitiative evaluation of gain and losses in quanternary lasers." IEEE J. Quantum Electron **21** pp.719.

Nag, B.R., and Sanghamitra, M., (1991), "Band offset in InP/$Ga_{0.47}In_{0.53}As$ heterostructures", Appl. Phys. Lett. **58**(10), pp.1056-1058.

Nag, B.R., (1980), Electron Transport in Compound Semiconductors. Springer-Verlag, New York.

Nahory, R.E., Pollack, M.A., Johnston, Jr. W.D., and Barns, R.L., (1978), "Band gap versus composition and demonstration of Vegard's law for $In_{1-x}Ga_xAs_yP_{1-y}$ lattice matched to InP" Appl. Phys. Lett. **33**, pp. 659-661.

Namegaya, T., Katsumi, R. Iwai, N., Namiki, S., Kasukawa, A., Hiratani, Y., and Kikuta, T., (1993), "1.48 μm high-power GaInAsP-InP graded-index separate-confinement-heterostructure multiple-quantum-well laser diodes." IEEE J. Quantum Electron. **29**(6), pp.1924-1931.

Nicholas, R.J., Sessions, S.J., and Portal, J.C., (1980), "Cyclotron resonance and the magnetophonon effect in $Ga_xIn_{1-x}As_yP_{1-y}$" Appl. Phys. Lett. **37**, pp.178-180.

Nye, J.F., (1957), Physical Properties of Crystals. At The Claredon Press, Oxford.

O'Gorman, J., Levi, A.F.J., Tanbun-Ek, T., Coblentz, D.L., and Logan, R.A., (1992), "Temperature dependence of long wavelength semiconductor lasers.", Appl. Phys. Lett. **60**(9), pp.1058-1060.

O'Gorman, Levi, A.F.J., Schmitt-Rink, S., Tanbun-Ek, T., Coblentz, D.L., and Logan, R.A., (1992), "On the temperature sensitivity of semiconductor lasers." Appl. Phys. Lett. **60**(2), pp.157-159.

Okada, T., (1993), "Relaxation related phenomena in $(In_{1-x}Ga_x)(As_yP_{1-y})$ strained layers grown on InP (001) substrates." private communication.

Okamoto, M., Sato, K., Mawatari, H., Kano, F., Magari, K., Kondo, Y., and Itaya, Y., (1991), "TM mode gain enhancement in GaInAs-InP lasers with tensile strained-layer superlattice." IEEE J. Quantum Electron. **27**(6), pp.1463-1469.

Ohtoshi, T., and Chinone, N., (1989), "Linewidth enhancement factor in strained quantum well lasers." IEEE Photon. Technol. Lett. **1**(6), pp.117-119.

Olshansky, R., Su, C.B., Manning, J. and Powazinik, W., (1984), "Measurement of radiative and nonradiative recombination rates in InGaAsP and AlGaAs light sources." IEEE J. Quantum Electron. **20**(8), pp.838-854.

Osbourn, G.C., (1982), "Strained-layer superlattices from lattice mismatched materials." J. Appl. Phys. **53**(3) pp.1586-1589.

Osinski, J.S., Zou, Y., Grodzinski, P., Mathur, A., and Dapkus, P.D., (1992), "Low-threshold-current-density 1.5 μm lasers using compressively strained InGaAsP Quantum Wells." IEEE Photon. Technol. Lett. **4**(1) pp.10-13.

Pankove, J.I., (1968), "Temperature dependence of emission efficiency and lasing threshold in laser diodes." IEEE J. Quantum Electron. **4**(4), pp.119-122.

Pearsall, T. P., (1990), *in* Strained-Layer Superlattices: Physics. Semi-conductors and Semimetals. Vol. 32. Academic Press, Inc., New York.

Perea, H.E., Mendez, E.E., and Fonstad, C.G., (1980), "Electron effective mass in $In_uGa_{1-u}P_vAs_{1-v}$ for $0 \le v \le 1$." J. Electron. Mater. **9**, pp.459-466.

Pikus, G.E., and Bir.G.L., (1960), "Effect of deformation on the hole energy spectrum of germanium and silicon." Soviet Phys.-Solid State **1**(136), pp. 1502-1517.

Poguntke, K.R., and Adams, A.R., (1992), "Analysis of radiative efficiency of long wavelength semiconductor lasers." Electron. Lett. **28**(1), pp.41-42.

Pollak, F.H., (1990), *in* Strained-Layer Superlattices: Physics, Semi-conductors and Semimetals. Vol. 32. Academic Press, Inc., New York.

Pollak, F.H., and Cardona, M., (1968), "Piezo-electroflectance in Ge, GaAs, and Si." Phys. Rev. **172**(3), pp.816-837.

Rezek, E.A., Holonyak, Jr., N., and Fuller, B.K., (1980), "Temperature dependence of threshold current for coupled multiple quantum-well $In_{1-x}Ga_xP_{1-z}As_z$-InP heterostructure laser diodes." J. Appl. Phys. **51**(5) pp.2402-2405.

Rosenzweig, M., Möhrle, M., Düser, H., and Venghaus, H., (1991), "Threshold-current analysis of InGaAs-InGaAsP multiquantum well separate-confinement lasers." IEEE J. Quantum Electron. **27**(6), pp. 1804-1810.

Sanders, G.D., and Chang, Y-C., (1985), "Effects of uniaxial stress on the electronic and optical properties of GaAs-$Al_xGa_{1-x}As$ quantum wells." Phys. Rev. B, B**32**(6), pp. 4282-4285.

Sermage, B., Heritage, J.P., and Dutta, N.K. (1985), "Temperature dependence of carrier lifetime and Auger recombination in 1.3μm InGaAsP." J. Appl. Phys. **57**(12), pp.5443-5449.

Streifer, W., Scifres, D.R., and Burnham, R.D., "Optical analysis of multiple-quantum-well lasers." Appl. Opt. **18**, pp.3547.

Su, C.B., Olshansky, R., Manning, J. and Powazinik, W., (1984), "Temperature dependence of threshold current in III-V semiconductor lasers: Experimental prediction and explanation." Appl. Phys. Lett. **44**(11) pp.1030-1032.

Suematsu, Y., Iga, K., and Kishino, K., (1982), *in* GaInAsP Alloy Semiconductors, *edited by* T.P. Pearsall, John Wiley & Sons Ltd, New York.

Sugimura, A., (1981), "Band-to-band Auger effect on the output power saturation in InGaAsP LED's." IEEE J. Quantum Electron. **17**(4). pp.441-444.

Takasaki, B.W., Preston, J.S., Evans, J.D., Simmons, J.G., and N. Puetz, (1993), "Observation of separate electron and hole escape rates in unbiased strained InGaAsP multiple quantum well laser structures." Appl. Phys. Lett. **62**(20), pp.2525-2527.

Takasaki, B.W., Preston, J.S., Evans, J.D., Simmons, J.G., Charbonneau, S., and Moss, D., (1992), "Carrier lifetimes in strained InGaAsP multiple-quantum-well laser structures." Can. J. Phys. **70** pp.1017-1022.

Takasaki, B.W., (1992), Relaxation of Optically Generated Carriers in Strained InGaAsP Multiple Quantum Well Laser Structures. M.Sc. Thesis, McMaster University, Hamilton, Ontario.

Tanbun-Ek, T., Logan, R.A., Temkin, H., Berthold, K., Levi, A.F.J., and Chu, S.N.G., (1989), "Very low threshold InGaAs/InGaAsP graded index separate confinement heterostructure quantum well lasers grown by atmospheric pressure metalorganic vapor phase epitaxy." Appl. Phys. Lett. **55**(22), pp.2283-2285.

Tanbun-Ek, T., Olsson, N.A., Logan, R.A., Wecht, K.W., and Sergent, A.M., (1991), "Measurements of the polarization dependent of the gain of strained multiple quantum well InGaAs-InP lasers." IEEE Photon. Technol. Lett. **3**(2), pp.103-105.

Temkin, H., Coblentz, D., Logan, R.A., van der Ziel, J.P, Tanbun-Ek, T., Yadvish, R.D., and Sergent, A.M., (1993), "High temperature characteristics of InGaAsP/InP laser structures." Appl. Phys. Lett. **62**(19), pp.2402-2011.

Temkin, H., Tanbun-Ek, T., Logan, R.A., Cebula, D.A., and Sergent, A.M., (1991), "High temperature operation of lattice matched and strained InGaAs-InP quantum well lasers." IEEE Photon. Technol. Lett., **3**(2), pp.100-102.

Temkin, H., Tanburn-Ek, T., Logan, R.A., Lewis, J.A., and Dutta, N.K., (1990), "InGaAs/InP graded-index quantum well lasers with nearly ideal static characteristics." Appl. Phys. Lett. **56**(13), pp.1222-1224.

Thijs, P.J.A., Tiemeijer, L.F., Kuindersma, P.I., Binsma, J.J.M., and Vand Dongen, T., (1991), "High-performance 1.5 μm wavelength InGaAs-InGaAsP strained quantum well lasers and amplifiers." IEEE J. Quantum Electron. **27**(6), pp.1426-1439.

Thijs, P.J.A., Montie, E.A., and Dongen, T.van, (1991), "Structures for improved 1.5 μm wavelength lasers grown by LP-OMVPE; InGaAs-InP strained-layer quantum wells a good candidate." J. Crystal Growth **107**, pp.731-740.

Thijs, P.J.A., and Dongen, T.V., (1989), "High quantum efficiency, high power, modulation doped GaInAs strained-layer quantum well laser diodes emitting at 1.5 μm." Electron. Lett. **25**(25), pp.1735-1737.

Thompson, G.H.B. (1981), "Temperature dependence of threshold current in (GaIn)(AsP) DH lasers at 1.3 and 1.5 μm wavelength." IEEE Proc. **128**, Pt.I, No.2, pp.37-43.

Tiemeijer, L.F., Thijs, P.J.A., de Waard, P.J., Binsma, J.J.M., and v. Dongen, T., (1991), "Dependence of polarization, gain, linewidth enhancement factor, and K factor on the sign of the strain of InGaAs/InP strained-layer multiquantum well lasers." Appl. Phys. Lett. **58**(24), pp.2738-2740.

Tsang, W.T., Kapre, R., Wu, M.C., and Chen, Y.K., (1992), "Low-threshold InGaAs strained-layer quantum well lasers (λ=0.98 μm) with GaInP cladding layers prepared by chemical beam epitaxy." Appl. Phys. Lett. **61**(7), pp.755-757.

Tsang, W.T., Choa, F.S., Logan, R.A., Tanbun-Ek, T., Sergent, A.M., and Wecht, K.W., (1992), "Reduced temperature dependence of threshold current by broadband enhanced feedback: A new approach and demonstration." Appl. Phys. Lett. **60**(1), pp.18-20.

Tsang, W.T., (1987), *in* Semiconductors and Semimetals Vol. 24: Applications of Multiquantum Wells, Selective Doping, and Superlattices. *edited by* R. Dingle, Academic Press, San Diego.

Verdeyen, J.T., (1989), Laser Electronics, 2nd ed. Prentice Hall, New Jersey.

Walpita, L.M., (1985), "Solutions for planar optical waveguide equations by selecting zero elements in a characteristic matrix." J. Opt. Xoc. Am. A., **2**(4), pp. 595-602.

Weisbuch, C., and Vinter, B., (1991), Quantum Semiconductor Structures: Fundamentals and Applications. Academic Press, Inc., Toronto.

Westbrook, L.D., (1986), "Measurement of dg/dN and dn/dN and their dependence on photon energy in λ=1.5 μm InGaAsP laser diodes." IEE Proceedings, **133**, Pt. J, No.2, pp.135-142.

Wood, T.H., Carr, T.H., Burrus, C.A., Miller, B.I., and Koren, U., (1988), "Large electroabsorption effect in GaInAs/InP multiple quantum well (MQW) optical modulator grown by OMVPE." Electron. Lett. **24**(14), pp.840-841.

Woodside, S. H., (1992), Linewidth of Short External Cavity Semiconductor Lasers. M.Eng. Thesis, McMaster University, Hamilton, Ontario.

Yablanovitch, E., and Kane, E.O., (1988), "Band structure engineering of semiconductor lasers for optical communications." IEEE J. of Lightwave Tech. **6**(8) pp.1292-1299.

Yamada, M., Ogita, S., Miyaba, T., and Nahida, Y., (1986), "A theoretical analysis of lasing gain and threshold current in GaAs-AlGaAs SCH lasers." Transactions of the IECE of Japan. **E69**(9), pp.948-954.

Yamakoshi, S., Wada, S.O., Umebu, I., and Sakurai, T., (1982), "Direct observation of electron leakage in InGaAsP/InP double heterostructure." Appl. Phys. Lett. **40**(92), pp.144-146.

Yano, M., Imai, H., and Takusagawa, M., (1981), "Analysis of threshold temperature characteristics for InGaAsP/InP double heterojunction lasers." J. Appl. Phys. **52**(5), pp.3172-3175.

Yano, M., Imai, H., and Takusagawa, M., (1981), "Analysis of electrical, threshold, and temperature characteristics for InGaAsP/InP double heterojunction lasers." IEEE J. Quantum Electron. **17**(9), pp.1954-1963.

Yano, M., Nishi, H., and Takusagawa, M., (1980), "Temperature characteristics of threshold current in InGaAsP/InP double-heterostructure lasers." J. Appl. Phys. **51**(98), pp.4022-4028.

Yokoyama, N., (1986), "Resonant-tunneling hot electron transistors (RHET): Potential and applications." Extended Abstracts of the 18th Conference on Solid State Devices and Materials, Tokyo, pp.347-350.

Yokoyama, N., Imamura, K., Muto, Shunichi, M., Hiyamizu, S., and Nishi, H., (1985), "A new functional, resonant-tunneling hot electron transistor (RHET)." Japanese J. Appl. Phys. **24**(11), pp.L853-L854.

Za, C.E., Bhat, R., Favire, Jr., F.J., Menocal, S.G., Andreadakis, N.C., Cheung, K.-W. Hwang, D.-M.D., Koza, M.A., and Lee, T.-P., (1991), "Low-threshold 1.5 μm compressive-strained multiple- and single-quantum-well lasers." IEEE J. Quantum Electron. **27**(6), pp.1440-1450.

Za, C.E., Bhat, R., Menocal, S.G., Favire, F., Lin, P.S.D., Gozdz, A.S., Andreadakis, N.C., Pathak, B., Koza, M.A., and Lee, T.P., (1991), "Low-threshold and narrow-linewidth 1.5 μm compressive-strained multiquantum-well distributed-feedback lasers." Electron. Lett. **27**(10), pp.1628-1630.

Zhang, G., Näppi, J., Vänttinen, K., Asonen, H., and Pessa, M., (1992), "InGaAs/GaAs/GaInP SCH-SQW Lasers with low threshold current and high internal quantum efficiency." Electron. Lett. **28**(6), pp.595-597.

Zhu, L.D., Zheng, B.Z. and Feak, G.A.B., (1989), "Temperature dependence of optical gain, quantum efficiency, and threshold current in GaAs/GaAlAs graded-index separate-confinement heterostructure single-quantum-well lasers." IEEE J. Quantum Electron. **25**(9), pp.2007-2012.

Zhuang, W., Zheng, B., Xu, J., Li, Y., Xu, J., and Chen, P., (1985), "Carrier loss resulting from Auger recombination in InGaAsP/InP double heterojunction laser diodes: Spectroscopy of 950 nm high energy emission." IEEE J. Quantum Electron. **21**(6), pp.712-715.

Zory, Jr., P.S., editor., (1993), Quantum Well Lasers. Academic Press, Inc. , Toronto.

Zou, Y., Osinski, J.S., Grodzinski, P., Dapku, P.D., Rideout, W.C., Sharfin, W.F., Schlafer, J., and Crawford, F.D., (1993), "Experimental study of Auger recombination, and temperature sensitivity of 1.5 μm compressively strained semiconductor lasers." IEEE J. Quantum Electron., **29**(6), pp.1565-1575.